



Universidad de Valladolid

FACULTAD DE CIENCIAS

**DEPARTAMENTO DE FÍSICA DE LA MATERIA
CONDENSADA, CRISTALOGRAFÍA Y MINERALOGÍA**

TESIS DOCTORAL:

**X-Ray Imaging Applied to the Characterization of Polymer
Foams' Cellular Structure and Its Evolution**

Presentada por Samuel Pardo Alonso para optar al grado de
Doctor por la Universidad de Valladolid

Dirigida por:

Dr. Eusebio Solórzano

Dr. Miguel Ángel Rodríguez Pérez

AGRADECIMIENTOS **11**

INTRODUCCIÓN EN ESPAÑOL **15**

MARCO DE LA TESIS Y NECESIDAD DE LA INVESTIGACIÓN	16
OBJETIVOS DE LA INVESTIGACIÓN	20
PRINCIPALES NOVEDADES DEL TRABAJO	23
ESTRUCTURA DE ESTA TESIS	24
REFERENCIAS	26

1. INTRODUCTION **33**

1.1. FRAMEWORK OF THIS THESIS	34
1.2. OBJECTIVES	39
1.3. MAIN NOVELTIES	41
1.4. STRUCTURE OF THIS THESIS	42
REFERENCES	47

2. BASIC CONCEPTS ON FOAMS **53**

2.1. DESCRIPTION OF FOAMED STRUCTURES	53
2.1.1. FUNDAMENTAL COMPONENTS	53
2.1.2. MACROSCOPIC DESCRIPTORS	55
2.1.3. PRIMARY MICROSCOPIC DESCRIPTORS	56
2.1.4. OTHER MICROSCOPIC DESCRIPTORS	58
2.1.5. ADVANCED DESCRIPTORS	61
2.2. POLYMER FOAMS PRODUCTION	64
2.2.1. BLOWING AGENTS	64
2.2.2. FOAMING TECHNOLOGIES	65
2.3. FOAMING DYNAMICS	69
2.3.1. FOAMING MECHANISMS	69
REFERENCES	79

3. MATERIALS SELECTION **83**

3.1. POLYURETHANE FOAMS	84
3.2. POLYOLEFIN FOAMS	88
3.3. NANOADDITIVES	92
3.4. COMMERCIAL FOAMS	96
3.5. LIST OF MATERIALS	97
REFERENCES	98

4. DIGITAL X-RAY IMAGING **103**

4.1. GENERAL CONCEPTS	105
4.1.1. ARCHITECTURE OF DIGITAL IMAGING	105
4.1.2. IMAGE RESOLUTION	107
4.2. OTHER ASPECTS OF IMAGE QUALITY	108
4.2.1. SIGNAL-TO-NOISE RATIO	109
4.2.2. DEFECTIVE PIXELS	110
4.2.3. ARTIFACTS	110
4.3. DIGITAL IMAGES PROCESSING	111
4.3.1. DIGITAL FILTERING	111
4.3.2. IMAGE BINARIZATION	114
4.4. X-RAY IMAGING FUNDAMENTALS	119
4.4.1. MATTER-BEAM INTERACTION	119
4.4.2. X-RAY SOURCES: GENERATION	121
4.4.3. X-RAY DETECTION	124
4.5. X-RAY RADIOSCOPY	126
4.5.1. MICROFOCUS X-RAY SYSTEM AT CELLMAT	127
4.6. X-RAY COMPUTED TOMOGRAPHY	133
4.6.1. VOLUMES RECONSTRUCTION PRINCIPLE: BACK-PROJECTION ALGORITHM	134
4.6.2. CELLMAT SCANNER	136
4.6.3. UGCT μ CT SCANNER	136
4.7. TOMCAT BEAMLINER AT SWISS LIGHT SOURCE	137
4.8. IMAGE ANALYSIS SOFTWARE	140
4.9. APPLICATION OF IMAGE CORRECTION PROCEDURES	141
4.9.1. DEFECTIVE PIXEL CORRECTION	141
4.9.2. BACKGROUND AND SHADING CORRECTION	142
4.9.3. X-RAY IMAGING ARTIFACTS	144

4.10. PROTOCOLS OF IMAGE ANALYSIS	146
4.10.1. <i>IN-SITU</i> : DENSITY AND CELL SIZE EVOLUTION	146
4.10.2. <i>EX-SITU</i> : MORPHOLOGICAL ANALYSIS	149
“APPLICATION OF A MICROFOCUS X-RAY IMAGING APPARATUS TO THE STUDY OF CELLULAR POLYMERS”	157
REFERENCES	166
<u>5. STUDIES ON FOAMING MECHANISMS</u>	<u>169</u>
5.1. SUMMARY	169
“IN-SITU EVIDENCE OF THE NANOPARTICLE NUCLEATING EFFECT IN POLYURETHANE-NANOCLAY FOAMED SYSTEMS”	173
“TIME-RESOLVED X-RAY IMAGING OF NANOFILLER-PU REACTIVE FOAM SYSTEMS”	183
“EFFECT OF CARBON NANOFILLERS ON FLEXIBLE POLYURETHANE FOAMING FROM A CHEMICAL AND PHYSICAL PERSPECTIVE”	191
“X-RAY RADIOSCOPY <i>IN-SITU</i> STUDIES IN THERMOPLASTIC POLYMER FOAMS”	207
<u>6. 3D STUDIES ON CELLULAR STRUCTURE</u>	<u>215</u>
6.1. SUMMARY	216
“3D ANALYSIS OF PROGRESSIVE MODIFICATION OF THE CELLULAR ARCHITECTURE IN POLYURETHANE NANOCOMPOSITE FOAMS VIA X-RAY MICROTOMOGRAPHY”	219
“μCT-BASED ANALYSIS OF THE SOLID PHASE IN FOAMS: CELL WALL CORRUGATION AND OTHER PRACTICAL MICROSCOPIC FEATURES”	227
<u>7. ULTRAFAST TOMOGRAPHY AT TOMCAT BEAMLINE</u>	<u>247</u>
7.1. SUMMARY OF THE SYNCHROTRON CAMPAIGN	247
“BUBBLE NUCLEATION AND GROWTH BY REAL-TIME SYNCHROTRON TOMOGRAPHY: A COMPARISON WITH CLASSICAL MODELS”	253
REFERENCES	261
<u>8. CONCLUSIONS AND PERSPECTIVES</u>	<u>267</u>
<u>RESUMEN EN ESPAÑOL</u>	<u>273</u>

AGRADECIMIENTOS

A mis padres,

A María,

Quiero expresar en estas líneas mi más sincero agradecimiento a todas las personas que con su ayuda han colaborado en los resultados de este trabajo y formado parte de él. En especial al Dr. Eusebio Solórzano y al Dr. Miguel Ángel Rodríguez Pérez por su propuesta de tesis, su orientación, su experiencia y la motivación que me han sabido trasladar a lo largo de estos años. Sin su esfuerzo y dedicación esta investigación no sería una realidad.

Especial mención requiere el interés mostrado por este trabajo y la oportunidad de realizar parte de él en las instalaciones científicas de las que forman parte los doctores Francisco García-Moreno (HZB, Berlín) y Rajmund Mokso (PSI, Villigen). Igualmente quiero agradecer la colaboración de las doctoras María del Mar Bernal y Raquel Verdejo (ICTP, CSIC), así como de todo el equipo del UGCT (Gante, Bélgica) y el resto de colegas que han colaborado. Agradezco el esfuerzo de los miembros del tribunal de tesis así como de los revisores por el interés que han mostrado en el trabajo y sus comentarios.

Quiero extender este agradecimiento al Dr. José Antonio de Saja. Sin su labor hoy no sería realidad la labor científica y tecnológica que se desarrolla en el laboratorio CellMat y en la Universidad de Valladolid. Igualmente, me gustaría expresar mi gratitud a todos mis compañeros que han formado y forma parte de CellMat y del Departamento de Física de la Materia Condensada, Cristalografía y Mineralogía de la Universidad de Valladolid. Es obligada la mención al apoyo económico recibido por la Universidad de Valladolid y del Fondo Social Europeo a través de la Junta de Castilla y León.

Concluyo con un agradecimiento muy especial a mis padres, mi hermana, familia y amigos. Mi más sincero agradecimiento por vuestro apoyo.

INTRODUCCIÓN EN ESPAÑOL

En la naturaleza es posible encontrar diversos ejemplos de materiales que poseen estructura celular. La madera, el corcho, el coral, las esponjas o incluso los huesos humanos son algunos de los ejemplos más representativos. Por otro lado, en la actualidad se fabrican multitud de materiales que tratan de imitar la estructura de estos materiales. Podemos citar múltiples ejemplos, que van desde aquellos que consisten en la repetición regular de una celda unidad dando lugar a estructuras tipo *honeycomb*, usadas en aplicaciones estructurales, hasta espumas de diferentes materiales (líquidos, polímeros, metales, cerámicas, etc.) que poseen una estructura interna porosa formada por una fase gaseosa que se dispone en forma de burbujas distribuidas aleatoriamente [1,2,3,4,5]. Es importante destacar que algunos de estos materiales son de uso tan cotidiano como las bandejas para envasado de alimentos. Otros ejemplos similares son los colchones, los asientos y sofás, varias piezas del interior de los automóviles, el pan o la espuma de detergente.

La estructura celular es la característica común de estos materiales que consiste en una fase gaseosa dispersada en un material sólido o líquido en el caso de espumas en base acuosa. La presencia de la fase gaseosa da lugar a una importante reducción de densidad, lo que se traduce en ahorro de materia prima que conlleva implícita una reducción de costes y energía consumida [6,7]. Desde este punto de vista, los materiales celulares pueden ser considerados como productos respetuosos con el medio ambiente, ya que existe un ahorro de materia prima durante su fabricación. Además del mencionado ahorro en peso, la inclusión de la fase gaseosa permite extender el rango de propiedades físicas en comparación con sus respectivos sólidos. Así pues, podemos encontrar materiales que presentan ultra-baja conductividad térmica, alta capacidad de absorción de energías de impacto, excelente rigidez y resistencia mecánica a bajo peso y, en algunos casos particulares, son excelente absorbentes acústicos. Finalmente, cabe destacar que el control sobre el proceso de inclusión/generación de la fase gaseosa permite diseñar estos materiales a medida para satisfacer un determinado requerimiento demandado por una aplicación concreta.

Todas estas razones hacen que los materiales celulares se empleen en multitud de aplicaciones de los sectores aeronáutico, automoción, energía renovables, construcción, confort, envasado, embalaje, biotecnología, biomedicina, etc. [8]. Como dato relevante dentro del sector del plástico, podemos destacar un consumo 300 millones de toneladas de plásticos celulares en el mundo durante el año 2012. Esta cantidad representa un 10% del consumo total de plásticos. Además el sector de los plásticos celulares presenta una tasa de crecimiento del 4% anual estimada para el período 2010-2016 [9].

Algunos ejemplos de aplicaciones con indudable éxito comercial de los materiales espumados, en particular de los plásticos, son la espuma de poliuretano (PU) utilizada en aislamiento térmico y asientos, el poliestireno expandido (EPS) utilizado en embalaje, el poliestireno extruido (XPS) empleado en aislamiento térmico y envasado alimentario, las espumas de PVC (tuberías y perfiles estructurales) o las espumas de poliolefinas (embalaje, flotación y aislamiento térmico y acústico). Cabe destacar además que el PU y el PS constituyen hasta el 90% del consumo total de materiales celulares. Sin embargo, a pesar del indudable éxito comercial, aún existen lagunas científicas en algunos aspectos de la relación proceso-estructura-propiedades de estos materiales. El desarrollo y la mejora de estos materiales han sido conseguidos gracias tanto a estudios empíricos como estudios científicos de fabricación y caracterización. De la misma manera han contribuido el análisis teórico y empírico de los mecanismos de espumado. No obstante, aún existe campo por explorar y fenómenos que no han sido completamente comprendidos o de los que se puede extraer más y más completa información que permita avanzar tanto el conocimiento sobre estos materiales como su desarrollo.

Es hacia algunas de estas lagunas científicas a las que se dirigen principalmente los objetivos de esta tesis. Con el objetivo de centrar al lector comenzamos se expone este capítulo introductorio dividido en tres secciones. En primer lugar se presenta el marco científico en que se desarrolla esta tesis. Posteriormente se enuncian los objetivos principales de la investigación y una descripción de los hitos propuestos para conseguir los objetivos fundamentales de la investigación. Finalmente se explica la estructura de los siguientes capítulos así como la organización de las publicaciones científicas que se presentan como parte de los resultados.

MARCO DE LA TESIS Y NECESIDAD DE LA INVESTIGACIÓN

Este trabajo de investigación forma parte de las investigaciones en materiales celulares dirigidas por Prof. Dr. Miguel Ángel Rodríguez-Pérez en el Laboratorio CellMat del Departamento de Física de la Materia Condensada de la Universidad de Valladolid.

El Laboratorio CellMat se creó en 1999 en la Universidad de Valladolid tras la defensa de la primera tesis doctoral dentro de una línea de trabajo sobre propiedades térmicas y mecánicas de las espumas de poliolefinas llevada a cabo por Miguel Ángel Rodríguez Pérez y dirigida por José Antonio de Saja [10]. En un principio la investigación estuvo orientada fundamentalmente a la caracterización de espumas de poliolefinas y como resultado se defendieron varias tesis doctorales y se publicaron diversos trabajos científicos [11, 12, 13, 14, 15, 16, 17, 18, 19, 20, 21, 22, 23, 24, 25, 26, 27, 28, 29, 30, 31, 32]. Gracias al conocimiento adquirido en la caracterización de las espumas poliolefínicas el grupo pudo avanzar en otras líneas de trabajo adentrándose en los procesos de producción de dichos materiales celulares. En 2002, se inició de forma paralela una línea de trabajo en espumas de aluminio [33]. Actualmente, las líneas de

investigación del grupo se dirigen fundamentalmente a cuatro grandes tipos de materiales de interés científico-tecnológico. Estos materiales son las espumas microcelulares y sub-microcelulares [34 , 35 , 36 , 37 , 38 , 39], espumas de nanocompuestos [40, 41, 42, 43, 44, 45, 46, 47, 48], en base bioplásticos [49, 50, 51, 52, 53, 54, 55, 56] y espumas de aluminio [57, 58, 59, 60, 61, 62, 63, 64, 65]. Estas líneas de trabajo tratan de cubrir la producción a escala de laboratorio, la caracterización y modelización de la estructura y determinación de propiedades sin descuidar las potenciales aplicaciones finales.

Además, paulatinamente se ha ido incorporando al grupo un conjunto de técnicas de caracterización “no convencionales” que permiten adquirir un conocimiento aplicable directamente al desarrollo tecnológico de estos materiales. Esta novedosa línea se dirige al desarrollo de técnicas no destructivas que permiten obtener información sobre los procesos [66, 67]. En este sentido durante los últimos años CellMat ha desarrollado diversos sistemas de adquisición de imagen y equipos de caracterización para investigar los mecanismos que ocurren durante los distintos procesos de espumado y que en definitiva son los responsables de la estructura celular resultante. El desarrollo de estas técnicas pretende obtener un conocimiento único sobre estos mecanismos que complementa el actual *know-how* de CellMat.

Hasta la obtención de los primeros resultados de esta tesis, los procedimientos tradicionalmente empleados para analizar los mecanismos de espumado se basaban en el estudio de los estados inicial y final del material sin evidencias empíricas sobre qué ocurre en los estados intermedios del proceso. Es decir, la estrategia habitual para obtener información sobre la conexión proceso-estructura sólo disponía del estudio de los estados inicial y final del proceso. Los estadios intermedios no eran analizados, por lo que parte de la información sobre los mecanismos físico-químicos responsables de la evolución de la estructura no se tenía en cuenta. Por ello, estos métodos tradicionales eran poco exactos cuando se trataba de estudiar los diferentes fenómenos físico-químicos que ocurren durante el espumado (nucleación, crecimiento, coalescencia, *coarsening* y drenaje) que son responsables de la estructura celular final observada.

La obtención de esta información, oculta a priori, hace necesarias las denominadas técnicas *in-situ*, gracias a las cuales estos estadios intermedios son accesibles y pueden ser investigados. Es en esta última necesidad donde los avances en instrumentación registrados durante los últimos años permiten desarrollar novedosas técnicas de estudio capaces de obtener información sin interferir en un proceso dinámico. Estas técnicas se convierten en herramientas fundamentales a la hora de saber qué ocurre en cada instante de un proceso. Además, el desarrollo de técnicas de imagen tales como la termografía o la imagen mediante rayos X han facilitado avances significativos. Su alto grado de desarrollo actual y su relativo bajo coste hace de algunas de estas técnicas de imagen herramientas idóneas para obtener y cuantificar datos sobre los estadios intermedios del cualquier proceso y en particular de los procesos de espumado.

Una secuencia de imágenes ópticas de un proceso de expansión es un ejemplo de técnica *in-situ* que nos permite obtener mediante el análisis de imagen información sobre la velocidad de expansión, el grado de expansión, la presencia de defectos, la morfología, etc. No obstante, el concepto *in-situ* puede ser definido de manera más restrictiva aplicado a aquellas técnicas que, además de obtener información sobre un proceso, son capaces de proporcionar información sobre la estructura interna sin interferir con él. Es decir, desde este punto de vista la imagen óptica no sería considerada técnicas *in-situ*, pues sólo permite observar la forma externa. En cambio, otras técnicas como la difracción de rayos X o la radiografía, ambas con resolución temporal si serían consideradas dentro de esta definición más restrictiva ya que son capaces de ir un poco más lejos y aportar información que permanece oculta en el proceso mientras éste evoluciona.

En concreto, una de las técnicas *in-situ* más versátiles y con mayor potencial es la radioscopia de rayos X, que consiste en la adquisición de secuencias de radiografías en el tiempo. La radioscopia, gracias a la resolución en el tiempo, permite la visualización y el posterior estudio de la evolución de la estructura interna de las espumas durante su expansión. También es importante destacar el carácter no destructivo y no invasivo de esta técnica como una de sus características más interesantes ya que permite observar y cuantificar la evolución de magnitudes durante los procesos de espumado. Además, el desarrollo actual de los equipos de radiografía hace que sea una técnica idónea para su aplicación en el área de los materiales celulares plásticos [68, 69, 70, 71]. Mención especial merecen los trabajos previos realizados que hace uso de la radioscopia en el campo de las espumas metálicas con excelentes resultados [72,73,74].

De manera opuesta a las técnicas *in-situ* pero a la vez complementaria en cuanto a la información que aportan, se encuentran las técnicas *ex-situ*. Éstas son aquellas que permiten obtener información sobre un estado estático. Como hemos mencionado la característica limitante de estas técnicas para el estudio de procesos dinámicos es la dificultad para extrapolar los resultados inferidos del estudio de la estructura final al resto de los estados intermedios del proceso. No obstante, como hemos mencionado en la actualidad las técnicas *ex-situ* son habitualmente utilizadas ya que se encuentran en un estado más avanzado de desarrollo. Estas técnicas son capaces de aportar un análisis detallado de las principales características de las estructuras celulares.

En particular, la microtomografía computerizada (μ CT) es una técnica *ex-situ* de imagen por rayos X que se emplea en multitud de aplicaciones. En este caso la técnica de imagen va un paso más allá con respecto a la radiografía o la microscopía y aporta alta resolución espacial en tres dimensiones. El hecho de obtener resolución espacial 3D permite realizar un análisis más detallado de la estructura celular. Además permite computar multitud de parámetros gracias al modelo tridimensional que se obtiene. Por el contrario se compromete la capacidad de aportar resolución temporal que ofrece la radioscopia. En general, se puede afirmar que ambas técnicas, radioscopia y

tomografía, aportan información complementaria. Su combinación puede contribuir con notoriedad a una descripción más avanzada de la relación *proceso-estructura-propiedades* [75].

Además, gracias a los recientes avances en ciertas líneas de sincrotrones, es posible realizar trabajos 3D con alta resolución temporal (denominada pues 4D). Recientemente han sido publicados trabajos que combinan las capacidades de resolución espacial 3D que aporta la tomografía y la resolución temporal de la radioscopia [76, 77, 78, 79]

Así pues el origen de la investigación recogida en esta tesis es el diseño y construcción de un equipo de imagen mediante rayos X cuya instalación se realizó en 2009 y que todavía se sigue mejorando, así como contribuir al conocimiento sobre los mecanismos físico-químicos que intervienen en la relación proceso-estructura durante el proceso de espumado mediante la realización de ensayos en dicho equipo. Complementariamente, durante el desarrollo de la investigación se han realizado ensayos de tomografía fundamentalmente en las instalaciones del UGCT de la Universidad de Gante y del Helmholtz Zentrum Berlin. Finalmente, se ha tenido acceso a tiempo de medida en grandes instalaciones científicas de luz sincrotrón (*Swiss Light Source, Paul Scherrer Institute*) que han permitido la realización de los estudios correspondientes a alta resolución temporal.

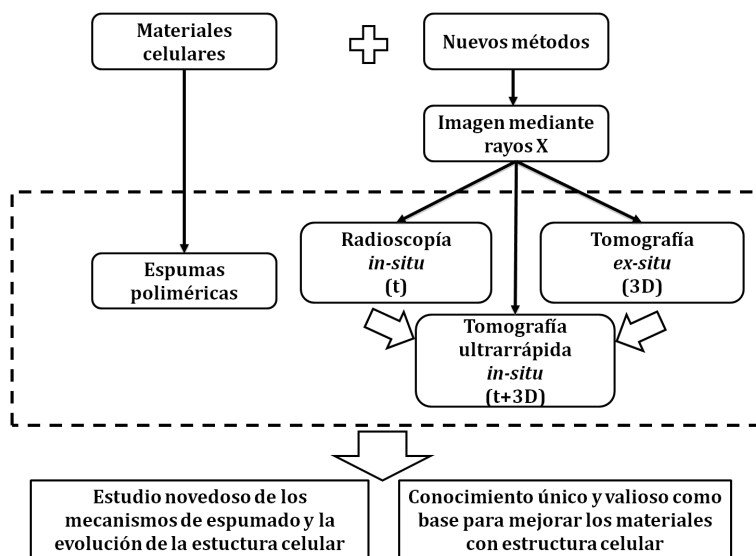


FIGURA 0-1.- ESQUEMA CONCEPTUAL DEL PLANTEAMIENTO DE LA INVESTIGACIÓN.

OBJETIVOS DE LA INVESTIGACIÓN

La investigación que se presenta se centra en el estudio de los mecanismos que ocurren durante el proceso de espumado y la estructura celular final obtenida como resultado del proceso. Para ello se seleccionaron sistemas poliméricos variados teniendo en cuenta el mecanismo objeto de estudio en cada caso. Fundamentalmente la investigación describe metodologías basadas en imagen mediante rayos X que permiten tanto el estudio *in-situ* de los procesos como *ex-situ* de los materiales espumados. Gracias a la combinación entre imagen por RX y el diseño, desarrollo y construcción de distintos sistemas de medida, ajustados a las condiciones de cada experimento, se presenta un estudio comparativo para los diferentes polímeros espumados seleccionados (termoestables y termoplásticos). Los experimentos están diseñados específicamente para dar respuesta a objetivos científicos concretos como son los obtener información novedosa sobre los mecanismos de nucleación, crecimiento y solidificación de la estructura celular. En este sentido, el estudio de la evolución de la estructura celular durante el proceso permite determinar tanto cuál es el mecanismo principal responsable de la estructura final como las variables del proceso que le afectan significativamente. Complementariamente, se presentan estudios de caracterización morfológica mediante tomografía de rayos X y se desarrollan métodos de cálculo de descriptores avanzados. Estos parámetros son capaces de explicar ligeras diferencias observadas en las propiedades y que no se explican mediante los parámetros usados de forma habitual para caracterizar la estructura celular.

Teniendo en cuenta esta perspectiva propuesta, los dos objetivos generales de la investigación se definen de la siguiente manera:

“Estudio y desarrollo de la aplicabilidad de sistemas de imagen basados en rayos X para la caracterización de materiales celulares poliméricos”

“Caracterización de la estructura celular y los mecanismos de espumado subyacentes en los sistemas poliméricos celulares seleccionados”

Con la finalidad de profundizar en el desarrollo se han definido objetivos parciales por una parte desde una perspectiva científica y por otra desde el punto de vista metodológico y técnico que pretenden desarrollar los dos grandes objetivos anteriormente mencionados:

- i) Estudio de los mecanismos que tienen lugar durante el proceso de espumado en la fase de nucleación y crecimiento de las celdas, así como en la fase del mantenimiento de la espuma donde se produce la degeneración celular a través de mecanismos de coalescencia. En particular se proponen cuatro objetivos:
 - Estudiar el efecto que tiene la adición de distintos tipos de nanopartículas sobre estos mecanismos en los procesos de espumado.
 - Analizar el efecto de la temperatura y la velocidad de calentamiento como parámetros del proceso en los distintos mecanismos y la cinética de la expansión durante la espumación.
 - Conocer la importancia del comportamiento reológico del polímero en la nucleación, el crecimiento de las celdas y estabilización final de las espumas.
 - Valorar los posibles efectos de aditivos que actúen como catalizadores, ayudantes o retardantes del proceso de expansión.

- ii) Estudio avanzado en tres dimensiones de la morfología y topología de distintas estructuras celulares. El reto en este caso es el estudio de distintos aspectos morfológicos no estudiados hasta ahora mediante esta técnica. Entre ellos podemos citar:
 - Cuantificar y discutir los parámetros morfológicos de mayor interés (tamaño de celda, orientación, conectividad de las celdas, etc.)
 - Determinar la distribución de la fase sólida en la estructura celular (paredes y aristas).
 - Cuantificar la presencia de arrugas inducidas durante el proceso en las paredes celulares y que pueden ser objeto de diferencias en el comportamiento físico.

Por otra parte, existen también una serie de objetivos metodológicos que pretenden ser los medios técnicos necesarios para la consecución de los objetivos científicos anteriormente descritos:

- i) Diseñar, construir y poner a punto un equipo de imagen mediante rayos X optimizado para la visualización de materiales poliméricos. Para ello se ajustarán los parámetros de visualización idónea (tiempo de exposición, corriente, energía, etc.) para materiales de baja absorción como los polímeros y espesor de material reducido.
- ii) Seleccionar un conjunto de sistemas poliméricos termoestables y termoplásticos que permitan estudiar los mecanismos clave de espumación por separado. De esta forma se podrán establecer metodologías de estudio para cada uno de los mecanismos sin interferencia con los demás.
- iii) Diseñar y construir instrumentación específica (moldes y sistemas de calentamiento) destinada a visualizar los procesos de espumado mediante rayos X. Se diseñarán a medida para obtener una correcta visualización y cuantificación del efecto de cada variable de proceso investigada.
- iv) Desarrollar metodologías y rutinas basadas en análisis de imagen que permitan obtener datos experimentales cuantitativos sobre la evolución de los distintos parámetros macro (densidad, expansión) y microscópicos (tamaño de celda, densidad de celdas y fenómeno de coalescencia). Estas características se recogerán por primera vez a lo largo de todos los estados intermedios de un proceso de espumado.

PRINCIPALES NOVEDADES DEL TRABAJO

Es importante mencionar algunas de las novedades de esta investigación sobre la literatura científica actual reportada. Con ello se pretende guiar al lector a lo largo de la tesis para que sea más sencillo identificar las principales aportaciones.

- Monitorización *in-situ* del proceso de espumado de polímeros haciendo uso de imagen por R-X con resolución temporal y con alta resolución espacial. El sistema de procesamiento de imagen permite, así mismo, una cuantificación original y novedosa.
- Visualización de los efectos de diferentes tipos de nanopartículas y parámetros de proceso como la temperatura en la nucleación, crecimiento y coalescencia de espumas poliméricas.
- Obtención de la distribución de la fracción sólida de material en la estructura celular mediante una metodología basada en análisis de imagen 3D de tomografías. Gracias a esta metodología es posible desestructurar virtualmente un material celular en aristas y paredes y realizar posteriormente análisis detallados de ambos elementos por separado.
- Cálculo de parámetros 3D avanzados tales como la presencia de arrugas en las paredes celulares mediante un análisis de segundo orden realizado sobre los elementos individuales (paredes y aristas) que componen la estructura celular gracias a la aplicación de la metodología de desestructuración.
- Visualización y análisis de la influencia de ciertas nanopartículas sobre el mecanismo de nucleación mediante tomografía de rayos X ultrarrápida.

Como resumen podemos decir que la novedad de este trabajo es presentar una serie de metodologías basadas en imagen que permiten obtener información tanto sobre los mecanismos de espumado como sobre la estructura celular. Es interesante destacar que la información obtenida gracias a estas metodologías es de gran utilidad a la hora de saber qué papel juega exactamente cada mecanismo de espumado. Igual de novedoso es el papel que juegan las técnicas basadas en imagen de rayos X para obtener información empírica en un campo de aplicación no estudiado hasta ahora mediante estas técnicas, como es el de las espumas poliméricas.

ESTRUCTURA DE ESTA TESIS

Esta tesis se presenta en formato compendio de artículos recogiendo las publicaciones en revistas científicas resultado de la investigación realizada. Algunos de los resultados se apoyan en artículos todavía no publicados, aunque si enviados para su publicación y actualmente en proceso de revisión. En la página 46 se recogen en varias tablas las publicaciones científicas, comunicaciones a congresos y los proyectos en los que se ha participado durante el desarrollo del trabajo presentado. La Figura 0-2 recoge en un esquema las publicaciones seleccionadas y la temática asignada a cada una de ellas. La memoria de la investigación se encuentra dividida en ocho capítulos cuya disposición y contenido se explican a continuación.

El capítulo 1 introduce el marco en el que surge esta investigación y describe detalladamente los objetivos principales del trabajo. En este primer capítulo se explica al lector la necesidad de desarrollar las técnicas de imagen mediante rayos X para obtener información sobre la evolución de la estructura celular durante el espumado.

En el capítulo 2 se describen los fundamentos de la estructura celular y los mecanismos (nucleación, crecimiento, coalescencia y drenaje) que intervienen en el proceso de espumado.

A continuación, en el capítulo 3, se presentan los materiales seleccionados para el estudio, sus características más importantes y las razones que han llevado a su selección. Por una parte se han seleccionado sistemas para el estudio del proceso de espumado mediante radioscopia y por otra parte espumas comerciales para el estudio de características avanzadas mediante tomografía.

El capítulo 4 se presenta dividido en tres secciones: la parte A define conceptos básicos sobre la imagen digital, la parte B describe los fundamentos físicos de la imagen por rayos X para terminar presentando el equipamiento utilizado en la investigación. Finalmente, la parte C aplica los conceptos descritos a las imágenes obtenidas en los equipos utilizados y describe el procesado necesario para cuantificar; objetivo ineludible de la imagen científica. Se adjunta un artículo que recoge describe el principal equipo de rayos X desarrollado para llevar a cabo la investigación.

En los capítulos 5, 6 y 7 se recogen los resultados de la investigación. Fundamentalmente se introducen según el esquema de la Figura 0-2, por una parte los resultados obtenidos mediante el desarrollo de técnicas *in-situ* aplicadas al estudio de los mecanismos de espumado y por otra parte los resultados relativos al análisis *ex-situ* mediante tomografía que proporciona información sobre la estructura final. El capítulo 8 recoge las principales conclusiones y propone líneas de investigación futuras que pueden tener como punto de partida la investigación presentada.

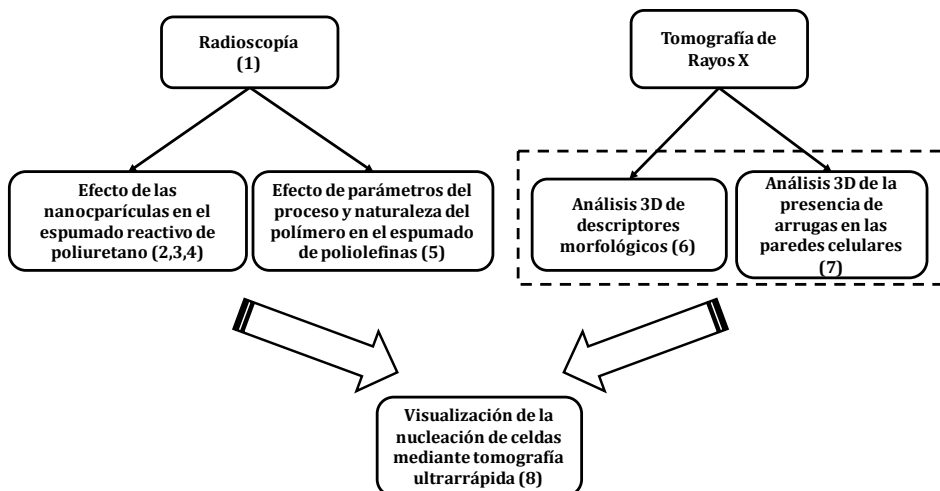


FIGURA 0-2.- ESQUEMA DE LAS PUBLICACIONES INCLUIDAS EN ESTA TESIS. LA NUMERACIÓN SE CORRESPONDE CON EL TEXTO.

En el capítulo 5 se presentan resultados obtenidos mediante radioscopia sobre los efectos de las nanopartículas en la nucleación (2) y la cinética de expansión (3) en el espumado de poliuretano rígido. También se incluyen resultados sobre el efecto de nanopartículas en la evolución de la estructura celular de las espumas de PU flexible (4). Además, se presenta un trabajo sobre el efecto de la temperatura, las propiedades físicas del polímero y la presencia de aditivos en el espumado de poliolefinas (5). A continuación, el capítulo 6 incluye dos trabajos que presentan los principales resultados relativos a la caracterización de estructuras celulares mediante tomografía. En primer lugar se presenta una caracterización de descriptores convencionales y avanzados en espumas de PU reforzadas con nanoarcillas (6). En segundo lugar, se adjunta una metodología para el análisis de la presencia de arrugas en las paredes de los poros que tienen influencia sobre las propiedades físicas de estos materiales (7). Seguidamente, en el capítulo 7, se presenta un trabajo novedoso sobre la visualización del fenómeno de la nucleación en espumas poliméricas mediante tomografía 4D (8). Como ya se ha mencionado, gracias a esta técnica es posible combinar la resolución temporal aportada por la radioscopia con la resolución espacial en 3D de la tomografía.

REFERENCIAS

- [1] D. Weaire, S. Hutzler, *The Physics of Foams*, Oxford University Press, United Kingdom, (1999)
- [2] Davies GJ, Zhen S. *J Mat Sci* 1983;18:1899.
- [3] D. Klemmner, V. Sendjarevic. *Handbook of Polymeric Foams and Foam Technology*. 2nd Edition. Hanser Publishers, Munich, (2004)
- [4] D. Eaves. *Handbook of Polymer Foams*. Rapra Technology, United Kingdom, (2004)
- [5] Sarit B. Bhaduri, *Science and technology of ceramic foams*, *Advanced Performance Materials*, 1994, Volume 1, Issue 3, pp 205-220
- [6] L. J. Gibson, M. F. Ashby, *Cellular Solids – Structure and Properties*, Second Edition, Cambridge University Press, Cambridge 1997, Ch 1
- [7] A. Cunningham, NC, Hilyard NC *Physical Behavior of Foams- an overview* In: Hilyard NC and Cunningham A (eds) *Low density Cellular Plastics: Physical Basis of Behaviour*, Chapman and Hall, London, (1994) Chap. 1
- [8] E. Solórzano, M.A. Rodríguez-Pérez, *Polymer Foams: Advanced Structural Materials in Transportation*. Eds: M. Busse, A.S. Herrmann, K. Kayvantash, D. Lehmhus
- [9] www.plasticseurope.es
- [10] M.A. Rodríguez-Pérez. *Propiedades Térmicas y Mecánicas de Espumas de Poliolefinas*. Tesis Doctoral, Universidad de Valladolid, (1998)
- [11] O. Almanza. *Caracterización y Modelización de las Propiedades Térmicas y Mecánicas en Espumas de Poliolefinas*. Tesis Doctoral, Universidad de Valladolid, (2000)
- [12] L.O. Arcos y Rábago. *Propiedades Térmicas y Mecánicas de Espumas de Poliolefinas Fabricadas en un Proceso de Moldeo por Compresión*. Tesis Doctoral, Universidad de Valladolid, (2002)
- [13] J.L. Ruiz-Herrero. *Impacto y Fluencia de Espumas con Base Polietileno*. Tesis Doctoral, Universidad de Valladolid, (2004)
- [14] J.I. González-Peña. *Efecto de los Tratamientos Térmicos en Bloques de Espuma de Polietileno de Baja Densidad Producidos Mediante Moldeo por Compresión*. Tesis Doctoral, Universidad de Valladolid, (2006)
- [15] M. Álvarez-Laínez. *Propiedades Térmicas, Mecánicas y Acústicas de Espumas de Poliolefina de Celda Abierta*. Tesis Doctoral, Universidad de Valladolid, (2007)

-
- [16] F. Hidalgo-González. Diseño Optimizado de los Parámetros de Proceso de Fabricación de Espuma de Poliolefina Reticulada mediante Moldeo por Compresión. Tesis Doctoral, Universidad de Valladolid, (2008)
- [17] R. Campo-Arnáiz. Aplicación de Técnicas Espectroscópicas al Estudio de la Morfología Polimérica, Propiedades Térmicas y de Emisión de Espumas de Baja Densidad con Base Poliolefina. Tesis Doctoral, Universidad de Valladolid, (2011)
- [18] M.A. Rodríguez-Pérez, O. Alonso, J. Souto, J.A. de Saja. Thermal Conductivity of Crosslinked Closed Cell Polyolefin Foams. *Polymer Testing* 16: 287-298, (1997).
- [19] M.A. Rodríguez-Pérez, S. Díez-Gutierrez, J.A. de Saja. The Recovery Behaviour of Crosslinked Closed Cell Polyolefin Foams. *Polymer Engineering and Science*, 38: 831-838, (1998).
- [20] M.A. Rodríguez-Pérez, A. Duijsens, J.A. de Saja. Effect of the Addition of EVA on the Technical Properties of Extruded Foamed Profiles of Low-Density Polyethylene/EVA Blends. *Journal of Applied Polymer Science* 36: 2587-2596, (1998).
- [21] J.I. Velasco, A.B. Martínez-Benasat, M.A. Rodríguez-Pérez, J.A. de Saja. Application of Instrumented Falling Dart Impact to the Mechanical Characterization of Thermoplastic Foams. *Journal of Materials Science* 34: 431-438, (1999).
- [22] M.A. Rodríguez-Pérez, O. Almanza, J.A. de Saja. Anomalous Thickness Increase in Crosslinked Closed Cell Polyolefin Foams during Heat Treatments. *Journal of Applied Polymer Science* 73: 2825-2835, (1999).
- [23] M.A. Rodríguez-Pérez, J.A. de Saja. The Effect of Blending on the Physical Properties of Crosslinked Closed Cell Polyethylene Foams. *Cellular Polymers* 18: 1-20, (1999).
- [24] O. Almanza, M.A. Rodríguez-Pérez, J.A. de Saja. The Microstructure of Polyethylene Foams Produced by a Nitrogen Solution Process. *Polymer* 42: 7117-7126, (2001).
- [25] O. Almanza, L.O. Arcos y Rábago, M.A. Rodríguez-Pérez, A. González, J.A. de Saja. Structure-Property Relationships in Polyolefin Foams. *Journal of Macromolecular Science, Part B: Physics* 40: 603-613, (2001).
- [26] J. Mills, M.A. Rodríguez-Pérez. Modelling the Gas-Loss Creep Mechanism in EVA Foam from Running Shoes. *Cellular Polymers* 20: 79-100, (2001).
- [27] O. Almanza, M.A. Rodríguez-Pérez, B. Chernev, J.A. de Saja, P. Zipper. Comparative Study on the Lamellar Structure of Polyethylene Foams. *European Polymer Journal* 41: 599-609, (2005).
- [28] M.A. Rodríguez-Pérez, R.A. Campo-Arnáiz, R. Aroca, J.A. de Saja. Characterization of the Matrix Polymer Morphology of Polyolefin Foams by Raman Spectroscopy. *Polymer* 46: 12093-12102, (2005).

- [29] M.A. Rodríguez-Pérez, J.L. Ruiz-Herrero, E. Solórzano, J.A. de Saja. Gas Diffusion in Polyolefin Foams during Creep Tests. Effect on Impact Behaviour and Recovery after Creep. *Cellular Polymers* 25: 221-236, (2006).
- [30] M.A. Rodríguez-Pérez, O. Almanza, J.L. Ruiz-Herrero, J.A. de Saja. The Effect of Processing on the Structure and Properties of Crosslinked Closed Cell Polyethylene Foams. *Cellular Polymers* 27: 179-200, (2008).
- [31] M.A. Rodríguez-Pérez, M. Álvarez-Laínez, J.A. de Saja. Microstructure and Physical Properties of Open Cell Polyolefin Foams. *Journal of Applied Polymer Science* 114: 1176-1186, (2009).
- [32] M. Álvarez-Laínez, M.A. Rodríguez-Pérez, J.A. de Saja. Thermal Conductivity of Open Cell Polyolefin Foams. *Advanced Engineering Materials* 10: 373-377, (2008).
- [33] E. Solórzano. Espumas de Aluminio: Proceso de Espumado, Estructura Celular y Propiedades. Tesis Doctoral, Universidad de Valladolid, (2008)
- [34] M.A. Rodríguez-Pérez, J. Lobos, C.A. Pérez-Muñoz, J.A. de Saja, L. González, B.M.A. del Carpio. Mechanical Behaviour at Low Strains of LDPE Foams with Cell Sizes in the Microcellular Range: Advantages of using these materials in structural elements. *Cellular Polymers* 27: 347-362, (2008).
- [35] J. Escudero, E. Solórzano, M.A. Rodríguez-Pérez, F. García-Moreno, J.A. de Saja. Structural Characterization and Mechanical Behaviour of LDPE Structural Foams. A Comparison with Conventional Foams. *Cellular Polymers* 28: 289-302, (2009).
- [36] M.A. Rodríguez-Pérez, J. Lobos, C.A. Pérez-Muñoz, J.A. de Saja. Mechanical Response of Polyolefin Foams with High Densities and Cell Sizes in the Microcellular Range. *Journal of Cellular Plastics* 45: 389-403, (2009).
- [37] C. Saiz-Arroyo, J. Escudero, M.A. Rodríguez-Pérez, J.A. de Saja. Improving the Structure and Physical Properties of LDPE Foams using Silica Nanoparticles as an Additive. *Cellular Polymers* 30: 63-78, (2011).
- [38] J.A. Reglero-Ruiz, C. Saiz-Arroyo, M. Dumon, M.A. Rodríguez-Pérez, J.A. de Saja, L. González. Production, Cellular Structure and Thermal Conductivity of Microcellular Methyl Methacrylate-Butyl Acrylate-Methyl Methacrylate Triblock Copolymers. *Polymer International* 60: 146-152, (2011).
- [39] M. Ardanuy, M.A. Rodríguez-Pérez, J.A. de Saja, J.I. Velasco. Foaming Behaviour, Cellular Structure and Physical Properties of Polybenzoxazine Foams. *Polymers for Advanced Technologies* DOI 10.1002/pat.1978 (2011).
- [40] J.I. Velasco, M. Antunes, O. Ayyad, J.M. López-Cuesta, P. Gaudon, C. Saiz-Arroyo, M.A. Rodríguez-Pérez, J.A. de Saja. Foaming Behaviour and Cellular Structure of LDPE /Hectorite Nanocomposites. *Polymer* 48: 2098-2108, (2007).

-
- [41] J.I. Velasco, M. Antunes, O. Ayyad, C. Saiz-Arroyo, M.A. Rodríguez-Pérez, F. Hidalgo, J.A. de Saja. Foams Based on Low Density Polyethylene/Hectorite Nanocomposites: Thermal Stability and Thermo-Mechanical Properties. *Journal of Applied Polymer Science* 105: 1658-1667, (2007).
- [42] R. Verdejo, F. Barroso-Bujans, M.A. Rodríguez-Pérez, J.A. de Saja, M.A. López-Manchado. Functionalized Graphene Sheets filled Silica Foam Nanocomposites. *Journal of Materials Chemistry* 19: 2221-2226, (2008).
- [43] R. Verdejo, C. Saiz-Arroyo, J. Carretero-González, F. Barroso-Bujans, M.A. Rodríguez-Pérez, M.A. López-Manchado. Physical Properties of Silicone Foams filled with Carbon Nanotubes and Functionalized Graphene Sheets. *European Polymer Journal* 44: 2790-2797, (2008).
- [44] R. Verdejo, F. Barroso-Bujans, M.A. Rodríguez-Pérez, J.A. de Saja, M. Arroyo, M.A. López-Manchado. Carbon Nanotubes Provide Self-Extinguishing Grade to Silicone-Based Foams. *Journal of Materials Chemistry* 18: 3933-3939, (2008).
- [45] S. Román-Lorza, M.A. Rodríguez-Pérez, J.A. de Saja. Cellular Structure of Halogen-Free Flame Retardant Foams based on LDPE. *Cellular Polymers* 28: 249-268, (2009).
- [46] S. Román-Lorza, M.A. Rodríguez-Pérez, J.A. de Saja. Cellular Structure of EVA/ATH Halogen-Free Flame Retardant Foams. *Journal of Cellular Plastics* 10: 1-21, (2010).
- [47] M.A. Rodríguez-Pérez, R.D. Simoes, C.J.L. Constantino. J.A. de Saja. Structure and Physical Properties of EVA/Starch Precursor Materials for Foaming Applications. *Journal of Applied Polymer Science* 212: 2324-2330, (2011).
- [48] Y. Ma, R. Pyrz, M.A. Rodríguez-Pérez, J. Escudero, J.C. Rauhe, X. Su. X-Ray Microtomographic Study of Nanoclay-Polypropylene Foams. *Cellular Polymers* 30: 95-110, (2011).
- [49] M.A. Rodríguez-Pérez, R.D. Simoes, S. Román-Lorza, M. Álvarez-Laínez, C. Montoya-Mesa. C.J.L. Constantino, J.A. de Saja. Foaming of EVA/Starch Blends: Characterization of the Structure, Physical Properties and Biodegradability. *Polymer Engineering and Science* 52: 62-70, (2012).
- [50] D. Simoes, M.A. Rodriguez-Perez, J.A. De Saja, C.J.L. Constantino, Thermomechanical Characterization of PVDF and P(VDF-TrFE) Blends Containing Corn Starch and Natural Rubber, *Journal of Thermal Analysis and Calorimetry* 99(2), 621-629 (2010)
- [51] R.D. Simoes, M.A. Rodriguez-Perez, J.A. de Saja, C.J.L. Constantino, Tailoring The Structural Properties of PVDF and P(VDF-TrFe) by Using Natural Polymers as Additives *Polymer Engineering and Science* 49, 2150-2157 (2009)
- [52] M.A. Rodriguez-Perez, R.D. Simoes, S. Roman-Lorza, M. Alvarez-Lainez, C. Montoya-Mesa, C.J.L. Constantino, J.A. de Saja, Foaming of EVA/ Starch Blends:

Characterization of the Structure, Physical Properties and Biodegradability, *Polymer Engineering and Science*, 52(1), 62-70, (2012)

[53] M.A. Rodríguez-Perez, R.D. Simoes, C.J.L. Constantino, J.A. de Saja, Structure and Physical Properties of EVA/ Starch Precursor Materials for Foaming Applications, *Journal of Applied Polymer Science* 121, 2324-2330 (2011)

[54] S. Ghosh, V. Gutierrez, C. Fernández, M. A. Rodríguez-Perez, J. C.Viana, R.L. Reis, J.F. Mano, Dynamic Mechanical Behavior of Starch-Based Scaffolds in Dry and Physiologically Simulated Conditions: Effect of Porosity and Pore Size *Acta Biomaterialia* 4, 950-959 (2008)

[55] N.M. Alves, C. Saiz-Arroyo, M.A. Rodríguez-Pérez, R.L. Reis, J.F. Mano Microhardness of Starch Based Biomaterials in Simulated Physiological Conditions, *Acta Biomaterialia* 3, 69 77 (2006)

[56] Y. Wang, M.A. Rodríguez-Pérez, R.L. Reis, J.F. Mano, Thermal and Thermomechanical Behaviour of Polycaprolactone and Starch/Polycaprolactone Blends for Biomedical Applications *Macromolecular Materials Engineering* 290, 792-801 (2005)

[57] E. Solórzano, M.A. Rodríguez-Pérez, J.A. de Saja, Thermal conductivity of cellular metals measured by the transient plane source, *Advanced Engineering Materials*, 10 (596-602) 2008

[58] E. Solórzano, M.A. Rodríguez-Pérez, J.A. Reglero, J.A. de Saja, Mechanical behaviour of internal reinforced aluminium foams, *Advanced Engineering Materials* 9(11), 955-958 (2007)

[59] E. Solórzano, M.A. Rodríguez-Perez, J.A. de Saja, Thermal Conductivity of Metallic Hollow Sphere Structures: an Experimental, Analytical and Comparative Study , *Material Letters* 63, 1128-1130 (2009)

[60] T. Fiedler, E. Solórzano, A. Öchsner, Numerical and Experimental Analysis of the Thermal Conductivity of Metallic Hollow Sphere Structures, *Materials Letters* 62, 1204–1207 (2008)

[61] J. Lázaro, E. Solórzano, J. A. de Saja, M. A. Rodríguez-Perez, Early anisotropic expansion of aluminium foam precursors, *Journal of Materials Science* (in press, 2013)

[62] J. Lázaro, E. Laguna, E. Solórzano, M. A. Rodríguez-Perez, Effect of microstructural anisotropy of PM precursors on the characteristic expansion of aluminium foams, *Metallurgical and Materials Transactions B* (in press, 2013)

[63] F. García-Moreno, E. Solórzano, J. Banhart, Kinetics of Coalescence in Liquid Aluminium Foams, *Soft Matter* 7, 9216-9223 (2011)

[64] T. Fiedler, E. Solórzano, F. García-Moreno, A. Öchsner, I.V. Belova, G.E. Murch, Lattice Monte Carlo and Experimental Analyses of the Thermal Conductivity of

Random Shaped Cellular Aluminium, *Advanced Engineering Materials* 11(10), 843-847 (2009)

[65] J. Lázaro, J. Escudero, E. Solórzano, M.A. Rodríguez-Pérez, J.A. de Saja, Heat Transport in Closed Cell Aluminium Foams: Application Notes, *Advanced Engineering Materials* 11. 825-831 (2009)

[66] E. Solórzano, M. Antunes, C. Saiz-Arroyo, M.A. Rodríguez-Pérez, J.I. Velasco, J.A. de Saja, Optical Expandometry: A Technique to Analyze the Expansion of Chemically Blown Thermoplastic Foams, *Journal of Applied Polymer Science* 125(2) 1059-1067 (2012)

[67] E.Solórzano, F. García-Moreno, N. Babcsan, J. Banhart, Thermographic monitoring of aluminium foaming processes, *Journal of Nondestructive Evaluation* 28(3) 141-148 (2009)

[68] Banhart J, *Advanced tomographic methods in materials research and engineering*. UK: Oxford University Press; 2008.

[69] Lambert J, Cantat I, Delannay R, Renault A, Graner F, Glazier JA, et al. *Colloids Surf A* 2005;263:295.

[70] Montminy MD, Tannenbaum AR, Macosko CW. *J Colloid Interface Sci* 2004;280:202.

[71] J. Banhart, *Manufacture, characterization and application of cellular metals and metal foams*, *Progress in Materials Science*, 46, 559 (2001)

[72] F. Garcia-Moreno, M. Mukherjee, C. Jimenez, A. Rack and J. Banhart, *Metals*, 2012, 2,10–21.

[73] F. García Moreno, M. Fromme, J. Banhart, Real time X-ray radiography on metallic foams using a compact microfocus source, *Adv. Eng. Mater.* 6 (2004) 416–420.

[74] A. Rack, F. García-Moreno, C. Schmitt, O. Betz, A. Cecilia, A. Ershov, T. Rack, J. Banhart, S. Zabler, On the possibilities of hard X-ray imaging with high spatiotemporal resolution using polychromatic synchrotron radiation, *J. X-Ray Sci Technol.* 18 (2010) 429–441.

[75] J. Banhart, *Prog. Mat. Sci*, Volume: 46 Issue: 6 Pages: 559-632, 2001

[76] Babcsan et al, *Coll. Surf. A* 309:1, 254-263, 2007

[77] Mokso et al, *Following Dynamic Processes by Xray Tomographic Microscopy with Subsecond Temporal Resolution*, *AIP Conf. Proc.* 1234, SRI2009, 2010

[78] A. Rack, F. Garcia-Moreno, T. Baumbach and J. Banhart, *J. Synchrotron Radiat.* 16, 432 (2009).

[79] K. Uesugi, T. Sera and N. Yagi, J. Synchrotron Radiat. 13, 403 (2006).

1. INTRODUCTION

It is possible to find in nature a significant number of materials showing an internal cellular structure. Wood, cork, coral, sponges and human bones are some of the most representative examples. On the other hand, different manufactured cellular materials aim nowadays at imitating these natural structures that exhibit excellent physical properties. These man-made materials cover from a simple unit cell repetition in the case of honeycombs (used as core in sandwich panel for structural applications) to three-dimensional stochastically structured foams made from liquids, polymers, metals, ceramics, etc. [1,2,3,4,5]. We can list numerous examples (see Figure 1-1) such blades of air generators, packaging trays, insulation panels, mattresses, car dashboards, seats, etc.



FIGURE 1-1.-DIFFERENT EXAMPLES OF CELLULAR MATERIALS: INTERIOR OF AIR GENERATOR BLADES, FOOD-PACKAGING TRAYS, INSULATION PANELS, MATTRESSES, CAR DASHBOARD AND SEATS.

A two phase cellular structure is the common feature to all of these materials. It consists in a gas phase dispersed into a solid matrix (liquid in the particular case of aqueous foams). This presence of gaseous phase provides density reduction in comparison to the dense solid [6,7]. This fact results less amount of raw material is necessary for their production and it saves costs and energy. From this point of view, cellular materials are considered “friendly environmentally products”. Moreover, these materials extend the range of available properties covered by their respective solid precursors. They exhibit extremely low thermal transport properties, high-energy absorption capability, excellent stiffness and mechanical resistance at low weights and, in some cases, high and acoustic absorption properties. In addition, it is important to mention that the control of the processing and structure and producing tailored

materials. This means that cellular materials can be designed to fit a specific requirement demanded by certain end-use application.

Nowadays, they fulfil a wide range of demands in consolidated and emerging industries such as aeronautic, automotive, building, cushioning, packaging, renewal energies, biotechnology, medical, etc. [8] As illustrative data, a total consumption of 300 million tonnes of cellular plastics was accomplished in the world market during 2012. This amount represents 10% of the total plastic consumption as seen in fig.1-2. Moreover the sector shows an estimated growth rate of 4 % per year in the period 2010-2016 [9].

Despite the commercial success of some worldwide well-known examples of cellular materials such as polyurethane (PU) foams used as thermal insulator and seats, expanded polystyrene (EPS) in packaging, extruded polystyrene XPS in packaging and insulation, PVC foams (pipes, profiles and structural foams) and polyolefin foams (packaging, buoyancy thermal insulation); nowadays there is still a lack of knowledge in several aspects of the process-structure-properties relationship in these materials.

This chapter is divided into three sections. It mainly exposes the scientific framework where this investigation takes place. Then, the main scope and principal objectives are enunciated. A detailed description of concrete milestones proposed to achieve the objectives is also presented. Finally, short description of each chapter and publications chart is aimed at helping the reader to follow the contents in the next chapters.

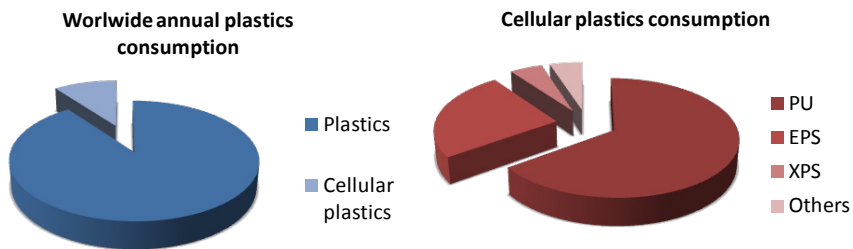


FIGURE 1-2.- CELLULAR PLASTICS REPRESENT AN IMPORTANT PERCENTAGE OF TOTAL ANNUAL PLASTIC CONSUMPTION.

1.1. FRAMEWORK OF THIS THESIS

This investigation is part of the research focused on cellular materials characterization and development led by Prof. Dr. Miguel Ángel Rodríguez-Pérez at CellMat Laboratory in the Condensed Matter Physics Department of the University of Valladolid.

CellMat laboratory was born in 1999 at University of Valladolid with the PhD thesis defence focused on thermal and mechanical properties of polyolefin foams of Miguel Ángel Rodríguez-Pérez directed by Prof. Dr. José Antonio de Saja [10]. CellMat research was initially mainly oriented to polyolefin foams characterization and several thesis

and scientific works were performed in this area [11,12, 13, 14, 15, 16, 17, 18, 19,20, 21, 22, 23, 24, 25, 26, 27, 28, 29, 30, 31, 32].

The knowledge acquired in the area of cellular materials characterization permitted to carry out research focused on the foaming routes. In 2002 a research topic focused on aluminium foams was started [33].

Nowadays, the research topics cover five hot areas of technological application. These topics are microcellular materials, sub-microcellular foams [34,35,36,37,38,39], nanocomposite foams [40, 41, 42, 43, 44, 45, 46, 47, 48], bioplastic based foams [49, 50, 51, 52, 53, 54, 55, 56] and aluminium foams [57,58,59,60,61, 62, 63, 64, 65]. The research includes the production at lab-scale, structural characterization, physical properties determination and modelling. All this is done keeping an eye on the final applications as shown in the materials tetrahedron of Figure 1-3.

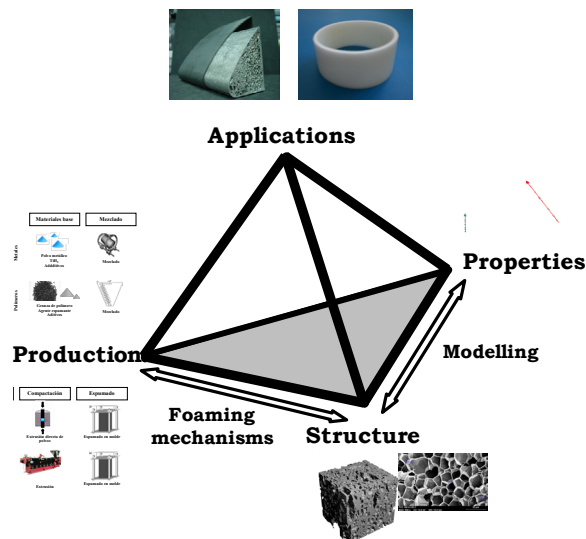


FIGURE 1-3.- MATERIALS TETRAHEDRON FOR FOAMED MATERIALS.

Furthermore, CellMat has recently developed non-conventional techniques that allow to gain further scientific knowledge. This information is applicable to technological development of cellular materials. This novel research is focused on non-destructive techniques to get information about the foaming processes [66, 67]. In this sense, several imaging systems and characterization devices have been developed. The main aim of these developments is to investigate the mechanisms occurring during foaming processes. These mechanisms are responsible of the final cellular structure. The development of these techniques is aimed at obtaining unique knowledge about physical mechanisms that complements the actual know-how.

Traditionally, the procedures to study foaming mechanisms use initial and final state of the material. Therefore, there is no empiric evidence about what occurs during intermediate stages of the process. This means that mostly the strategy to obtain information about *process-structure* relationship only is only based on initial and final stages, i.e. intermediate stages are not analysed. Part of the information of the physico-chemical mechanisms responsible of cellular structure evolution is not available.

This fact results in low accuracy of traditional procedures. This is of particular important when the objective is to study evolving intermediate phenomena such as nucleation, growth, coalescence, drainage and coarsening. Moreover, there mechanisms condition the final cellular structure.

The investigation of this “hidden” information requires *in-situ* techniques. These techniques allow to investigate intermediate stages without affecting the measured dynamic system. Technical advances during the last years permit nowadays the development of such novel techniques. Subsequently, they are suitable to address what is occurring at every instant of any evolving process. Latest developments reaches on image techniques such as IR thermography and X-ray imaging facilitate significant advances in this area. High technified state and relatively low cost make some of these techniques a suitable choice to study and quantify any dynamic process and in particular foaming processes.

A sequence of optical images about an expansion process is a simple example of *in-situ* technique. Image analysis allows to obtain information about expansion velocity, expansion grade, defects presence, external morphology, etc. However, *in-situ* concept can be defined in a more restrict way. It only refers to those techniques that are able to obtain information about internal structure in a process without interfering it. From this point of view, optical image would not be considered an *in-situ*. Contrary, other techniques such as X-ray diffraction or X-ray imaging both with temporal resolution would be. These are able to go further and provide information that lays hidden in the process while it evolves.

In particular, one of the most versatile *in-situ* techniques is X-ray radioscopy. It consists in sequential acquisition of radiographic images. It permits visualization and analysis of cellular structure evolution during foaming process thanks to temporal resolution. It is also important to remark that X-ray radioscopy is a non-invasive and non-destructive technique that allows observation and quantification of magnitudes evolution. Actual state-of-the-art of radiographic equipment makes it a suitable choice to investigate cellular plastics [68, 69, 70, 71]. There are some remarkable works in the literature that investigate metallic foams with excellent results by means of X-ray radioscopy [72, 73, 74].

Contrary but providing complementary information, we can mention *ex-situ* techniques offer complementary information. These techniques permit to obtain

information about a static state. As mentioned before, the limiting peculiarity of such techniques is the impossibility to address dynamic studies by extrapolation of few intermediate static stages. Nevertheless, *ex-situ* techniques are nowadays highly developed. Especially those related to imaging, such as microscopies. These techniques are able to provide a detailed analysis of the main characteristics of cellular structures.

Namely, computed microtomography (μ CT) is an *ex-situ* techniques using X-ray imaging. It is nowadays extensively used. In this case, imaging goes beyond 2D spatial resolution and offers the possibility of resolving any object in the 3D space. This feature allows to characterize in detail cellular structures. Moreover, computation of multiple parameters is available thanks to 3D modelling. Nevertheless, temporal resolution capability, which characterizes X-ray radioscopy, becomes now compromised. In general, both techniques offer complementary information. Both together contribute to a more advanced description of process-structure-properties [75].

Last but not least, some beamlines at synchrotrons permit to obtain 3D tomographies with temporal resolution (denoted as 4D). There are recent publications that combine these two capabilities: 3D spatial and temporal resolution [76]. This ultrafast tomography allows imaging with resolutions higher than 1-3 μ m and temporal resolution in the sub-second range.

We can state the origin of this investigation since we have introduced and explained motivations of X-ray imaging with temporal and 3D resolution. This investigation began with the design and construction of an X-ray imaging device in 2009. This device is continuously under development. It is important to note that one of the main motivations is to get knowledge about the mechanisms governing process-structure connection during foaming processes. Complementarily, proposals for beamtime application at large-scale facilities have been accepted and thus some of the presented studies were done in synchrotrons.

Fig. 1-4 summarizes the main workflow of this thesis and helps to introduce the objectives in next section.

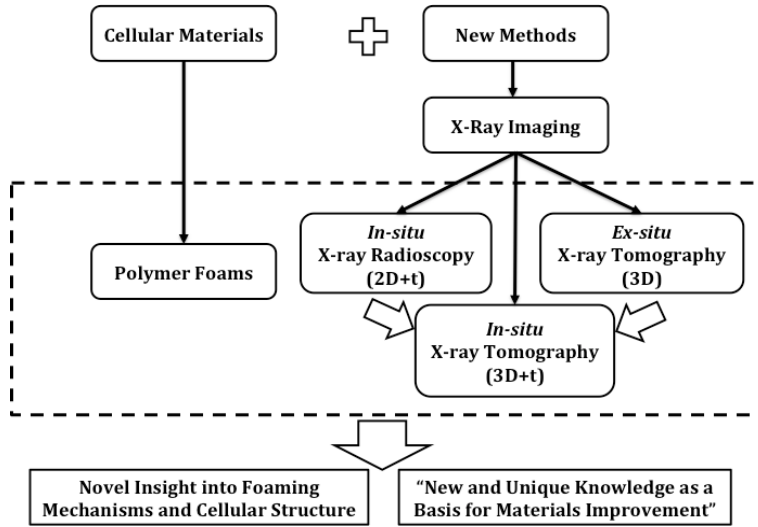


FIGURE 1-4.- SCHEMATIC VIEW OF THE FRAMEWORK OF THIS INVESTIGATION.

1.2. OBJECTIVES

This research aims to investigate the mechanisms occurring during the foaming process and the final cellular structure resulting from the expansion process. A varied selection of polymeric systems has been carefully done according to every particular phenomena of study. It mainly addresses methodologies based on X-ray imaging allowing both *in-situ* monitoring of the foaming process and *ex-situ* analysis of the foamed materials. Based on the mentioned technique and different setups designed and developed, a comparative analysis for different selected systems (thermosets and thermoplastics) has been performed. The experiments are designed to understand the underlying phenomena affecting cell nucleation, growth and cellular structure solidification. It is possible to determine which are the main mechanisms governing the final cellular structure. This is done in terms of cellular structure evolution throughout the foaming process. Complementarily, advanced cellular architecture features are described and analysed thanks to *ex-situ* analysis of the produced materials by X-ray computed tomography. These parameters are able to detect and explain some slight differences of properties that are not accessible by using conventional parameters of cellular structure characterization.

Under this perspective, the general purposes of this thesis can be established as follows:

“To study and develop the applicability of X-ray imaging systems to characterizing cellular polymers”

“To characterize cellular structure and mechanisms underlying the foaming of selected polymeric systems”

Some partial objectives have been defined to develop and fulfil the challenging general goals stated before. On the one hand general objectives are developed from scientific perspective. On the other hand methodological and technical objectives are scheduled as concrete milestones achieved by their own specific methodology.

- i) To study the mechanisms occurring during foaming process: cells nucleation and growth and stabilization stage where coalescence may happen place. Namely, four specific objectives are proposed:

CHAPTER 1

- To study the effect of selected nanoparticles addition on these foaming mechanisms.
 - To analyze the effect of temperature and heating rate as process parameters affecting mechanisms and expansion kinetics during foaming.
 - To know the importance of polymer rheological behaviour in cells nucleation, growth and cellular structure stabilization.
 - To evaluate the possible effects of chemical agents acting as catalysts, process-aids or foaming retardants.
- ii) To study morphology and topology of cellular structures in 3D. The challenge is the study of different morphological aspects not studied by means of computed microtomography until now. We can cite among others studied:
- To quantify and discuss morphological parameters of interest (cell size, orientation, connectivity, etc.)
 - To determine material distribution across the cellular structure (walls and struts).
 - To detect and quantify corrugation in the cell walls induced during the foaming process. This can be origin of differences in physical properties.

On the other hand, there are other methodological objectives aimed at being the technical means to achieve scientific objectives previously described:

- v) To design, build and optimize an X-ray imaging device aimed at visualizing polymeric cellular materials. Visualization parameters (exposure time, current, energy, etc.) will be adjusted for materials with reduced thickness and such a low absorption as polymers.
- vi) To select a series of thermoset and thermoplastic polymeric systems to permit the separate study of key foaming mechanisms. Subsequently, it will be possible to establish methodologies to study each mechanisms without interfering the others.
- vii) To design and build specific scientific instruments (moulds and heating systems) aimed at visualization of polymer foaming processes. These instruments require tailored design to obtain high quality visualization that allows quantification of every process variable.

viii) To develop methodologies and routines based on image analysis to obtain experimental data about evolution of different macroscopic (density, expansion) and microscopic (cell size, cell density and coalescence) parameters. This empiric information will be collected during all intermediate stages of a foaming process for the first time.

1.3. MAIN NOVELTIES

It is worth pointing out that the main novelties of this work over current scientific literature are:

- *In-situ* monitoring of foaming process by means of X-ray imaging with temporal resolution and high spatial resolution. The image processing methodology permits novel quantification.
- Visualization of the effect of different nanoparticles and processing parameters such as temperature on the cells nucleation, growth and coalescence in polymeric foams.
- It is possible to calculate the solid fraction distribution across the cellular structure by 3D analysis of tomographies. It is possible to de-structure a cellular material in struts and walls to perform separately detailed analysis of single elements.
- Calculate advanced 3D parameters such as corrugation in the cell walls by using a second order analysis of the individual elements (walls and struts) that compose a cellular structure.
- Visualization and analysis of nanoparticles influence on nucleation mechanism by ultra-fast X-ray tomography.

To summarize this investigation collects several methodologies to get knowledge about the foaming mechanisms and cellular structure. However, it is important to point out that a more practical knowledge is overall aimed; i.e. formulation improvement and optimization of the processes to fabricate tailored cellular materials. This means that the methodology developed should allow optimizing processing parameters by monitoring the exact role that they are playing. It is also remarkable the applicability of X-ray imaging techniques in the polymeric foams area.

1.4. STRUCTURE OF THIS THESIS

This thesis is written as a *compendium of publications*. Apart from published articles, some of the results are supported by papers pending of publication. Tables 1-1, 1-2 and 1-4 summarize all the scientific publications, oral communications in international conferences and projects realized during this investigation. Fig. 1-5 shows selected papers for this thesis and the topic of each of them. The manuscript is divided into eight chapters exposed as follows:

Chapter 1 introduces the framework and states the main objectives of this investigation. It justifies the necessity of applying X-ray imaging techniques to obtain information about cellular structure evolution during the foaming processes.

Chapter 2 describes the main elements of cellular structures and physic-chemical mechanisms (nucleation, growth, drainage, coalescence and coarsening) occurring in foaming processes.

Chapter 3 provides a description of the materials selected for this research. It includes the main characteristics and the reasons why they were selected. A selection of polymeric systems is used for the study of foaming mechanisms by X-ray radiography. On the other hand commercial foams have been chosen to investigate advanced characteristics by X-ray microtomography.

Chapter 4 is divided in three different sections: part A serves as a general overview about basic concepts on digital imaging, secondly part B describes the X-ray physics underlying imaging devices used in this work. Finally part C contains a description of the digital analysis concepts applied to the images obtained in this research and describes the image processing necessary for quantification.

The main results of this investigation are presented in chapters 5, 6 and 7, as seen in Table 1-1. They are basically introduced according to scheme in fig. 1-5. On the one hand the results concerning foaming mechanisms obtained by *in-situ* techniques. On the other hand quantitative analysis and remarkable results related to *ex-situ* microtomography investigation of cellular structure.

Chapter 8 collects the main conclusion and propose future research topics for further work.

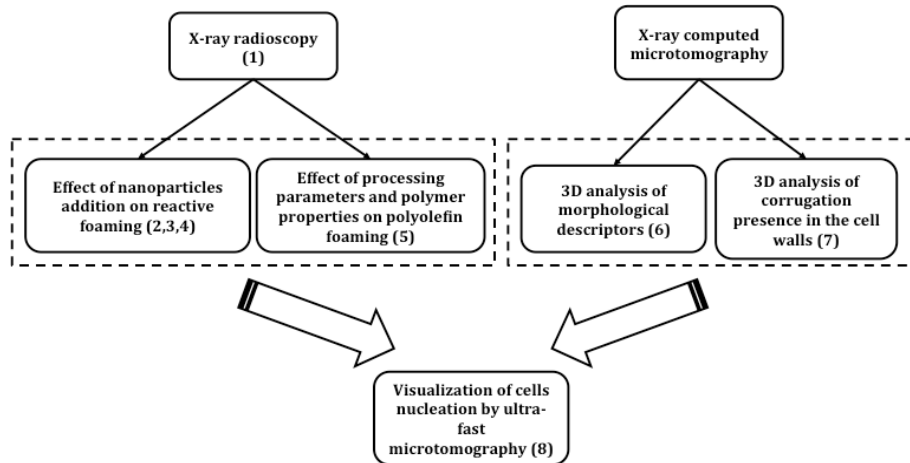


FIGURE 1-5.- SUMMARY OF PUBLICATIONS CONTRIBUTING TO THIS INVESTIGATION. NUMBERS CORRESPOND TO TABLE 1-1.

Chapter 5 presents results obtained by means of X-ray radioscopy. It addresses the effects of nanoparticles in the cells nucleation (paper no.2) and expansion kinetics (paper no.3) of rigid polyurethane. It also includes and study of carbon based nanoparticles effects on cellular structure evolution of flexible polyurethane foams (paper no.4). Finally, it shows a research on temperature, polymer properties and additives presence effects on cellular structure evolution during foaming (paper no.5). Then, chapter 6 includes two works with the principal results concerning cellular structures characterization by microtomography. Firstly, conventional descriptors are characterized for polyurethane nanocomposite foams (paper no.6). Secondly, paper no.7 presents a methodology to characterize and analyse the presence of corrugation in the cell walls, which influence the physical properties of cellular materials. Chapter 7 presents a novel work (paper no.8) about nucleation phenomena visualization in polymeric foams by 4D ultra-fast tomography. This technique permits to combine both temporal resolution of radioscopy and 3D spatial resolution of tomography. Finally, chapter 8 summarizes the most remarkable conclusions of this investigation and it proposes topics for further work.

TABLE 1-1

No.	Scientific publications with results contributing to this thesis	Chapter
(1)	E. Solórzano, J.Pinto, S. Pardo-Alonso, M.A. Rodríguez-Pérez, F. García-Moreno Application of a Microfocus X-Ray Imaging Apparatus to the Study of Cellular Polymers Polymer Testing, 32 (2013) 321-329	4
(2)	S. Pardo-Alonso, E. Solórzano, S. Estravis, M.A. Rodríguez-Pérez, J.A. de Saja In-situ Evidences of Nanoparticles Nucleating effect in Polyurethane-Nanoclay Foamed Systems Soft Matter (2012) 8, 11262	5
(3)	S. Pardo-Alonso, E. Solórzano, M.A. Rodríguez-Pérez Time-resolved X-ray imaging of nanofiller-polyurethane reactive foam systems Colloids Surf. A: Physicochem. Eng. Aspects (2013), 438, 119-125	5
(4)	E. Solórzano, S. Pardo-Alonso, J.A. de Saja, M.A. Rodríguez-Pérez X-ray radioscopy in-situ studies in thermoplastic polymer foams, Colloids Surf. A: Physicochem. Eng. Aspects (2013), 438, 167-173	5
(5)	M.M. Bernal, S. Pardo-Alonso, E. Solórzano, M. A. López-Manchado, R.Verdejo, M.A. Rodríguez-Pérez Effect of Carbon Nanofillers on PU Foaming from a Chemical and Physical Perspective Physical Chemistry Chemical Physics (<i>under revision</i>)	5
(6)	S. Pardo-Alonso, E. Solórzano, L. Brabant, P.Vanderniepen, L. Van Hoorebeke, M.A. Rodríguez-Pérez Progressive Modification of Cellular Architecture in Nanocomposite Polyurethane Foams European Polymer Journal, 49, 999-1006	6
(7)	S. Pardo-Alonso, E. Solórzano, J. Vicente, L. Brabant, L. Van Hoorebeke, I. Manke, A. Hilger, E. Laguna, M.A. Rodríguez Pérez mCT-based analysis of the solid phase in foams: cell wall corrugation and other practical microscopic features Microscopy and microanalysis (<i>under revision</i>)	6
(8)	E. Solórzano, S.Pardo-Alonso, R. Mokso, M.A. Rodríguez-Pérez, Bubble Nucleation and Growth by Real-Time Synchrotron Tomography: A Comparison with classical models (<i>draft in preparation</i>)	7

TABLE 1-2

Oral communications, posters and contributions to international conferences
S. Pardo-Alonso, M.A. Rodríguez-Pérez, M. Dumon, J.A. de Saja Submicrocellular polymer foams based on nanostructured precursors European School on Molecular Nanoscience, Madrid, Spain, October 2010 Oral communication
S. Pardo-Alonso, S. Estravís, E. Solórzano, M.A. Rodríguez-Pérez, J.A. de Saja Effect of Nanoadditives in Rigid Polyurethane Foam Nucleation Monitored by X-ray Radioscopy SPE Eurotec® Conference, Barcelona, Spain, November 2011 Oral communication
E. Solórzano, S. Pardo-Alonso, J. Pinto, M.A. Rodríguez-Pérez, J.A. de Saja X-Ray Radioscopy In-Situ Studies in Thermoplastic Foams EUFOAM 2012, Lisbon, Portugal, July 2012 Oral communication
M.M. Bernal M. Martín-Gallego, L.J. Romasanta, S. Pardo-Alonso, E. Solórzano, M.A. Rodríguez-Pérez, M. A. López-Manchado, R. Verdejo Effect of Carbon Nanofillers on PU Foaming from a Chemical and Physical Point of View NANOFUN POLY, Prague, Czech Republic, April 2012 Oral communication
E. Solórzano, S. Pardo-Alonso, M.A. Rodríguez-Pérez, J.A. de Saja Study of Aqueous Foams Evolution by Means of X-Ray Radioscopy EUFOAM 2012, Lisbon, Portugal, July 2012 Oral communication
S. Pardo-Alonso, E. Solórzano, M.A. Rodríguez-Pérez In-situ Monitoring of Nanofiller-Polyurethane Reactive Foaming Systems EUFOAM 2012, Lisbon, Portugal, July 2012 Oral communication
S. Pardo-Alonso, E. Solórzano, M.A. Rodríguez-Pérez In-situ X-Ray Radioscopy Applied to Cellular Polymeric Materials and their Foaming Mechanisms 2012 PSI Summer School on Condensed Matter Research - Imaging Life and Matter, Institut Montana Zugerberg/Zug, Switzerland Poster
S. Pardo-Alonso, E. Solórzano, J. Vicente, L. Brabant, L. Van Hoorebeke, M.A. Rodríguez-Pérez Foam De-Structuration Via X-Ray Microtomography and Image Analysis SPE-FOAMS 2012, Barcelona, Spain Poster
S. Pardo-Alonso, E. Solórzano, J. Vicente, L. Brabant, L. Van Hoorebeke, M.A. Rodríguez-Pérez Advanced 3D Architectural Descriptors in Foams International Conference on Tomography Applied to Materials Science, ICTMS 2013 Gent, Belgium Oral Communication
S. Pardo-Alonso, E. Solórzano, J. Vicente, L. Brabant, L. Van Hoorebeke, M.A. Rodríguez-Pérez Advanced 3D Architectural Descriptors in Foams International Conference on Tomography Applied to Materials Science, ICTMS 2013 Gent, Belgium Oral Communication
S. Pardo-Alonso, E. Solórzano, L. Brabant, J. Vicente, L. Van Hoorebeke, M.A. Rodríguez-Pérez Computational Approaches for Tortuosity Determination in 3D structures International Conference on Tomography Applied to Materials Science, ICTMS 2013 Gent, Belgium Oral Communication

TABLE 1-3

Other scientific peer-reviewed publications
E. Solórzano, et al. Study of aqueous foams evolution by means of X-ray radioscopy Colloids Surf. A: Physicochem. Eng. Aspects (2013), 438, 159-166
E. Solórzano, S. Pardo-Alonso, N. Kardijlov, I. Manke, F. Wieder, F. García-Moreno and M.A. Rodríguez-Pérez Comparison between Neutron Tomography and X-ray CT Tomography: a Study on Polymer Foams Nuclear Methods and Instruments (<i>accepted, print proofs</i>)

TABLE 1-4

Research funded projects
FP7 European Commission. NANCORE 214148.
Ministerio de Ciencia e Innovación. FEDER. MAT 2009-14001-C02-01.
Ministerio de Economía y Competitividad. FEDER. MAT 2012-34901.
European Spatial Agency. MAP-AO-99-075

REFERENCES

-
- [1] D. Weaire, S. Hutzler, *The Physics of Foams*, Oxford University Press, United Kingdom, (1999)
- [2] Davies GJ, Zhen S. *J Mat Sci* 1983;18:1899.
- [3] D. Klemperer, V. Sendjarevic. *Handbook of Polymeric Foams and Foam Technology*. 2nd Edition. Hanser Publishers, Munich, (2004)
- [4] D. Eaves. *Handbook of Polymer Foams*. Rapra Technology, United Kingdom, (2004)
- [5] Sarit B. Bhaduri, *Science and technology of ceramic foams*, *Advanced Performance Materials*, 1994, Volume 1, Issue 3, pp 205-220
- [6] L. J. Gibson, M. F. Ashby, *Cellular Solids – Structure and Properties*, Second Edition, Cambridge University Press, Cambridge 1997, Ch 1
- [7] A. Cunningham, NC, Hilyard NC *Physical Behavior of Foams- an overview* In: Hilyard NC and Cunningham A (eds) *Low density Cellular Plastics: Physical Basis of Behaviour*, Chapman and Hall, London, (1994) Chap. 1
- [8] E. Solórzano, M.A. Rodríguez-Pérez, *Polymer Foams: Advanced Structural Materials in Transportation*. Eds: M. Busse, A.S. Herrmann, K. Kayvantash, D. Lehms
- [9] www.plasticseurope.es
- [10] M.A. Rodríguez-Pérez. *Propiedades Térmicas y Mecánicas de Espumas de Poliolefinas*. Tesis Doctoral, Universidad de Valladolid, (1998)
- [11] O. Almanza. *Caracterización y Modelización de las Propiedades Térmicas y Mecánicas en Espumas de Poliolefinas*. Tesis Doctoral, Universidad de Valladolid, (2000)
- [12] L.O. Arcos y Rábago. *Propiedades Térmicas y Mecánicas de Espumas de Poliolefinas Fabricadas en un Proceso de Moldeo por Compresión*. Tesis Doctoral, Universidad de Valladolid, (2002)
- [13] J.L. Ruiz-Herrero. *Impacto y Fluencia de Espumas con Base Polietileno*. Tesis Doctoral, Universidad de Valladolid, (2004)
- [14] J.I. González-Peña. *Efecto de los Tratamientos Térmicos en Bloques de Espuma de Polietileno de Baja Densidad Producidos Mediante Moldeo por Compresión*. Tesis Doctoral, Universidad de Valladolid, (2006)
- [15] M. Álvarez-Laínez. *Propiedades Térmicas, Mecánicas y Acústicas de Espumas de Poliolefina de Celda Abierta*. Tesis Doctoral, Universidad de Valladolid, (2007)

- [16] F. Hidalgo-González. Diseño Optimizado de los Parámetros de Proceso de Fabricación de Espuma de Poliolfina Reticulada mediante Moldeo por Compresión. Tesis Doctoral, Universidad de Valladolid, (2008)
- [17] R. Campo-Arnáiz. Aplicación de Técnicas Espectroscópicas al Estudio de la Morfología Polimérica, Propiedades Térmicas y de Emisión de Espumas de Baja Densidad con Base Poliolfina. Tesis Doctoral, Universidad de Valladolid, (2011)
- [18] M.A. Rodríguez-Pérez, O. Alonso, J. Souto, J.A. de Saja. Thermal Conductivity of Crosslinked Closed Cell Polyolefin Foams. *Polymer Testing* 16: 287-298, (1997).
- [19] M.A. Rodríguez-Pérez, S. Díez-Gutierrez, J.A. de Saja. The Recovery Behaviour of Crosslinked Closed Cell Polyolefin Foams. *Polymer Engineering and Science*, 38: 831-838, (1998).
- [20] M.A. Rodríguez-Pérez, A. Duijsens, J.A. de Saja. Effect of the Addition of EVA on the Technical Properties of Extruded Foamed Profiles of Low-Density Polyethylene/EVA Blends. *Journal of Applied Polymer Science* 36: 2587-2596, (1998).
- [21] J.I. Velasco, A.B. Martínez-Benasat, M.A. Rodríguez-Pérez, J.A. de Saja. Application of Instrumented Falling Dart Impact to the Mechanical Characterization of Thermoplastic Foams. *Journal of Materials Science* 34: 431-438, (1999).
- [22] M.A. Rodríguez-Pérez, O. Almanza, J.A. de Saja. Anomalous Thickness Increase in Crosslinked Closed Cell Polyolefin Foams during Heat Treatments. *Journal of Applied Polymer Science* 73: 2825-2835, (1999).
- [23] M.A. Rodríguez-Pérez, J.A. de Saja. The Effect of Blending on the Physical Properties of Crosslinked Closed Cell Polyethylene Foams. *Cellular Polymers* 18: 1-20, (1999).
- [24] O. Almanza, M.A. Rodríguez-Pérez, J.A. de Saja. The Microstructure of Polyethylene Foams Produced by a Nitrogen Solution Process. *Polymer* 42: 7117-7126, (2001).
- [25] O. Almanza, L.O. Arcos y Rábago, M.A. Rodríguez-Pérez, A. González, J.A. de Saja. Structure-Property Relationships in Polyolefin Foams. *Journal of Macromolecular Science, Part B: Physics* 40: 603-613, (2001).
- [26] J. Mills, M.A. Rodríguez-Pérez. Modelling the Gas-Loss Creep Mechanism in EVA Foam from Running Shoes. *Cellular Polymers* 20: 79-100, (2001).
- [27] O. Almanza, M.A. Rodríguez-Pérez, B. Chernev, J.A. de Saja, P. Zipper. Comparative Study on the Lamellar Structure of Polyethylene Foams. *European Polymer Journal* 41: 599-609, (2005).
- [28] M.A. Rodríguez-Pérez, R.A. Campo-Arnáiz, R. Aroca, J.A. de Saja. Characterization of the Matrix Polymer Morphology of Polyolefin Foams by Raman Spectroscopy. *Polymer* 46: 12093-12102, (2005).

-
- [29] M.A. Rodríguez-Pérez, J.L. Ruiz-Herrero, E. Solórzano, J.A. de Saja. Gas Diffusion in Polyolefin Foams during Creep Tests. Effect on Impact Behaviour and Recovery after Creep. *Cellular Polymers* 25: 221-236, (2006).
- [30] M.A. Rodríguez-Pérez, O. Almanza, J.L. Ruiz-Herrero, J.A. de Saja. The Effect of Processing on the Structure and Properties of Crosslinked Closed Cell Polyethylene Foams. *Cellular Polymers* 27: 179-200, (2008).
- [31] M.A. Rodríguez-Pérez, M. Álvarez-Laínez, J.A. de Saja. Microstructure and Physical Properties of Open Cell Polyolefin Foams. *Journal of Applied Polymer Science* 114: 1176-1186, (2009).
- [32] M. Álvarez-Laínez, M.A. Rodríguez-Pérez, J.A. de Saja. Thermal Conductivity of Open Cell Polyolefin Foams. *Advanced Engineering Materials* 10: 373-377, (2008).
- [33] E. Solórzano. Espumas de Aluminio: Proceso de Espumado, Estructura Celular y Propiedades. Tesis Doctoral, Universidad de Valladolid, (2008)
- [34] M.A. Rodríguez-Pérez, J. Lobos, C.A. Pérez-Muñoz, J.A. de Saja, L. González, B.M.A. del Carpio. Mechanical Behaviour at Low Strains of LDPE Foams with Cell Sizes in the Microcellular Range: Advantages of using these materials in structural elements. *Cellular Polymers* 27: 347-362, (2008).
- [35] J. Escudero, E. Solórzano, M.A. Rodríguez-Pérez, F. García-Moreno, J.A. de Saja. Structural Characterization and Mechanical Behaviour of LDPE Structural Foams. A Comparison with Conventional Foams. *Cellular Polymers* 28: 289-302, (2009).
- [36] M.A. Rodríguez-Pérez, J. Lobos, C.A. Pérez-Muñoz, J.A. de Saja. Mechanical Response of Polyolefin Foams with High Densities and Cell Sizes in the Microcellular Range. *Journal of Cellular Plastics* 45: 389-403, (2009).
- [37] C. Saiz-Arroyo, J. Escudero, M.A. Rodríguez-Pérez, J.A. de Saja. Improving the Structure and Physical Properties of LDPE Foams using Silica Nanoparticles as an Additive. *Cellular Polymers* 30: 63-78, (2011).
- [38] J.A. Reglero-Ruiz, C. Saiz-Arroyo, M. Dumon, M.A. Rodríguez-Pérez, J.A. de Saja, L. González. Production, Cellular Structure and Thermal Conductivity of Microcellular Methyl Methacrylate-Butyl Acrylate-Methyl Methacrylate Triblock Copolymers. *Polymer International* 60: 146-152, (2011).
- [39] M. Ardanuy, M.A. Rodríguez-Pérez, J.A. de Saja, J.I. Velasco. Foaming Behaviour, Cellular Structure and Physical Properties of Polybenzoxazine Foams. *Polymers for Advanced Technologies* DOI 10.1002/pat.1978 (2011).
- [40] J.I. Velasco, M. Antunes, O. Ayyad, J.M. López-Cuesta, P. Gaudon, C. Saiz-Arroyo, M.A. Rodríguez-Pérez, J.A. de Saja. Foaming Behaviour and Cellular Structure of LDPE /Hectorite Nanocomposites. *Polymer* 48: 2098-2108, (2007).

[41] J.I. Velasco, M. Antunes, O. Ayyad, C. Saiz-Arroyo, M.A. Rodríguez-Pérez, F. Hidalgo, J.A. de Saja. Foams Based on Low Density Polyethylene/Hectorite Nanocomposites: Thermal Stability and Thermo-Mechanical Properties. *Journal of Applied Polymer Science* 105: 1658-1667, (2007).

[42] R. Verdejo, F. Barroso-Bujans, M.A. Rodríguez-Pérez, J.A. de Saja, M.A. López-Manchado. Functionalized Graphene Sheets filled Silica Foam Nanocomposites. *Journal of Materials Chemistry* 19: 2221-2226, (2008).

[43] R. Verdejo, C. Saiz-Arroyo, J. Carretero-González, F. Barroso-Bujans, M.A. Rodríguez-Pérez, M.A. López-Manchado. Physical Properties of Silicone Foams filled with Carbon Nanotubes and Functionalized Graphene Sheets. *European Polymer Journal* 44: 2790-2797, (2008).

[44] R. Verdejo, F. Barroso-Bujans, M.A. Rodríguez-Pérez, J.A. de Saja, M. Arroyo, M.A. López-Manchado. Carbon Nanotubes Provide Self-Extinguishing Grade to Silicone-Based Foams. *Journal of Materials Chemistry* 18: 3933-3939, (2008).

[45] S. Román-Lorza, M.A. Rodríguez-Pérez, J.A. de Saja. Cellular Structure of Halogen-Free Flame Retardant Foams based on LDPE. *Cellular Polymers* 28: 249-268, (2009).

[46] S. Román-Lorza, M.A. Rodríguez-Pérez, J.A. de Saja. Cellular Structure of EVA/ATH Halogen-Free Flame Retardant Foams. *Journal of Cellular Plastics* 10: 1-21, (2010).

[47] M.A. Rodríguez-Pérez, R.D. Simoes, C.J.L. Constantino. J.A. de Saja. Structure and Physical Properties of EVA/Starch Precursor Materials for Foaming Applications. *Journal of Applied Polymer Science* 212: 2324-2330, (2011).

[48] Y. Ma, R. Pyrz, M.A. Rodríguez-Pérez, J. Escudero, J.C. Rauhe, X. Su. X-Ray Microtomographic Study of Nanoclay-Polypropylene Foams. *Cellular Polymers* 30: 95-110, (2011).

[49] M.A. Rodríguez-Pérez, R.D. Simoes, S. Román-Lorza, M. Álvarez-Laínez, C. Montoya-Mesa. C.J.L. Constantino, J.A. de Saja. Foaming of EVA/Starch Blends: Characterization of the Structure, Physical Properties and Biodegradability. *Polymer Engineering and Science* 52: 62-70, (2012).

[50] D. Simoes, M.A. Rodriguez-Perez, J.A. De Saja, C.J.L. Constantino, Thermomechanical Characterization of PVDF and P(VDF-TrFE) Blends Containing Corn Starch and Natural Rubber, *Journal of Thermal Analysis and Calorimetry* 99(2), 621-629 (2010)

[51] R.D. Simoes, M.A. Rodriguez-Perez, J.A. de Saja, C.J.L. Constantino, Tailoring The Structural Properties of PVDF and P(VDF-TrFe) by Using Natural Polymers as Additives *Polymer Engineering and Science* 49, 2150-2157 (2009)

[52] M.A. Rodriguez-Perez, R.D. Simoes, S. Roman-Lorza, M. Alvarez-Lainez, C. Montoya-Mesa, C.J.L. Constantino, J.A. de Saja, Foaming of EVA/ Starch Blends:

Characterization of the Structure, Physical Properties and Biodegradability, Polymer Engineering and Science, 52(1), 62-70, (2012)

[53] M.A. Rodríguez-Perez, R.D. Simoes, C.J.L. Constantino, J.A. de Saja, Structure and Physical Properties of EVA/ Starch Precursor Materials for Foaming Applications, Journal of Applied Polymer Science 121, 2324-2330 (2011)

[54] S. Ghosh, V. Gutierrez, C. Fernández, M. A. Rodríguez-Perez, J. C.Viana, R.L. Reis, J.F. Mano, Dynamic Mechanical Behavior of Starch-Based Scaffolds in Dry and Physiologically Simulated Conditions: Effect of Porosity and Pore Size Acta Biomaterialia 4, 950-959 (2008)

[55] N.M. Alves, C. Saiz-Arroyo, M.A. Rodríguez-Pérez, R.L. Reis, J.F. Mano Microhardness of Starch Based Biomaterials in Simulated Physiological Conditions, Acta Biomaterialia 3, 69 77 (2006)

[56] Y. Wang, M.A. Rodríguez-Pérez, R.L. Reis, J.F. Mano, Thermal and Thermomechanical Behaviour of Polycaprolactone and Starch/Polycaprolactone Blends for Biomedical Applications Macromolecular Materials Engineering 290, 792-801 (2005)

[57] E. Solórzano, M.A. Rodríguez-Pérez, J.A. de Saja, Thermal conductivity of cellular metals measured by the transient plane source, Advanced Engineering Materials, 10 (596-602) 2008

[58] E. Solórzano, M.A. Rodríguez-Pérez, J.A. Reglero, J.A. de Saja, Mechanical behaviour of internal reinforced aluminium foams, Advanced Engineering Materials 9(11), 955-958 (2007)

[59] E. Solórzano, M.A. Rodríguez-Perez, J.A. de Saja, Thermal Conductivity of Metallic Hollow Sphere Structures: an Experimental, Analytical and Comparative Study Material Letters 63, 1128-1130 (2009)

[60] T. Fiedler, E. Solórzano, A. Öchsner, Numerical and Experimental Analysis of the Thermal Conductivity of Metallic Hollow Sphere Structures Materials Letters 62, 1204–1207 (2008)

[61] J. Lázaro, E. Solórzano, J. A. de Saja, M. A. Rodríguez-Perez, Early anisotropic expansion of aluminium foam precursors, Journal of Materials Science (in press, 2013)

[62] J. Lázaro, E. Laguna, E. Solórzano, M. A. Rodríguez-Perez, Effect of microstructural anisotropy of PM precursors on the characteristic expansion of aluminium foams, Metallurgical and Materials Transactions B (in press, 2013)

[63] F. Garcia-Moreno, E. Solórzano, J. Banhart, Kinetics of Coalescence in Liquid Aluminium Foams, Soft Matter 7, 9216-9223 (2011)

[64] T. Fiedler, E. Solórzano, F. García-Moreno, A. Öchsner, I.V. Belova, G.E. Murch, Lattice Monte Carlo and Experimental Analyses of the Thermal Conductivity of Random Shaped Cellular Aluminium, *Advanced Engineering Materials* 11(10), 843-847 (2009)

[65] J. Lázaro, J. Escudero, E. Solórzano, M.A. Rodríguez-Pérez, J.A. de Saja, Heat Transport in Closed Cell Aluminium Foams: Application Notes, *Advanced Engineering Materials* 11. 825-831 (2009)

[66] E. Solórzano, M. Antunes, C. Saiz-Arroyo, M.A. Rodríguez-Pérez, J.I. Velasco, J.A. de Saja, Optical Expandometry: A Technique to Analyze the Expansion of Chemically Blown Thermoplastic Foams, *Journal of Applied Polymer Science* 125(2) 1059-1067 (2012)

[67] E.Solórzano, F. García-Moreno, N. Babcsan, J. Banhart, Thermographic monitoring of aluminium foaming processes, *Journal of Nondestructive Evaluation* 28(3) 141-148 (2009)

[68] Banhart J, *Advanced tomographic methods in materials research and engineering*. UK: Oxford University Press; 2008.

[69] Lambert J, Cantat I, Delannay R, Renault A, Graner F, Glazier JA, et al. *Colloids Surf A* 2005;263:295.

[70] Montminy MD, Tannenbaum AR, Macosko CW. *J Colloid Interface Sci* 2004;280:202.

[71] J. Banhart, *Manufacture, characterization and application of cellular metals and metal foams*, *Progress in Materials Science*, 46, 559 (2001)

[72] F. Garcia-Moreno, M. Mukherjee, C. Jimenez, A. Rack and J. Banhart, *Metals*, 2012, 2,10–21.

[73] F. García Moreno, M. Fromme, J. Banhart, Real time X-ray radioscopy on metallic foams using a compact microfocus source, *Adv. Eng. Mater.* 6 (2004) 416–420.

[74] A. Rack, F. García-Moreno, C. Schmitt, O. Betz, A. Cecilia, A. Ershov, T. Rack, J. Banhart, S. Zabler, On the possibilities of hard X-ray imaging with high spatiotemporal resolution using polychromatic synchrotron radiation, *J. X-Ray Sci Technol.* 18 (2010) 429–441.

[75] J. Banhart, *Prog. Mat. Sci*, Volume: 46 Issue: 6 Pages: 559-632, 2001

[76] R Mokso, F Marone, S Irvine, M Nyvlt, D Schwyn, K Mader, G K Taylor⁵, H G Krapp⁴, M Skeren and M Stampanoni, Advantages of phase retrieval for fast x-ray tomographic microscopy, *J. Phys. D: Appl. Phys.* 46 (2013) 494004

2. BASIC CONCEPTS ON FOAMS

This chapter describes the basic concepts related to foaming mechanisms and cellular structure of foamed systems that are needed to understand the results presented in the following chapters. The first part of this chapter is focused on meaning statement of the main parameters required to address the description of cellular structures. The second part focuses on the foaming mechanisms.

2.1. DESCRIPTION OF FOAMED STRUCTURES

Cellular materials are two-phase structures constituted by a continuous solid/liquid phase and either continuous or discontinuous gaseous phase [1,²,³,⁴]. As explained in the introduction it is possible to find a large variety of materials with a cellular structure (polymers, wood, metals, etc.). If we have a look into cellular structures topology, it is possible to establish a classification between open cell materials that show continuity of the gas and solid phase and closed cell structures in which the gas is enclosed in the pores (continuous solid phase and discontinuous gas phase).

It is possible to distinguish three different types according to their structural features: lattice-like materials, engineered cellular materials and foams. Lattice-like structures are produced by repetition of a regular structure with a certain regular topology. Engineered cellular materials are constituted by random repetition of a regular or irregular unit cell (pores). Finally, the main distinctive feature in between lattice-like structures, engineered cellular materials and foams is the fact that foams are produced from liquid state and gas is randomly dispersed which results in cellular structure with a completely stochastic morphology and topology (see Figure 2-1).

2.1.1. FUNDAMENTAL COMPONENTS

As mentioned, any cellular structure is constituted by two phases. The solid/liquid phase, which was the precursor before the introduction of the gaseous, is called matrix. Typical examples of foamable solids are metals, polymers, glasses and ceramic [1]. However, this investigation focuses specifically on foams based on polymeric matrixes since they are one of the main topics covered by the research developed at CellMat.

Within the two dispersed phases we can distinguish different elements of interest. The main element of any cellular structure is the cell that is generated due to gaseous phase introduction. It is called indistinctively cell, pore or bubble. It is made from the matrix material and it physically encloses a portion of the gas phase, see Figure 2-2.

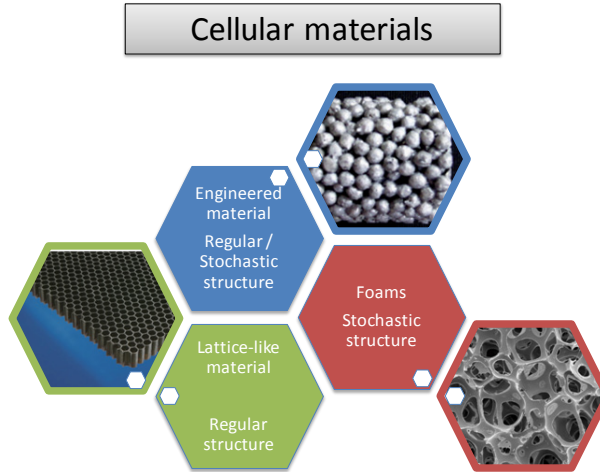


FIGURE 2-1.- DIFFERENT CELLULAR MATERIALS: THERMOPLASTIC HONEYCOMB (LEFT), METALLIC CELLULAR SOLID (CENTRE) AND POLYURETHANE FOAM (RIGHT).

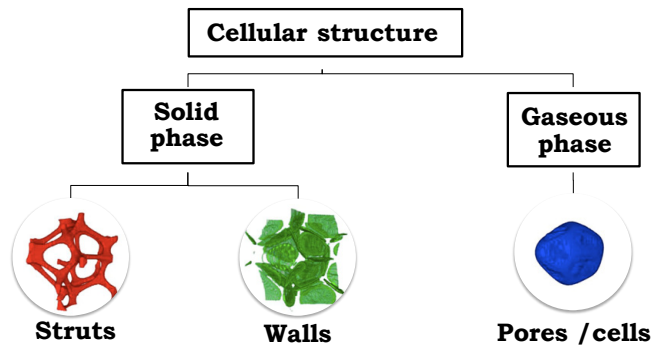


FIGURE 2-2.- MAIN COMPONENTS OF CELLULAR STRUCTURES: STRUTS, WALLS AND CELLS.

Geometrically, faces (F), edges (E) and vertexes (V) constitute the solid phase of cellular structure comprising the solid skeleton of any foam. These elements are mathematically linked by Euler’s equation (Eq. 2-1) in three-dimensional space. In addition, the relation in Eq. 2-2 connects the average number of faces $\langle F \rangle$ per cell and the average number of edges per face, $\langle E \rangle$. Particularly for a pentagonal dodecahedron, $\langle F \rangle = 12$ and $\langle E \rangle = 5$; there are 12 faces, 30 edges and 20 vertexes.

$$F - E + V = 2 \quad \text{EQ. 2-1}$$

$$\langle F \rangle = \frac{12}{6 - \langle E \rangle} \quad \text{EQ. 2-2}$$

In addition, it is known that macroscopic properties of foams such as thermal conductivity, permeability, stiffness, toughness and acoustic absorption are highly influenced by the microstructure [1,2,3]. Subsequently, it is important to characterize at a microstructural level the cellular structure of foams. Vertices and edges together form the struts (also called Plateau borders), which can be considered as the structural skeleton of the porous structure (see Figure 2-2). These elements support the cellular structure itself. As an example of microstructure relevance we can mention that foam modelling often considers regular struts, however strut thickness varies locally, i.e. struts cross-section not only differs from one strut to another but it also does at every position for a given strut. Hence, these variations are known to have an impact on the elastic and thermal properties of foams.

On the other hand, the cell walls (often termed films) are the faces separating two contiguous pores. In general thick cell walls improve the mechanical performance for a certain fixed density. Besides the absence or presence of small holes determine the existence of throats connecting two consecutive pores giving as a result open-cell structure. In the case of total absence of cell walls, we see open cell foams which are basically networks of struts. Nevertheless, an intermediate situation in between closed and open cells is typically observed as shown in Figure 2-3.

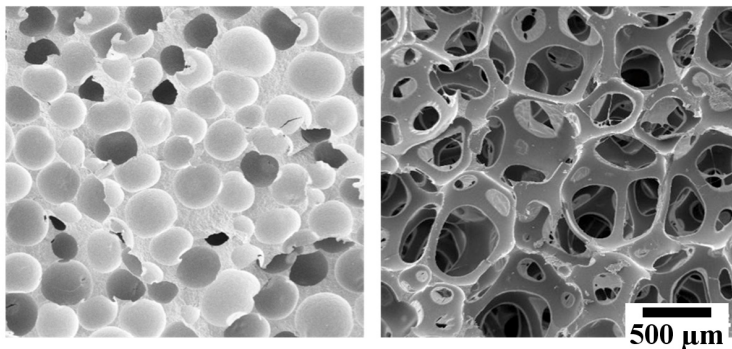


FIGURE 2-3.-OPEN-CELL FOAM (RIGHT) AND CLOSED CELL FOAM (LEFT).

In general, several important magnitudes are used to describe and characterize the main macroscopic and microscopic features of cellular structures. These magnitudes are described in the following paragraphs.

2.1.2. MACROSCOPIC DESCRIPTORS

Relative density expresses the ratio between the foam density and the density of the former solid precursor (Eq. 2-3). It is also called solid/liquid fraction depending on the aggregate state of the matrix. The main reason of relative density key importance is that foamed materials present lower densities than their former solids due to the gaseous phase presence. This is a tuneable characteristic that permits to cover a wide

range; from 1 up to 0.015; materials with $\rho_{relative} > 0.6$ are considered high-density foams whereas materials with $\rho_{relative} < 0.3$ are low-density foams.

$$\rho_{relative} = \frac{\rho_{foam}}{\rho_{solid}} \quad \text{EQ. 2-3}$$

Related to relative density, the expansion grade or expansion ratio (EG) is calculated as the inverse value of the relative density. It indicates the volume ratio of the foamed material in comparison with that of the initial precursor (Eq. 2-4) [1,2]. In other words, this value expresses how many times the solid material has been expanded.

$$EG = \frac{1}{\rho_{relative}} \quad \text{EQ. 2-4}$$

2.1.3. PRIMARY MICROSCOPIC DESCRIPTORS

CELL SIZE

The average cell size is one of the most representative parameters of a cellular structure. It generally refers to the mean diameter of bubbles/pores/cells although some other definitions are possible. Cell size is a key parameter for properties such as thermal conductivity, toughness and ultimate mechanical properties. In fact, some of the most important research topic directly focuses nowadays on reducing the cell size to the micro-scale (microcellular foams) and nanoscale (sub-microcellular and nanocellular foams).

Cell size is generally measured according to ASTM D3576 by counting the number of cell walls intersections in a specified distance using optical or scanning electron microscopy (SEM) micrograph [5,6,7,8]. In electron microscopy, polymer foams often become deformed under vacuum conditions and metallic sputtering since they are very light structures. This can result in inaccurate measurements. Moreover, these conventional procedures consider a cell size value extracted from micrographs (2D) regardless average cell size is a 3D concept. The results can be skewed since microscopy relies on 2D cross sections of polyhedral pores. Furthermore, cells growth is often oriented along certain preferential direction. This results into anisotropic cross sections as seen in Figure 2-4. This leads to the presence of different cell sizes depending on which cross section is measured. The use of 2D images to calculate average cell size does not allow to analyze all possible projections produced by planes in 3D space. As an example for the three Cartesian directions we can calculate three different average cell size values, i.e. ϕ_x , ϕ_y and ϕ_z are obtained. These differences are useful for anisotropy study. Nevertheless, there exist several methodologies described in the literature aimed at extrapolating the 2D value to real 3D value [9]. In addition,

there are several possible ways to define an average cell diameter. Equivalent diameter is that one obtained from an equivalent sphere containing the same volume as the cell. Another possibility is to define maximum and minimum diameters for every pore. Finally, feret diameter defined as the maximum caliper diameter is also often used.

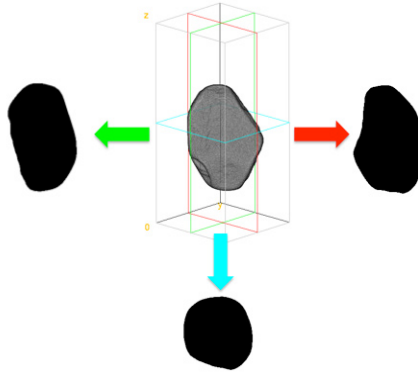


FIGURE 2-4.-SINGLE CELL IN AND CROSS-SECTIONS PROJECTED ON CARTESIAN PLANES.

It is important to remark that an average value of cell size is not always enough to provide an accurate description since foams are stochastic structures. In these cases, cell size distribution analysis provides useful information. Bimodal, Gaussian and monodisperse are typical distributions found in cellular materials (see Figure 2-5). They appear as a result of different foaming mechanisms. As exemplary, a bimodal distribution can appear as a result of having two types of nucleating sites where cells appear. These distributions may result in similar average cell size but they correspond to clearly different cellular structures.

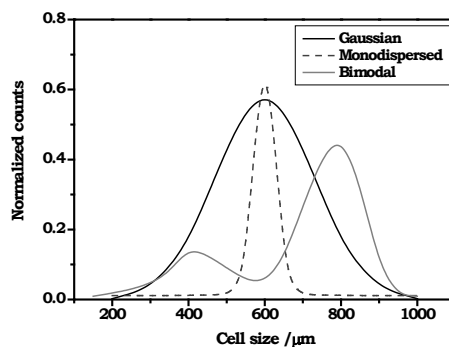


FIGURE 2-5.-TYPICAL CELL SIZE DISTRIBUTIONS (GAUSSIAN, MONODISPERSE AND BIMODAL) OBSERVED IN FOAMS.

CELL DENSITY

This magnitude, as defined in Eq. 2-5 indicates the number of cells (pores or bubbles) per unit volume. Cell density reaches a value more realistic since it merges the information of foam density and cell size. For instance, microcellular foams have been typically defined as materials with cell densities higher than 109 independently of the density.

$$N_v = \frac{6}{\pi\phi^3} \left(\frac{1}{\rho_{relative}} - 1 \right)$$

EQ. 2-5

It is important to note the inverse cubic dependence of the cell density with the cell size and macroscopic density. It means that at same relative density if we observe smaller cells, the cell density will much be higher. Figure 2-6 shows two representative volumes of foamed materials showing different cell size at same density. In this case, cell density characterizes the differences existing between the two structures. An average cell size value of 750 μm yields 9×10^5 cells/ cm^3 whereas a value of 350 μm yields 8.8×10^6 cells/ cm^3 . All mentioned reasons make cell density to be relevant parameter used throughout this investigation due to its direct usefulness to describe cellular structure evolution during the foaming processes.

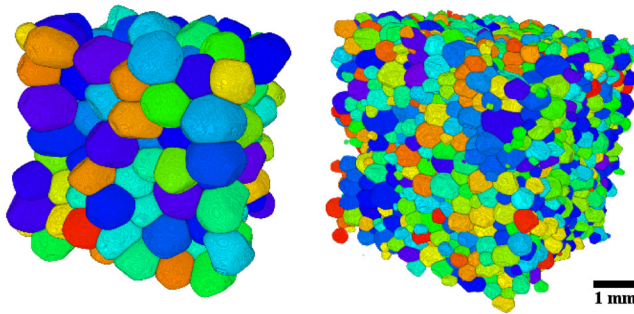


FIGURE 2-6. - 3D RENDERING VIEW OF FOAMS WITH DIFFERENT CELL DENSITIES.

2.1.4. OTHER MICROSCOPIC DESCRIPTORS

Cell shape is an important morphological feature for physical properties, especially when there is a preferred orientation of the cellular structure. From a theoretical point of view, a significant variety of cell geometrical shapes is possible in a three dimensional space, e.g. tetrahedron, triangular prism, hexagonal prism, octahedron, rhombic dodecahedron, pentagonal dodecahedron, tetrakaidecahedron and icosahedrons. Plateau (1873) identified the rhombic dodecahedron (12 faces) as the most energy efficient single unit to partition the 3D space until Kelvin (1887) minimized the unit cell surface thanks to the use of tetrakaidecahedron with slightly

curved surfaces. In 1994 Weaire and Phelan minimized even more this surface by six 14-sided cells made up of 12 curved pentagonal and 2 hexagonal plane faces [10]. Cell shapes in foamed structures tend to these theoretical geometries, although dispersions in shape are always observed.

ANISOTROPY AND CELL ORIENTATION

As a result of processing peculiarities, measured cell size often varies with direction. Subsequently, the properties of the material are anisotropic, i.e. they exhibit a different value depending on the testing direction. In the particular case of polymer foams, they usually show cells elongated in the rise direction as seen Figure 2-7. This anisotropy can be measured as the ratio, R_{ij} , between the length in the rise direction and that in the perpendicular plane having as a reference a Cartesian system generally with one axis aligned with the processing direction [1,3]. Specifically, Eq. 2-6 indicates the anisotropy in the ij -plane calculated as the ratio between length in i -axis, ϕ_i , and length in j -axis, ϕ_j . Then, Eq. 2-7 expresses the anisotropy in i -direction obtained as the average in between R_{ij} and R_{ik} , constrained in a plane containing i and the perpendicular j -axis. In general, the value of R for polymer foams can vary from 1 up to 10.

Furthermore, anisotropic pores can be also oriented with a certain angle with respect a predefined direction. Cell orientation differs from anisotropy since it is not referred to any specific direction. It is also possible to define two angles θ , φ to express cells orientation in the 3D space.

From the properties point of view, a highly anisotropic/oriented structure can be important for structural applications where a preferential direction of pores improves stiffness and strength. Contrary, from a thermally point of view the insulation capability of foams is reduced in the elongation direction [8, 11]

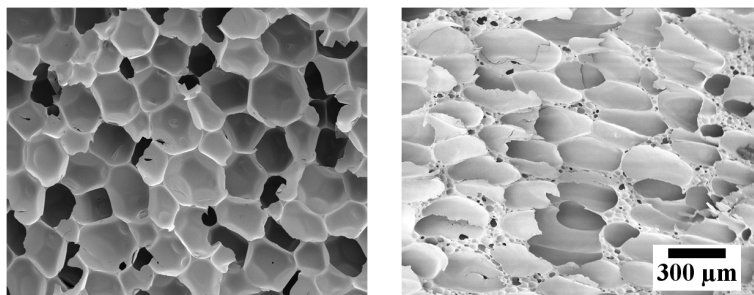


FIGURE 2-7. - MICROGRAPHS OF ISOTROPIC FOAM (LEFT) AND ANISOTROPIC PORES (RIGHT) ORIENTED IN THE HORIZONTAL DIRECTION.

$$R_{ij} = \frac{\phi_i}{\phi_j} \quad \text{EQ. 2-6}$$

$$R_i = \frac{R_{ij} + R_{ik}}{2} \quad \text{EQ. 2-7}$$

COORDINATION NUMBER

Complementarily, coordination number provides topological indication of cellular packaging. It expresses the average number of neighbours for every pore, as seen in Figure 2-8. This feature is also closely related to physical behaviour. As an example, large pores are typically surrounded by many neighbours can be the origin of mechanical failure. Neighbourhood is also linked to cell size distribution. In this sense, the large distribution dispersion in cell size, the wider is coordination number distribution. The influence of these parameters on properties is still not fully understood due to the difficult task of preparing materials with significant differences in these parameters while keeping all the others (density, average cell size, anisotropy, etc.) constant. As a result, controversial results can be found in the literature. The real values of neighbours are typically different to the theoretical ones.

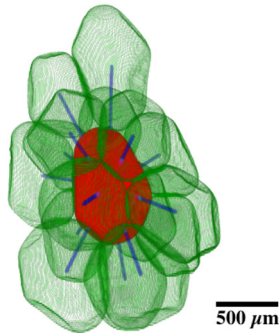


FIGURE 2-8.- ONE SINGLE PORE (RED), NEIGHBOURS (GREEN) AND LINES CONNECTING THE OBJECT CENTRES (BLUE).

INTERCONNECTIONS AND OPEN-CELL CONTENT

On the other hand, the presence of interconnections is of extreme importance for transport-related properties. Figure 2-9 shows an interconnected cellular structure where the cell connections are highlighted in colours. This type of interconnected structure is important for some acoustic and thermal properties. For instance we can mention mass transport membranes, scaffolds for tissues regeneration and food-packaging absorbing trays where a certain amount of liquid has to be absorbed through connections between pores. The number, size and shape of these throats also have an influence on the physical behaviour of these materials. Consequently, structural and thermal insulating applications demand closed cell structures. Regarding cells connectivity, an intermediate situation between open and closed cell foams is usually seen in many cellular structures. Open-cell content (percentage) is defined as the volume fraction of interconnected cells in Eq. 2-8.

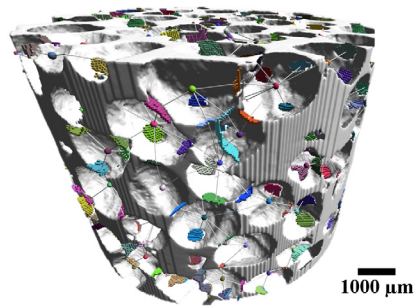


FIGURE 2-9. - PORE THROATS (IN COLOURS) INTERCONNECTING THE GASEOUS PHASE.

Gas pycnometry is the common experimental technique used for solid foams that permits to obtain the open-cell content as a function of the geometric volume (V) and the displacement volume (V_p). The displacement volume is determined using gas pycnometer and then V_s takes into account the exposed cells at the surface of the sample.

$$O_v (\%) = \frac{V - V_p + V_s}{V \left(1 - \frac{\rho_{foam}}{\rho_{solid}} \right)} \quad \text{EQ. 2-8}$$

Nevertheless, calculation based on the 3D cellular structure obtained from tomographic techniques allows a more accurate study of several interconnections parameters such as total number of throats, shape, size, distribution, etc.

2.1.5. ADVANCED DESCRIPTORS

Up to this point, several magnitudes conventionally used in the study of cellular structures have been defined. Nevertheless, foam features are not completely described by them. Therefore, there is a need of measuring and defining other descriptors to characterize additional peculiarities of cellular structures that requires advanced calculations. The following paragraphs describe the material distribution across the structures, the walls corrugation and the tortuosity (both in the gaseous and the solid phases).

Firstly, struts and walls are theoretically considered as elementary elements and the amount of material located in each of these parts is important for various properties. In general, the analysis of cellular structures is focused on the pore analysis (air-phase) whereas the solid phase is less studied and, as a maximum, an analysis on material thickness distribution is carried out. The separation of the continuous solid structure into two clearly differentiated parts would be an extreme value. The material fraction

distribution varies locally and thus it is interesting to set its characterization under study.

The ratio between the amount of material located at struts (vertexes and edges) and the total amount of material quantifies the solid fraction at struts. It is given by Eq. 2-9, also named strut factor, f_s .

$$f_s = \frac{m_{struts}}{m_{struts} + m_{walls}} \quad \text{EQ. 2-9}$$

A similar concept can be defined as expressed in Eq. 2-10 for tomographic volumes analysis and it is called strut volumetric fraction, SVF .

$$SVF = \frac{V_{struts}}{V_{total}} \quad \text{EQ. 2-10}$$

Conventional methodologies aimed at determining the solid fraction in the struts (f_s) are in part theoretical and part empirical. These methodologies are based on 2D micrographs. They use manual methods to approximate the projected cross-section of the struts either in an equivalent circle [7] or triangle occupying two-thirds area of an equilateral triangle [8] and later using a dodecahedron-based model to estimate the final f_s value. Nonetheless, 3D imaging provides alternative methods to quantify this feature.

It is well known that this parameter has a strong influence in the physical properties of cellular materials. Stiffness, strength and thermal conductivity are examples of the properties affected. Therefore, a method for the determination of f_s is of a capital influence for a fine modelling of the mentioned properties. Figure 2-10 represents a visualization where material fraction at struts is identified in red and walls separating cells is highlighted in green.

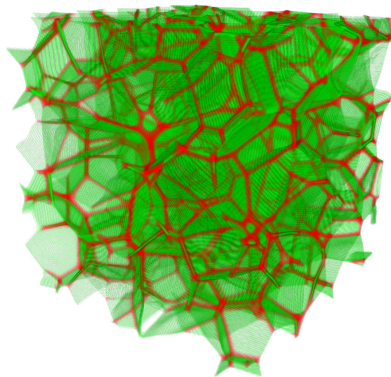


FIGURE 2-10. - POLYMER FOAM WITH STRUTS IDENTIFIED IN RED AND CELL WALLS IN GREEN.

The existence of non-flat cell walls is an important aspect that has been investigated from the theoretical and experimental points of view, but it has not been studied from semi-automatic 3D methods [^{12, 13, 14}]. Models to describe foams behaviour consider flat cell walls and straight struts. Nevertheless, real manufactured foams often show corrugations in their cell walls and tortuous struts due to processing conditions. As an example, temperature variations might cause excessive gas expansion followed by a shrinkage, which results in wrinkles in the films separating pores (see Figure 2-11).

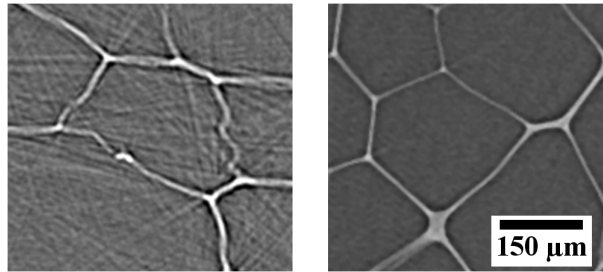


FIGURE 2-11.-SLICES FROM FOAM TOMOGRAMS WITH HIGHLY CORRUGATED CELL WALLS (LEFT) AND VERY FLAT CELL WALLS (RIGHT).

Some modelling such as Gibson-Ashby equation for collapse-stress assume that the microstructure of cellular materials consists of a large number of thin threads, connected at their ends by non-deformable volumes constituting a three-dimensional network [1]. This fact may result in an overestimated collapse strength value according to Gibson-Ashby for the post-collapse zone in Eq. 2-11, where the first contribution is the collapse stress and P_0 is the effective pressure of gas enclosed in cells.

$$\sigma = EG\left(\frac{\rho_f}{\rho_s}\right)^2 + \frac{P_0\varepsilon}{1 - \varepsilon - \frac{\rho_f}{\rho_s}} \quad \text{EQ. 2-11}$$

This investigation presents in chapter 6 some methodological approaches based on CT images analysis to determine the wrinkles presence at cell walls. It is often difficult to do an extensive analysis of walls by analyzing the continuous foam network. However, this type of analysis is performed thanks to prior foam de-structuration of foam elements, i.e. struts and walls. It is then possible to do accurate study of these discontinuous elements and detect weak differences such as mentioned wall wrinkles that are not strictly considered in Gibson-Ashby equation.

On the other hand, estimation of the path length that a fluid has to cover through an interconnected structure is also a parameter of extremely high importance for material transport properties. This parameter can be calculated both in solid and gaseous phases and it is called tortuosity. It is a geometrical concept that expresses the ratio between the distance of any real path and the shortest distance between two points. In this sense, it also related to the continuity or discontinuity of air phase that

comes determined by the open cell content. Moreover it is related to physical properties of cellular structures. Particularly, it plays an important role for mass and heat transport properties among other properties.

Mathematically, tortuosity is defined as the ratio between geodesic distance (the path length through solid/gaseous phase) and the Euclidean distance (shortest straight distance projection over the Cartesian axis, see Eq. 2-12). The geodesic distance includes the extra distance that has to be covered by “travelling” through the gaseous/solid phase.

$$\tau = \frac{\text{dist}_{\text{geodesic}}(p_1, p_2)}{\text{dir}(\|p_1 - p_2\|)} \quad \text{EQ. 2-12}$$

It is important to note that tortuosity is a directional parameter; therefore we can obtain a value for any direction in the 3D space. Three principal directional values are commonly used corresponding to the three Cartesian axes (X, Y and Z).

2.2. POLYMER FOAMS PRODUCTION

2.2.1. BLOWING AGENTS

Nowadays there are various industrial and laboratory processes able to generate the gaseous phase in the solid/liquid continuous matrix. In general, any foam can be produced by either a physical or chemical procedure. A common characteristic is the necessity of a blowing agent, which is the responsible of the gas phase generation. The blowing agent can be blended with the plastics before processing or fed directly into the hopper present in the processing machine.

A physical foaming procedure basically consists in gas dissolution process either under pressure or by turbulent mixing into the matrix that afterwards nucleates the bubbles. Physical blowing agents (PBA) generate gas due to change of physical state or gas/polymer system solubility. Normally, they are low boiling point liquids or gases such as hydrocarbons or inert gases, CO₂ or N₂. The gas/polymer system is located under pressure increasing gas solubility into the matrix. This decreases considerably the glass transition temperature, T_g , and viscosity of the polymer melt. Rapid depressurization promotes cell nucleation that growth until the polymer solidification/vitrification stabilizes the cellular structure [15]. They are mostly used to produce low-density foams (less than 50 kg/m³) and they are relatively low-cost, but require special equipment for production. Physical foaming processes are not used in our investigations since they involve the use of pressure and thus difficult X-ray use for visualization.

The other strategy to produce cellular structure is the chemical foaming technology. These processes use a chemical compound (CBA) that releases the gas phase when it is heated above certain temperature. From a thermodynamically point of view, those

chemical agents can have endothermic or exothermic decompositions. A careful selection is crucial for the processing and the final aimed foamed product. It is important to select carefully the most appropriate since the parameters such as the temperature range of decomposition, the chemical volatiles or the amount of gas released strongly condition the processing window and the final usability of the foamed material. One of the most extended CBA is azodicarbonamide (ADC). ADC decomposes in a temperature range between 200 and 240°C and produces a large amount of gas (250 cm³/g) generating N₂ (approx. 65%) and lower amounts of CO, CO₂ or NH₃ [2, 8].

2.2.2. FOAMING TECHNOLOGIES

Producing a foamed structure requires a complex process where many physical and chemical mechanisms occur simultaneously. Several processes have been proposed and some of them successfully scaled to industry since Munters and Tandberg published the first patent in 1935 [16]. The adequate election of the suitable process depends mainly on two factors: polymer matrix nature and final aimed features (density, structure, properties, shape, applications, etc.). Nowadays, many matrixes are foamed by reactive foaming, free foaming, extrusion, injection moulding, compression moulding, rotational moulding, etc. [2, 3]. All the main production routes are based on common basic foaming mechanisms and stages that are described in next section in page 69.

We present a short description of few prototypical foaming processes of interest. We focus on some of the most representative and used technologies, which are schematically presented in Figure 2-12. They can be classified regarding the use of a pressure drop to promote the foaming process. The processes that do not involve the use of pressure are then extensively used in this investigation, i.e. reactive foaming and free foaming. In fact, they facilitate the study of physical mechanisms and cellular structure evolution by X-ray imaging techniques.

FREE FOAMING

In a first step, the chemical blowing agent is dispersed into the polymer matrix. This is typically performed using twin-screw extruders. In a second step, foaming takes place by heating the foamable precursor at temperatures above the decomposition temperature of the blowing agent. It is one of the simplest foaming processes in which temperature, time and formulation are the key control parameters. It is industrially used for the production of cross-linked polyolefin sheets, microcellular foam sheets and foam parts by roto-moulding. In addition, it is a simple process that can be seen as a model system for producing foams. It allows to obtain a large amount of information by simple tests and it is lab-scale handling. In this case, no external pressure is applied and CBA decomposition takes place because of temperature increase. It is important to remark that this process requires simple instrumentation and permits the use of X-ray

CHAPTER 2

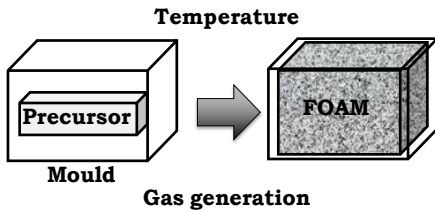
imaging to visualize cellular structure evolution. All these reasons motivate working with free foaming since it allows investigation of foaming mechanisms and cellular structure evolution. The obtained information may serve as a basis for further development of formulations to be foamed in more complex processes such as extrusion machines, injection or compression moulding procedures described in the following paragraphs.

Foaming technologies

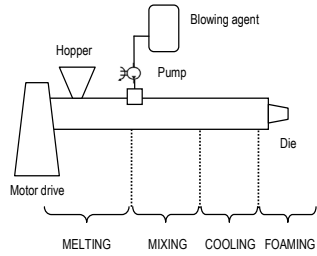
Without pressure

With pressure

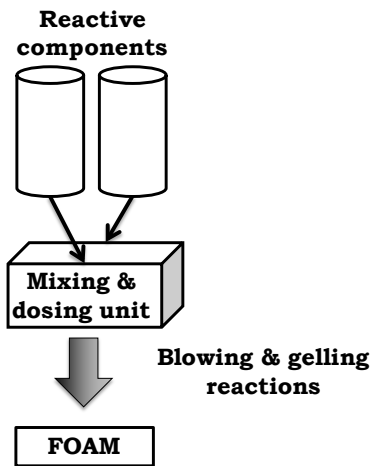
Free foaming



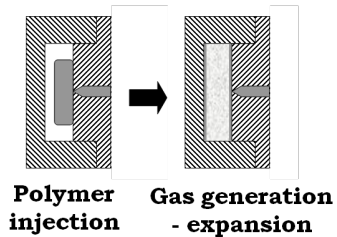
Extrusion foaming



Reactive foaming



Injection moulding



Compression moulding

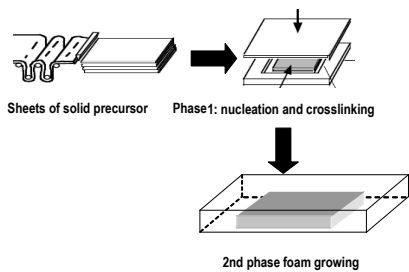


FIGURE 2-12.- SCHEME OF DIFFERENT FOAMING TECHNOLOGIES.

CHAPTER 2

REACTIVE FOAMING

In this process the expansion takes place during the reactive process of certain mixture of components. This occurs generally after turbulent mixing. It is the process generating the cellular structure in polyurethane foams. The reactive process induces simultaneous both blowing and polymerization of such a system. The blowing agent is generally present in the one of the reactants. As a result of the blowing agent reaction with any other reactant present in the mixture the blowing gas drives cells growth. Finally the polymerization provides foam stability and stops expansion. Industrial production of such processes is generally associated to pressure injection machines that spray the mixed reactants promoting the foaming reaction due to shear mixing.

EXTRUSION FOAMING

This is a continuous process working under similar principles of solid polymer extrusion. It allows to produce simple geometries (pipes, panels, profiles, etc.) of low and high-density foams. Nevertheless, temperature and pressure need to be controlled carefully due to foaming agent presence. The main stages of this process are polymer melting, blowing agent injection and dissolution into the polymer melt (for PBA), decomposition temperature (for CBA), cooling of the melt containing the blowing agent to a temperature close to the melting temperature of the base polymer and pressure drop at the die which allows expansion to occur. Then cell nucleation occurs, expansion starts and bubbles grow out of the die reaching stabilization of the resultant cellular structure by cooling and solidification. The extrusion foaming can use a single extruder or tandem extruders. This last one is often used in industry to produce very low-density foams of PS, XPS, PE and PP, in which a second large extruder, is needed to cool down the melt before foaming at the die exit.

INJECTION MOULDING

This technique is the most extended together with extrusion and complementarily allows manufacturing a large variety of complex geometries [17,18]. There are parts of the mould with a high relative densities (higher than 0.6) allowing foaming. The first stages are similar to those in extrusion foaming and the rest of the process (cell nucleation and growth) continues inside a mould until the foamed part solidifies. There are two main technologies. In the low-pressure injection a small amount of gas/polymer is injected inside the mould and fills it fully by expansion achieving the desired density. Contrary in the high-pressure injection, the polymer/gas system fills completely a specifically designed mould.

COMPRESSION MOULDING

In this process we can find variations depending whether one or two expansions stages take place. In a first step the polymer, blowing agent, additives and cross-linkers are mixed in a twin-screw extruder below the blowing and cross-linking temperature. After

this mixing the compound is placed inside a mould and pressure is applied. Meanwhile, temperature increases to induce CBA and cross-linking agents' decomposition. Finally, pressure is eliminated and the foam expands. *EG* obtained by this process are typically limited to 10 and therefore when low densities are required two-steps compression moulding process is used. In this process first a pre-expanded precursor is produced using the procedure described previously, and then the second step allows remaining CBA decomposition inducing expansion up to 40 times and fully filling a pre-heated mould.

2.3. FOAMING DYNAMICS

2.3.1. FOAMING MECHANISMS

During any type of foaming process, regardless it is based on PBA or CBA, several foaming mechanisms are responsible for cells formation, growth and stabilization. All of them condition the development of the foaming process and thus the cellular structure at every instant. As exemplary of their important role, we can have two materials with the same average cell at the final stage but one of them may have shown an increased cell nucleation and later cell coalescence whereas the other could have achieved the same final average cell size by poorer nucleation but absence of cells coalescence. In such a case, it is not trivial to attribute to one of them the responsibility of the final cellular structure. In fact, some of them may play simultaneous roles.

The main physical mechanisms, typically present during foam generation, are cell nucleation, growth, drainage, coalescence and coarsening. We can separate them into those governing cells creation (nucleation and growth) and those driving cellular structure degeneration (drainage, coalescence and coarsening).

Figure 2-13 shows visually the different stages occurring during a foaming process represented together with a typical expansion curve. It is important to note that the information about what is happening during the evolving process becomes essential to understand the final cellular structure produced. It is also important to study the mechanisms promoting foam stabilization such as solidification in polymer or metallic foams. These foaming stages can occur in very different temporal ranges. For example they occur practically instantaneous in extrusion foaming as the melt drops out of the extruder die or they can occur within a few tens of seconds in very slow reactive systems such as polyurethanes. Stabilization and solidification depends on the polymer system behaviour and foaming method and can vary from few up to some hours.

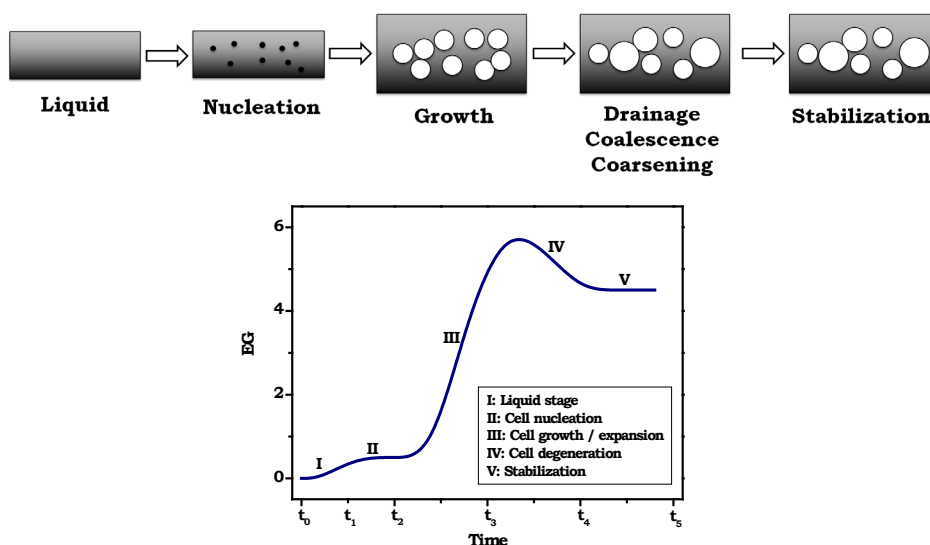


FIGURE 2-13.- VISUALIZATION SCHEME DIFFERENT STAGES DURING FOAM EXPANSION TOGETHER WITH TYPICAL MACROSCOPIC EXPANSION CURVE.

MECHANISMS OF CELLS GENERATION

CELL NUCLEATION

Cell nucleation is the mechanism responsible of cells generation. It is usually seen as one of the key mechanisms to optimize foam production since highly efficient nucleation often results into successful foaming. During the early stages of foaming cells start to appear. The nucleation mechanisms initiate the formation of tiny cells as gas phase generation is activated. This gas phase segregation occurs either by temperature induced decomposition of a CBA or an abrupt pressure change that reduces gas solubility into the polymer in the case of PBA. The new disposal of the gas into cells tends to reduce the free energy of the foaming systems.

In general, nucleation theories consider two possibilities: homogeneous and heterogeneous nucleation. Thermodynamics governs the main equations to describe nucleation mechanisms. Homogeneous nucleation occurs without the presence of impurities that can promote gas segregation and form gas cavities. In this case, the Gibbs free energy barrier (ΔG) for the homogeneous nucleation is given by Eq. 2-13. Pressure difference between gas cells and solid (Δp) and material properties such as the surface tension, σ , are the main variables.

$$\Delta G_{\text{hom}}^* = \frac{16\pi\sigma^3}{3\Delta p^2} \quad \text{EQ. 2-13}$$

Homogeneous nucleation theory developed by Colton and Suh provides an expression for the nucleation rate, N_{hom} (see Eq. 2-14) [19, 20]. The pre-exponential factors C_{hom} and f_{hom} are related to the kinetics of gas diffusion and both together they express the number of gas molecules per unit volume.

$$N_{hom} = C_{hom} f_{hom} \cdot \exp\left(-\frac{\Delta G_{hom}}{k_B T}\right) \quad \text{EQ. 2-14}$$

However, the most common type of nucleation in polymer foams is heterogeneous one since polymers usually contain particles and impurities. This heterogeneous nucleation assumes that cell nucleation will form a cell on liquid/solid interface of these pre-existing particles acting as nucleating sites (e.g., impurities, nucleating agents, etc.). In this specific case, there is an energy reduction factor, $f(\theta)$ that depends on the nucleating sites geometry [21]. Therefore not all the potential nucleating sites necessarily originate cells. Otherwise, an extremely high amount of cells would appear and this is not experimentally observed. In this situation the free energy barrier for cell formation is given by Eq. 2-15.

$$\Delta G_{heterogeneous}^* = f(\theta) \Delta G_{hom}^* \quad \text{EQ. 2-15}$$

According to this theory of heterogeneous nucleation, the classical nucleation theory states that a cell with a radius greater than the critical radius (R_{cr}) tends to grow spontaneously whereas a cell with smaller radius collapses and the gas contained in it is again distributed into the melting matrix. Curiously, this critical radius in the homogeneous and heterogeneous nucleation turns out to be the same, see Eq. 2-16. Once again, surface tension (σ) and pressure difference (Δp) are involved in the critical nucleation radius.

$$R_{cr} = \frac{2\sigma}{\Delta p} \quad \text{EQ. 2-16}$$

To study nucleation it is relevant to calculate dynamic magnitudes since this mechanism evolves with time. In this sense, the nucleation rate expresses the number of bubbles formed per unit time. An Arrhenius law, as shown in Eq. 2-17, governs it. [19,20]. The nucleation rate in heterogeneous nucleation behaves similar to that of homogeneous nucleation but the factors C_{het} and f_{het} are now different. They express the number of gas molecules per unit surface area of the nucleating agents [21,22].

$$N_{het} = C_{het} f_{het} \cdot \exp\left(-\frac{\Delta G_{het}}{k_B T}\right) \quad \text{EQ. 2-17}$$

On the other hand, it is possible to estimate the maximum nucleation density of added fillers in a system dominated by heterogeneous nucleation. This is useful to calculate nucleating efficiency in particular foaming systems. The number of nucleating centres

per unit volume is given by Eq. 2-18 [23]. Where w is the weight fraction of the particle, $\rho_{particle}$ is the particle density, ρ_{blend} is the density of the mixture and $V_{particle}$ is the filler volume. It is possible to estimate nucleation efficiency by using the ratio between the nucleating centres previous to cell formation (potential nuclei) and the cell density obtained in the final foamed material for certain particle concentration. According to Eq. 2-18, the $V_{particle}$ is a key parameter. The smaller the volume of the nucleating centre the higher number of cells is created. This occurs because the gas tends generate cells at the liquid/gas interphase. The total interphase available for gas adsorption is much larger for a high number of small particles than for agglomerated ones. Therefore, a high dispersion of fillers and exfoliation in the particular case of layered fillers is always necessary.

$$nucleants / cm^3 = \frac{w}{\rho_{particle}} \frac{\rho_{blend}}{V_{particle}} \quad \text{EQ. 2-18}$$

Finally expressions for the nucleation rate are derived in Eq. 2-19 and Eq. 2-20 [24]. N takes into account thermodynamic fluctuations and it is the number of gas molecules per unit surface area of the nucleating agents (heterogeneous nucleation), m is the mass of a gas molecule and Q is the ratio of the surface area of the liquid-gas interface to that of a spherical cell with the same radius.

$$J_{hom} = N \sqrt{\frac{2\sigma}{\pi m}} \exp\left(-\frac{16\pi\sigma^3}{3K_B T \Delta p^2}\right) \quad \text{EQ. 2-19}$$

$$J_{het} = N^{2/3} Q \sqrt{\frac{2\sigma}{\pi m f}} \exp\left(-\frac{16\pi\sigma^3 f}{3K_B T \Delta p^2}\right) \quad \text{EQ. 2-20}$$

CELLS GROWTH

Once those cells are nucleated, they start to grow and the expansion of individual bubbles takes place as observed in Figure 2-13. Cell growth involves a large number of cells expanding in proximity to each other in the melt-gas solution. In order to describe the growth of a cell, we can look a single cell surrounded by a liquid of molten material. The concentration of adsorbed gas is reduced as cell expands. This concentration can be restored by one of two processes: the Marangoni effect that makes the material can flow from areas of low surface tension to those of high surface tension (low concentration), or Gibbs effect that makes surfactant in the interior of the liquid to diffuse towards the surface without restoring the cell wall. The gas inside the cell is assumed to behave as an ideal gas and its pressure is always greater than the pressure in the molten surrounding material. The released gas diffuses from high-pressure regions (matrix) to low-pressure regions (cells). Therefore, generated cell expands due to pressure difference. Cell growth continues until it stops as the cellular structure becomes stabilized by cooling and/or polymerization. The rate at which

bubbles grow is a function of the polymer viscosity (η_0), the diffusivity of the gas (D), the pressure inside the cell (P_g), and the external pressure (P_a) under which the growth is allowed to occur. The cell growth is described in the literature by coupled mass and momentum conservation equations. Patel derived modelling equations for a Newtonian fluid with constant viscosity; see Eq. 2-21 and Eq. 2-22 [25]. The pressures inside (P_g) and outside the cell (P_a), the materials viscosity (η_0) and the surface tension (σ) are involved in these growth equations. The gas molecular weight, diffusion coefficient, material density and temperature are all included under the constant a .

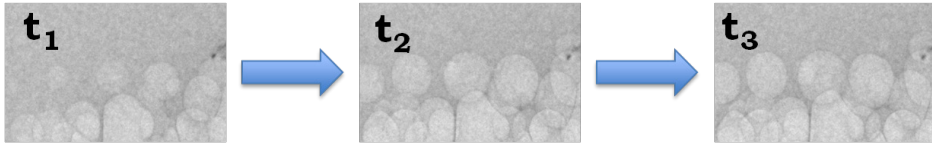


FIGURE 2-14.- VISUALIZATION OF CELL GROWTH IN POLYMERIC FOAM AT THREE CONSECUTIVE INSTANTS.

$$\dot{R} = R \left(\frac{P_g - P_a - \frac{2\sigma}{R}}{4\eta_0} \right) \quad \text{EQ. 2-21}$$

$$\frac{dP_g}{dt} = a \left(\frac{(P_{g0} - P_g)^2}{P_g R^3 - P_{g0} R_0^3} \right) - 3P_g \frac{\dot{R}}{R} \quad \text{EQ. 2-22}$$

Nevertheless, it is important to comment that Patel modelling predicts infinite cell growth since it considers a single cell model [26]. To solved this unreal behaviour, Amon and Denson derived a model taking into account the limited gas supplied and the physical impossibility of infinite growth due to presence of surrounding cells [27]. They modelled every single cell as enveloped by a liquid (polymer) shell of radius $S(t)$ which radius decreases with expansion. They also included a limited gas concentration $c(t)$ and did not assume simplification of the diffusion equation as reported by Patel. With these considerations, they achieved to predict saturation pressure limiting cell growth thanks to Eq. 2-26 and Eq. 2-27.

$$\dot{R} = R \left(\frac{P_g - P_a - \frac{2\sigma}{R}}{4\eta_0} \right) \left(\frac{S^3}{S^3 - R^3} \right) \quad \text{EQ. 2-23}$$

$$\frac{dP_g}{dt} = aR^2 \frac{dc}{dr} - 3P_g \frac{\dot{R}}{R} \quad \text{EQ. 2-24}$$

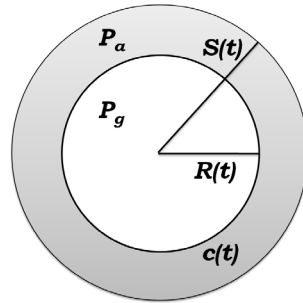


FIGURE 2-15.- CELL GROWTH SCHEME USED FOR AMON AND DENSON GROWTH MODEL.

In the specific case of polymers, rheology and the extensional behaviour condition cells growth. It is important to note that polymer physical behaviour changes as gas diffuses towards the cells. Moreover the material suffers stretching as cells growth. If the polymer reaches the stretching limit or stabilisation does not take place the cellular structure degenerates, i.e. cell ruptures may occur (see below mechanisms of cellular degeneration). In general, the underlying physics of this foaming mechanism is complex. Many variables influence the polymer's rheological response to the deformation induced by expansion. There is extensive literature proposing and reporting growth models similar to those commented here [28, 29, 30, 31, 32, 33, 34]. These theoretical assumptions are governed by physical polymer gas solubility, gas diffusivity, surface tension, rheology and relaxation time. These studies report diffusion induced growth models for Newtonian, power-law and viscoelastic polymers. They always include the mass and momentum transfer to take into account cells interaction similarly to Paten and Amon and Denson models mentioned here.

CELLULAR STRUCTURE DEGENERATION MECHANISMS

As already mentioned, cellular structure may degenerate during expansion if it is not stable enough. We focus in these paragraphs on foam destruction. This can occur by combination of three main mechanisms: drainage, coalescence and coarsening. These mechanisms are affected by complex interactions in between them. It is not correctly understood which of them dominates over the others at every moment and for a specific foaming system. As a general rule, it is a question driven by thermodynamical stability since the fewer cells the more stable the foam is.

DRAINAGE

Drainage takes place during foaming at a microscopic level as the liquid phase drains out of equilibrium in the thin films separating cells. It is caused by capillary forces action that produces transport of the liquid material from the cell walls towards the struts network. This mechanism is extensively studied in the literature and several equations to model it are proposed.

As a consequence of microscopic drainage gravity forces often leads to macroscopic density gradients of the material concentrated on the bottom of the foam, i.e. the liquid polymer drains through the struts network that acts as a kind of piping system. The resulting effect is seen in Figure 2-14. This mainly occurs in very low viscosity systems (aqueous foams, metallic foams or very low viscous polymeric foams). On the other hand, drainage continues at the liquid/gas interface during foaming. In fact, the liquid can be completely drained from the interface in systems with very low surface tension, but this does not frequently occur in polymers.

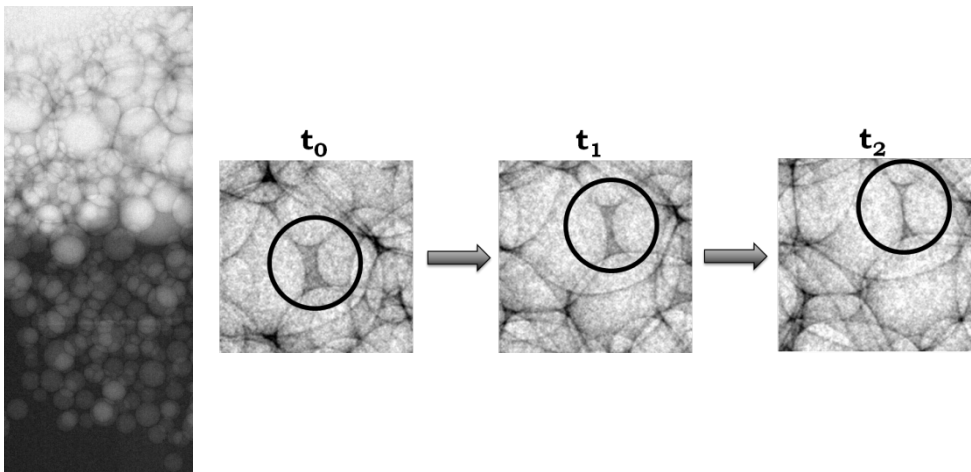


FIGURE 2-16.- MACROSCOPIC DRAINAGE (LEFT) VS. MICROSCOPIC DRAINAGE (RIGHT)

The basic assumption to model drainage through struts is a fluid velocity calculation for a cross sectional area, A , of a narrow channel (cell wall). Gravity, capillary forces and viscous resistance to flow, η , are the main parameters driving this phenomenon [35]. The continuity equation applied to the cross section gives an expression to calculate drainage flow in Eq. 2-25. Further expression can be obtained for drainage evolution of monodisperse cells in one dimension is given in Eq. 2-26 where, δ , is a geometric constant determined for curved triangular cross section of the cell walls [36,37].

$$\frac{\partial A}{\partial t} + \frac{\partial}{\partial \xi} \left(\alpha^2 - \frac{\sqrt{\alpha}}{2} \frac{\partial \alpha}{\partial \xi} \right) = 0 \quad \text{EQ. 2-25}$$

$$\frac{\partial A}{\partial t} + \frac{\rho g}{\eta} \frac{\partial A^2}{\partial z} - \frac{\gamma \delta^{1/2}}{2\eta} - \frac{\partial}{\partial t} \left(A^{1/2} \frac{\partial A}{\partial z} \right) = 0 \quad \text{EQ. 2-26}$$

Furthermore, this expression for drainage dynamics can be approximately related to relative density if $\rho_r \ll 1$ by using Eq. 2-27, where C_n is a geometry factor accounting for the number of faces of the cell and ϕ the average cell size [38,39].

$$A = C_n \left(\frac{\phi}{2} \right)^2 \frac{\rho_r}{1 - \rho_r} \quad \text{EQ. 2-27}$$

COALESCENCE

As a result of excessive cell wall thinning due to microscopic drainage, coalescence may occur. The material drainage can end into excessive cell wall thinning. This can reach up to a few nanometers in very stable systems with very low surface tension. This results into subsequent cells rupture which is called coalescence. It is the natural result of a very thin cell wall stretching that it is not strong enough to continue separating two cells as cell expansion goes on. This mechanism can be seen as responsible of cellular structure degeneration or contrary as a growth mechanism since it generates larger cells. Neither of cell growth models, previously commented, considers this mechanism.

It is mainly a statistical phenomenon that occurs spontaneously. Typically the resulting rupture events take place as a cascade. In this sense, it is important to note that coalescence is more likely to occur in large cells with thinner walls. Moreover, this mechanism slows down as the system becomes stabilized since it depends on surface tension which varies with temperature. There are several works in the literature reporting empiric characterization of coalescence by different techniques such as acoustic emission detection, optical visualization and even ultrafast X-ray imaging [40, 41, 42, 43]. As illustrative example, detection methods based on image analysis basically subtracts two consecutive images and detects local grey pixel difference in those cell walls that disappear during a cell rupture. Figure 2-17 shows an exemplification of the image analysis method.

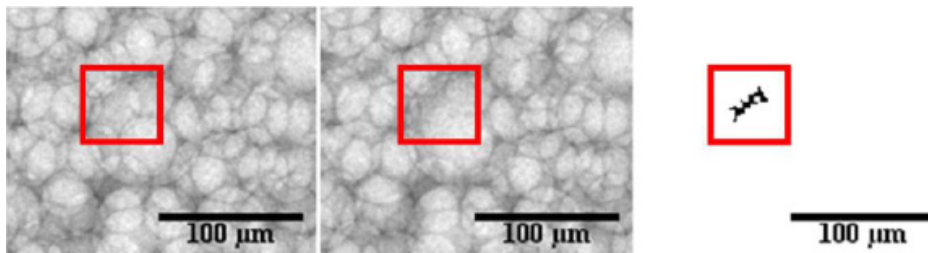


FIGURE 2-17.- TWO CONSECUTIVE RADIOGRAPHIES AND THE DETECTED GREY LEVELS DIFFERENCE.

Conventional experiments to study coalescence dynamics consists in air injection at the base of a water/soap places inside a cylindrical vessel. Burnet *et al.* studied the evolution of breaking foams in three differentiated phases [44]. At first cells rearrange and tiny ones break. Then during intermediate regime coalescence is the major mechanism and ruptures cascade takes place. Finally small ruptures occur due to latest stages of drainage. Vanderwalle *et al.* [45] observed these popping coalescence events mainly localized at the top of the foam. They also showed that dynamics of

coalescence occurs in a discontinuous way formed intervals of activity separated by period of calm. But, in contrast to intuitive thinking of cell size is not a critical parameter underlying coalescence dynamics. There is no rupture threshold in the size of the cell wall. Contrary, relative density or liquid fraction plays drives coalescence events. This was proved by Carrier et al by using a column experiment and combining dielectric measurements with optical inspection [46]. Therefore, there is a critical relative density which is function of the material nature that governs ruptures dynamics. A complete review of these works is addressed in [47].

As seen, this phenomenon is strongly related to instability and therefore surfactants to control rheological behaviour of the matrix play an important role. This is of capital importance in polymer systems. In the specific case of thermoplastics the use of a polymer with a suitable rheological behaviour (in general showing high melt strength) for foaming is useful to control this mechanism. These specific polymers can sustain large stresses and deformations without breaking.

COARSENING

The third degeneration is coarsening (also named Ostwald ripening or disproportionation). It consists in gas motion promoted by diffusion from the smaller cells to the larger ones. Gas diffusion coefficient and liquid material permeability to gas diffusion are the main parameters driving this mechanism. Pressure gradient (Δp) induces this gas diffusion and can be defined according to Eq. 2-28 where σ indicates the surface tension. Figure 2-18 shows a schematic view of the coarsening mechanism. In the melt state, diffusivity is expected to be higher through cell walls than in the solid state. Coarsening may be also responsible of cell collapse since gas diffuses across films due to pressure differences between two cells. Smaller cells will disappear in benefit of those larger ones. As material expands the material fraction becomes lower in the interface and therefore it may yield collapse of one of the two bubbles (R_1, R_2).

$$\Delta p = \sigma \left(\frac{1}{R_1} + \frac{1}{R_2} \right) \quad \text{EQ. 2-28}$$

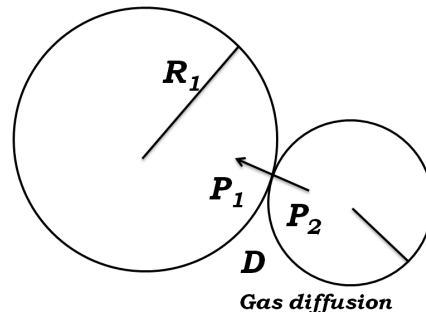


FIGURE 2-18.- SCHEME OF COARSENING WORKING PRINCIPLE: CELL NO.2 DISSAPPEARS SINCE GAS DIFFUSES TOWARDS CELL NO. 1.

If we consider foam of constant relative density, then the cell radius is expected to increase indefinitely until other factor, such as solidification in the case of polymer foams, impedes the growth. This evolution can be assumed to behave according to general model in. The constant of proportionality must depend on permeability of cell walls defined by Fick's law. On the other hand, this constant depends on surface tension which scales with pressure difference as indicated.

$$\frac{dR}{dt} \propto \kappa \sigma^{1/2} \quad \text{EQ. 2-29}$$

An important issue is to elucidate the effect of the gas, which affects the coarsening process. Foams coarsen because of pressure differences between bubbles of different sizes. This results in an increase of the mean bubble size. Coarsening and drainage may interfere, depending on the timescales of these two effects. There is a coupling in between these two mechanisms. Recent results have shown that coarsening can enhance drainage, but some questions remain unsolved, especially about the dependence of the coarsening rate on the relative density, and about the mechanisms of drainage enhancement [48,49,50].

If we assume 2D foam, Von Neuman's law is reported to govern coarsening [4,⁵¹]. According to Eq. 2-30 a cell with more than 6 edges will grow whereas a cell with $n < 6$ will shrink. In 3D foams some other expressions such as Eq. 2-31 can be obtained where the volume of a cell V_F and diffusion coefficient (D) are involved and it replaces the number of edges for the number of faces, F . However, this coarsening mechanism is not typically observed in polymer foams since gas permeability of polymers is typically very low.

$$\frac{dA}{dt} \propto (n - 6) \quad \text{EQ. 2-30}$$

$$V_F^{-1/3} \frac{\partial V_F}{\partial t} = DG(F) \quad \text{EQ. 2-31}$$

As a summary we of the explained foaming mechanisms present Figure 2-19 that visually connects the fifth mechanisms related to cellular structure generation and generation. This figure schematically indicates the virtual travel of the liquid material during a cellular structure generation. It is firstly nucleated and disposed into tiny cells and then it gradually grows. During this growth it suffers drainage since the material flows from the cell walls to the struts leading to ruptures produced by coalescence and facilitating gas diffusion. This coarsening mechanism also makes the liquid material to drain and yield larger cells therefore influencing cellular structure growth.

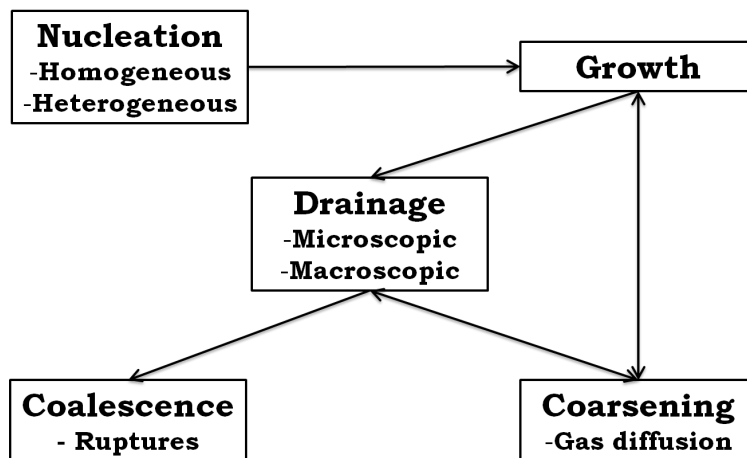


FIGURE 2-19.- FOAMING MECHANISMS ARE CLOSELY RELATED IN BETWEEN THEM.

REFERENCES

-
- [1] L. J. Gibson, M. F. Ashby, Cellular Solids – Structure and Properties, Second Edition, Cambridge University Press, Cambridge 1997, Ch 5
- [2] D. Klemperer, V. Sendjarevic. Handbook of Polymeric Foams and Foam Technology. 2nd Edition. Hanser Publishers, Munich, (2004)
- [3] D. Eaves. Handbook of Polymer Foams. Rapra Technology, United Kingdom, (2004)
- [4] D. Weaire, S. Hutzler, The Physics of Foams, Oxford University Press, United Kingdom, (1999)
- [5] ASTM D3572, Annual Book of ASTM standards, 8.02, 1994.
- [6] Rodríguez-Pérez MA. Cell Polym 2002;21:165.
- [7] Kuhn J, Ebert HP, Arduini-Schuster MC, Buttner D, Fricke J. Int J Heat Mass Transfer 1992;35:1795.

- [8] Glicksman LR. In low density cellular plastics: physical basis of behaviour. In: Hilyard NC, Cunningham A, editors. London:Chapman & Hall; 1994.
- [9] J. Pinto, E. Solórzano, M. A. Rodríguez-Perez, J. A. de Saja, Characterization of the cellular structure based on user-interactive image analysis procedures, *Journal of Cellular Plastics*, Volume 49 (6) 554-574 (2013).
- [10] D. Weaire and R. Phelan, "A counterexample to Kelvin's conjecture on minimal surfaces", *Phil. Mag. Lett.* 69, 107-110 (1994)
- [11] A. Cunningham, NC, Hilyard NC Physical Behavior of Foams- an overview In: Hilyard NC and Cunningham A (eds) *Low density Cellular Plastics: Physical Basis of Behaviour*, Chapman and Hall, London, (1994) Chap. 1
- [12] SIMONE, A.E. & GIBSON, L.J. (1998). The effects of cell face curvature and corrugations on the stiffness and strength of metallic foams, *Acta Materialia* 46 (11), 3929-3935
- [13] ANDREWS, E., SANDERS, W., GIBSON, L.J. (1999). Compressive and tensile behaviour of aluminum foams, *Materials Science and Engineering: A* 270, 2, 30, 113-124
- [14] GRENESTEDT, J.L. (1998) Influence of wavy imperfections in cell walls on elastic stiffness of cellular solids, *Journal of the Mechanics and Physics of Solids*, 46 (1), 29-50
- [15] K.T. Okamoto. *Microcellular Processing*. Hanser Publishers, Munich, (2003).
- [16] G. Munters, J.G. Tandberg. U. S. Patent nº 2,023,204, (1935).
- [17] T.A. Osswald, L.S. Turng, P.J. Gramann. *Injection Moulding Handbook*. Hanser Publishers, Munich, (2002).
- [18] X. Xu, C.B. Park, *Injection Foam Moulding in Injection Moulding Technology and Fundamentals*, Eds, M.R. Kamal, I. Avraam, L. Shih-Jung, Carl- Hanser Verlag, Munich, 2009
- [19] Colton, J.S., "The Nucleation of Microcellular Foams in Semicrystalline Thermoplastics," *Materials and Manufacturing Processes*, Vol. 4, No. 2, pp. 253-262, 1989
- [20] Colton, J.S. and Suh, N.P., "The Nucleation of Microcellular Thermoplastic Foam with Additives: Part II: Experimental Results and Discussion," *Polymer Engineering and Science*, Vol. 27, No. 7, pp. 493-499, 1987
- [21] Ramesh, N.S., Rasmussen, D.H. and Campbell, G.A., "The Heterogeneous Nucleation of Microcellular Foams assisted by the Survival of Microvoids in Polymers Containing Low Glass Transition Particles. Part I: Mathematical Modeling and Numerical Simulation," *Polymer Engineering and Science*, Vol. 34, No. 22, pp. 1685-1697, 1994.

-
- [22] Ramesh, N.S., Rasmussen, D.H. and Campbell, G.A., "The Heterogeneous Nucleation of Microcellular Foams Assisted by the survival of microvoids in polymers containing Low Glass Transition Particles. Part II: Experimental Results and Discussion," *Polymer Engineering and Science*, Vol. 34, No. 22, pp. 1698-1706, 1994.
- [23] L. J. Lee, et al., *Compos. Sci. Technol.*, 2005, 65, 2344–2363.
- [24] Blander, M. and Katz, J.L., "Bubble Nucleation in Liquids," *AIChE Journal*, Vol. 21, No. 5, pp. 833-848, 1975.
- [25] Patel, R.D. (1980), "Bubble growth in a viscous Newtonian liquid", *Chemical Engineering Science*, Vol. 35, pp. 2352-6.
- [26]R. Elshereef, J. Vlachopoulos, A. Elkamel, Comparison and analysis of bubble growth and foam formation models, *Engineering Computations: International Journal for Computer-Aided Engineering and Software* Vol. 27 No. 3, 2010 pp. 387-408
- [27] Amon, M. and Denson, C.D., "A Study of the Dynamics of Foam Growth: Simplified Analysis and Experimental Results for Bulk Density in Structural Foam Molding," *Polymer Engineering and Science*, Vol. 26, No. 3, pp. 255-267, 1986.
- [28] Ramesh, N. S., D. H. Rasmussen, and G. A. Campbell, Numerical and experimental studies of bubble growth during the microcellular foaming process, *Polym. Eng. Sci.* 31, 1657–1664, 1991.
- [29] Arefmanesh, A., and S. G. Advani, "Diffusion-induced growth of a gas bubble in a viscoelastic fluid," *Rheol. Acta* 30, 274–283 1991.
- [30] Arefmanesh, A., S. G. Advani, and E. E. Michaelides, A numerical study of bubble growth during low pressure structural foam molding process, *Polym. Eng. Sci.* 30, 1330–1337 1990.
- [31] Venerus, D. C., and N. Yala, Transport analysis of diffusion-induced bubble growth and collapse in viscous liquids, *AIChE J.* 43, 2948 – 2959,1997.
- [32] Venerus, D. C., N. Yala, and B. Bernstein, "Analysis of diffusion-induced bubble growth in viscoelastic liquids," *J. Non-Newtonian Fluid Mech.* 75, 55–75, 1998.
- [33] Barlow, E.J. and Langlois, W.E., "Diffusion of Gas from a Liquid into an Expanding Bubble," *IBM Journal of Research of Development*, Vol. 6, No., pp. 329-337, 1962.
- [34] Street, J.R., The Rheology of Phase Growth in Elastic Liquid, *Journal of Rheology*, Vol. 12, No. 1, pp. 103-131, 1968.
- [35] S. A. Koehler, H. A. Stone, M. P. Brenner, and J. Eggers, Dynamics of Foam Drainage, *Phys. Rev. E* 58, 2, 1998.
- [36] D. Weaire, S. Hutzler, G. Verbist, and E. Peters, *Adv. Chem. Phys.* 102, 315, 1997.

- [37] I. I. Gol'dfarb, K. B. Kann, and I. R. Shreiber, *Izv. Akad. Nauk SSSR* 2, 103, 1988.
- [38] A. Bhakta and E. Ruckenstein, *Langmuir* 11, 1486, 1995.
- [39] Glazier, J. A., 1993, *Phys. Rev. Lett.* 70, 2170.
- [40] Al-Masry, W. A., Ali, E. M. and Aqeel, Y. M., Determination of bubble characteristics in bubble columns using statistical analysis of acoustic sound measurements, *Chem. Eng. Res. Design*, 83(A10), 2005, 1196–1207.
- [41] Fluid dynamics of evolving foams, Raquel Verdejo, Francisco J. Tapiador, Lukas Helfen, M. Mar Bernal, Natacha Bitinisa and Miguel A. Lopez-Manchado, *Phys. Chem. Chem. Phys.* 2009, 11 10860-10866
- [42] F. Garcia-Moreno, E. Solórzano and J. Banhart, Kinetics of coalescence in liquid aluminium foams, *Soft Matter*, 2011, 7, 9216
- [43] A. Rack, F. García-Moreno, T. Baumbach and J. Banhart, Synchrotron-based radioscopy employing spatio-temporal micro-resolution for studying fast phenomena in liquid metal foams, *J. Synchrotron Rad.* (2009). 16, 432–434.
- [44] G.D. Burnett, J.J. Chae, W.Y. Tam, M.C. de Almeida and M. Tabor. Structure and dynamics of breaking foams. *Phys. Rev. E*, 51: 6, 1995.
- [45] N. Vandewalle, J.F. Lentz, S. Dorbolo and F. Brisbois. Avalanche of draining foams. *Phys. Rev. Lett.*, 86(1): 179–82, 2001.
- [46] V. Carrier and A. Colin. Coalescence in draining foams. *Langmuir*, 19(11): 4535–8, 2003.
- [47] A. Collin. Coalescence in Foams in *Foam Engineering: Fundamentals and Applications*, First Edition. Edited by Paul Stevenson. 2012 John Wiley & Sons, Ltd.
- [48] Xu, D., Pop-Iliev, R., Park, C.B. and Fenton, R.G., "Fundamental Study of CBA-Blown Bubble Growth and Collapse under Atmospheric Pressure," *Journal of Cellular Plastics*, Vol. 41, No. 6, pp. 519-538, 2005.
- [49] Zhu, Z., Xu, D., Park, C.B. and Fenton, R.G., "Finite Element Analysis of Cell Coarsening in Plastic Foaming," *Journal of Cellular Plastics*, Vol. 41, pp. 475-486, 2005.
- [50] Taki, K., Tabata, K., Kihara, S. and Ohshima, M., "Bubble Coalescence in Foaming Process of Polymers," *Polymer Engineering and Science*, Vol. 46, No. 5, pp. 680-690, 2006.
- [51] Arnaud Saint-Jalmes, Physical chemistry in foam drainage and coarsening, *Soft Matter*, 2006, 2, 836–849

3. MATERIALS SELECTION

The cellular structure and mechanisms present during foaming stages have been revised in previous chapter 2. This chapter introduces the key characteristics of the matrix materials used in this research; namely polyurethane foams as typical of thermosetting materials and polyolefins (polypropylene and polyethylene) as examples of thermoplastic foams. Table 3-1 summarizes all selected foams produced in this investigation as optimum systems to address visualization of foaming mechanisms and study of cellular structure by computed tomography. It is important to remark that all the systems have been carefully selected in terms of the mechanism or cellular characteristic intended to study. However, there is a large list of materials also eligible for the application of the imaging techniques addressed in this research. Foaming systems selection and setup design are done taking into account the peculiarities of each polymer foaming process and requires the use of specific instrumentation.

TABLE 3-1

	Aim of study	Selected material	Reason
In-situ 2D	Nanoparticles effects on nucleation and growth	Nanoclays / rigid PU	Cell size reduction
	Nanoparticles effects on nucleation and expansion kinetics	Nanosilica / rigid PU	Expansion kinetics modification + cell size reduction
	Nanoparticles effects on foaming	Carbon nanoparticles / flexible PU	Cell size reduction, expansion kinetics variation, induced coalescence
	Influence of temperature, polymer nature and additives on polymer foaming	Polyolefin (PE, PP) + ADC + ZnO	Enhanced cell nucleation, cellular structure stability
Ex-situ 3D	3D cellular structure description and nanofillers effect on morphology	Nanoclays / rigid PU	Cell size reduction and other architectural features variation
	Corrugation presence in the cell walls	LDPE foams	Different collapse strength due to cell wall corrugations
In-situ 3D	3D visualization of nucleation with temporal resolution	Nanosilica / rigid PU	Cell size reduction

The designed and developed setups are further described in each particular work contributing to this thesis (chapter 5 and 7). On the other hand a set of different commercial foams have been selected to investigate cellular architecture features by X-ray microtomography. In this case, the main reason for each choice was the structural feature object of the investigation.

3.1. POLYURETHANE FOAMS

Polyurethane (PU) foams are a type of thermoset foams widely investigated. They are produced by the reactive process of two primary components; polyol and isocyanate to create the urethane group [1,2,3]. The polyol and isocyanate, mixed together, react exothermally to form a thermoset polymer. This is a physical foaming process that starts thanks to the gaseous phase generated as a result of a chemical reaction. This chemical reaction is promoted by mechanical stirring of the two components during a few seconds. Other reactions may occur depending on particular composition. In general, the reactions can be divided into those contributing to expansion (blowing) and those responsible of structure stabilization (gelling). The blowing reaction forms carbamic acid from isocyanate and water, which is unstable and results in CO₂ gas and urea. On the other hand, the gelling reaction also referred as polymerization forms the urethane groups due to isocyanate groups and OH groups in the polyol. Other secondary polymerization reactions involve production of biuret and allophanates among others. PU foams cellular structure results from these two simultaneous reactions. During expansion different stages are commonly identified: cream, rising, cells packing, polymer gelation and structure solidification [4]. Reaction times characterize these foaming stages. Cream time occurs until the material begins to increase its volume (typically a few seconds, 15-40 seconds, after the initial stirring). Then cells start to grow increasing the foam volume due to the generated gas. This short interval time allows to spread the material into the moulds often used in industrial processes. Therefore, cream time will be relevant in this investigation since we are interested in obtaining as much as possible information about the mechanisms occurring during early expansion. Other characteristic times are often used such as gel time that expresses the interval between the initial stirring and the formation of a non-flowing, semi-solid, jelly like system due to the curing reaction. This gel time separates not-cured foam where coalescence may still occur from a semi-cured PU. Cell opening occurs in flexible PU in this semi-cured state.

Namely, the PU foams used in this research work are produced in presence of water. As the blowing agent evaporates during this exothermic reaction a low-density cellular structure is created. The water-generated CO₂ fills and expands cells during the reaction process. In addition, other additives such as catalysts, blowing agents or surfactants are present in the formulation to stabilize the cellular structure.

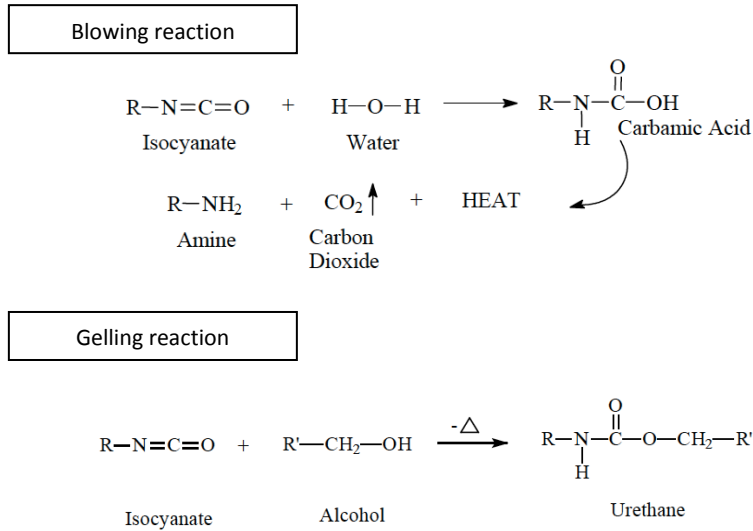


FIGURE 3-1.- PU CHEMICAL REACTIVE PROCESS [5].

Polyols are alcohol compounds containing at least two hydroxyl groups per molecule, i.e. polyhydroxyl compounds. The hydroxyl number characterizes the number of OH groups and is inversely proportional to molecular weight. The number of reactive OH groups per polyol molecule and the size and flexibility of its molecular structure conditions the degree of cross-linking between molecules. This has an important effect on the mechanical properties of the polymer and permits to establish a classification in rigid and flexible PU foams depending on the matrix mechanical behaviour.

Isocyanate is the other reactant necessary. It contains two or more functional groups (NCO) that show high reactivity with compounds containing hydrogen (alcohols, water, amines). The two most widely used are MDI (diphenylmethane diisocyanate) and TDI (toluene, diisocyanate). They are the essential components required for the formation of urethane groups.

Molecular weight and functionality are important parameters to select the optimum polyol system and fit particular requirements [6]. The main differences between flexible and rigid PU foams are the selection of polyols and isocyanates that upon polymerization produce rigid/flexible foam and the different surfactants. The NCO content, which indicates how many groups a single molecule contains, characterizes these components. The higher NCO/OH equivalent ratio is, the higher indentation hardness results. In the case of flexible PU, high molecular weight polyols are involved and phase separation results into amorphous urea rigid segments and flexible polyol segments. Contrary, rigid PU involves the use of low-molecular weight polyols containing a higher number of reactive OH groups.

Surfactants are used to provide a higher stability of the cell walls suppressing/allowing the opening of the connections/throats between cells. A delicate balance between the two reactions is essential to achieve a stable cellular structure showing good physical

properties and preventing undesirable collapse, defects, and cells opening (in rigid PU foams). In fact, the amount of surfactants present in the polyol component is of great importance since, below a minimum concentration the foam may collapse [7]. This leads to the typical open-cell structure in the case of flexible foams; in contrast rigid foams are conventionally closed cell structures.

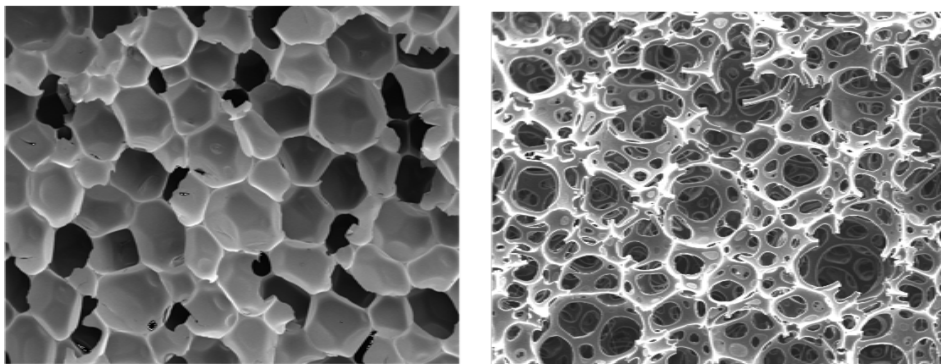


FIGURE 3-2.-RIGID (LEFT) AND FLEXIBLE (RIGHT, COURTESY OF M.M. BERNAL).

Table 3-2 summarizes typical component proportions and applications of both rigid and flexible polyurethane foams. In commercial formulations, a wide variety of substances such as colorants, surfactants, stabilizers, bacteriostats or plasticizers is also present. Rigid foams are often used in insulating purposes whereas flexible PU foams find the most extensive application at comfort, in automotive and furniture markets.

TABLE 3-2

Component	Parts by weight	
	Rigid / closed-cell	Flexible / open-cell
Polyol	100	100
Isocyanate	120-160	40-80
Water	2-6	2-6
Surfactants	2-5	0.2-2
Catalysts	0.0-1.5	0.0-1.5
Other additives	0.0-5	0.0-5

SELECTED POLYURETHANES

Two different formulations of PU foams, rigid and flexible, have been chosen in this work. The main objective is to investigate the effect of nanoparticles addition on the reaction kinetics and the physical mechanisms taking place during foaming process.

Moreover, differences between closed-cell structure of rigid PU foam and open cell morphology of the flexible one are of special interest. In addition, cell ruptures events taking place due to coalescence are degeneration mechanisms suitable to be addressed by such techniques.

In general, the experimental procedure starts mixing the components placed in a vessel by using an overhead stirrer in this investigation. Then, immediately the specific reactive mixture is placed in the experimental setup. Moreover, for the particular case of the ultra-fast tomography experiments, an in-place mechanical stirrer is developed to allow mixing inside the synchrotron beamline.

RIGID PU FOAM: BASF ELASTOPOR[®] H

Elastopor[®] H is closed-cell polyurethane rigid foam used for many applications in the field of insulation due to its excellent thermal properties. It is a commercial bi-component rigid PU formulation from BASF. The polyol component, Elastopor[®] H 1501/1 (1.07 g cm⁻³), is a mixture of polyols, catalysts, stabilizers and water. In this case the blowing agent is the water present in the polyol. The isocyanate, IsoPMDI 92140 (1.23 g cm⁻³), is a diphenylmethane diisocyanate.

There are some behind the choice of this particular system for this investigation:

- 1) It is a widely investigated system, very stable under foaming conditions variations.
- 2) It was previously observed a significant cell size reduction when nanoparticles are added [8].
- 3) It is challenging to investigate the effect of nanoparticles addition both during the foaming stages and at the final foamed structure.
- 4) The low viscosity values (650 mPa s for the polyol and 300 mPa s for the isocyanate), which makes the mixing process of the reactants easier and facilitates nanoparticles dispersion.
- 5) The reasonably long cream, gel and rise times of this particular formulation that fits with the contrast resolution of the laboratory X-rays imaging system used in this investigation.

FLEXIBLE PU FOAM

A particular flexible PU formulation was used as part of research collaboration with R. Verdejo and M.M Bernal from ICTP-CSIC (Madrid, Spain). The research was focused on investigating physical and chemical modifications occurring during foaming in presence of carbon-based nanoparticles. Studies on the foaming kinetics of this flexible PU had already been reported in the literature [9,10]. These works showed by means of other *in-situ* techniques (FTIR, temperature increase study) effects of carbon based fillers addition on foaming kinetics.

The polyol is Voranol 6150 from Dow Plastics, a highly reactive polyether-based triol. The isocyanate component Voranate M2940 is a methylene diphenyl diisocyanate

(MDI). The blowing agent is distilled water present in the formulation. Other additives including catalysts, surfactant and cross-linker are also present. The foams were prepared according to the proportions summarized in table 3-3. Additionally, the reactants were cooled to 5°C prior to the liquid-liquid dispersion to slow down the expansion velocity and allow foaming dynamics characterization. The mixture was initially sonicated (Sonics VibraCell) during 10 min in a water/ice bath, and was then stirred under high shear at 2400 rpm for 6 h. Then, the surfactant, catalysts and distilled water were added to the polyol/nanofiller mixture and stirred at 2400 rpm for 3 min. Finally, the foaming was promoted by stirring of the original polyol/nanofiller mixture and the additives with the isocyanate during 20 seconds.

TABLE 3-3

	Components	Parts per weight
Polyol	Voranol 6150	100
Isocyanate	Voranate M2940	43.4
Cell-opener	Voranol CP1421	4
	FASCAT 4202 (dibutyl tin dilaurate)	0.05
Catalysts	TEDA L-33B (33% triethylendiamine in 1,4-butanediol)	0.25
	NIAX E-A-1 (70 % bis(2-dimethylaminoethy)	0.1
Crosslinker	DEOA (85 % diethanolamine in water)	0.8
Surfactant	SH-2009	0.4

3.2. POLYOLEFIN FOAMS

Polyethylene (PE) and polypropylene (PP) are the most common examples of polyolefins produced from simple ethylene and propylene monomers repetition (C_nH_{2n}). These matrixes show low density, chemical stability, mechanical strength and they are eligible to be foamed for multiple purposes [11].

SELECTED MATERIALS

A common characteristic to any thermoplastic foaming processes is the incorporation of a blowing agent to generate the final cellular structure. They play an important role and their intrinsic nature conditions the processes. X-rays visualization of foaming processes will be carried out on thermoplastics incorporating a CBA since it is possible to promote foaming by thermal activation using heated mould, furnaces, etc. This is a critical aspect since we have to combine the setup design where the foaming is carried out and some restrictions imposed by the imaging technique.

AZODICARBONAMIDE

One of the most extended CBAs is azodicarbonamide (ADC) [1,2]. ADC decomposes in a temperature range between 200 and 220°C and produces a large amount of gas (250 cm³/g) generating N₂ (approx. 65%) and lower amount of CO, CO₂ and NH₃. We have selected Porofor ADC/M-C1 (Lanxess) that is widely used in the plastic foam industry as blowing agent. There exist also decomposition activators for azodicarbonamide [12]. In this sense ZnO addition is addressed thoroughly in one of the works presented in this investigation since it reduces decomposition temperature of ADC. For instance, very low content (0.05%) of ZnO induces a decrease of 20°C in the ADC decomposition temperature.

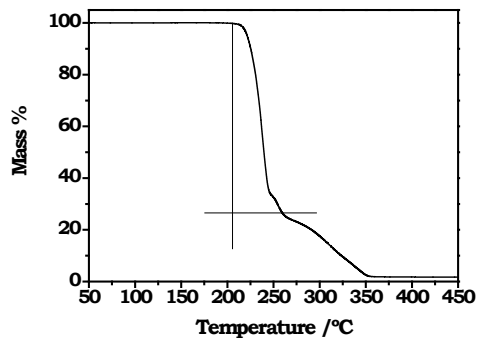


FIGURE 3-3.- ADC THERMOGRAMMETRIC ANALYSIS SHOWING DECOMPOSITION MASS LOOSE AT 238°C.

Different thermoplastics have been selected for the study of foaming mechanisms and process-induced phenomena observed in the final cellular structure. All are summarized in Table 3-4. Some of them are bulk materials in which different proportions of ADC as blowing agent are introduced by twin-screw extruder.

POLYETHYLENE

The polyethylene used in this investigation has been an ALCUDIA® PE-003, which is a low-density polyethylene from Repsol, with special molecular characteristics. This grade has excellent processability that makes it a good choice to observe foaming mechanisms. The recommended melt temperature range varies from 150 to 180°C. According to the melting point of this polymer, ADC is typically incorporated together with small amounts of ZnO in order to activate blowing agent decomposition at lower temperatures. This matches better with the melting point of this polymer.

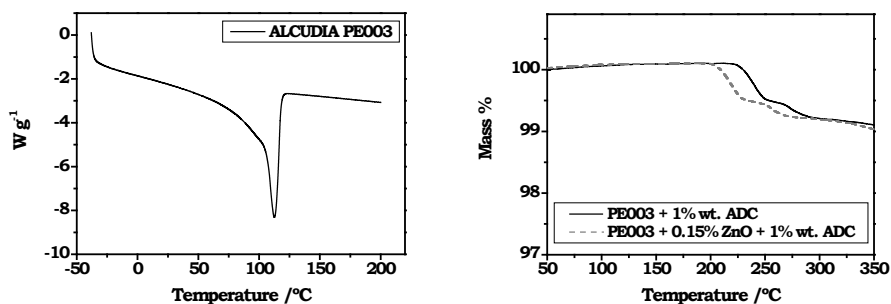


FIGURE 3-4.- DSC CURVE OF POLYETHYLENE ALCUDIA PE-003 (LEFT). THERMOGRAVIMETRIC ANALYSIS SHOWS ADC DECOMPOSITION DISPLACEMENT TO LOWER TEMPERATURES DUE TO ZNO ADDITION.

POLYPROPYLENE

Two different classes of polypropylenes (PP) with different molecular structure have been selected for comparison. It is known that the different molecular structure of polymers changes completely the rheological behaviour (extensional viscosity and melt strength). As a consequence the foamability becomes altered. These rheological characteristics are of a key importance to any polymer. Specifically the branched material (HMS-PP) shows strain hardening and a higher melt strength whereas the linear one (PPH) does not, which is associated to a poorer foamability. The typical crystalline grade of polypropylene is circa 45-50%.

HIGH MELT STRENGTH POLYPROPYLENE (HMS-PP)

Daploy WB135HMS from Borealis is a structurally isomeric modified propylene homopolymer not crosslinked but long chain branched. It is widely used in the extrusion foam industry to meet particular demands of the end-user application due to the wide processing window and the possibility of blending with other polyolefinic products.

The basic extensional rheological properties of the long branched Daploy HMS products make it suitable for foaming purposes, in comparison to those of standard linear polypropylenes. The window in the high melt strength and extensibility area of this graph defines the requirements for a high performance foaming grade. With long chain branched polymers, it is possible to produce very low-density ($20 - 50 \text{ kg/m}^3$) PP foams which possess a fine and controlled closed cell structure. This is not possible with standard linear polypropylenes that do not show this behaviour called strain hardening [13]. Typical strain hardening behaviour is seen in Figure 3-5 by extensional rheology curve.

LINEAR POLYPROPYLENE HOMOPOLYMERS (PPH)

The selected material is a linear polypropylene from Total Petrochemicals. Polypropylene PPH 4070 is homopolymer that has been designed for excellent processability and allows the production of films with a very high modulus. However this polymer do not show strain hardening at high stress that is a desirable property for foaming purposes. This can be seen in Figure 3-5 right side. It shows an extensional viscosity experiment for Daploy HMS that presents strain hardening and PPH that behaves linearly. Daploy HMS shows a value of 9.33 for strain hardening determined at 1s^{-1} speed at 200°C . On the other hand, linear PPH shows melt flow index of 3.1.

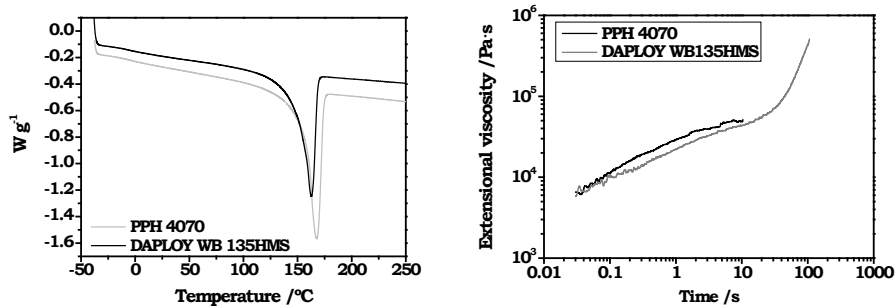


FIGURE 3-5.- DSC CURVES AND EXTENSIONAL RHEOLOGY OF DAPLOY HMS AND LINEAR PPH.

TABLE 3-4

Polymer	Name	Density (g/cm ³)	MFI (g/10min)	X _c (%)	Strain hardening (1s and 200°C)	T _g (°C)
PE	ALCUDIA® PE-003	0.920	2	42	-	112
PP	Daploy WB135HMS	0.905	2.4	45	9.33	152
	PPH 4070	0.905	3	52	3.1	157

COMPOUNDING AND FOAMING: EXTRUSION, PRECURSOR, ADDITIVES

A two-stage process is used to perform the foaming experiments [14]. The process involves firstly melt-compounding of the polymer and blowing agent (ADC in this case) and the required additives, such as ZnO when indicated, to produce a homogeneous blend. Blend mixing occurs as the material travels through the screws configuration. Twin-screw extruders have developed into most popular continuous mixing devices over Banbury mixers, single-screw or static mixers. Specifically, a bench top co-rotating twin-screw extruder (Mod. ZK 25 T, Dr. Collin) with L/D of 24 is used for the preparation of blends and compounds in this work.

For the polypropylenes temperature profile varies from 130°C in the hoper to 155°C in the die and at a rotation speed of 100-160 rpm. In the case of the PE $110\text{-}130^\circ\text{C}$ at 100-160 rpm are typically used.

After the mixture at extrusion die exit the blend is water-cooled and pelletized. Then two different strategies were followed. A defined mass of compound is then placed in a mould and press-cured to produce a solid precursor with the desired thickness. Two-hot plates and two-cold-plates hydraulic press up to 30 Tm is used to this end. Alternatively, the pellets are placed directly inside the mould designed for the foaming visualization experiment.



FIGURE 3-6.- POLYPROPYLENE PELLETS.

3.3. NANOADDITIVES

The inclusion of nanofillers as reinforcement in conventional material systems is nowadays a cutting edge strategy aimed at developing new advanced and tailored materials with improved mechanical, thermal or electrical properties [15,16,17,18,19,20,21]. Nanocomposites generally incorporate small amounts of nanofillers but properties change dramatically due to large surface-to-volume ratio of these particles. In the particular case of foams, presence of nanofillers may result in synergistic effects, not only summing the advantages of the conventional material and nanoadditives but also yielding new and/or superior final properties due to significant changes in cellular structure [22]. In this sense, we can cite several already reported examples: nanofillers in act as nucleation centres facilitating cell formation [23,24,25], they can reduce gas diffusivity in the polymer matrix resulting in coarsening reduction [26] and presence of fillers is associated to an enhanced stability since they inhibit cell wall ruptures [23,27].

As illustrative example, it is important to mention that cell size reduction thanks to nanoparticles addition is one of the most investigated strategies in the last years to improve the performance of cellular polymers [28]. It has been reported that cell size reduction is usually connected to properties improvement [29]. In addition, cell walls may become modified by the addition of nanoparticles that also contributes to properties enhancement. For this reason, nanocomposite foams are promising materials currently under study. Although some progress on this area has been reached, it is necessary to note that the final effect of nanofillers addition on polymers is a complex phenomenon not perfectly understood. Interaction with other involved processing parameters such as chemical formulation, blowing agents, processing time,

temperature, pressure or humidity could have an unexpected effect on the final cellular structure and properties of the manufactured materials.

SHAPE CLASSIFICATION

Different types of nanofillers can be added to the polymer matrix depending on the desired functionality. Nanoparticles possess dimensions of a few nanometers at least in one direction. They can be classified according to the shape in unidirectional, platelet-like showing large aspect ratio and spherical nanoparticles, see Figure 3-7 [30]. Carbon nanotubes and nanofibres are examples of unidirectional particles. Clays and graphene sheets are layered and fumed nanosilicas are examples of round fillers. It is also possible to find nanocrystals, gold and other metal nanofillers. It is important to note that the shape determines the interacting surface in between the filler and the polymer matrix. Subsequently, this geometrical feature is strongly related to foaming kinetics and foaming mechanisms.

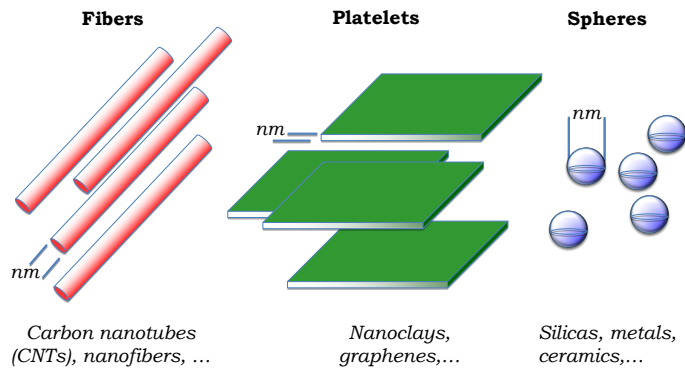


FIGURE 3-7.-NANOFILLERS WITH DIFFERENT SHAPE: SCHEMATIC CLASSIFICATION.

DISPERSION, EXFOLIATION AND COMPATIBILIZATION

Superior properties of nanocomposites can be obtained by maximizing the matrix-nanoparticle contact surface, i.e. obtaining optimum dispersion. Otherwise, poorly dispersed nanoparticles will appear aggregated in the micro-scale and the properties will be those of a conventional composite. Achievement of a controlled dispersion of these particles is challenging since they present extremely high surface to volume ratio and tend to agglomerate [15,31]. Other particles such as clays (layered stacks) need to be further exfoliated, which means in practice a significant amount of technical difficulties. If particles are well dispersed and there is a good filler-matrix interaction, then properties are expected to be optimum.

Typical dispersion methods comprise high shear mixing (double screw extrusion, agitation with impellers, etc.) and ultrasonication [32]. In many cases dispersion/exfoliation needs to be assisted via special surface chemistry that promotes “adhesion” in between the polymer matrix and the particles. These surface chemical treatments in the particles will also have an important role in the final properties of the

foamed nanocomposites. The use of surfactants in inorganic nanoparticles and functionalization chemicals in the carbon surface [33] are the most conventional ones. Surfactants in the clays surface increase the hydrophobicity and compatibility through ion exchange reactions with the polymer matrixes [34]. Studies on polymer-CNTs and polymer-CNFs composites demonstrate the importance of this functionalization [35, 36]. The introduction of appropriate links between the matrix and the filler improves the intercalation of polymer chains between the layers. In general, we can distinguish three different ways: chemical functionalization to introduce covalent bonds, physical functionalization by non-covalent treatments and surface deposition by plasma techniques.

SELECTED MATERIALS

Cloisite 30B (Southern Clay Products) is the nanoclay selected in this research. It is a natural montmorillonite (1.96 g cm^{-3}) organically modified with a quaternary ammonium salt. Nanoclays in general and montmorillonites in particular, are commonly employed as additives for plastic and rubbers in order to improve various physical properties, such as stiffness and strength, heat distortion temperature, thermal expansion, flame retardant and barrier properties. This type of nanoparticles possesses a platelet-like structure, which means that it has only one dimension in the nanoscale; i.e. from a few nanometers to microns in the lateral dimension than few nanometers in thickness. They possess an organofillization consisting on chemical surface modification. Increasing chemical affinity between polymer matrix and clays is the most effective method to obtain optimal exfoliation [37]. Exfoliation consists on the physical separation between the platelets thus confining these polymeric chains and resulting in enhanced mechanical properties and cellular morphology.

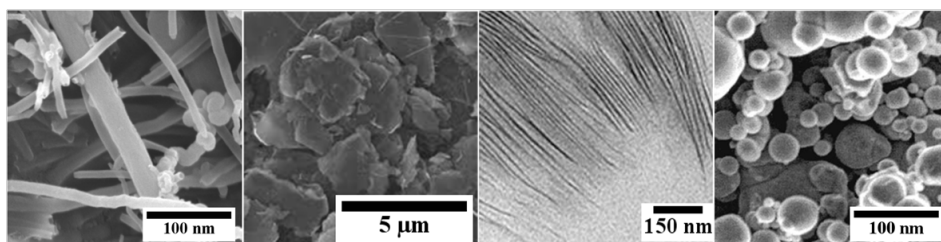


FIGURE 3-8.- SEM AND TEM MICROGRAPHS OF DIFFERENT SHAPED NANOPARTICLES: CNTS, GRAPHENE SHEETS, NANOCLEYS AND NANOSILICAS.

Two commercial types of hydrophilic/hydrophobic-fumed silicas (pyrogenic silicon dioxide) provided by Evonik Industries were selected. Their commercial names are Aerosil 200 and Aerosil R812 respectively. The nanometric silica powder has an extremely low density and high surface area. Its three-dimensional structure may result in viscosity increase when used as reinforcing filler. Namely, Aerosil R812 is

after-treated with hexamethyldisilazane so only in a small fraction of the surface hydroxyl groups are free. These methyl groups protect about 90% of the surface with low density of free OH groups (0.29 groups/nm²). Both fillers present a specific surface area of 200 m²/g and average primary particle size of 12 nm.

The CNTs used in this research were multi-wall carbon nanotubes (MWCNTs) grown by the chemical vapour deposition (CVD) injection based on the injection of a ferrocene/toluene solution at a constant rate in a tube furnace, under an inert argon atmosphere and at a temperature of 760 °C in atmospheric pressure. These MWCNTs were chemically treated with a concentrated sulphuric/nitric acid mixture and refluxed to obtain oxidized f-MWCNTs with hydrophilic nature. R. Verdejo and M.M Bernal from the research group at ICTP-CSIC (Madrid, Spain) kindly provided these materials. Carbon nanotubes (CNT) present a nanometric diameter and length higher in some orders of magnitude in comparison with its nanoscaled diameter. These particles might show in ideal conditions Young modulus values up to 1 TPa. Nevertheless, production purity, and dispersion in the matrix have to be considered.

Functionalized GS provided were produced from the adiabatic expansion of graphite oxide, synthesized from natural graphite according to the Brödie method [38], at 1000°C under an inert atmosphere. ICTP-CSIC also supplied these particles. OH, COOC and epoxy bonds in their surface functionalize these particles. Graphene sheets (GS) are layered particles composed of pure carbon, with atoms arranged in a regular hexagonal pattern. They are supposed to be ideally one-atom thick layer of graphite since many of them stack together form crystalline graphite. They show impressive properties but once again their behaviour strongly depends on purity and particular features directly related to production method. There are various production methods to obtain from exfoliated to epitaxial grown graphene [39]. Furthermore it is possible to obtain graphene from CNTs or directly from graphite by sonication.

The total nanocomposite foams produced by using different thermoset matrices and varying nanofillers contents are summarized in Table 3-5.

TABLE 3-5

Polymer	Rigid PU										Flexible PU					
Nanofiller	Cloisite 30B					A200					R812		MWCNT	f-MWCNT	f-GS	
Content (%)	0	0.5	1	3	5	0	0.5	1	3	0	0.5	1	3	0.3	0.3	0.3

3.4. COMMERCIAL FOAMS

Complementary, a set of commercial low-density polyethylene (LDPE) foams has been part of this investigation. In this case, the study has been focused on the 3D morphological analysis based on computed microtomography results. Several polyolefin-based foams produced by different technologies and showing different cellular structures have been characterized. The materials were all commercial foams kindly supplied by different worldwide companies: Epoli (Portugal), Zotefoams (UK) and Microcel (Spain).

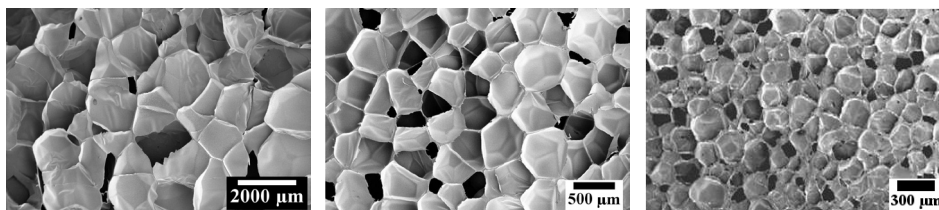


FIGURE 3-9.- MICROGRAPHS OF COMMERCIAL POLYOLEFIN FOAMS: EXTRUSION LDPE FOAM (LEFT), GAS DISSOLUTION FOAM (CENTRE) AND COMPRESSION MOULDING FOAM (RIGHT).

EXTRUDED FOAMS

These foams were produced by direct extrusion method (EPOLI) using iso-butane as blowing agent. The materials are non-crosslinked foams with very low densities [40]. Samples density is approximately 30 kg/m^3 . The resin employed is a LDPE for foam extrusion with a density of 0.92 g/cm^3 and melt flow index of 1.9 g/10 min at 190°C . Average cell size is about $1500 \mu\text{m}$ and collapse strength ranges $7\text{-}10 \text{ MPa}$.

GAS DISSOLUTION FOAMS

Zotefoams materials are produced by a batch gas dissolution technology using N_2 as physical blowing agent. The materials are cross-linked polyolefin foams with very homogeneous cellular structure free of residues of chemical blowing agents. The material selected has a density of 65 kg/m^3 and $600 \mu\text{m}$ cell size. The main reason for this choice is the Zotefoams unique production process. This technology results in very flat cell walls across the internal foam structure. This particular morphology is thought as one of the main reasons for improved mechanical response of this foam. As exemplary of its high performance mechanical response the collapse strength modulus is 62 kPa [41].

COMPRESSION MOULDING FOAMS

The foam under study was produced by the 2-steps compression moulding technology using dycumil peroxide as crosslinking agent and ADC as chemical blowing agent [42]. This Microcel PE40X is non-crosslinked polyethylene foam with closed cell structure and 150 μm cell size and 27 k/m^3 of density. In this case this foam is chosen because it presents highly corrugated cell walls that may worsen mechanical performance [43]. Collapse strength of this foam is 25 kPa.

TABLE 3-6

Sample	Density (Kg/m^3)	Cell size (μm)	Collapse strength (kPa)
<i>Zotefoams</i>	65	600	60.2
<i>EPOLI-1</i>	27	1500	9.7
<i>EPOLI-2</i>	29	1500	7.1
<i>PE40X</i>	27	152	25

3.5. LIST OF MATERIALS

To sum up this chapter we present the following tables. Table 3-7 and Table 3-8 summarize all concrete materials selected for different mechanisms and cellular structure features under investigation in this work. Namely, Table 3-7 includes all the thermoset and thermoplastic foaming systems chosen for mechanisms responsible of cellular structure generation and evolution. On the other hand Table 3-8 shows the commercial foams characterized by X-ray microtomography.

TABLE 3-7

List of foams produced and investigated by X-ray radioscapy (in-situ 2D & 3D)		
Nanocomposite thermoset foams		Cloisite 30B
	Elastopor BASF rigid PU	Aerosil 200
		Aerosil R818
		MWCNTs
	Voranol flexible PU	f-MWCNTs
		FGS
Thermoplastic foams		ALCUDIA PE-003 1%ADC
		PP DAPLOY WB HMS135 1%ADC
		PPH-4070 1%ADC

TABLE 3-8

List of commercial foams characterized by X-ray computed microtomography (ex-situ 3D)		
Nanocomposite thermoset foams	Elastopor BASF rigid PU	Cloisite 30B
Thermoplastic foams	Commercial foams	Extruded foams Epoli LDPE Gas dissolution foams Zotefoams VA65 Compression moulding foams Microcell PE40X

REFERENCES

- [1] D. Klemmner, V. Sendjarevic. Handbook of Polymeric Foams and Foam Technology. 2nd Edition. Hanser Publishers, Munich, (2004)
- [2] D. Eaves. Handbook of Polymer Foams. Rapra Technology, United Kingdom, (2004)
- [3] R. Herrington, K. Hock, Flexible Polyurethane Foams, 2nd Ed., The Dow Chem Company, (1998)
- [4] C. Torres-Sanchez, J. Cornell, *Journal of Polymer Research*, 16, 461-470 (2009)
- [5] M. Mar Bernal, M.A. Lopez-Manchado, R. Verdejo, *Macromolecular Chemistry and Physics*, 212, 971-979 (2011)
- [6] H.J.M. Grünbauer, J. Bicerano, et al. Rigid Polyurethane Foams, Systems, in *Polymeric Foams: Mechanisms and Materials*, Ed. S.T.Lee, N.S. Ramesh, CRC Press LLC, 2004, Ch 7, 262-318
- [7] Myagotin A, Ershov A, Helfen L, Verdejo R, Belyaev A, Baumbach T. , Coalescence analysis for evolving foams via optical flow computation on projection image sequences, , *J Synchrotron Radiat*. 2012 Jul;19(Pt 4):483-91
- [8] S. Pardo-Alonso, E. Solórzano, M.A. Rodríguez-Pérez, J.A. de Saja, In-situ evidences of nanoclays nucleating effect in polyurethane reactive systems, *Soft Matter*, 8
- [9] M. Mar Bernal, M.A. Lopez-Manchado, R. Verdejo, *Macromolecular Chemistry and Physics*, 212, 971-979 (2011)
- [10] M. Mar Bernal, Isabel Molenberg, Sergio Estravis, Miguel Angel Rodriguez-Perez, Isabelle Huynen, M.A. Lopez-Manchado, R. Verdejo, Comparing the effect of carbon-

based nanofillers on the physical properties of flexible polyurethane foams, *Journal of Materials*. 01/2012; 47:5673-5679. DOI:10.1007/s10853-012-6331-4

[11] L. Garrido, L. Ibarra, C. Marco. *Ciencia y Tecnología de Materiales Poliméricos*. Volumen II. Instituto de Ciencia y Tecnología de Polímeros-CSIC, Madrid, (2004).

[12] *Blowing Agent Systems: Formulations and Processing*, Rapra Technology Limited (1998)

[13] Zhixin Xu, Zhuang Zhang, Yong Guan, Dafu Wei, Anna Zheng , Investigation of extensional rheological behaviors of polypropylene for foaming. Zhixin Xu, Zhuang Zhang, Yong Guan, Dafu Wei, Anna Zheng, *Journal of Cellular Plastics* July 2013 vol. 49 no. 4 317-334

[14] R.R. Puri K.T. Collington *Cell. Polym.* 7:219(1988)

[15] X. Cao, L. J. Lee, T. Widya, C. Macosko, *Polymer*, 46, 775–783 (2005)

[16] C. Zeng, X. Han, L. J. Lee, K. W. Koelling, D. L. Tomasko, *Advanced Materials*, 15(20), 1743-1747 (2003).

[17] S.C. Tjong, *Materials Science and Engineering*, 53, Issues 3-4, 73-197, 30 (2006)

[18] EP Giannelis. *Adv Mater* 1996;8(1):29.

[19] M. Alexandre, P Dubois. *Mater Sci Eng, R: Reports* 2000;R28(1–2):1.

[20] R.A. Vaia, E.P. Giannelis. *Polymer nanocomposites: Status and opportunities*. *MRS Bull* 2001;26(5):394.

[21] E. Hammel, X. Tang, M. Trampert, T. Schmitt, K. Mauthner, A. Eder, et al. *Carbon* 2004;42(5–6):1153.

[22] James Lee L. et al, *Composites Science and Technology*, 65, 2344-2363 (2005)

[23] W. Zhai; J. Yu, L. Wu, W. Ma and J. He, *Polymer*, 47, (2006), 7580-7589; Sandler et al., op.cit.

[24] W. Zhai, C. B. Park, M. Kontopoulou. *Industrial & Engineering Chemistry Research*, 50, 7282-7289, (2011).

[25] W. Zhai, T. Kuboki, L. Wang, C. B. Park, E.K. Lee, H.E. Naguib. *Ind. Eng. Chem. Res.* 49, 9834-9845, (2010)

[26] C. Saiz-Arroyo, J. Escudero, M.A. Rodríguez-Pérez, J.A. de Saja; *Cellular Polymers*, 30, 63-78, 2011.

[27] W. Zhai, C. B. Park, M. Kontopoulou. *Industrial & Engineering Chemistry Research*, 50, 7282-7289, (2011).

- [28] S.C. Tjong, *Materials Science and Engineering*, 53, 73-197 (2006)
- [29] L. J. Gibson, M. F. Ashby, *Cellular Solids – Structure and Properties*, Second Edition, Cambridge University Press, Cambridge 1997.
- [30] R. Verdejo, M.M. Bernal, Reactive Nanocomposite Foams, *Cellular Polymers*, vol.30, 2, 2011
- [31] H. Farzana and H. Mehdi, Review article: Polymer-matrix Nanocomposites, Processing, Manufacturing, and Application: An Overview, *Journal of COMPOSITE MATERIALS*, Vol. 40, No. 17/2006
- [32] J Sandler, M.S.P. Shaffer, T. Prasse, W. Bauhofer, K. Schulte, A.H. Windle. *Polymer* 1999;40:5967.
- [33] X Gong, J. Liu, S. Baskaran, R.D. Voise, J.S. Young *Chem Mater*, 2000;12:1049.
- [34] BKG. Theng *The Chemistry of clay-organic reactions*. New York: Wiley; 1974.
- [35] J. Zhu, J. Kim, H. Peng, J.L. Margrave, VN. Khabashesku, EV.Barrera. *Nano Lett* 2003;3:1107
- [36] K Liao, S. Li *Appl Phys Lett* 2001;79:4225.
- [37] Zhong-bin Xu, Wei-wei Kong, Ming-xing Zhou, Mao Peng , Effect of surface modification of montmorillonite on the properties of rigid polyurethane foam composites, *Chinese Journal of Polymer Science* July 2010, Volume 28, Issue 4, pp 615-62
- [38] B.C. Brodie, »Sur le poids atomique du graphite«, *Ann. Chim. Phys.* 59, 466–472 (1860)
- [39] Kosidlo, Urszula; Arias Ruiz de Larramendi, Marta; Tonner, Friedemann; Park, Hye Jin; Glanz, Carsten; Skakalova, Viera; Roth, Siegmur; Kolaric, Ivica. Production methods of graphene and resulting material properties Poster at 7th NanoEurope Symposium 2009
- [40] E. Laguna, E. Solórzano, S. Pardo-Alonso, M.A. Rodríguez-Pérez, Modelling the compression behaviour of low-density flexible foams with a partially inter-connected cellular structure, *SPE-FOAMS Conference*, Barcelona (2012)
- [41] O. Almanza, M.A. Rodríguez-Pérez, J.A. de Saja, Prediction of the Radiation Term in the Thermal Conductivity of Crosslined Closed Cell Polyolefin Foams, *Journal of Polymer Science: Part B. Polymer Physics* 38, 993-1004 (2000)
- [42] M. A. Rodríguez-Pérez, Crosslinked Polyolefin Foams: Production, Structure, Properties, and Applications, *Adv Polym Sci* (2005) 184

[43] J.A. Martínez-Díez, M.A. Rodríguez-Pérez, J.A. de Saja, L.O. Arcos y Rábago, O. Almanza, The Thermal Conductivity of a Polyethylene Foam Block Produced by a Compression Molding Process , Journal of Cellular Plastics 37, 21-42 (2001)

4. DIGITAL X-RAY IMAGING

Image comes from Latin word *imago* that means visual perception thus it can be said that scientific imaging is an extension of natural human vision that involves quantification [1]. Hence, imaging matter aims at obtaining quantitative information and therefore it may provide useful information in topics such as physics, chemistry, biology, materials science, etc. [2,3]. A common characteristic within any imaging technique is the necessity of certain excitation energy (source) and a detection system. In this sense, image is the result of the interaction of matter with radiation. However, imaging techniques comprise not only the use of electromagnetic waves but also particles, atoms and other types of optical and electrical waves. We can cite well-known imaging devices such as microscopes or satellites and techniques such as thermography, artificial vision, nuclear magnetic resonance, radiography, endoscopy and Doppler echography [2].

Namely, X-rays offers nowadays one of the most versatile and successful examples of radiation used for imaging purposes. Thanks to penetrating power of X-rays they are certainly useful radiation for imaging in science. X-rays imaging techniques permit non-destructive inspection of materials and monitoring of dynamic processes. Moreover, X-ray techniques can be handled at lab-scale thanks to X-ray compact tubes. On the other hand, large-scale facilities such as synchrotrons offer coherent and stable X-rays to carried out multiple [4].

This chapter is divided into three parts. It includes digital imaging concepts, physics of X-ray, the imaging setups and explanation of image analysis procedures applied to the acquired images in this investigation. Part A in this chapter explains crosscutting concepts and definitions of digital imaging. This includes pixel as fundamental element and main features of an image, i.e. histogram, pixel depth and contrast. Complementary, these paragraphs introduce spatial and temporal resolutions as important concepts related to image quality. Finally, signal-to-noise ratio is presented as an image quality measure and filtering techniques are introduced as image enhancement procedures. Part B focuses on the physics of X-rays generation, interaction with matter and detection. Complementary, this part describes devices based on X-ray imaging used throughout this research. Namely, radioscopy involves acquisition of a sequence of 2D radiographies with and temporal resolution. Computed microtomography allows 3D spatial resolution but compromises the capability imaging dynamic processes. Finally, ultrafast tomography combines both mentioned capabilities of radioscopy and tomography. It permits to obtain simultaneously 3D spatial and temporal resolution. Part C described the basic post-processing procedures applied to the acquired X-ray images in this investigation.

PART A

Concepts on digital imaging

4.1. GENERAL CONCEPTS

4.1.1. ARCHITECTURE OF DIGITAL IMAGING

Conversion of analogical signals into digital discrete values permits image digitalization. As far as we are using digital images, all the information contained inside is stored into bits that will be discrete elementary units. A pixel (voxel referred to 3D) is the smallest element of an image that contains all the information about intensity/colour at certain position within the image [1].

It is important to note that digital discretization occurs at two levels. On the one hand we have defined an image as a matrix of single pixels, as shown in Figure 4-1. Every pixel behaves separately and independently from another, despite there is a correspondence in the image features. On the other hand the information contained inside every pixel is also discretized into elementary units called bits.

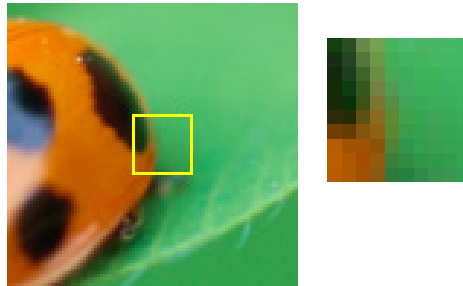


FIGURE 4-1.- IMAGE AND ZOOMED-IN TO SEE THE PIXEL UNITS.

The number of intensity levels is expressed by the pixel depth. It is the number of bits used to resolve the grey levels [1]. The different possible levels contained in pixel information are given by 2^{bits} . An 8-bits image contains 8 possible levels and this yields 256 (2^8) pure levels. If the image is monochrome these levels range from pure white to pure black. On the other hand, a 16-bits image contains 65536 possible levels. It is important to note that some detectors have limited dynamic range, i.e. they do not capture the complete pixel depth range. In this case a new calibration extends the pixel depth of the image. This means that it is possible to recalibrate levels of a 12-bits image into 65536 levels that correspond to a 16-bits image.

In general there is a correspondence between intensity and grey-levels that works linearly, i.e. two times intensity yields two times detected counts. This linearity does not always exist and thus a calibration between signal intensity and detector response is as a minimum necessary.

All the pixels contained in an image can be represented in a histogram as shown in Figure 4-2. It graphically expresses the counts or relative frequencies of the available grey levels in the image [1]. This is an important and practical tool for image analysis. It

is extensively used as guide for the visualization and base for segmentation methods. It is of special interest in binarization methods for morphological analysis.

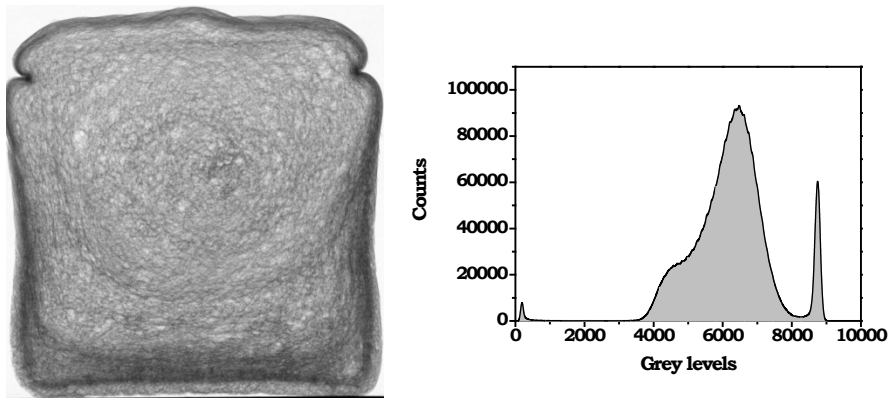


FIGURE 4-2.- 16-BITS FOAM RADIOGRAPHY AND HISTOGRAM REPRESENTATION.

The detector spectral response plays also an important role. This magnitude expresses the relative efficiency of signal detection as a function of the signal energy/wavelength. In other contexts, it expresses the quantum efficiency (QE) or probability of getting a captured electron as a function of wavelength [⁵, ⁶]. In general, image detectors present low response at high or low energies of their spectral response. In the particular case of X-rays detectors used in this investigation, the spectral response grows exponentially because ionizing radiation detection mechanisms. This is further explained in the paper attached to this chapter.

Furthermore, the contrast resolution (C) is defined as the ratio of the luminance of the brightest colour (white) to that of the darkest colour (black) that the imaging system is able to produce. In a specific image, contrast expresses the ability to distinguish between different intensities. It can be calculated according Eq. 4-1 as the ratio of difference of foreground ($I_{foreground}$) and background intensities ($I_{background}$) and the standard deviation of the background signal (σ). This value permits to know the measurable values in a certain image which is the main purpose of scientific imaging [1,2,3]. Figure 4-3 shows two images of same object acquired at lower and higher contrast.

$$C = \frac{I_{foreground} - I_{background}}{\sigma} \quad \text{EQ. 4-1}$$

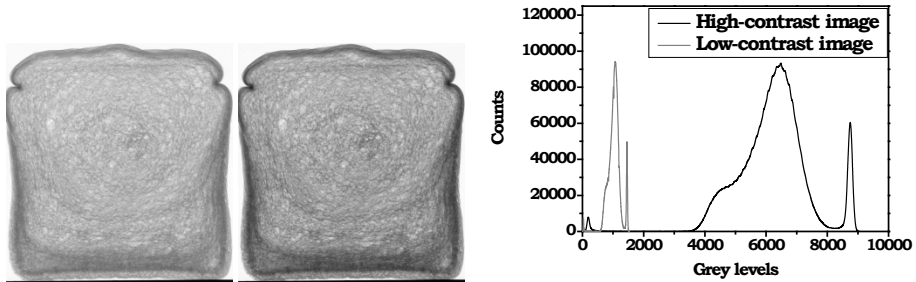


FIGURE 4-3.- COMPARISON OF TWO IMAGES WITH LOW (LEFT) AND HIGH (RIGHT) CONTRAST.

4.1.2. IMAGE RESOLUTION

SPATIAL RESOLUTION

Spatial resolution is one of the most relevant characteristics of any imaging system. It is the ability to differentiate two different spatial points. This feature basically depends on three factors: acquisition parameters (intensity and exposure time), detector optics and pixel size [1,2,4]. In general, a smaller physical pixel size allows higher resolution. However, optics, geometric setup configuration and acquisition process yields the real resolution which does not strictly corresponds to the pixel size. Therefore, resolution is sometimes lower than expected. This fact makes necessary the calculation and use of modulated transfer function (*MTF*). In this sense, the ability of any imaging device to transfer an object into an image is more realistically described by *MTF*. This function considers both spatial resolution and contrast of an image at the same time [7,8].

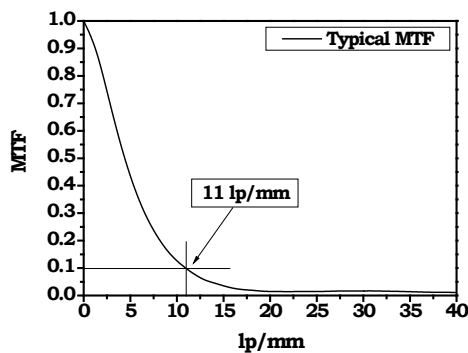


FIGURE 4-4.- MTF OF AN IMAGING SYSTEM THAT IS ABLE TO RESOLVE 11 LP/MM.

There are two mathematical methods to calculate this function. Firstly, the Fourier transform of the point spread function (*PSF*) that gives the system response to an ideal point object. Meanwhile in an ideally perfect system the image of a punctual object should be a point, it always becomes spread in any real imaging system. *PSF* gives a

measure of this blurring and thus the characteristic transfer function of the imaging system. Alternatively, it is possible to calculate the *MTF* as the relation between amplitude and absolute value of object transfer function (*OTF*). This *OTF* correlates the input and output modulation of the system and the phase as function of spatial frequency [7,8].

A typical test pattern to measure *MTF* contains areas (usually lines) with different spatial frequencies. As the lines get smaller and closer, the spatial frequency increases. The highest spatial frequency (or minimum separation) at which the separation of the lines can be distinguished indicates the resolution expressed in line pairs per mm (*lp/mm*). In practice, it is often used a percentile of the *MTF* normalized, One line pair consists of one lead strip and one adjacent separation space. Nominally a value at 10% of the maximum *MTF* is commonly assigned as a characteristic of any imaging setup.

TEMPORAL RESOLUTION

Similarly to spatial resolution, temporal resolution determines the ability to differentiate two different instants. In this case, the main limiting factors are introduced by the detection sensibility and electronics [4]. In general, spatial and temporal resolutions are containments since high spatial resolution typically requires long exposure times. Furthermore, temporal resolution often becomes compromised by the necessity of very fast electronics (short readout time) in the case of dynamic processes evolving rapidly. This allows to reduce the interval time between acquired images in a sequence and therefore improves time resolution. On the other hand, fast electronics often reduces spatial resolution.

It is also important to comment that lag is generally an undesirable property in photosensitive detectors. It occurs as a result of incomplete readout of image signals and it can be seen as a blurring of the image whenever there is relative movement between the moving phenomena and the detector. It can also be seen as the finite time it takes for an image to build up following initiation of the detector and to decay following termination of the exposure to radiation.

4.2. OTHER ASPECTS OF IMAGE QUALITY

Imaging systems are not always, we should say rarely, perfect; low signal-to-noise ratio (*S/N*), gradients, artifacts, detector inhomogeneity, optical aberrations or detector lag often have to be taken into account. The source, the object and the detector will affect the final image quality. This study is usually addressed by analyzing the performance of features already explained: contrast resolution, spatial resolution, temporal resolution and quantitative accuracy of meaningful features obtained from the image analysis.

4.2.1. SIGNAL-TO-NOISE RATIO

Noise is the natural random background signal that all systems present. It adds randomness to both the object and its background. It may come from several sources such as temperature, background signal fluctuations or electronics readout. It is important to note that the temperature can also have an effect heating the sensor and increase the amount of noise. The influence of noise is more evident when imaging low contrast objects or using insufficient excitation. If the object contrast is low it decreases the ability to discriminate it might be masked by the noise. In the presence of signal amplitude fluctuations, the ability to discern the low contrast objects is severely compromised. However, noise typically can be removed by subtracting a black frame from the image. It can also be significantly reduced by means of integration procedure. This noise-reducing methodology consists in acquiring the same image consecutively several times and calculating the average of them. This contributes to reduce the natural noise of the detector defining better the poor contrast areas.

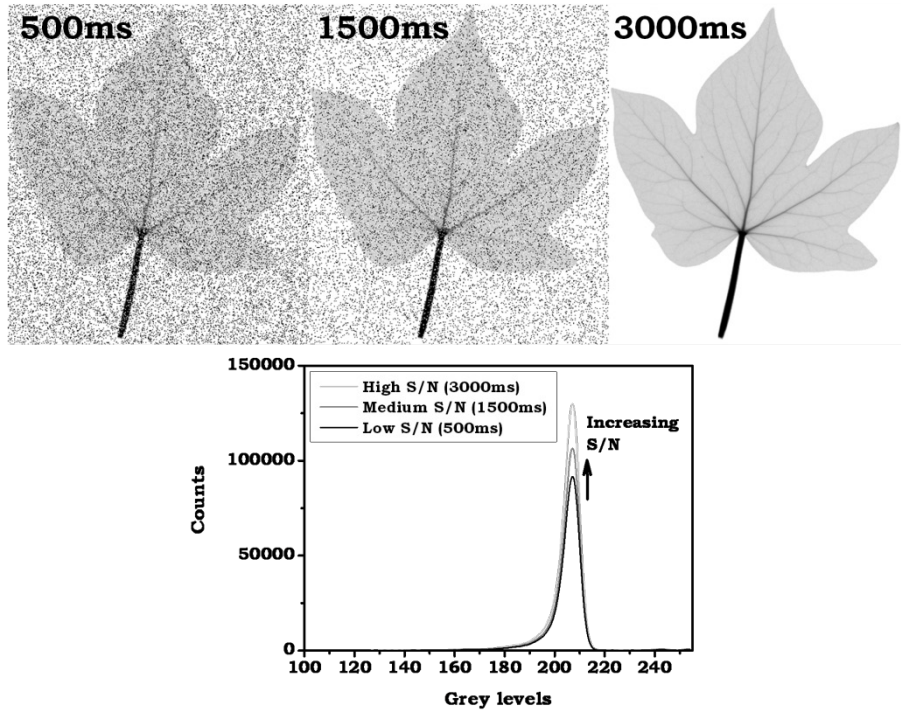


FIGURE 4-5.-. THREE DIFFERENT IMAGES OF THE SAME OBJECT AT INCREASING EXPOSURE TIMES, I.E. NOISE IS REDUCED AND S/N INCREASED.

The signal-to-noise ratio (S/N) is a general concept applied in image analysis. It quantifies the ratio of average signal to the noise signal as indicates Eq. 4-2. In general, S/N increases as exposure time does. This is seen in Figure 4-5. High S/N implies enhanced image quality since less amplification of the signal is necessary.

$$S / N = \frac{I}{\sigma} \quad \text{EQ. 4-2}$$

4.2.2. DEFECTIVE PIXELS

Assuming an expected linear response of the detecting system when exposed to a certain excitation a defective pixel can be defined as the one not behaving as expected, i.e. deviating from linearity. In general, a good criterion is identifying those above or below certain threshold (90%, 95%, 98%). We can find dead pixels (without response), hot pixels (response without excitation) and anomalous (out of the mentioned threshold). Figure 4-6 shows individual dead (black) and hot (red) pixels and lines. They can be found individually or stuck in arrays forming defective lines. They can be generally corrected by using a mask that eliminates the values corresponding to those pixels and assigning them an interpolated value of the neighbours.

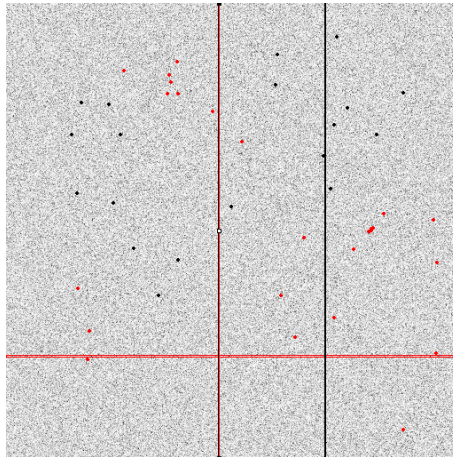


FIGURE 4-6.- MASK CONTAINING HOT (IN RED) AND DEAD (IN BLACK) PIXELS AND DEFECTIVE LINES.

4.2.3. ARTIFACTS

We can cite the most common artifacts, as follows:

- Geometrical distortions due to optical conditions. In general, all those corresponding to optical system such as piston, tilting, defocusing, spherical aberration, field curvature, coma or astigmatism if a lenses system is present, etc.
- Background noise of the detector electronics. This can be usually removed satisfactory by applying background correction with a darkfield image. This will be further explained for the particular case of X-ray images in part C of this chapter. Noise of detectors usually increases with time. In general, it is

advisable to take a reference image both to study service life and compare eventual different background corrections.

- Non-uniformity of the illumination and detector. It is rarely to have homogeneous images and thus intensity gradients need correction. This is explained also explained in part C under the terminology shading correction.
- Lag time of the detection sensors can affect radiation readout and therefore acquired information to build up the image. This produce problem to realize consecutive experiments in time with temporal resolution.

4.3. DIGITAL IMAGES PROCESSING

The possibilities to process and analyze any acquired image are extensive. A typical workflow for usually begins by image enhancement. This is mainly aimed at noise filtering and/or image optimization. The binarization is often applied to if the final purpose is to extract morphological information. This step separates foreground from background features. The part C in this chapter explains the specific image analysis procedures used for the X-ray images acquired and analyzed in this investigation.

4.3.1. DIGITAL FILTERING

A filter is a mathematical operation either in the spatial or frequency domain (see Figure 4-7) that alters the original image to suppress or enhance information using a set of neighbourhood pixels [1,3,⁹]. In general, the most used filter is applied in the spatial domain being possible to define a neighbourhood, i.e. the number of pixels that are involved in a filtering operation. From the mathematical point of view a filter is the kernel of the convolution operation [9]. Figure 4-8 shows 1x1 pixels neighbourhood in a 2D array; the larger the neighbourhood considered, the stronger the filter is. In this case 4-connectivity in 2D and 6-connectivity in 3D are show. In general filtering techniques are used to reduce the noise whereas preserve the sharp edges.

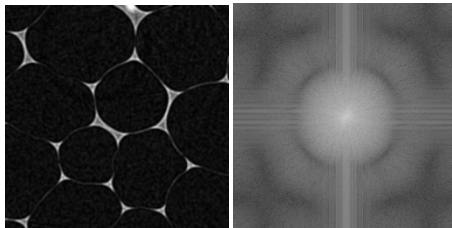


FIGURE 4-7.- IMAGE INTO SPATIAL (LEFT) AND FREQUENCY (RIGHT) DOMAIN.

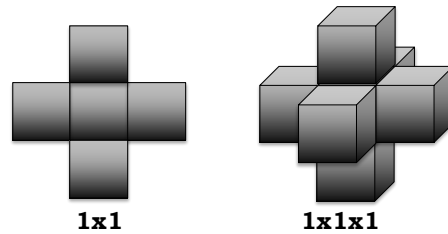


FIGURE 4-8.- DIFFERENCE BETWEEN 2D NEIGHBOURS KERNEL AND 3D NEIGHBOURS OF A FILTER KERNEL.

The weight function applied in each of the neighbouring pixels conditions the type of filter. Figure 4-9 summarizes some of the most used filters and their effects on the image: mean, Gaussian, median and maximum/minimum. Mean filter is probably the simplest and most intuitive smoothing filter. It uses the normalized function and considers that all pixels have the same value. For increasing kernel (number of pixels in the neighbourhood) dimensionality the transfer function decays rapidly and hence the smoothing properties of mean value filters improve. Gaussian filter uses a kernel that is a probability density function of the n-dimensional Gauss distribution. It gives as a result for every pixel/voxel a linear combination of the pixels/voxels within the kernel. This filter significantly decreases the noise but it also results in less defined edges. Median filter is a non-linear filter replacing every pixel by the median of its neighbouring pixels. This filter is very good at reducing noise in the active image while it preserves sharp edges. It is more successful in preserving edges than Gaussian filter but at higher computational costs. This is a time consuming operation because, for each pixel in the selection, the nine pixels in the 1×1 neighbourhood must be sorted and the centre pixel replaced with the median value (the five). Finally, maximum filter performs each pixel replacement in the image with the largest pixel value from the neighbourhood. Contrary, minimum filter replaces each pixel in the active image with the smallest pixel value in that pixel's neighbourhood. These filters remove the local maximum/minimum value depending on the dynamic range. In binary images minimum and maximum filters corresponds to erosion/dilation operations as we will see in the following section.

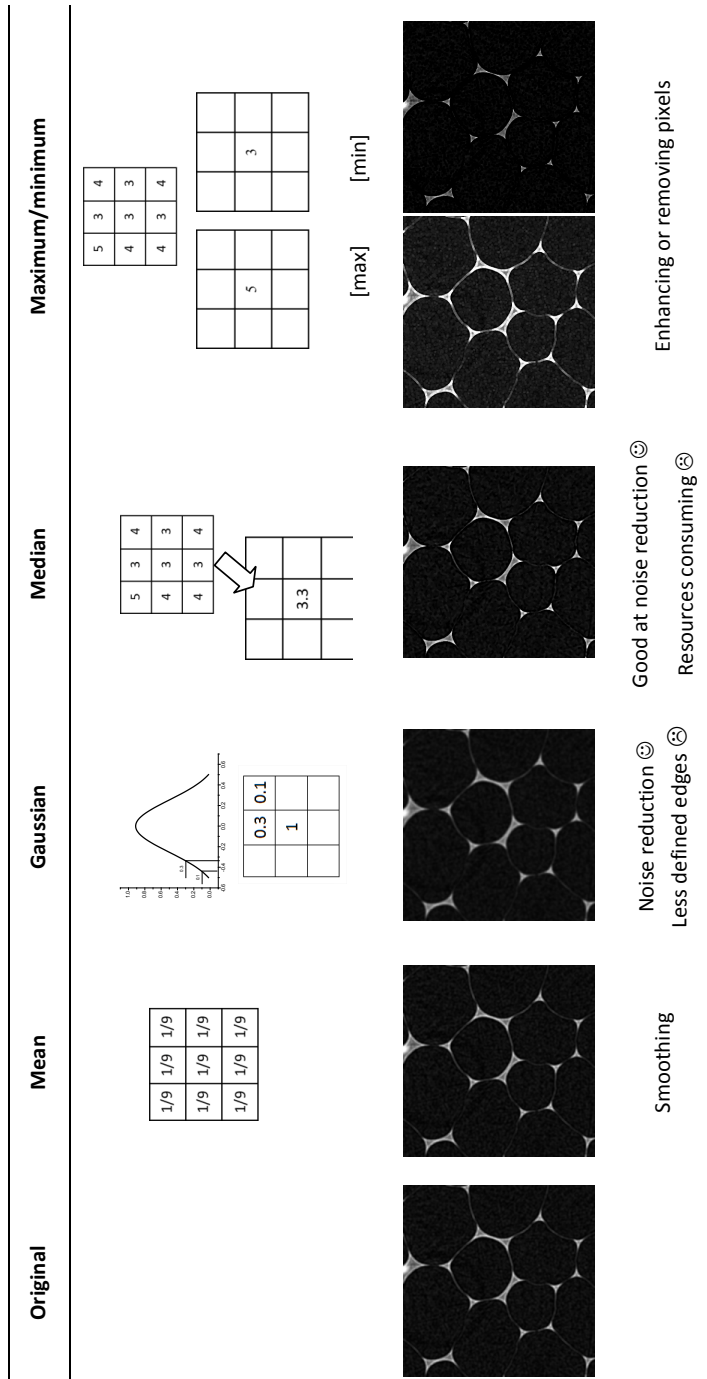


FIGURE 4-9.- DIFFERENT FILTERING OPERATIONS AND THE RESULT OF APPLYING THEM TO AN ORIGINAL GREY-SCALE IMAGE.

4.3.2. IMAGE BINARIZATION

During image processing it is sometimes necessary to convert grey-scale information into binary facilitating the subsequent object separation and quantification steps. The simplest approach for this process consists in setting a threshold value and converting all the higher intensity levels into one single upper value (pure white) and the lower intensity values into pure black). The purpose is to separate and identify features representing objects or structures from the background, so that count, measurement, or matching operations can be performed. It is often selected a single threshold determining the foreground grey-scale either below/above the selected value. In the literature there are several automated methods to analyze the histogram and calculate a threshold value. In the specific case of two phases image, the inflexion point separating background and foreground intensities is typically selected. Otsu's method assumes two components with a certain distribution that overlaps and separates the histogram into two regions where the weighted sum of the variances is minimal and the separation can be maximized. However, manual determination of the threshold value based on the researcher experience reveals as the most successful determination method. Figure 4-10 shows the result of selecting three different threshold levels for binarization. We observe the excessive noise addition in case (A) and the cell walls missing in case (C).

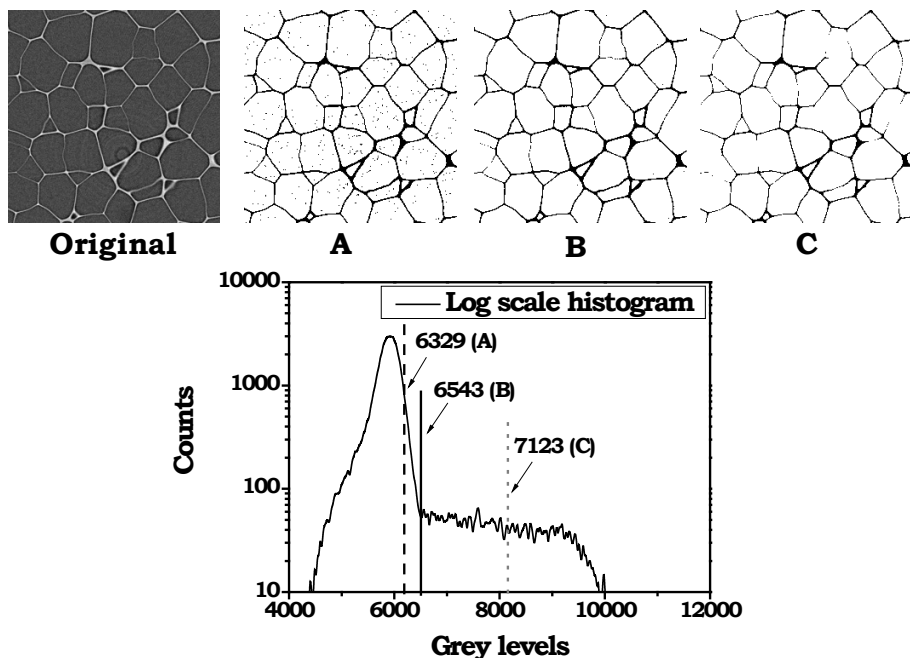


FIGURE 4-10.- THREE DIFFERENT THRESHOLD VALUES RESULTS IN VERY DIFFERENT (INCREASING THRESHOLD VALUE) BINARY IMAGES.

BINARY OPERATIONS

After appropriate noise filtering and binarization some residual erroneously identified pixels/voxels might still remain. Different specific operators can be applied since the use of conventional filters would result in grey-scale image thus eliminating the binary properties of the image. These operators are based on removing or adding individual pixels to the original image according to a certain neighbouring rule. They search pixels according to a criterion and replace them as indicated.

As an example erosion removes pixels from the foreground in the original image by associating zero values to remove or add pixels that should not be there or are not of interest for the analysis regarding the original. Contrary, dilation does exactly the opposite operation setting to one value background pixels. In this case we get as a result mask expansion containing features from foreground.

Nevertheless, erosion and dilation often add or remove too much information. Open/close are combined operations useful to remove undesired entities such as thin lines and isolated pixels from noise. Open applies an erosion followed by a dilation to break some foreground not too overlapped entities and immediately correct any dimension shrinkage of the remaining features at the foreground. On the other hand closing sequence performs a dilation followed by an erosion so as to merge any separated entities due to threshold selection. These operations typically affect the shape of foreground components whereas remove superfluous entities.

Skeletonization is the process of reducing foreground regions in a binary image to the lower dimensional subset preserving the original foreground connectivity. It preserves topology; they are one-pixel thickness and located in the medial position of the boundary pixels of the object.

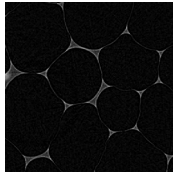
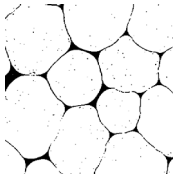

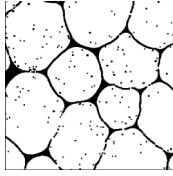
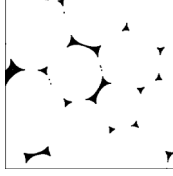
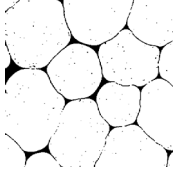
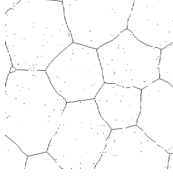
Original	Binary	Erode	Dilate	Open	Close	Skeleton
Grey-scale 	Auto threshold 	Eliminate superfluous pixels 	Reappear missing pixels 	Eliminate superfluous pixels 	Reappear missing pixels 	Foregound connectivity 
	Binarized image	Foregound mask erosion	Foregound mask shrinkage	Affect original shape whereas remove superfluous entities	Reappear original shape whereas remove superfluous entities	Calculate original topology

FIGURE 4-11.- SUMMARY CHART OF SELECTED BINARY OPERATIONS.

[¹] The Image Processing Handbook, Third Edition by John C. Russ. CRC Press, CRC Press LLC.

[²] Banhart J, Advanced tomographic methods in materials research and engineering. UK: Oxford University Press; 2008.

[³] Joachim Ohser, Katja Schladitz, 3D Images of Materials Structures: Processing and Analysis. Wiley-VCH Verlag GmbH & CO. KGaA

[⁴] Rack A, Garcia-Moreno F, Schmitt C, Betz O, Cecilia A, Ershov A, Rack T, Banhart J and Zabler S 2010 On the possibilities of hard x-ray imaging with high spatio-temporal resolution using polychromatic synchrotron radiation J. X-ray Sci. Technol. 18 429–41

[⁵] M. H. F. Wilkinson and F. Schut (1998). Digital Image Analysis of Microbes: Imaging, Morphometry, Fluorometry and Motility Techniques and Applications. John Wiley and Sons. ISBN 0-471-97440-4.

[⁶] Peter G. J. Barten (1999). Contrast Sensitivity of the Human Eye and Its Effects on Image Quality. SPIE Press. ISBN 0-8194-3496-5.

[⁷] I.A. Cunningham, A. Fenster, A method for modulation transfer function determination from edge-profiles with correction for finite element differentiation, Medical Physics, 14, 4 (1987) 533-587

[⁸] Ehsan Samei, Egbert Buhr, Paul Granfors, Dirk Vandenbroucke and Xiaohui Wang, Comparison of edge analysis techniques for the determination of the MTF of digital radiographic systems, Phys. Med. Biol. 50 (2005) 3613–3625

[⁹] RASBAND, W.S. (1997-2012). ImageJ, U. S. National Institutes of Health, Bethesda, Maryland, USA, <http://imagej.nih.gov/ij/>

PART B

Physics and technology of X-ray imaging

4.4. X-RAY IMAGING FUNDAMENTALS

Wilhelm Conrad Roentgen discovered X-rays in 1895. The first commercial devices to produce them were successfully used in medicine and industry from the very early months [1]. This electromagnetic radiation ranges from 10^{-8} m (soft X-rays) to 10^{-12} m (hard X-rays) wavelength in the spectrum. The typical energy of photons ranges from 100 eV up to 20 MeV (see Figure 4-12). Therefore this penetrating radiation seems to be appropriate for obtaining structural information of matter since the distance in between atoms is 10^{-10} m approximately. The penetration power of X-rays is rather high and thus it allows for transmission imaging. However, for imaging purposes the useful energies are 5-150 keV, except in some special cases (industrial processes) where 500 keV can be applied. Too soft X-rays do not penetrate deeply enough and too hard X-rays simply are not absorbed leading to poor contrast

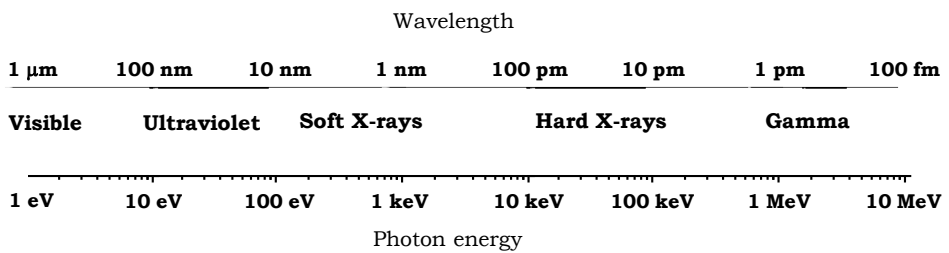


FIGURE 4-12.- ELECTROMAGNETIC SPECTRUM OF ENERGIES AND WAVELENGTHS.

In the beginning radiographs were directly recorded by sensitive films. This detection method is still used in medical imaging, although the films have improved in sensitivity, resolution and ease of use. Lately, digital sensors are finding their way into the field of X-ray radiography, with the introduction of imaging plates, CCD and CMOS-based digital detectors. The replacement of classical film screens by digital detectors opens a lot of possibilities. Images can be nowadays stored easily and improved by special filtering algorithms.

4.4.1. MATTER-BEAM INTERACTION

X-rays interact with matter in a number of different ways that can be used for imaging: electron photoemission, elastic and inelastic scattering fluorescence, (see Figure 4-13). Hence, X-ray detection techniques can be classified based on the particle-matter interaction that is used to form the image. Conventional X-ray imaging relies on transmission measurement that is determined by object beam absorption. Photoelectric absorption and inelastic scattering are mainly contributing to absorption. Elastic scattering is also contributing to absorption although it is more related to macroscopic refraction effect.

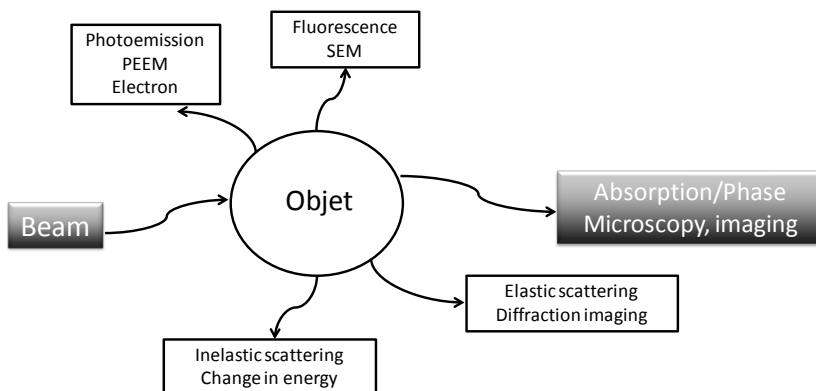


FIGURE 4-13.- X-RAYS AND MATTER INTERACT PRODUCING ELASTIC AND INELASTIC PHENOMENA AS A RESULT.

The physical fundamentals of radiation absorption are based on the Beer-Lambert equation shown in Eq. 4-3. This expression predicts the attenuation of incident monochromatic (it is usually not true in this simple form for polychromatic beams) X-ray radiation by an exponential function of the linear absorption coefficient (μ), the element concentration (c) and the thickness (t). Additionally, it is possible to estimate an effective linear attenuation coefficient, μ_{eff} , if several elements are contained in the irradiated material and for polychromatic beam, as shown in Eq. 4-4. Finally, it is sometimes used more conveniently mass attenuation coefficient by defining $\mu_m = \mu_{\text{eff}}/C$. All these relationships are further discussed in the articles included at the end of this chapter.

$$I = I_0 e^{-\mu ct} \quad \text{EQ. 4-3}$$

$$I = I_0 e^{-\mu_{\text{eff}} ct} \quad \text{EQ. 4-4}$$

The attenuation coefficient, μ , also varies with incident radiation wavelengths and energy. It is also important to note that a relationship of the captured intensity (non-absorbed by the material) and the density (ρ) can be established. In the specific case of monochromatic beam and pure element, the attenuation coefficient can be further extended and related to atomic number, Z . High atomic weight (Z) materials such as metals will stop X-ray radiation immediately (either by absorbing, reflecting or dispersing it), whereas materials with light molecular weight made for instance from carbon and hydrogen (polymers) will let almost all light to pass.

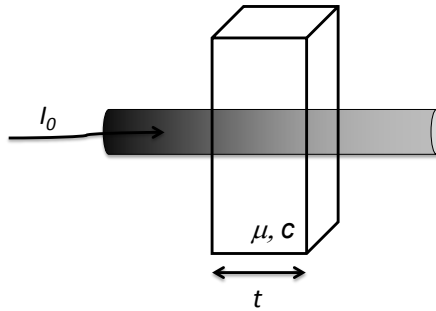


FIGURE 4-14.- RADIATION BEAM IS ABSORBED AS IT TRAVELS THROUGH A MATERIAL OF WIDTH t .

Imaging mainly works on absorption phenomena since we have seen that matter attenuates X-ray radiation. Therefore, in transmission imaging, the transmitted radiation is the information captured by the detection system as 2D image (radiography).

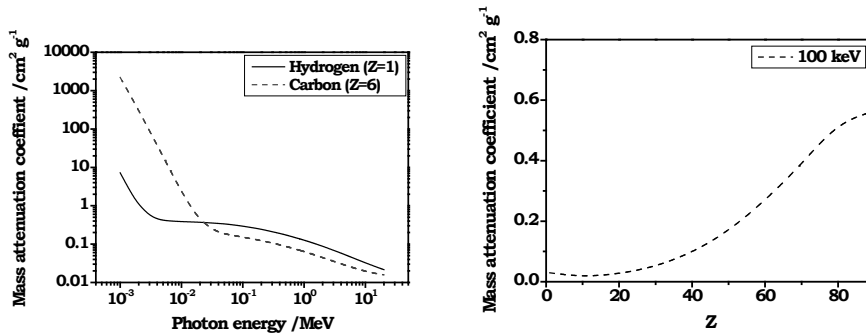


FIGURE 4-15.- LEFT: ATTENUATION COEFFICIENT OF ELEMENTS TYPICALLY CONTAINED IN POLYMER: HYDROGEN AND CARBON. RIGHT: ATTENUATION COEFFICIENT VARIATION WITH Z IN PERIODIC TABLE.

4.4.2. X-RAY SOURCES: GENERATION

X-rays are generally obtained from compact sources (tubes) or synchrotron radiation beam in large-scale research facilities. The very early X-ray tubes were the cold cathode tubes. The working principle was based on a high voltage generated in between the cathode/anode pair of a glass tube filled with very low-pressure gas that becomes ionized. The resulting free electrons are accelerated and strike the target resulting in Bremsstrahlung and fluorescence X-rays. The main disadvantage of this first approach X-ray tube was that X-rays generated were of low-energy unsuitable to penetrate human body.

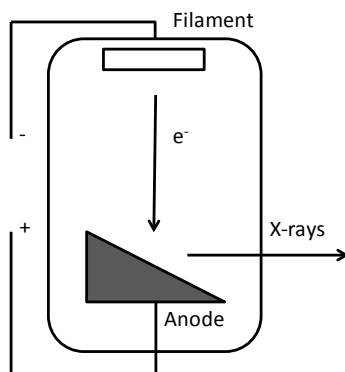


FIGURE 4-16.- X-RAY TUBE BEAM PRODUCTION SCHEME

In 1913 Coolidge tube was invented. This new design emitted electrons at much higher voltages from a heated filament towards the anode under vacuum inside the glass tube (larger currents are achieved). The anode is the part of the tube from which the X-ray radiation is emitted. The strongest advantage of this setup is the tunability of the beam by the possibility of changing the voltage. Hence, some of the actual nowadays-compact X-ray sources are still working under this concept and using improved design and electronics. Actually, this design did not allow to obtain energies over a certain threshold. The heat generated into the filament that may result into undesired anode melting. Firstly, anode cooling by water circuit was introduced to avoid target melting during X-ray generation. Subsequently, X-ray tubes provided with rotating anode were introduced in order to get better heat distribution. These advances allowed to produce and handle successfully higher power levels (kW). Since the 1895 the discovery of X-rays, the beam power capacity has increased up to six orders of magnitude.

Furthermore during the last decades developments have been concentrated on downsizing the focus area as shown in Figure 4-18. The main goal of reducing focal spot size is to obtain images with higher resolution. Mini, micro, sub-micro and nanofocus tubes are nowadays available by using electron lenses that allow the beam to focus onto the target. The smaller the focus spot size is, the lower current (power) available. The heat dissipation limits the use of high X-rays energy. High power induces anode melting. It is still a problem combining rotating anode principle with microfocus sources. Latest developments are basically focusing on developing new materials to build targets dissipating heat better. In this sense, liquid-jet based technology develops a new concept of non-solid anode already melted circulating continuously and thus providing better thermal dissipation.

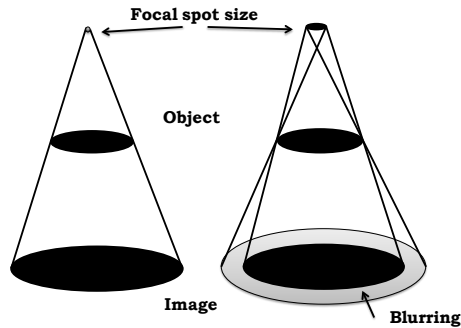


FIGURE 4-17.- FOCAL SPOT SIZE REDUCTION PERMITS TO AVOID OBJECT BLURRING IN CONE-BEAM CONFIGURATION.

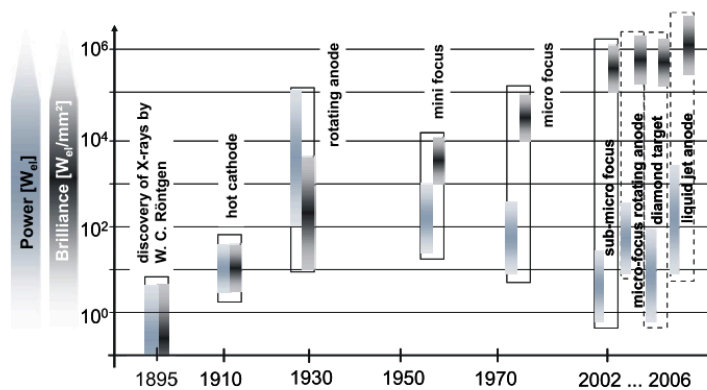


FIGURE 4-18.- X-RAYS SOURCES DEVELOPMENT DIAGRAM IN TIME [2].

On the other hand, synchrotron radiation is created by accelerating free particles in high vacuum that leads to the emission of electromagnetic radiation [3]. Particles in a linear accelerator are one possibility, but ring storage to accelerate them in a closed trajectory is more practical to obtain continuous radiation source. Magnets are used to keep circular trajectory and radial acceleration is the responsible of radiation generation. During the last decades a large number of synchrotron facilities have been built across the world. Synchrotrons have been developed from first to third generation rapidly increasing brilliance of these radiation sources [2, 4].

BEAM GEOMETRY

X-ray imaging setups can work under different beam configurations. Historically, cone-beam geometry was firstly used since it is available from X-ray tubes. In this geometry configuration, we can find resolution problems due to the size of focal spot. If spot size is not small enough a penumbra region appears distorting the image as shown schematically in Figure 4-19. That explains why the spot size has been reduced up to the nanometers. Subsequently, high-resolution imaging relying on parallel beams become of more interest thanks to the development of synchrotron sources. A third possibility is the focused beam geometry, but it requires X-ray optics and lenses which makes its technology very complex and expensive. Cone-beam and focused beam permit optical magnification of the irradiated object thanks to particular beam geometry. On the contrary, parallel beam do not allow object magnification. Alternatively, improved optical design of cone-beam permits to increase resolution. This basically consists on scintillating window placed and high-resolution X-ray optics between the sample and the detector.

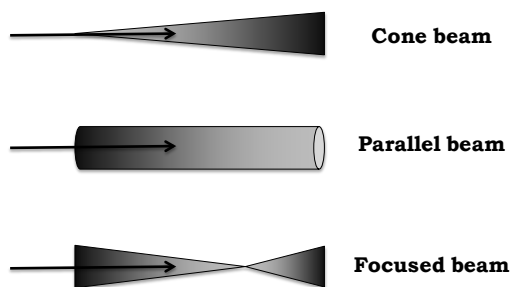


FIGURE 4-19.- DIFFERENT BEAM GEOMETRY CONFIGURATIONS.

4.4.3. X-RAY DETECTION

Nowadays, there are a large variety of X-ray detection technologies. In particular X-ray detection for imaging purposes is often classified into indirect and direct detection, see Figure 4-20.

Indirect detection uses a scintillating material or screen that converts X-ray photons into visible light by luminescence process. A charge-couple device (CCD) chip or a photodiodes screen converts the visible photons into electrical current intensities. This detection principle is predominantly used in X-ray imaging since the energy response of the detector can be easily optimized varying the scintillating material and thickness. Besides detectors in the optical range are numerous and well known so it is possible to select the best one. The scintillators are made of materials with high-density and high effective atomic number. Some common scintillating materials are ceramics, phosphore (P), silicium (Si) and cesium iodide (CsI). One of the main disadvantages of this

detection technique is that spectral information is typically lost and the light scattering inside the scintillator strongly limits the resolution. Doping scintillators with rare earths or fluorescent ions permits to overcome this limitation. These materials emit more light and therefore thickness can be reduced avoiding scattering. CdTe is commonly used to produce linear and small 2D detectors in synchrotrons and makes the process of detection more efficient. Other available possibilities are crystals such as Cerium-doped Lutetium Yttrium Orthosilicate (LYSO), Cadmium tungstate (CWO) and Gadolinium oxysulfide (GOS).

Flat panels combine and merge large area CMOS image sensor with a scintillator and all amplifying circuitry in a lightweight way. They provide high sensitivity and low noise and are specially used in digital radiography.

Contrary, in a direct detector, incoming X-rays interact in the sensitive layer of the detector, creating electron-hole pairs that are collected by an electric field. This mechanism counts every single photon (imaging) and its energy (energy dispersive principle, EDX). We shall focus on detection fundamentals for imaging. In practice, direct photon detectors need to overcome some problems. Firstly, X-ray flux needs to be sufficiently low in order to match the frame rate of the detector since the charge deposited by a photon needs to be read out before a second photon interacts with the detector. As most detectors are made of Si, only low energy X-rays can be detected since to determine the energy, all of the photon's energy needs to be deposited into the detector, so the photon needs to interact through photo-electric absorption. Therefore, direct detectors are currently limited to application in high resolution imaging of low absorbing objects. These detectors are under development because they require sophisticated electronics.

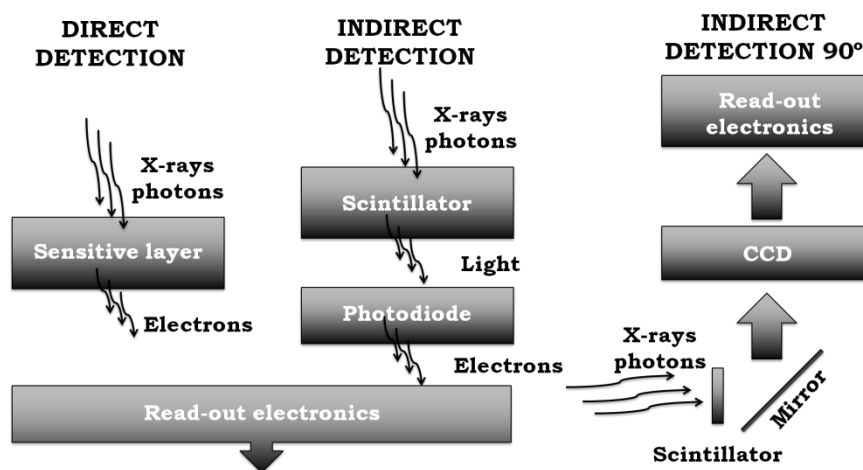


FIGURE 4-20.- SCHEME OF WORKING PRINCIPLE OF X-RAY DIRECT, INDIRECT AND DIRECT 90° DETECTION.

X-ray imaging is mainly based transmission measurements. Nevertheless, the fact of using absorption as imaging principle becomes an inconvenient for thick samples, especially at soft X-rays with low depth penetration. On the contrary, phase imaging relies on amplitude distinctions. It is known that all electromagnetic waves experience a change in amplitude and phase when they go through a medium related to the real and the imaginary part of the refractive index. The fundamental key is to convert variations in phase into variations in intensity. In the case of thick samples irradiated with low energy photons or samples made from different materials showing similar attenuation, it is possible to relay image reconstruction on phase change. Therefore, imaging based on phase retrieval is mainly aimed at poorly or non-absorptive materials. It is important to differentiate between phase contrast and phase retrieval. Phase contrast permits to obtain qualitative shape information but phase retrieval invert modulated intensity images to calculate the phase.

There are two basic requirements to work on this phase change by applying phase-retrieval. Firstly, beam illuminating the sample needs coherence that can be achieved either in synchrotrons (large distance from the source) or using a small source size. The second condition frequently requires that two intensity measurements are taken under different conditions, although it can be skipped. Some of the algorithms to work on phase-contrast imaging are based on intensity propagation [5,6,7]. Nevertheless these methods are only strictly exact for non X-ray absorbing material. Unfortunately, most materials absorb and induce phase changes at the same time. Paganin's algorithm solved this problem in 3D and some variations are nowadays implemented [8,9,10,11]. Thanks to them it is possible to provide quantitative results for samples containing several materials. This reconstruction algorithm is applied for the ultrafast tomographies in this investigation. A broader review of these approaches can be found in the literature [8,12,13,14].

4.5. X-RAY RADIOSCOPY

As previously commented imaging techniques may provide not only spatial but also temporal resolution when a sequence of images is acquired. In this sense, X-ray radioscopy consists on a sequence of radiographies acquired with temporal resolution. Namely, Figure 4-21 shows a sketch of the typical setup to perform X-ray radioscopy experiments. This technique allows non-invasive evolution of dynamic processes and is a powerful tool for science and industry.

In the particular case of polymer foams of the main advantages of X-ray radioscopy against those other non-destructive techniques (NDT) and conventional thermo-mechanical studies during foaming is that X-ray radioscopy is sensitive to density. This is achieved thanks to Beer-Lambert intensity dependence. A description on the particular setup developed in this investigation based on this technique is provided in

this section. This description is further discussed in the publication Polymer Testing 32 (2013) 321-329 attached to this chapter.

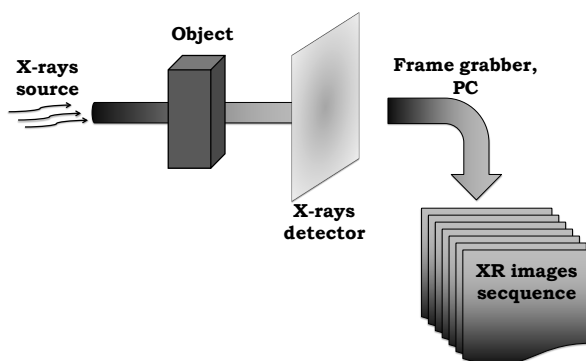


FIGURE 4-21.- SKETCH OF THE WORKING BASIS OF AN X-RAY RADIOSCOPY SETUP.

4.5.1. MICROFOCUS X-RAY SYSTEM AT CELLMAT

This X-ray imaging device has been built as part of this work. It is described and characterized in the paperwork attached at the end of this chapter. It is a valuable tool able to obtain information about polymer foaming processes. Both the X-ray tube and the detector needed careful selection since polymers present low X-rays absorption coefficient and foaming is a process evolving rapidly. In this sense low energies of the emitted X-rays are suitable for imaging polymers although detectors are not conceived for low energies. The high sensitivity of the detector response is thus of extreme importance. Moreover, dimensions of cellular structure are in the order of microns and therefore high resolution is also relevant, thus needed small spot focus size and small pixel size in the detector.

MICROFOCUS X-RAY SOURCE L10101

A closed air-cooled microfocus X-ray source L10101 from Hamamatsu, Japan, is used to produce the X-rays. In this tube an ultrafine electron beam produces X-rays, striking on a tungsten target in high vacuum atmosphere. Then the tungsten surface that is irradiated by the electrons produces X-rays. X-rays come out the source through a Beryllium 150 μm -thick window forming an X-ray conic beam of 39°. The microfocus spot size of 5 μm tends to slightly broaden as electron acceleration voltage or current become increased up to a maximum of 20 μm . Nevertheless, the spot size remains in its smaller size meanwhile these values keep below 40% of maximum power. The maximum intensity (current) is limited by the produced voltage according to graph in Figure 4-22. The technical characteristics are summarized in Table 4-1.

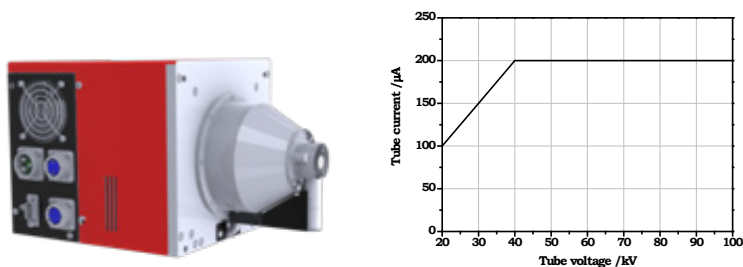


FIGURE 4-22.- X-RAY TUBE L10101 FROM HAMAMATSU. MAXIMUM POWER OUTPUT CURVE.

TABLE 4-1

Spot size	5-20µm
Voltage	20-100kV
Current	0-200µA
Maximum power output	20W

FLAT PANEL DETECTOR

The detection system is a flat panel (FP) form Hamamatsu (Japan) C7940DK-02. This high resolution detector is composed by a matrix of 2240 x 2344 pixels with a pixel size of 50 µm, i.e. sizing 111.50 x 117.20 mm. The digital output is a 12 bits depth resolution with maximum acquisition velocity up to 9 fps working at 4 x 4 binning mode.

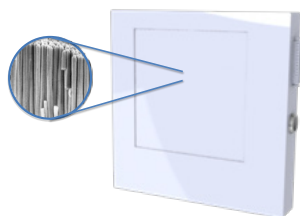


FIGURE 4-23.- FLAT PANEL DETECTOR AND MICROGRAPH OF CSI NEEDLE GROW CRYSTALS.

This flat panel detection technology consists in deposited scintillator material CsI, layer directly in front of a CMOS detector. One of its main advantages yields in the small dimensions of the complete high resolution imaging apparatus. The scintillating material is grown in special needle-like shape in order to improve light transmission in the normal direction and thus reduce photons scattering. It is important that the diameter of the grown needled material is smaller or similar than CMOS pixel size, i.e. 50 microns for our particular case. A more detailed description of this FP response even at such low energies is presented in the published work, Polymer Testing, 32

(2013) 321-329 included at the end of this chapter 4. Fig.5 in the paper shows how the contrast resolution becomes reduced at higher energies over 40 kV since the best response range provided by the FP is concentrated on lower energies. This figure in the attached paper shows an example where a 2 mm thick sample with 12% porosity is imaged at increasing (25, 30, 40 kV) voltages and varying current values (100, 135, 170 μ A). Finally, the CPU connection and FP data acquisition is done thanks to a frame grabber (Dalsa-Coreco, USA). Frames per second...

SYSTEM CONFIGURATION

X-ray tube and FP detector are settled on in front of each other inside a X-ray shielded lead cabinet, as seen in Figure 4-25. In principle it is possible to position them at any distance, *SDD*, but in general optimum distances are in the range of 0.3 to 1.2 m. As the beam is cone-spread the more distant the less radiation the FP-detector receives, which, in principle, is positive for its lifetime but reduces image quality since different artifacts effects increase with distance. In this particular device, the box dimensions limit this distance and it was chosen at 580mm, becoming a compromise distance for all the involved factors. The objects to be imaged can be placed at any position in between the detector and the source. The fact of having diverging (cone-beam) X-ray beam allows for object magnification. Magnification factor (*M*) is a function of the object to source distance (*OSD*) compared to the total distance from the source to the detector (*SDD*). Thus magnification is defined as indicated in Eq. 4-5.

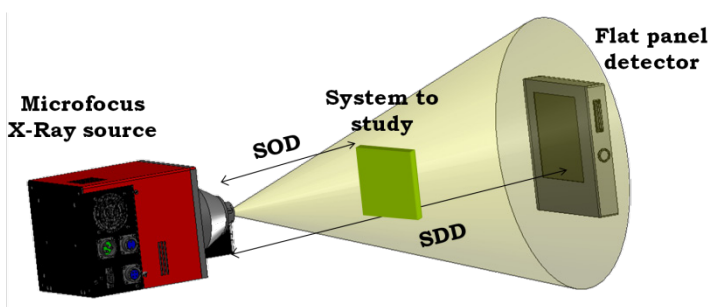


FIGURE 4-24.- MAGNIFICATION SCHEME OBTAINED THANKS TO CONE-BEAM GEOMETRY.

$$M = \frac{SDD}{OSD}$$

EQ. 4-5

The CellMat device also includes a metric lab-jack mounted on displacement rails for sample positioning, power and thermocouple connections, compressed air and PID controller. All these complements are installed in order to facilitate polymer foaming experiments which frequently require temperatures over 200°C inside the shielded cabinet. A thermostat controls inside temperature. Additionally a pneumatic shutter is placed to avoid unnecessary exposure time of the detector during X-rays source

heating up or during long experiments. This extends life of the flat panel detector and prevents lag undesired effects.

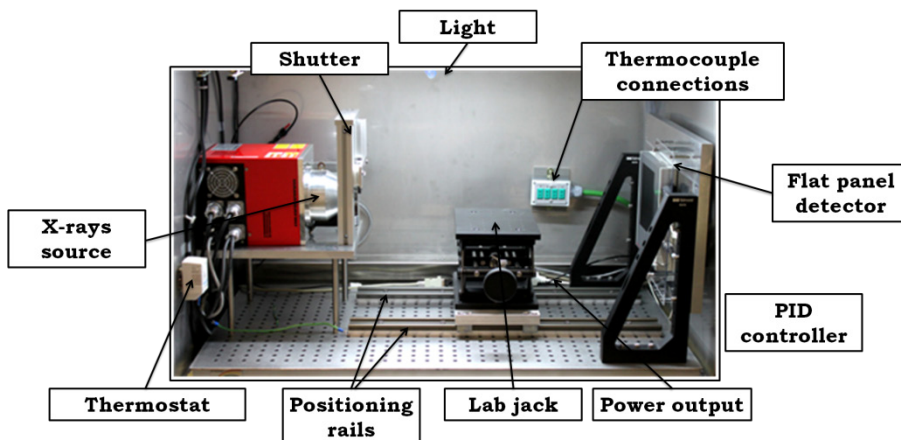


FIGURE 4-25.- X-RAY DEVICE WITH ALL COMPLEMENTARY CONNECTIONS.

SYSTEM COMPLIANCE

Considerations about, temporal and spatial resolution of the system are presented in the publication attached at the end of this chapter. In a rough approach, pixel resolution is the result of dividing the pixel size by the magnification factor. Nevertheless, some other facts have to be considered in order to calculate the real resolution (*MTF*, *PSF*, *QE*, etc.) as previously explained in the Part A of this chapter. Figure 4-26 shows the *MTF* for this system calculated by the slanted edge procedure [15]. It shows a value of 7.2 lp/mm at 10% of total *MTF*. Objects can be, in principle, of any size, however the maximum size depends on the magnification factor and the total detector's active pixels area (approx. 120 x 120mm). Figure 4-27 shows maximum object size for a *SOD* of 580 mm in this system. Object thickness (in the direction of the X-rays) also influences the image as it is discussed in the publication attached to this chapter. The system allows theoretically 9 fps acquisition. Nevertheless, for the particular case of low-absorbing polymer foams we usually set this circa. 4-5fps.

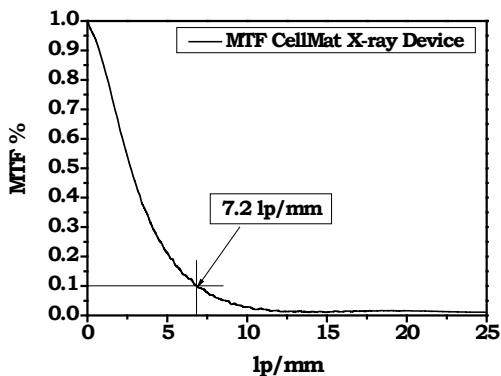


FIGURE 4-26.- MTF CALCULATED BY THE SLANTED EDGE PROCEDURE FOR THE CELLMAT DEVICE.

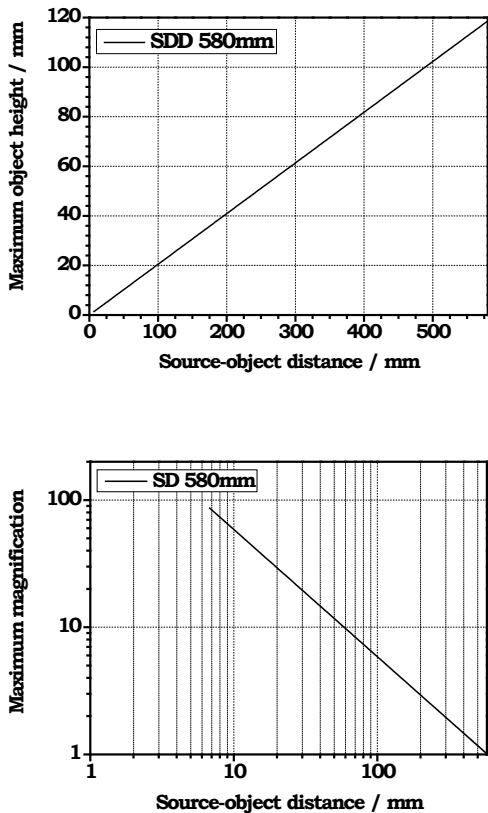


FIGURE 4-27.- (UP) MAXIMUM OBJECT SIZE (FOV) AND (DOWN) MAGNIFICATION REPRESENTED AGAINST SOD FOR A CERTAIN FIXED SDD.

ACQUISITION SOFTWARE AND HARDWARE

With respect to the software for controlling the complete imaging device, the X-ray tube has its own control tool (MFX Control Software) which facilitates the warm-up process and the beam emission control. The commercial software HiPic v8.3 from Hamamatsu is used to control the acquisition and store the images.

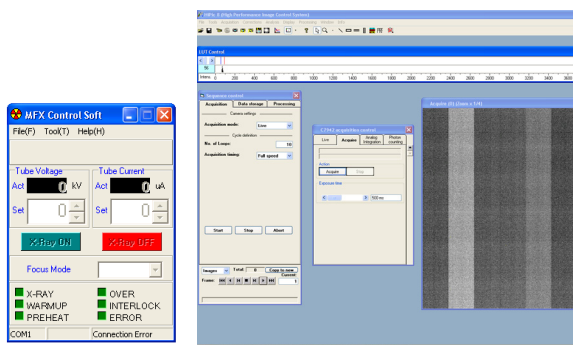


FIGURE 4-28.- HAMAMATSU SOFTWARE FOR THE X-RAY SOURCE BEAM CONTROL AND THE DETECTOR ACQUISITION.

Complementarily, self-developed software has been programmed under LabView environment. The main objective is to have integrated software which controls temperature, X-ray tube and image acquisition in a single window. The software is programmed based on a states machine workflow. The detector control by Labview is done thanks to SDK library already implemented by Hamamatsu Germany. This library includes the SubVIs necessary to run in a batch mode all the HiPic v8.3 functionalities.

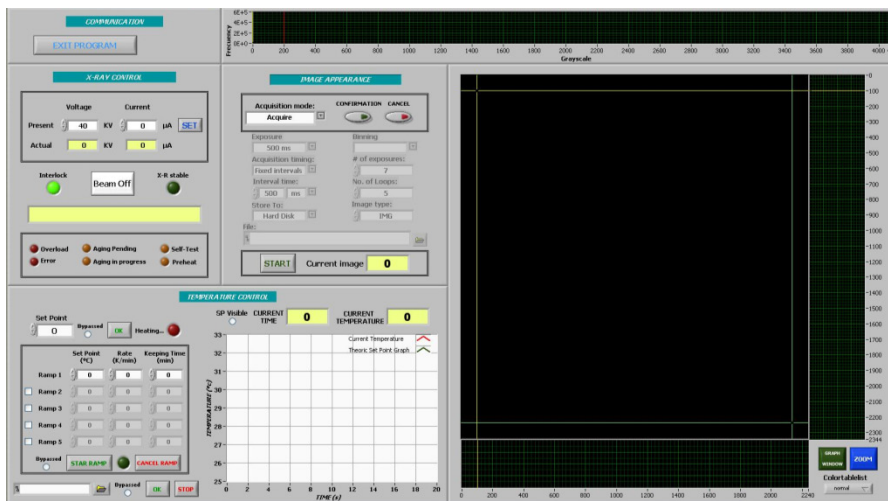


FIGURE 4-29.- INTEGRATED CONTROL SOFTWARE DEVELOPED AS PART OF THIS INVESTIGATION.

4.6. X-RAY COMPUTED TOMOGRAPHY

X-ray imaging permits not only 2D images acquisition as mainly referred until now. Besides, reconstruction of 3D real structures is possible. The result of this reconstruction process is called tomogram. Since “tomos” is a Greek word meaning slicing, tomography gives a description of a slice of matter within a bulky object based on several images collected at various angles. Very first tomograms were developed in 1957 with computer capacities improvement. It is important to note that both techniques radiography and tomography, share the same principles of radiation generation, matter interaction, radiation attenuation, detection and conversion. An X-ray radiography device provided with sufficient small spot size and sensitive enough detector can be easily converted into a CT scanner by simply mounting a rotary stage between source and detector.

This section focuses on X-Ray CT; however it is important to mention that other tomographic techniques are available working under similar principles depending on the radiation used. Once again depending on the beam geometry we can face parallel beam, fan-beam, cone-beam and helical (or spiral) cone-beam in latest fourth generation CT scanners aimed at improving quality in certain applications. We describe the main tomogram reconstruction principles and visualization capabilities of this technique.

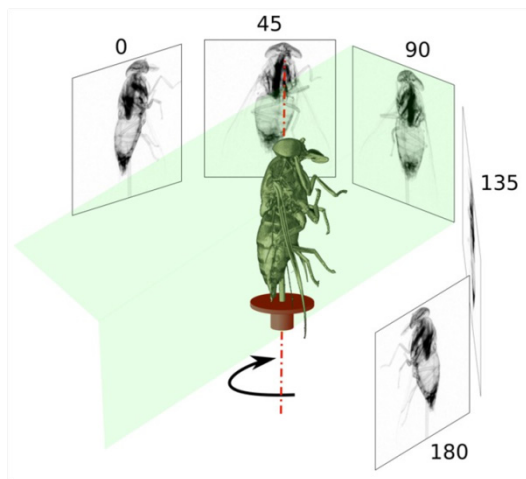


FIGURE 4-30.- BASIC TOMOGRAM ACQUISITION STEPS: RADIOGRAPHIC AROUND 360° [1].

4.6.1. VOLUMES RECONSTRUCTION PRINCIPLE: BACK-PROJECTION ALGORITHM

In tomogram reconstruction, the primary goal is to reconstruct an object considered as a 2D distribution of some kind of function $\mu(x,y)$ which for us it can be said that it represents the linear attenuation coefficient of the object considered. But the ultimate question is how we can calculate the attenuation distribution given for arbitrary object by using an image. At the end the main purpose of tomography is to reconstruct the object cross-sections by computing its object projection data.

There are two different methods to compute tomograms:

- Direct analytical inversion consists in solving N equations with N unknowns simultaneously providing an exact solution to the mathematical problem.
- Algebraic reconstruction technique (ART): that is basically an approximation; it uses iterative reconstruction methods of image estimation, pseudo-projection and comparison with the original projection and error minimization.

The exact solution to the tomographic reconstruction problem was found in 1917 but it is numerically impractical since it assumes a continuous and infinite function while we have a finite number of detector points. Fourier slice theorem, also known as projection-slice-theorem becomes essential. It permits to link sample and projected data. It states that the one dimensional direct Fourier transform (1D FT) of a parallel projection of a 2D object function $f(x,y)$ at an angle θ with respect to the X-axis, gives a slice of the 2D FT of the function $f(x,y)$ at an angle θ with respect to the u -axis. Collecting projections from 0° to 180° can fill the entire Fourier space, although we collect 360° to improve the statistics. Finally we can recover the object itself by inverse Fourier transform. In short, a tomogram reconstruction implies a series of 1D Fourier transforms followed by 2D inverse Fourier transform.

$$F(u, v) = \int_{-\infty}^{\infty} \int_{-\infty}^{\infty} f(x, y) e^{-i2\pi(ux+vy)} dx dy \quad \text{EQ. 4-6}$$

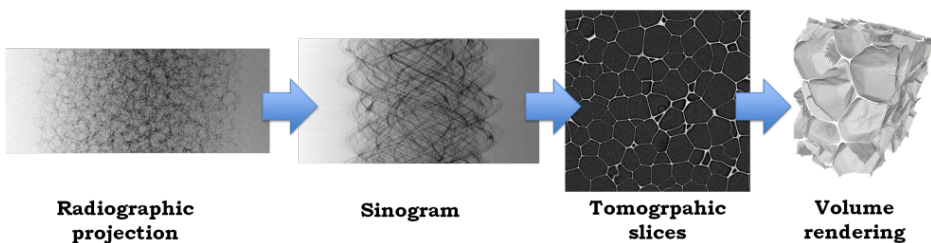


FIGURE 4-31.- BASIC TOMOGRAM RECONSTRUCTION STEPS: RADIOGRAPHIC PROJECTION, SINOGRAMS, SLICES AND VOLUME RENDERING.

In 3D the extension of Fourier slice theorem is done thanks to definition of Radon transform. If a function (attenuation coefficient, μ) represents an unknown density, the Radon transform represents the data obtained as the output of a tomographic scan. The inverse of the Radon transform can be used to reconstruct the original density from the scattering data, and thus it forms the mathematical underpinning for tomographic slides reconstruction. This Radon transform is called sinogram. We can say that Radon transform is the image principle encoding in tomographic reconstruction. The 3D volume exact reconstruction is computed thanks to Radon transform since each Radon value defines a unique point in the object space. In other words, if we can obtain the 3D Radon values in the object space (for a finite support), we can calculate the 3D Fourier transform of $F[f](u)$ and derive $f(x)$ in the spatial domain. The Radon values can be derived from the projection data acquired.

This reconstruction process is usually implemented in several software packages. Namely, in this investigation the Octopus reconstruction package has been used. The reconstruction process easily allows obtaining a volume rendering of tomographic reconstruction following basically in the steps below:

- The raw projection images coming from the detector are first filtered using a spot filter.
- These filtered images are then normalised by flat field (integrated if possible) and background images. Flat field images are acquired by moving the sample out of the detector's field of view while the X-ray source is on. Flat field images contain the intensity profile of the X-ray beam. Offset images are taken when the X-ray bundle does not hit the detector (by turning off the source or shielding the detector) and correct for the detector's dark current. Then the normalised projection images are obtained from the measured projections. A more detailed description of this step is presented in part C of this chapter.
- The obtained images are now reordered into generated sinograms that contain the projection data of a single detector row for all projection angles. Sinograms are used for the reconstruction algorithms implemented as explained before, where each sinogram can be used to reconstruct one cross-section through the object.
- A tilting angle can be selected to correct misalignment. Other algorithms implementing artifacts correction are also available.
- It is possible to reconstruct only a single slice at any location in the object to evaluate the effect of every parameter that can be adjusted in the reconstruction. These parameters include corrections for misalignment of the system, application of a noise filter, ring filtering, beam hardening correction, etc. After each of these parameters is carefully selected, the reconstruction of the 3D object function is performed.

4.6.2. CELLMAT SCANNER

An X-ray imaging device with source and detector can be easily converted into a tomography setup by simply mounting the sample on a rotating stage, see Figure 4-32. This allows to acquire radiographic projections at different angles and thus 3D image reconstruction. In the future a rotary stage is planned to be mounted between tube and flat panel detector. This will simply convert the image setup design and developed in this work into a μ CT and thus obtaining 3D images.

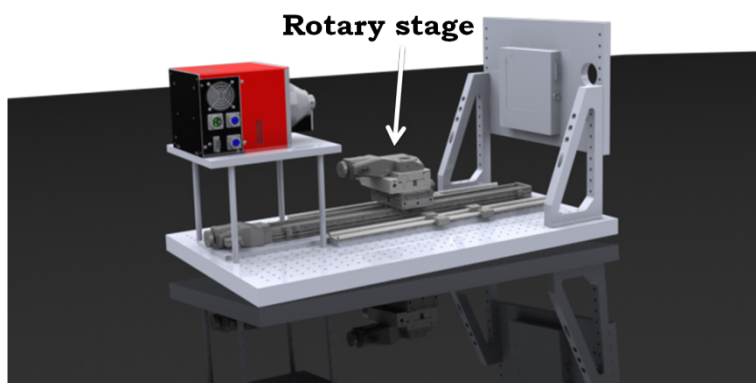


FIGURE 4-32.- CAD DESIGN OF FUTURE CELLMAT μ CT DEVICE.

4.6.3. UGCT μ CT SCANNER

Figure 4-33 shows a picture of the high resolution X-ray CT scanner built at the Centre for X-ray Tomography at Ghent University (UGCT) ^[2]. This particular customized setup is used in this investigation. It consists in a microfocus X-ray tube FXE-160.50 source from Feinfocus (minimal spot size: 0.9 μ m, Voltage: 20-160 kV, Current: 0-200 μ A) with a maximum output power of 20 W. The Feinfocus X-ray tube is equipped with a dual head system, of which the transmission head is currently shown. The transmission head is optimized for high resolution applications, while a second directional head is mostly suited to scan relatively large objects in a short time interval. The detection system works on indirect detection principle and the model is PerkinElmer XRD 1620 CN3 CS a-Si flat panel with CsI screen (2048x2048, 200 μ m pixel size). Various motors are used to manipulate the sample. A rotary stage from MICOS (UPR-160F AIR) is placed in between these two basic components allowing image acquisition at different angles. It is mounted over a linear stage which provides movement in a wide gap (1.4 m approx.) in between the source and the detector varying the magnification factor, M . Two extra piezoelectric positioning

devices on top of the rotation stage facilitate the sample centring. Additional horizontal and vertical axes are used to position the sample inside the field of view of the detector and allow to acquire flat field images while the sample is not visible on the detector. These flat field images are then necessary to remove the illumination inhomogeneities and the noise in the detector response before further processing.

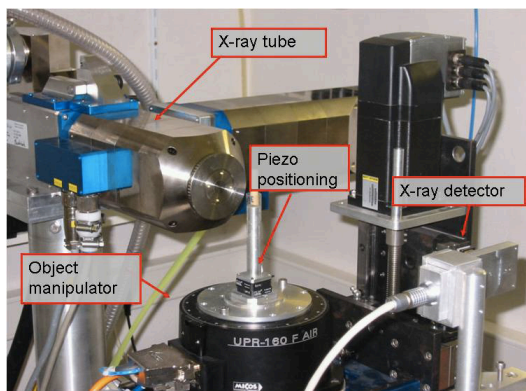


FIGURE 4-33.- UGCT SCANNER SETUP WITH A DIFFERENT X-RAY DETECTOR MOUNTED (COURTESY OF UGCT-UNIVERSITEIT GENT).

4.7. TOMCAT BEAMLINE AT SWISS LIGHT SOURCE

The beamline for TOMographic Microscopy and Coherent rAdiology experimentTs (TOMCAT) offers a synchrotron radiation instrument for fast non-invasive, high resolution, quantitative investigations on diverse samples [3,4]. Thanks to latest developments towards improving temporal resolution custom devices for *in-situ* experiments can be easily installed on the sample stage. Therefore, dynamic processes can be followed in 3D for the first time thanks to the new ultrafast tomographic endstation with sub-second temporal resolution [7].

The X-rays source is a synchrotron beam from 2.9T superbend and the sample is placed 25 m far from it. Focal spot size is 123 \AA and the photon flux is 1013 photons/s/0.1%bw. This high flux is one of the main requirements to perform ultrafast scans since statistics based on detected transmitted photons need to be sufficient in the shortest possible interval time. This is necessary to achieve successful tomogram reconstruction in a very short time. Absorption and phase contrast imaging are available at TOMCAT with a voxel size ranging from 0.16 up to 14.8 microns (field of views from $0.42 \times 0.35 \text{ mm}^2$ up to $30 \times 30 \text{ mm}^2$, respectively) are routinely performed in an energy range of 8-45 keV of monochromatic beam.

For ultrafast tomographic applications, the rotation axis and detector system are of extreme importance. They strongly influence the acquisition speed and quality of tomographic datasets. Synchronization between axis rotation and detector acquisition is crucial. In this case the maximum rotation speed of the high-precision stage is 600 rpm and by that the limit of the tomographic acquisition speed is set to 20 Hz. Typical acquisition times for a single tomogram are below 1s and complete tomographic sequences are usually on the order of few minutes.

Figure 4-34 illustrates the system with two detectors (with two scintillators and cameras) in parallel, to record two intensity measurements simultaneously. For fast tomography purposes we use the first detector D1 of the system coupled to a thin optical mirror, which is transparent to hard X-ray photons. It reflects the light converted by the first, thin ($20\mu\text{m}$) LuAG:Ce scintillator onto the first detector D1.

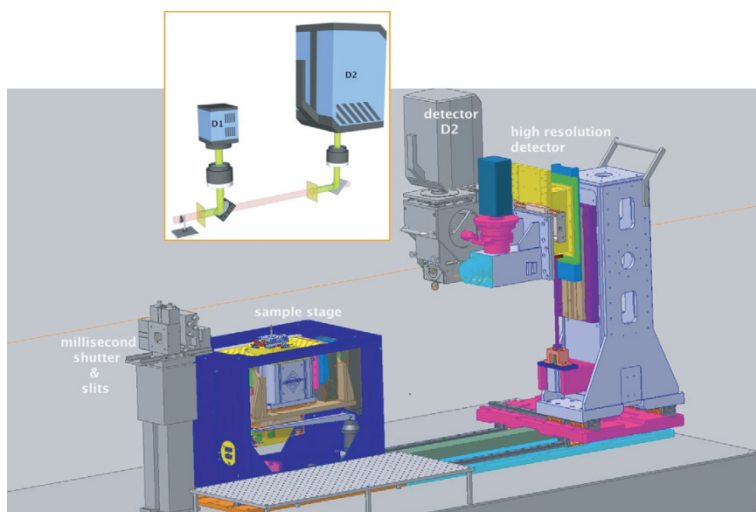


FIGURE 4-34.- TOMCAT BEAMLINE SETUP (COURTESY OF R. MOKSO FROM TOMCAT BEAMLINE AT SLS, PAUL SCHERRER INSTITUTE)

PART C

Post-processing of acquired X-ray images

4.8. IMAGE ANALYSIS SOFTWARE

Nowadays, it is possible to make use of a long list of existing commercial and open-source packages for image analysis. We have selected those packages showing successful performance and aiming exclusive tools for cellular materials and their image analysis. Each package offers specific capabilities depending on the desired target. We do not intend to give any software advice and/or comparison but we present a short and subjective set of selected tools we have found useful for the presented studies. It is always necessary to select computing tools bearing in mind the necessity of a good compromise between user interaction, complexity and time saving programming libraries.

HIPIC

It is the commercial image acquisition and analysis software developed by Hamamatsu [1]. It supports a wide range of Hamamatsu cameras in an easy and understandable way with risk minimization for wrong operation. It allows camera control, 16-bits full speed acquisition and controls of other special features such as binning and external trigger to synchronize acquisition with other events. Apart from image acquisition, HiPic has been used to carry out the background and shading corrections in the time series acquired.

IMAGEJ/FIJI

ImageJ/Fiji is an open source platform with numerous image-processing tools implemented [9, 2]. Moreover, it allows to develop self-programmed fast processing workflows. It is a very versatile tool extensively used in comparison to closed commercial suites. It does not offer the best rendering methods for final visualization. ImageJ platform has been used for automated analysis macros to evaluate both density and cell size evolution. It has been also used for filtering and as a first approach to test results of time-consuming image analysis at a glance before running them fully.

AVIZO FIRE

AVIZO FIRE offers a commercial complete suite for image enhancement and quantification [3]. It includes a large amount of different kernels for filtering, object separation algorithms, quantification tools and rendering for visualization. We have used it mainly for rendering and visualization purposes. Some filters have also used since it easily allows to select the kernel and connectivity of the operation.

MORPHO+

Morpho+ is a 3D analysis software package written in a C++ environment which provides several structural 3D parameters for CT data [^{4,5}]. It was developed at the Centre for X-Ray Tomography of the Ghent University. Morpho+ can process large datasets in a reasonable amount of time. It has an intuitive user interface and visualizes the different steps of the analysis to enable easy interpretation of the results. Morphological analysis of tomograms has been fully run in this platform.

IMORPH

iMorph is an intuitive platform for 3D image analysis software developed at *Institute Universitaie des Systèmes Termiques Industriels (IUSTI – Université Aix-Marseille)* [⁶]. It permits the morphological characterization of porous media and more precisely cellular materials. It allows porosity and tortuosity determination. One of the most powerful implemented tools is the solid classification algorithm based on comparison of the inertia moment of every pixel. This programme has extensively used for solid classification in one work of this investigation.

4.9. APPLICATION OF IMAGE CORRECTION PROCEDURES

A typical step after acquisition is image correction. Actually, image correction can be implemented to be done just during the image acquisition. Nevertheless, these corrections cannot be reversed and therefore we decided to carry out them *a posteriori*, then keeping the original images. In the particular case of defective pixel correction, this needs to be defined prior to image acquisition so the detector does not acquire these defective pixels.

4.9.1. DEFECTIVE PIXEL CORRECTION

As already mentioned all detection systems present a small amount of defective pixels that either higher response (hot) or do not detect any photon (dead). These pixels can be eliminated from the image thanks to software corrections. In fact, it is possible to eliminate dead pixels or even lines by interpolation procedures. Some steps are usually followed:

- In case we are planning to correct for hot pixel only we need acquire a darkfield image to use it as background with the beam off and exposure time desired.
- Acquisition of an illuminated brightfield (open beam) image for the hot pixels determination. Alternatively this image can be used for both the hot and dead pixel corrections.

- Selection of a reasonable threshold for discriminating normal pixel from bad pixel. The threshold is an intensity value which is related to the average intensity value and the standard discrimination of the reference image. There exist no general recommendations for optimizing the threshold. Usually a value greater than 80% leads to reasonable results. Specifically, for CellMat flat panel detector a threshold of 95% has been selected leading to 4 defective columns, 12 defective lines and 4422 defective pixels.
- The software generates a function to correct defective pixel of a sensor by replacing them with not defective neighbours.

4.9.2. BACKGROUND AND SHADING CORRECTION

Radiographies are always corrected by background image subtraction and shading image normalization. This step is also briefly mentioned in the paper Polymer Testing 32 (2013) 321-329 at the end of this chapter. Background subtraction allows noise reduction of the detector and enhances S/N . On the other hand, shading correction aims at suppressing any gradients in the image. Eq. 4-7 expresses mathematically these operations. Background intensity (I_b) is subtracted to remove noise floor from the image intensity (I). Then normalization is done by flatfield which is an open beam image, also called brightfield (I_o), in which the background subtraction has also been run. This shading image should represent the sensitivity variation of your system, which you want to account for. Both images (background and brightfield) should be taken under the same conditions as the image we want for the experiment (i.e. mode, binning, image size, exposure time, settings etc.) as well as the same kV and mA used for the experiment.

$$I_{corrected} = \frac{I - I_b}{I_o - I_b} \quad \text{EQ. 4-7}$$

Specifically, in tomography scans several background and flatfield images are acquired, both at the beginning and at the end of the scan for correction purposes. Sometimes they are also acquired in the middle of the projections so as to take into account any beam stabilization problems in long scans.

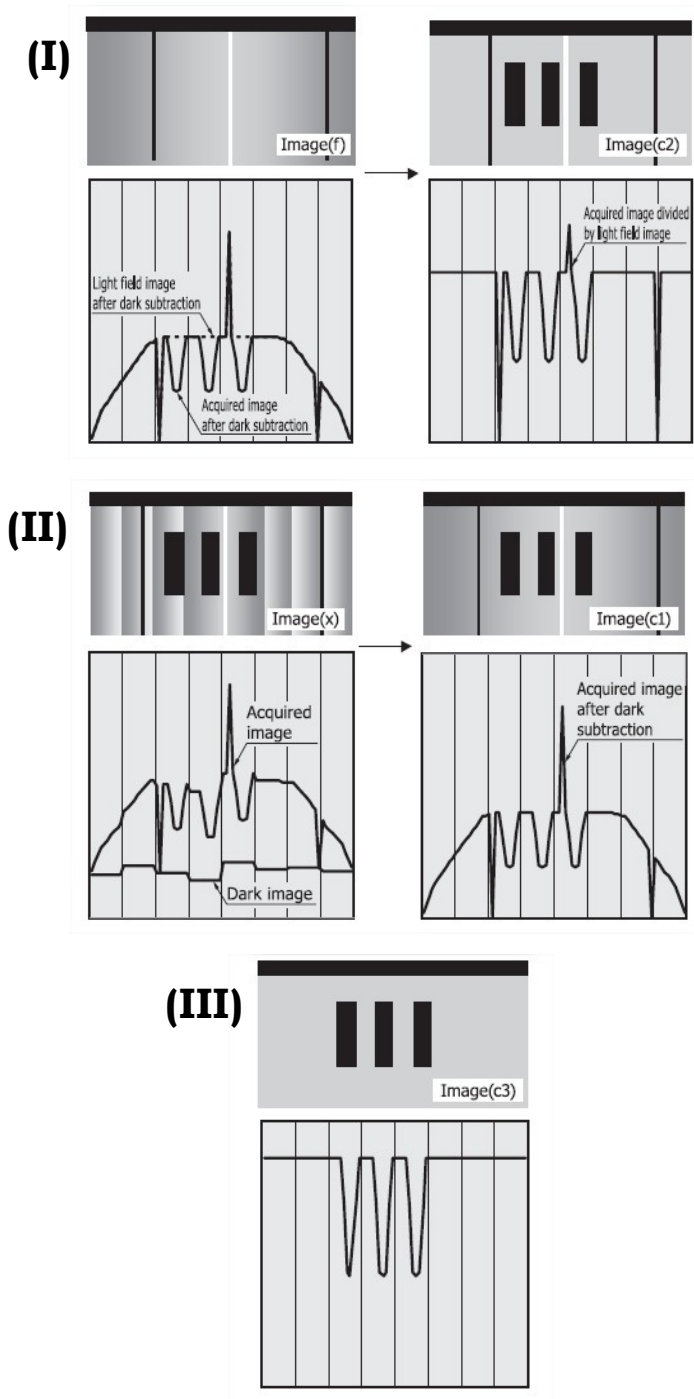


FIGURE 4-35.- BACKGROUND SUBTRACTION (I) AND SHADING (II) CORRECTIONS TO GET AN ENHANCED IMAGE (III). [FROM HAMAMATSU X-RAYS DETECTORS HANDBOOK]

4.9.3. X-RAY IMAGING ARTIFACTS

Some specific artifacts occurring in X-ray imaging are briefly commented in the following paragraphs. In general, artifacts avoidance is of more necessity for tomograms computation than for radiography.

BLURRING AND MOTION

Blurring has already been commented in part B when remarking the importance of focal spot size to image objects. Motion artifacts have to do with inherent structure changes in the sample due to temperature or simply because it is a live been or evolving system. This leads to image blurring unless temporal resolution is enough to detect these movements successfully.

LAG AND GHOSTING

This occurs when a sequence of images is acquired. It is a residual signal present in image frames subsequent to the frame in which the residual signal was generated. Ghosting refers to the change of detector pixel sensitivity to X-rays because of previous exposures of the detector [7, 8, 9, 10, 11].

BEAM HARDENING

Most X-ray sources generate polychromatic X-ray beam instead of monochromatic. The linear attenuation coefficient of most materials decreases with energy for the typical energy range used. Therefore, low-energy photons are attenuated more frequently than higher ones, causing the transmitted beam to contain proportionally more high energy photons. This effect consisting in higher mean energy of the transmitted than the incoming beam is called beam hardening. It causes smearing of the tomograms of cellular structures, by which pores in the object appear to be partially filled. However, this artifact does not apply to this work since polymer foams present low Z elements and it typically occurs for elements with high Z. An illustration of the beam hardening effect for a homogeneous object is shown in Figure 4-36.

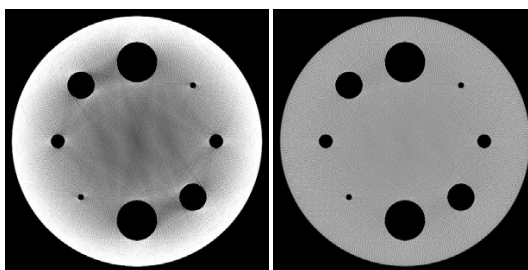


FIGURE 4-36.- HOLES IN METALLIC STRUCTURE WITHOUT BEAM HARDENING CORRECTION (LEFT) AND CORRECTED (RIGHT). [REF]

GEOMETRIC DIVERGENCE DISTORTIONS

Probably the most important among them is the effect of beam divergence in the projected image of an object with significant thickness, t as illustrated in figure 4.

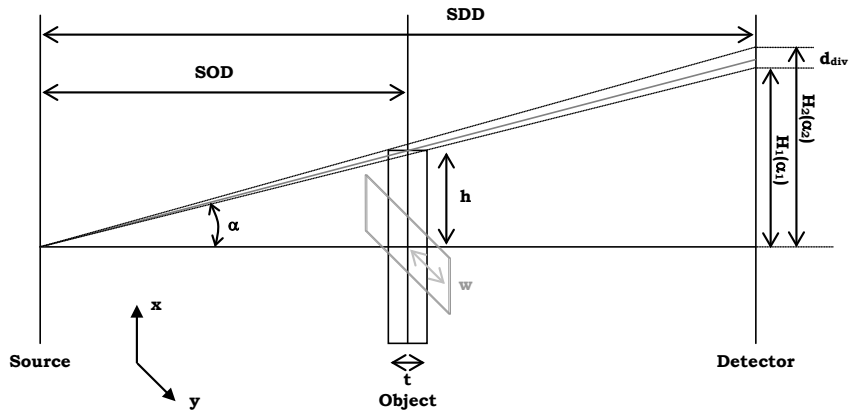


FIGURE 4-37.- X-RAY IMAGING PROJECTION GEOMETRY.

According to Figure 4-37 the cone beam divergence produces two minor effects:

- Effective thickness increase due to beam path increase out of the centre of the image the beam path slightly increases in comparison with the orthogonal direction.
- *Edge distortion* due to effective thickness reduced at any region in between H_1 and H_2 , the effective thickness can be calculated as.

The region in between H_1 and H_2 is also called divergence distortion, d_{div} [12] and can be estimated (assuming $t \ll SOD$) by Eq. 4-8. It is important to mention that divergence distortion is of different nature than penumbra region caused by finite size of focal spot size already mentioned.

$$d_{div} = hM_2 - hM_1 = h \cdot t \frac{SDD}{SOD^2 + t^2 / 4} \quad \text{EQ. 4-8}$$

RING ARTIFACTS

This effect results from systematic pixel deviation due to miscalibration and appears at reconstructed slices of tomograms. This is usually caused by imperfections in the scintillating detectors. They are concentric rings centre around the rotation axis. They can be frequently corrected by filtering the image during the reconstruction process.

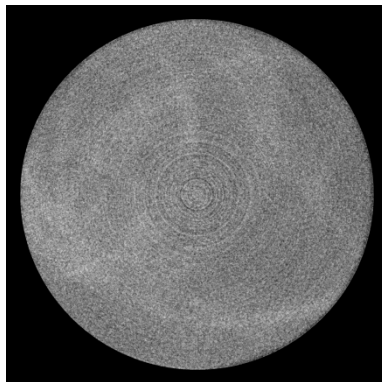


FIGURE 4-38.- RING ARTIFACTS

PHASE CONTRAST AT EDGES

This occurs at interfaces separating two regions with different attenuation coefficients resulting in edge enhancement in the image [13]. As explained in part B, this is the basis for phase contrast imaging but it is an undesired phenomenon in absorption imaging. It is common to try to avoid this artifact by reducing *SOD* as much as possible.

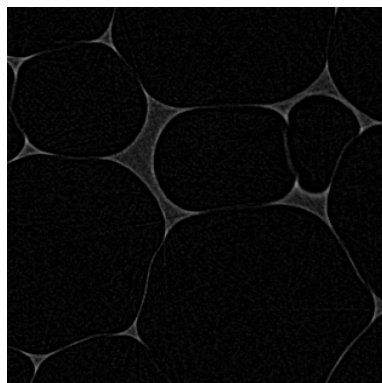


FIGURE 4-39.- PHASE CONTRAST.

4.10. PROTOCOLS OF IMAGE ANALYSIS

4.10.1. *IN-SITU*: DENSITY AND CELL SIZE EVOLUTION

DENSITY EVOLUTION

One of the most direct results that can be inferred from radiographic imaging is density determination from grey levels information contained in every pixel/voxel. Thanks to this information about attenuation coefficients it is possible to investigate defects or density profiles and evolution. Calculations based on Beer-Lambert

equation are commented and discussed in the work Polymer Testing 32 (2013) 321-329. Here, we present few additional considerations that could, eventually, need to be taken into account.

Density evolution calculation is possible using the existing connection between the collected intensity by the detector and the material's macroscopic density. A two-point or three-point calibration is generally used in order to convert intensity data into relative density values. The two used references for the spatial density determination are commonly a region in the radiography with no material (air, 100% porosity) and the average intensity within the area occupied by the material (bulk density of the foam). In this investigation, the final relative density and initial density of the liquid components are the selected for calibrating the grey scale intensity with the real relative density as indicated in Eq. 4-9 where c is the porosity.

$$c_{air}(x, y) = c_{REF-1} + \frac{\ln \frac{I_{REF-1}(x, y)}{I(x, y)}}{\ln \frac{I_{REF-1}}{I_{REF-2}}} (c_{REF-1} - c_{REF-2}) \quad \text{EQ. 4-9}$$

CELL SIZE

Automated macros have been programmed for the analysis of cell size evolution in acquired sequences of radiographic images during foaming processes. The general workflow for the analysis includes filtering, threshold selection for binarization, cells segmentation and cell size analysis. Two different methods are developed depending on the particular characteristics of images, resolution, noise, etc. The main difference relies on the procedure to segment cells in the images. Both have been implemented in ImageJ/FIJI platform.

- This first macro is used in the works studying the reactive foaming. Firstly the images are scaled to convert pixels into distances. Brightness and contrast adjustment and normalization are done in a selected region of interest (ROI). A median filter is applied to considerably reduce noise while preserving edges. Threshold values were selected to binarize ten representative images of the process. It is important to select individually the lower and upper threshold limits for single representative radiographies. These values are subsequently fitted to a logarithmic function. This fitting calculates the threshold values for the full image sequence. After this binarization the cells are segmented based on watershed algorithm. Finally, the masks are segmented by size-selective criterion to remove failures corresponding to noise or incorrect watershed. Statistical measurements of feret diameter were done on the obtained binary masks. The complete

procedure was carried out on a blinded experiment basis (to prevent conscious or subconscious bias). This macro is used in the

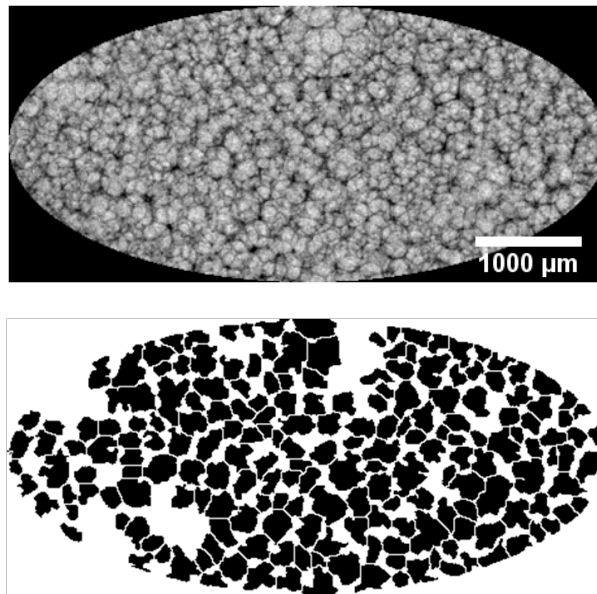


FIGURE 4-40.- RADIOGRAPHY OF ANALYZED ROI AND BINARY, THRESHOLDED AND AREA-SEGMENTED MASK FOR CELL SIZE CALCULATION.

- A median filter is applied for image enhancement. In this case manual edges selection of representative cells is done before binarization. This provides segmentation of cells and thus watershed-based separation is not necessary in this case. The remaining steps are exactly the same including binarization and particles analysis. This macro is used to obtain the results of cell nucleation and growth in thermoplastics.

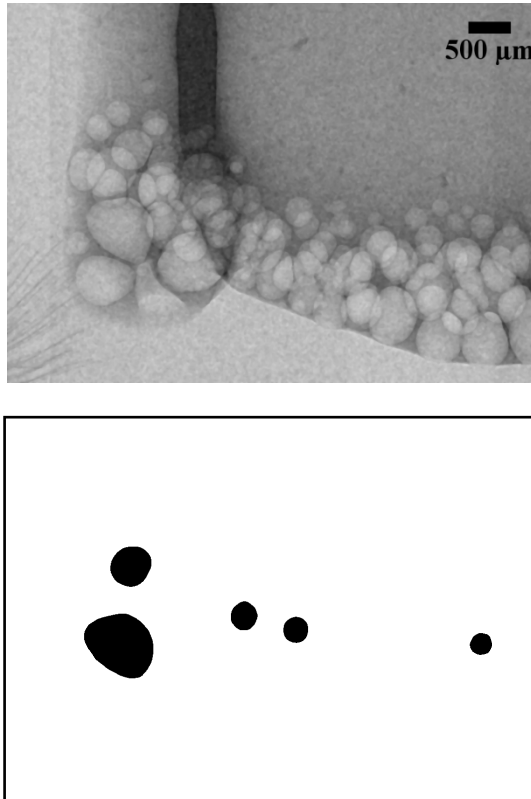


FIGURE 4-41.- RADIOGRAPHY AND CELLS EDGES IDENTIFICATION FOR QUANTIFICATION.

4.10.2. *EX-SITU*: MORPHOLOGICAL ANALYSIS

MORPHOLOGICAL ANALYSIS USED FOR TOMOGRAMS

The tomographic analysis of a cellular material basically consists in several steps aimed at extracting quantitative data. They are summarized in Figure 4-42.

- Image enhancement that is mainly aimed at noise filtering and/or optimization.
- Thresholding and binarization allows to separate material (foreground features) from background.
- Objects labelling and segmentation into separated objects. The distance transform and watershed segmentation algorithms help this step in 3D.
- Evaluation of different quantitative parameters for every single object.
- Rendering for proper and attractive visualization.

Binarization is a first approach to segmentation. It can be supervised or unsupervised by the user if the algorithm needs or do not the input from a human as seed for the

processing. Classification is usually established regarding regions identification based on characteristic properties (intensity, colour, texture, etc.). Then labelling process is performed and it basically consists in identifying individual items from a classified image.

A classical simple algorithm to find the threshold of an image can find a value that minimizes the in-class variance or maximize the in-class variance. This permits to establish a histogram-based classification.

Object separation is the process to convert the pixels of an image into a limited (small) number of classes/objects depending on the histogram of the image, a-priori knowledge of the statistics in the image and neighbourhood information. This step is used to find the components of interest in an image and identify connected objects or regions. This process consists in a unique label assignment to all pixels/voxels of each element in the image thanks to a certain defined algorithm and image scanning. A simple algorithm scans an image and chooses a label for a pixel if none of the neighbouring pixels have been labelled. Otherwise if it finds a neighbouring pixel with a certain label, this label is also used for the pixel. This step permits to establish a list of objects in which position, features and unique label characterize every object. Once the objects are identified second step segmentation procedures can be applied for optimum features identification and analysis.

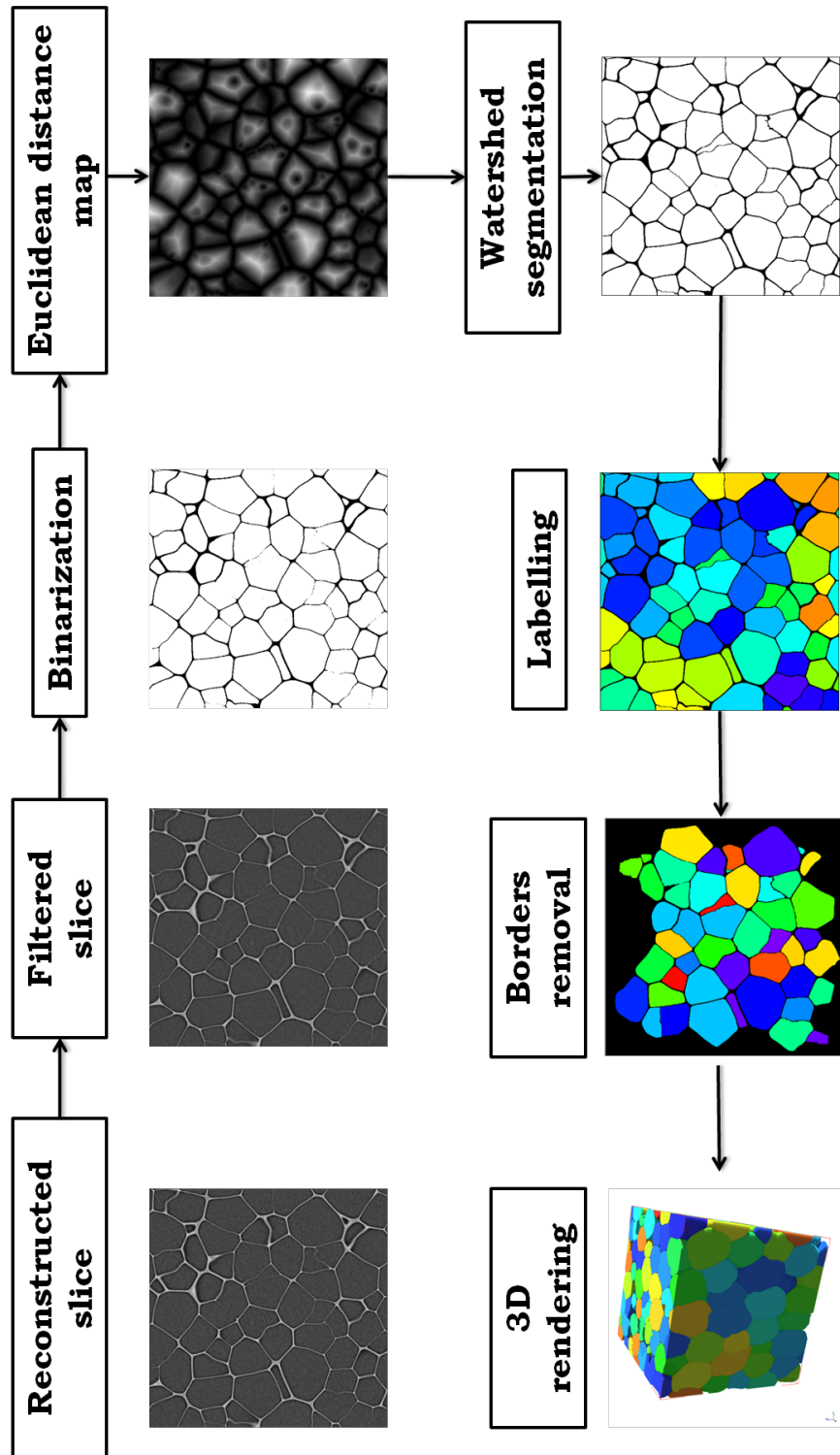


FIGURE 4-42.- BASIC TOMOGRAM RECONSTRUCTION STEPS FOLLOWED IN THIS INVESTIGATION.

One of the strongest tools for segmentation is based on the watershed transform. Once individual components are labelled in a first step, some of them typically remain interconnected whereas they are not in reality. For instance, limited resolution is a common source of entities absence in an image after binarization. Nevertheless watershed-based separation algorithm succeeds in reconstruction of these non-resolved features. This algorithm assigns a connected region to each local minimum in a grey-value image. In 2D it can be interpreted as the flooding of a topographic surface, where the height is given by the grey value of every corresponding pixel. All local minima are water sources and the water rises uniformly with growing grey-value. Pixels, where waters from different sources meet are chosen as the watershed pixels.

Combined with the Euclidean distance transform, the watershed can be used for satisfactory separation of connected particles such as pores in foams or grains in metals. Nevertheless advanced operations are often necessary to clean-up misclassified pixels since the separation and classification processes are not always 100% satisfactory.

Thanks to the workflow described several parameters can be quantitatively determined either from 2D or 3D images. We try to mention in these words the most useful parameters for the analysis of materials showing a cellular structure since they are under the scope of this investigation. A complete work using this type of morphological analysis is presented in Chapter 6.

- The ratio of the gaseous phase volume fraction respect the total material volume gives the porosity.
- Maximum opening is the diameter of circumscribed circumference.
- Equivalent sphere/circle contains the same number of voxels/pixels as the analysed object.
- Equivalent diameter gives the diameter of a sphere or circle containing the same number of pixels as the object.
- Specific surface gives a measure of the object surface.
- Sphericity is calculated as the ratio of the equivalent sphere surface and the specific surface.
- Equivalent ellipsoid orientation is a free reference measurement of the object orientation through the largest elongation direction of each individual pore. To determine this orientation, an equivalent ellipsoid with the same moments of inertia than the object, is used.
- Anisotropy is referred to a certain axis and it is calculated as the ratio of that fixed dimension and the dimension of the object in the complementary axes.
- Coordination number is the number of neighbours of a certain object.

- Feret diameter is defined as the maximum diameter in a certain direction. It is usually defined over the Cartesian axes.

ADVANCED 3D PROTOCOLS

CT analysis allows to obtain some other advanced cellular descriptors (and more difficult to be calculated). Some examples are material thickness, strut volume fraction, corrugation ratio, curvature, and tortuosity. The works presented in Chapter 6 propose a novel strategy for the solid phase analysis, which virtually separates the continuous solid structure into two clearly differentiated parts characterized by shape, local topology and location: cell walls and struts. This de-structuration technique offers the possibility of analysing separately structural features of each component. Subsequently, some of these descriptors can be computed as a second order analysis can be computed on the tomograms in order to provide more complete morphological information. We list and comment in these paragraphs some of the fundamental ideas developed for the de-structuration technique and the tortuosity calculation. We think that this is not required to understand the rest of the parameters which are mathematical concepts widely used.

DE-STRUCTURATION: STRUTS AND CELL WALLS

This procedure is based on the different morphology/topology of the two elements aimed to separate; struts and walls. Iterative erosion-dilation operations allow eliminating the walls whereas struts remain preserved. We follow two different approaches depending on the morphological and topological differences between struts and walls.

- 3D erosion-dilation technique

This method applies two consecutive 3D erosions followed by three consecutive 3D dilations give as a result a mask containing over-dilated struts that are subtracted from the original binary stack to avoid the presence of any over-dilated pixel. It is important to note that this apparently rough approach is valid for materials with a high fraction of material located at the struts (such as PU analyzed in our case). Materials like the LDPE foams (analyzed in this chapter 6) will not fulfil these requirements of strong topological differences in between struts and walls.

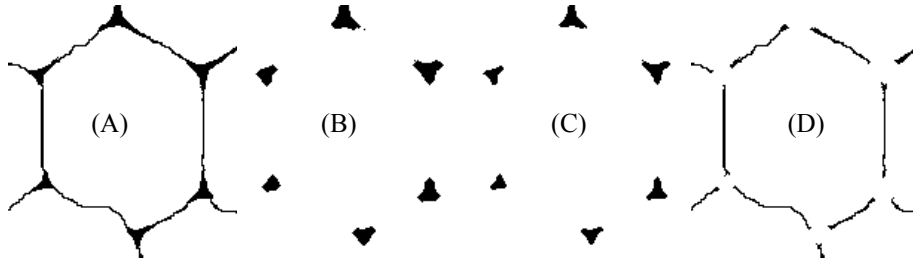


FIGURE 4-43.- SEQUENCE OF EROSION-DILATION PROCEDURE: (A) ORIGINAL BINARY PORE, (B) OVERDILATED MASK (C) RESULTING STRUTS (D) RESULTING CELL WALLS.

- Solid classification algorithm

This approach is the finest method for materials with low f_s . It is based on propagation growth computation technique [6]. The algorithm (implemented in Imorph software) performs an iterative analysis of elongation inertial moment at every voxel within the selected phase. Voxels showing unidirectional continuity must be edges (uniaxial oriented), whereas those showing 2D or 3D connectivity constitute either walls or vertexes (biaxial or triaxial oriented). Once the struts have been identified, the remaining steps are refinements based on dilation operations. The mask containing those over-dilated struts projections is subtracted from the original binary image containing both struts and walls.

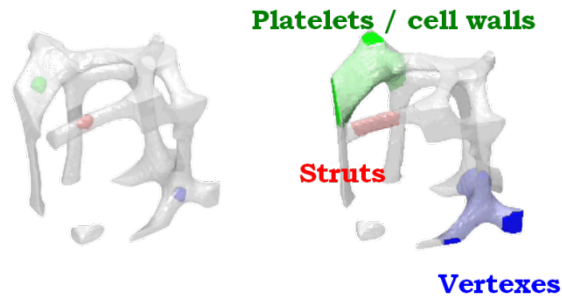


FIGURE 4-44.- ILLUSTRATION OF THE SOLID CLASSIFICATION ALGORITHM: STRUTS (1D CONNECTIVITY), WALLS (2D CONNECTIVITY) AND VERTEXES (3D CONNECTIVITY)

TORTUOSITY

It is a parameter of a key importance to study transport properties is either solid phase (thermal, electrical) and/or fluid one (acoustics, mass/heat flow, etc). This structure-related parameter expresses mathematically the real pathway distance in comparison to the straightest one when travelling along certain direction through the material's internal structure. Tortuosity determination is not reliable in 2D and need to be computed in 3D structures. However, computation requires the use of 3D algorithms in complex structures and thus it is not an easy task.

All methods are based on the definition of tortuosity as the ratio in between geodesic distance (the path length through the cells) and the Euclidean distance (shortest straight distance, projection over the Cartesian axis. The geodesic distance includes the extra distance needed to be covered by “travelling” through the gaseous/solid phase. The methods proposed in this section are self-developed algorithms that will be comparatively tested in these materials for the different phases. A description of each method is given in the following sections.

PORE-THROAT-PORE DISTANCES METHODS

This method consists of an iterative computational approach, determining the cumulative distance ratio on between pore-throat-pore distances and Euclidean distance. In this case the Euclidean distance between to pore centres is compared with the summed distances of the centre of the first pore and the centre of mass of the pore interconnection (throat) and the centre of the second pore and the centre of mass of the same throat. In this case the geodesic distance is the distance of the pore-throat-pore track. This is illustrated by the blue line in Figure 4-45. The pore-throat-pore distance method was implemented in the Morpho+ software.

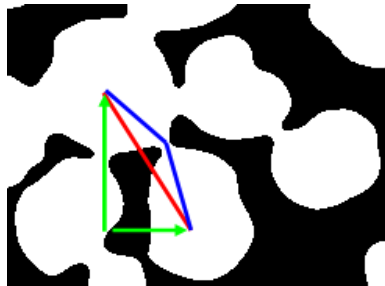


FIGURE 4-45.- SCHEME PORE-INTERCONNECTION-PORE (BLUE) GEODESIC DISTANCES AND EUCLIDEAN DISTANCE (RED). PROJECTIONS OF THE EUCLIDEAN DISTANCE ON X-AXIS AND Y-AXIS ARE SHOWN IN GREEN.

FAST MARCHING ALGORITHM

This method is based on the fluid propagation technique and it follows a completely different concept. It consists in computation of a parallel fluid wave virtually travelling from certain point and propagating at virtual constant speed without intersecting any other pixel than those contained in the selected phase [6]. This procedure calculates the virtual arrival time of the fluid at the all the end points in the final plane and calculates an average. The result is normalized by the arrival time obtained for a single-phase material and the ratio is directly output as a tortuosity value. The assumption is correct since the virtual velocity has been kept constant and thus the delay directly corresponds to a higher distance tracked. This approach can be applied to both solid and fluid phases and is implemented in Imorph.

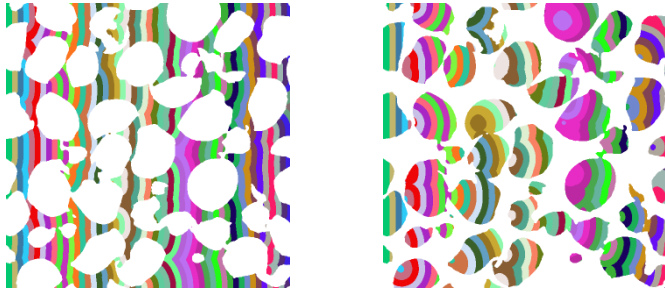


FIGURE 4-46.- PROPAGATION OF THE WAVEFRONT THROUGH THE SOLID (LEFT) AND GASEOUS (RIGHT) PHASE. THE COLOUR CODE CORRESPONDS TO DIFFERENT TIMES AFTER THE INITIAL PROPAGATION.

“APPLICATION OF A MICROFOCUS X-RAY IMAGING APPARATUS^a TO THE STUDY OF CELLULAR POLYMERS”

Author's personal copy

Polymer Testing 32 (2013) 321–329



ELSEVIER

Contents lists available at SciVerse ScienceDirect

Polymer Testing

journal homepage: www.elsevier.com/locate/polytest



Test equipment

Application of a microfocus X-ray imaging apparatus to the study of cellular polymers

E. Solórzano^{a,b}, J. Pinto^a, S. Pardo^a, F. Garcia-Moreno^b, M.A. Rodriguez-Perez^{a,*}

^a Cellular Materials Laboratory (CellMat), Condensed Matter Physics Department, University of Valladolid, 47011 Valladolid, Spain
^b Institute of Applied Materials, Helmholtz-Centre Berlin, Hahn-Meitner-Platz 1, D-14109 Berlin, Germany

ARTICLE INFO

Article history:
Received 16 October 2012
Accepted 30 November 2012

Keywords:
Cellular polymers
X-ray imaging
Radioscopy
Image analysis
Cellular structure

ABSTRACT

This paper describes an X-ray based non-destructive imaging method to study polymer foams. A broad description of the main hardware elements – tube and detector specially adapted for low X-ray absorbing materials – is provided. Recommendations on the optimum imaging parameters for polymer foams are also reported. The mathematical equations and methodology to obtain quantitative information from the images are extensively explained, providing further discussion on the limitations and resolution of the technique. Some of the main potential applications of the technique are also summarised.

© 2012 Elsevier Ltd. All rights reserved.

1. Introduction

Non-Destructive testing (NDT) comprises a wide group of analytical techniques used in science and industry to evaluate the properties of a material, component or system without causing damage [1]. The terms Non-Destructive Examination/Evaluation (NDE) and Non-Destructive Inspection (NDI) are also commonly used to describe these methods [2]. Because NDT does not alter the article being inspected, it is a highly valuable technique that permits saving both money and time in product evaluation, troubleshooting and research. Common NDT methods include vibration analysis, infrared thermography, acoustic emission analysis, ultrasonic imaging, X-ray computed tomography, digital radiography, ground penetrating radar, optical testing methods, magnetic-particles, penetrating liquids, gammagraphy, eddy-current testing and low coherence interferometry [2].

Since the 1920s, NDT has progressively developed from a laboratory curiosity to a powerful tool for science and industry. Modern non-destructive X-ray imaging is used by manufacturers to ensure product integrity and reliability, to improve product design and to provide in-line manufacturing control [3]. Alternatively, from the scientific point of view, X-ray imaging techniques in materials science have become more and more important since the early 1990's, and time and spatial resolution are, nowadays, beyond the microscale level [4]. In the particular case of cellular polymers, one of the most common non-destructive methods used by scientists is X-ray micro-tomography [5–10]. This ex-situ characterization method allows obtaining a detailed analysis of the internal architecture of the cellular polymer, which permits obtaining information both on the mesoscale (density profiles and presence of large defects) and on the microscale (cell size, cell wall thickness, anisotropy, etc). However, this powerful X-ray method has the main limitation of the relatively high scanning time required to obtain a high resolution 3D image, which makes extremely difficult to perform real-time experiments with time resolutions of a few seconds. In fact, this is only possible under very special conditions [11].

* Corresponding author. University of Valladolid, Condensed Matter Physics Department, Cellular Materials Laboratory (CellMat), C/Prado de la Magdalena, 47011 Valladolid, Spain. Tel.: +34 983 184035; fax: +34 983 423192.

E-mail address: marrod@fmc.uva.es (M.A. Rodriguez-Perez).

In contrast, the alternative use of 2D X-ray imaging (radiography) and time resolved X-ray imaging (radio-scopic) can be useful for the study of this type of materials both ex-situ and in-situ. Due to the small size of the structures to be resolved (cell walls thicknesses of a few microns) this technique necessarily involves the use of high resolution detectors and micro/nanofocus sources. This versatile technique enables observing structural details by encoding in its 2D projection the spatial variations in specimen density and atomic number though their transmitted intensities.

In-situ analysis of the foaming behaviour of cellular plastics has appeared in recent years. Different experimental challenges have to be considered depending of the type of base material: thermoset or thermoplastic. In the case of thermosets - usually foamed at room temperature and atmospheric pressure - the experimental set-up is simpler [12–15] than that needed for thermoplastic foams, foamed at higher temperatures. In this particular case, thermo-mechanical analysis [16,17] and optical expandometry [18] techniques have been used. In addition, advanced approaches to in-situ examine the foamability of thermoplastics in autoclaves by optical methods have been proposed recently [19]. On the other hand, the use of X-ray radioscopia to in-situ follow the foaming process of polymeric foams is still an emerging topic. Cunningham [20] evaluated the potential of X-ray radiography for the study of polymer foams and composites by film-radiography, showing diverse examples, and our laboratory has recently published a paper in this area, studying the foaming behaviour of a polyurethane system containing nanoclays [21].

X-ray radioscopia has been revealed as a powerful technique to examine the foaming behaviour of aluminium foams. The first successful results were obtained using synchrotron radioscopia in 2001 [22,23]. With this experience, a microfocuss X-ray laboratory facility was built with the objective of analysing the foaming mechanism in these cellular materials [24–30].

Taking into account that there is a need for a better understanding of the foaming mechanisms in polymeric foams, a X-ray imaging system has been built. The low density of polymers and, as a consequence, the low contrast of the X-ray imaging makes the development of this system challenging from the technical point of view. This paper presents the technical requirements, the final design and the optimum operation parameters of this novel system. The method for density determination is explained in detail. In the final part, the outlook for the possible uses of this technique is provided.

2. Experimental techniques

2.1. Hardware description and mode of operation

The new microfocuss X-ray equipment consists basically of two main elements. A closed, air-cooled microfocuss X-ray source from Hamamatsu (Japan) is used to produce the X-rays (focal spot size: 5–20 μm , voltage: 20–100 kV, current: 0–200 μA .) with a maximum output power of 20 W. A flat panel (FP) detector from Hamamatsu (Japan) in

combination with a frame grabber, Dalsa-Coreco, USA, provides the digital X-ray images. The high resolution detector is composed of a matrix of 2240×2344 pixels², with a pixel size of 50 μm , measuring 120×120 mm². Digital output is 12 bits depth resolution with an imaging capacity up to 9 fps at maximum acquisition velocity. Dedicated software from Hamamatsu (HiPic) is used to control the acquisition and storing of images.

The X-rays come from the source through a 150 μm -thick beryllium window forming an X-ray cone beam with an angle of 39° (see Fig. 1). Characteristic spot size is 5 μm for powers below 40% of the maximum level. For higher powers the spot size increases up to 20 μm . Flat panel (FP) detector technology essentially consists of a combination of a deposited scintillator material (CsI, GOS, Se, etc) layer in front of a CMOS detector.

The selection of both the X-ray tube and the detector was done taking into account that polymers are low absorbing materials and, therefore, we need to have sufficient soft X-rays to provide optimum contrast in the final image. In this sense, the source was selected due to its small spot size (related to final spatial resolution) and low minimum X-ray output energy (20 kV). On the other hand, the particular detector selected consisted of a custom-made *direct deposition* of CsI (scintillator material) on the CMOS surface. Direct deposition technology improves the efficiency by collecting in the CMOS detector a higher amount of the light produced in the scintillator, in comparison with other FP technologies in which scintillator is deposited on another substrate and there is a gap between it and the CMOS. This particular type of FP detector is covered by a 1 mm-thick carbon fibre plate, thus reducing the X-ray absorption as much as possible.

Both main elements are settled, one in front of each other, as shown in Fig. 1. In principle, it is possible to position them at any source to detector distance (SD) but, in general, optimum distances are in the range of 0.3 to 1.2 m. In this particular set up, the distance chosen was 600 mm.

The object is located at any position in between the detector and the source. The fact of having a cone X-ray beam allows for object magnification. Magnification factor, M , is a function of the object to source distance, OS , compared to SD :

$$M = \frac{OS}{SD} \quad (1)$$

As a first approach, pixel resolution is the result of dividing the pixel size by the magnification factor. Objects to be examined can, in principle, be of any size. Nevertheless, the maximum size depends on the magnification factor and on the total detector active area (120×120 mm²). Thus, maximum field of view (at $M = 1$) corresponds to the active area and reduces with magnification. Object thickness (in the direction of the X-rays) also influences the image as discussed in the following sections.

2.2. Spatial, temporal and contrast resolution

Magnification, M , presents certain optical limits due to the finite size of both the focal spot, F , and the pixel size, P_s .

Author's personal copy

E. Solórzano et al. / Polymer Testing 32 (2013) 321–329

323

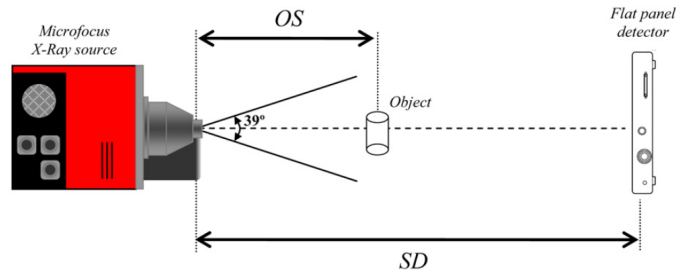


Fig. 1. Schematic diagram of the high resolution X-ray imaging system.

Finite size of the focal spot is responsible for poorly defined edges of the visualized object, presenting a characteristic apparent density gradient in the object edges (penumbra region). Similarly, digitalization by means of a detector with finite pixel size limits the spatial frequency, f . Optical resolution limits for this particular X-ray set-up are determined by the cut-off frequency (f_c in Fig. 2). The cut-off frequency is defined as the value at which the two equations (see Fig. 2) describing the resolution of the source and detector reach the same value, as shown in Fig. 2. This cut-off frequency determines the maximum magnification (M_{max})

It can be appreciated how the cut-off frequency is found for a magnification factor of 21; over this value the blurring effects dominate. This value for M corresponds to a distance OS of 23.8 mm, an effective pixel size of 2.4 microns and a field of view of 5.7 mm. The particularly selected source presents a focus to object distance (FOD), i.e. distance from the target to the nearest point out of the beryllium window of 6.8 mm, which means an object at that magnification needs to be at 17 mm from the external beryllium window. The cut-off frequency represents the optical limits under ideal conditions although real resolution might be limited by other factors.

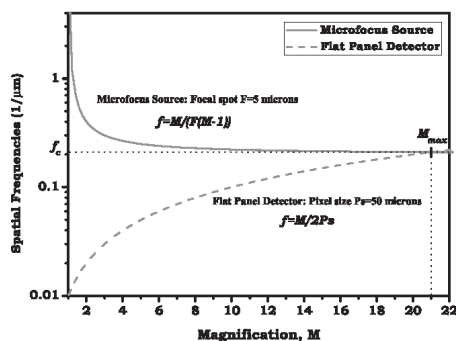


Fig. 2. System cut-off frequency assuming 5 microns spot size of the microfocus source and 50 microns pixel size detector.

In this sense, the ability of any imaging set-up to transfer an object into image is more realistically described by the modulation transfer function (MTF) since MTF considers both spatial and contrast resolution at the same time. Nominally, a value of MTF for any imaging set-up is assigned at 10% of the maximum MTF. The value found for this detector at $M = 1$ using a resolution target mod 07-553 from Nuclear Associates is approximately 10 lp/mm (line pairs per mm), which corresponds to 50 microns, i.e. current pixel size of the detector [31]. This means that the assumption of 50 microns pixel size used for the cut-off frequency calculations in Fig. 2 is valid for this particular set-up.

On the other hand, it must be considered that contrast in the MTF targets is high since high absorbing elements, typically Mo, are used to create the pattern. Therefore, it is expected that in the case of low absorbing materials such as polymers and cellular polymers, the final resolution will be slightly limited by the lower absorption (lower image contrast) of these materials. In this sense, the image quality in terms of contrast depends on the experimental conditions as follows:

- Radiation conditions: To obtain optimum contrast, X-ray energy must be rather low (polymers present higher absorption at lower energies). Nevertheless, as mentioned, the detector response might be insufficient, so in order to compensate for this it is recommended to use high X-ray intensities (photon flux).
- Exposure time: Similar to the increase of X-ray intensities, it is recommended to use higher than usual exposure times in the detector (as an example double exposure time implies double number of photons i.e. double signal since linearity of the used detector is very good). Recommended acquisition time for this kind of materials is in the range 1-3 seconds, thus limiting time resolution that needs to be slightly over these values.
- Type of material and thickness: It is known that the X-ray absorption coefficient, μ , depends on the density and the elements present (Z number) in the irradiated object [32]. Polymers are mainly constituted by light elements: C, O, H and less frequently F, S, P, Cl, etc, thus the presence of light elements makes most of polymers almost X-ray transparent and, in the case of low

density cellular polymers, the effective absorption is much lower as density is reduced. On the other hand, according to the Beer-Lambert equation (see eq. 2) thickness, t , will also play a fundamental role in the image contrast and correlates exponentially with the transmitted intensity.

$$I = I_0 \cdot e^{-\mu t} \quad (2)$$

The image quality can be improved by means of an integration procedure, losing time resolution. This noise-reducing methodology consists of acquiring the same image consecutively (generally up to 16 times). The image integration contributes to reduce the natural noise (random nature) of the detector, thus defining better the areas with a poorer contrast.

Time resolution can be improved by another special procedure called pixel binning. This procedure collects the energy of 2×2 or 4×4 pixels at once and, therefore, the required exposure time for similar pixel intensity is 0.25 or 0.125 times the original value. The handicap of this procedure lies in the reduction of the original spatial resolution according to the pixel binning applied. Integration and binning procedures are frequently used in digital imaging, although not all detection systems allow for them. Our particular system allows for both of them and its maximum acquisition velocity is limited up to 9 fps at 4×4 binning conditions.

2.3. Image correction

Another important aspect is that it is necessary to implement an image correction procedure. Original images inevitably contain unevenness of dark offset, non-uniformity of X-ray intensity distribution, blemish of scintillating material and a few pixels with defects. Therefore, correction of these defects is needed. The correction is carried out by a two-step process that computes the image together with two additional images, called darkfield and flatfield, previously acquired. Correction process is automatically done by the HiPic software used.

The first step of image correction consists in a background subtraction process, thus the darkfield image (also called background, i.e. an image without X-rays at the same exposure time) is subtracted from the one that is being corrected. The background-subtracted intensity, I_{BS} , of each pixel can be calculated as the difference of the intensity in the original image, $I(x,y)$, and the intensity of the darkfield image, $I_d(x,y)$ (eq. 3):

$$I_{BS}(x,y) = I(x,y) - I_d(x,y) \quad (3)$$

Secondly, flatfield correction basically corrects the varying sensitivity within the full detector area as well as spatial non-uniformity of the X-ray source, aiming at obtaining homogeneous intensity in the whole area, i.e. similar intensity in all the pixels. Flatfield image is acquired at similar conditions (kV, μ A, SD distance and exposure time) as the radiography to be corrected. Correction procedure implies the calculation expressed in eq. 4, with $I_f(x,y)$ the intensity of the individual pixels in the flatfield image:

$$I_{FC}(x,y) = \bar{I} \cdot \frac{I_{BS}(x,y)}{I_f(x,y) - I_d(x,y)} \quad (4)$$

where \bar{I} is the average intensity of $I_f(x,y) - I_d(x,y)$ through the whole panel.

Darkfield and flatfield correction images need to be periodically updated to preserve image quality considering that dark offset and sensitivity evolve with time.

3. Density determination

3.1. Calculations based on Beer-Lambert equation

The X-ray attenuation is an exponential function of the mass attenuation coefficient of the material (single element), μ , and its thickness, t . Thus, the transmission is accurately predicted by the Beer-Lambert expression (eq. 2).

Nevertheless, the mass absorption coefficient is not a constant and depends on the incident energy of the beam. Therefore, this expression is only valid for a monochromatic beam. A similar expression predicts the attenuation in the case of incident multispectral X-ray beam (so-called *white beam* or *bremsstrahlung*) by substituting the attenuation coefficient by the effective multispectral one, $\bar{\mu}$. This approximation is valid for a sample with a thickness low enough to assess that a beam hardening effect is not present, so selected energies are not absorbed.

Similarly, if the material is constituted by diverse elements, the absorption coefficient is a weighted average of their individual multispectral absorption coefficients (μ_i) and their concentrations (c_i) (if beam hardening is not predominant):

$$\bar{\mu}_{eff} = \sum_i c_i \cdot \mu_i \quad (5)$$

In the particular case of a cellular material, it is valid to assume the behaviour of a bi-component system, therefore the effective absorption coefficient can be described as

$$\bar{\mu}_{eff} = c_{air} \cdot \bar{\mu}_{air} + (1 - c_{air}) \cdot \bar{\mu}_{solid} \quad (6)$$

Therefore, by using two reference intensities, I_{REF-i} ($i = 1, 2$), in strict correspondence with two known concentrations (i.e. two known reference densities) it is possible to calculate the porosity at any point of the material, $c_{air}(x,y)$, through the projected intensity, $I(x,y)$, in the radiography through eq. 8.

$$I_{REF-i} = I_0 e^{-[c_{REF-i} \mu_{air} + (1 - c_{REF-i}) \mu_{solid}] t} \quad (7)$$

$$c_{air}(x,y) = c_{REF-1} + \frac{\ln \frac{I_{REF-1}(x,y)}{I(x,y)}}{\ln \frac{I_{REF-1}}{I_{REF-2}}} (c_{REF-1} - c_{REF-2}) \quad (8)$$

The two references used for the spatial density determination are typically:

- i) A region in the radiography with no material (air, 100% porosity)

- ii) The average intensity within the area occupied by the bulk material (bulk density of the foam). Alternatively, it is possible to use a solid precursor with the same thickness as the reference intensity value for 0% porosity, and hence calculating the density at any point without measuring the bulk density of the material examined.

Fig. 3 shows a radiograph (left) for an extruded XPS foam with an average density of 32 kg/m^3 . The density profile (right) obtained from the dashed region is also shown in the figure. The density determination was done by using the background and the average grey level in the foam as known references (air and foam density) applying eq. 8. A clear parabolic profile with a thin, denser outer skin of roughly 0.2 mm can be observed. In this thin area, the density reaches values of around 57 kg/m^3 . The obtained curve is rather smooth along the profile.

3.2. Limitations of the method

The precision of the obtained density depends on several factors. The most important limitation is the relationship between the dynamic range of the detector and the precision in the density determination. A 12 bit output expresses, potentially, 4096 intensity levels to be correlated with density. Nevertheless, for a certain object the particular grey scale covering the transmitted intensities of that object is restricted to a reduced grey level range (see Fig. 4-b). In this sense, the number of grey levels covering the density "spectrum" is related to the acquisition parameters (voltage, current and exposure time) that need to be optimized depending on the material characteristics (foam density, polymer type and thickness). Therefore, the contrast associated with a certain material is a competition between the absorption/transmission and the detector response. In particular, the detector response always increases at higher energies/intensities, whereas the transmittance decreases with energy [33]. As a result, the contrast does not monotonically increase with X-ray energy and it is difficult to find

the optimum imaging parameters, in particular the optimum tube voltage, for a specific material and thickness. Based on eq. 2, it is possible to find the optimum kV after choosing a certain transmittance criterion. In our particular case we have chosen $T = I/I_0 = 0.135$, according to that reported by Grodzins [34].

Table 1 shows the optimum monochromatic energy calculated for diverse polymeric materials for $t = 2 \text{ mm}$ of solid material (20 mm of a foam with relative density of 10%) and $T = I/I_0 = 0.135$ from eq. 2. Please note that for a polychromatic tube emission (bremsstrahlung, as in our case) the emitted kV is the maximum energy of the emitted spectrum, kVp. Therefore, in practice the average energy emitted is significantly lower than kVp, and kVp is only a small fraction of the total emitted energy spectrum. From results in Table 1, it can be appreciated how the optimum energies for polymers under the specified conditions are lower than the minimum energies that the tube used in this paper can emit, (20 kV), although, on the other hand, the detector response at such low energies would be insignificant. As a compromise, higher energies had to be used.

An illustrative example of comparative grey scale precision is depicted in Fig. 4 for three PE slab-shaped foamed materials of different thicknesses. The foams have different grey level ranges depending on their thickness (contrast in the images has not been individually optimized and only for the three materials simultaneously, according to the diagonal line in Fig. 4-b). Apart from the average grey level shift, the representative histogram presents distinctly different shape (width, height) for the different materials under similar imaging parameters. Particularly in the example of Fig. 4, the full width at half-maximum (FWHM) representing the different materials is 19.3, 15.5 and 14.1 for thicknesses of 2, 1 and 0.5 mm, respectively.

From these results, we can confirm that not only the acquisition parameters but also the characteristics of the studied sample (thickness, polymer type and/or relative density) influence the imaging results. In general, excessive or too low energies/intensities may cause a reduction in the

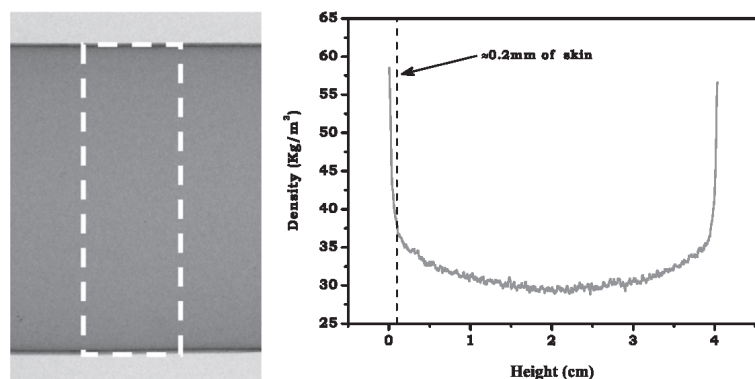


Fig. 3. Radiography (left) and calculated vertical density profile (right) of a foam with average density of 32 kg/m^3 . The white dashed region is the one from which the vertical profile was calculated.

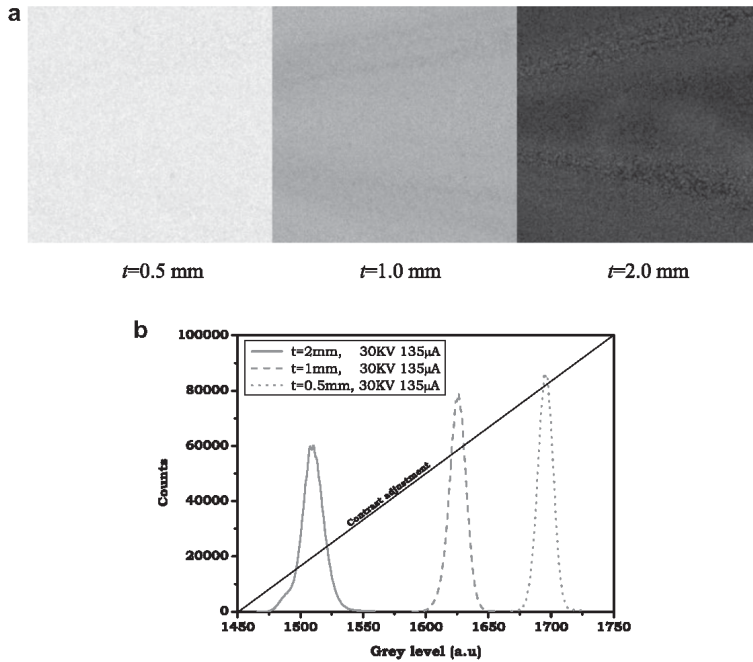


Fig. 4. a) Radiographies of injected polypropylene slabs of 0.5, 1 and 2 mm with 18% porosity, (from left to right), b) Grey level histograms of the regions visualized in Fig. 4a).

number of grey levels contained within the acquired image, later associated with density levels.

Fig. 5 shows the different histograms obtained under different X-ray energies and intensities for a PP sample of 2 mm thickness and 12% porosity. It is possible to observe that the increasing energy/intensity causes a broadening in the characteristic histogram, thus offering better precision (levels contained in the histogram) for the density determination. This observation is, in this particular case, associated with a better detector response versus the competitive transmittance reduction. Therefore, it would be expected that the histogram becomes narrower (contrast resolution reduces) at a certain energy over 40 kV.

Table 1

Calculated optimum energies for different 2 mm-thick solid polymers and aluminium under the $T = 0.135$ criterion.

Material	kV _{opt.} (Exp.) ^a	kV _{opt.} (Th.) ^b
PE (C ₂ H ₄) _n	5.88	5.62
PP (C ₃ H ₆) _n		5.66
PS (C ₈ H ₈) _n	6.00	6.09
PC (C ₁₄ H ₁₄ O ₂) _n		6.98
PMMA (C ₅ H ₈ O ₂) _n	7 aprox	7.28
PI (C ₂₂ H ₁₉ N ₂ O ₅) _n		7.59
PTFE (C ₂ F ₄) _n	9 aprox	11.21
Aluminium (Al)	13.88	18.97

^a μ interpolated from [35].

^b T obtained from [33].

4. Other potential applications of the technique

Probably, one of the best known/expected applications for X-ray nondestructive testing apparatus is the analysis of defects and inhomogeneities in produced materials for quality control [36]. Fig. 6A shows an example of a PE foam produced with evident density inhomogeneities, illustrating this application. Fig. 6B- and C- show other types of defects such as microporosity in the skin of an integral PP foam and gas entrapments in the cellular structure of a rigid PU foam. In general, this type of analysis does not require quantification and the image is simply used for visual inspection, with various objectives. Among others, radiography is particularly useful for the inspection of prototypes [37], both to analyse the sample quality and to elucidate how it developed during processing. X-ray analysis can also be applied to study failed or previously mechanically tested parts with the objective of gaining knowledge about the internal structure around the failed area.

A second possible application based on radiography is the determination of various structural parameters such as density profile, skin thickness [37] or the approximate cell size [21,38]. These types of determination involve the extraction of numerical variables from the image. The variables can be associated simply with dimensional aspects of the image (sizes, i.e. distances) or related to the

Author's personal copy

E. Solórzano et al. / Polymer Testing 32 (2013) 321–329

327

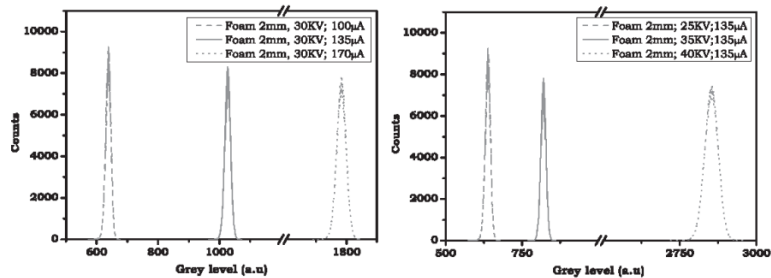


Fig. 5. Characteristic histograms obtained for a sample of thickness 2 mm and 12% porosity, under different intensities (left) and different kV_p (right).

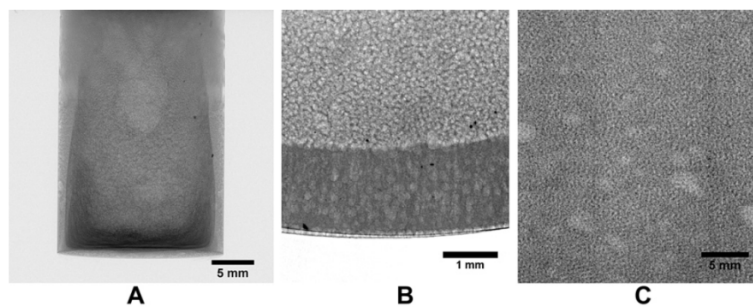


Fig. 6. A- Radiography of an in-homogeneous non-crosslinked PE foam cylinder. B- Microporosity present in the skin of a integral PP foam C- Gas entrapments in a rigid PU foam of density 180 Kg/m³.

intensity value of the radiography (converted to density afterwards). Furthermore, it is possible to combine the pixel value and the pixel position, creating density profiles or 2D maps. Fig. 3 illustrates an example of this application where both density profile and skin thickness were determined. Fig. 6-b, shows a clear example of the possibility of dimensional quantification since from the radiograph it is possible to extract the skin thickness and even the average porosity of that region.

Nevertheless, the X-ray equipment described here offers by far its best application in the particular case of in-situ studies, i.e., monitoring the sample evolution while foaming by means of sequences of radiographs, the so called radioscopy method [39]. With this methodology, it is possible to carry out analysis of the physical mechanisms

taking place during foaming for both thermoplastic and thermoset materials. Therefore, under special setting up conditions (X-ray transparent furnaces and/or moulds) it is possible to on-line monitor the dynamics of the cellular structure and calculate the cell wall rupture rate [40], determine density profiles [24], monitor the rupture speed of a cell wall using ultrahigh speed radioscopy in a synchrotron [4] and/or characterize the macroscopic expansion [24].

Images in Fig. 7 show the expansion and cellular structure evolution of rigid PU foam (BASF, polyol A-component Elastopor[®] H 1501/1, isocyanate B-component IsoPMDI 92140) growing in a paper mould of $\varnothing = 16$ mm. Based on final density of the sample, the density evolution can be accurately calculated. Furthermore, the pore size evolution can be roughly discriminated [21].

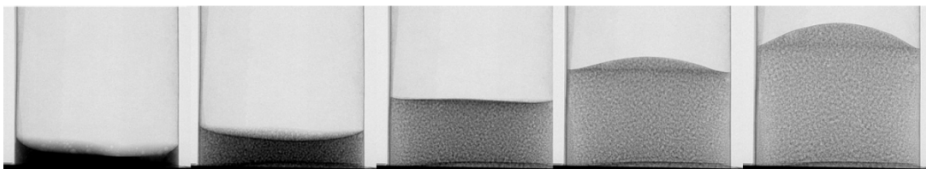


Fig. 7. Series of radiographs obtained during an in-situ radioscopic experiment of a rigid PU foam during its expansion at times 0, 30, 60, 90, 120 seconds.

5. Conclusions

X-ray techniques based on a microfocus/nanofocus X-ray tube in combination with a high resolution and high sensitivity detector offers several advantages for the study of cellular polymers:

- It is a non-destructive technique with a high spatial resolution (down to 1 micron, if a nanofocus tube is used).
- There is no depth of field limitations; the specimen is imaged sharply throughout its entire depth.
- The penetration is high and tuneable through the sample. It is possible to appreciate inner parts.
- It is suited both for ex-situ imaging (already produced foam parts) and in-situ experimentation (during the production process).
- It is also possible to set up small adapted furnaces between the tube and the detector which powers up the system flexibility to monitor any phenomena taking place in the mould.
- The system allows continuous variable magnification.
- In general, sample preparation is simple; a controlled thickness is the main requirement.
- Using appropriate methodologies, it is possible to extract quantitative information from the images (density profiles, size and shape of defects, cell size, local expansion ratio, etc).
- The system is compatible with the possibility of obtaining 3D information of the foam structure –via performing X-ray microtomography– by using a rotating table with the axis suitably adjusted.

Nevertheless, not all the X-ray systems are identical. In particular, microfocus X-ray systems are distinctly different from synchrotron X-ray facilities, although both can be used for the study of polymer foams. In principle, the laboratory systems offer a daily use availability, much less cost per working hour and significantly larger field of view but, in contrast, synchrotron X-rays offers orders of magnitude higher photon flux, parallel beam configuration, higher spatial resolution and the possibility of using tuneable monochromatic X-rays which enables multiple working modes [41].

The specific system presented in this paper has been designed to be used with low X-ray absorbing materials. The high sensibility of the detector which provides better image contrast is one of the critical parameters in the system. The examples and explanations given in the paper show the potential of the method. In addition, the key methodologies that it is necessary to set-up in order to obtain images with high quality and to extract quantitative and precise information have been described in detail.

Acknowledgements

Financial support from the Spanish Ministry of Science and Innovation and FEDER program (MAT2009-14001-C02-01 and MAT 2012-34901), the European Spatial Agency (Project MAP AO-99-075), the European Union (Nancore Project, EC Project Number 214148), PIRTU

contract of S. Pardo-Alonso by Junta de Castile and Leon (EDU/289/2011), FPU contract of J. Pinto (Ref-AP-2008-03603) and Juan de la Cierva contract of E. Solórzano by the Ministry of Economy and Competitiveness (JCI-2011-09775) are gratefully acknowledged.

References

- [1] L. Cartz, *Nondestructive Testing*, ASM International, 1995.
- [2] C. Hellier, *Handbook of Nondestructive Evaluation*, McGraw-Hill, 2003.
- [3] S.A. Wenk, R.C. McMaster, *Choosing NDT: Applications, Costs and Benefits of Nondestructive Testing in Your Quality Assurance Program*, American Society for Nondestructive Testing, 1987.
- [4] A. Rack, F. García Moreno, T. Baumbach, J. Banhart, *Synchrotron-based radiography employing spatio-temporal micro-resolution for studying fast phenomena in liquid metal foams*, *J. Synchrotron. Radiat.* 16 (3) (2009) 432–434.
- [5] S. Youssef, E. Maire, R. Gaertner, *Finite element modelling of the actual structure of cellular materials determined by X-ray tomography*, *Acta Mater.* 53 (3) (2005) 719–730.
- [6] J. Adrien, E. Maire, N. Gimenez, V. Sauvant-Moynet, *Experimental study of the compression behaviour of syntactic foams by in situ X-ray tomography*, *Acta Mater.* 55 (5) (2007) 1667–1679.
- [7] A. Elmoutaouakkil, G. Fuchs, P. Bergounhon, R. Péres, F. Peyrin, *Three-dimensional quantitative analysis of polymer foams from synchrotron radiation X-ray microtomography*, *J. Phys. D Appl. Phys.* 36 (2003) A37.
- [8] M.D. Montminy, A.R. Tannenbaum, C.W. Macosko, *The 3D structure of real polymer foams*, *J. Colloid Interf. Sci.* 280 (1) (2004) 202–211.
- [9] P. Babin, G. Della Valle, R. Dendievel, D. Lourdin, L. Salvo, *X-ray tomography study of the cellular structure of extruded starches and its relations with expansion phenomenon and foam mechanical properties*, *Carbohydr. Polym.* 68 (2) (2007) 329–340.
- [10] S. Roux, F. Hild, P. Viot, D. Bernard, *Three-dimensional image correlation from X-ray computed tomography of solid foam*, *Compos. Part A-Appl. S.* 39 (8) (2008) 1253–1265.
- [11] M. Di Michiel, J.M. Merino, D. Fernandez-Carreiras, T. Buslaps, V. Honkimäki, P. Falus, T. Martins, O. Svensson, *Fast microtomography using high energy synchrotron radiation*, *Rev. Sci. Instrum.* 76 (2005) 043702.
- [12] R.J. Jennings, *J. Cell Plast.* 5 (1969) 159–172.
- [13] R.L. Rowton, *J. Cell Plast.* 16 (1980) 287–292.
- [14] A. Van Thuyne, B.J. Zeegers, *J. Cell Plast.* 14 (1978) 150–160.
- [15] Y. Jianqiu, Z. Jianyaun, W. Dening, H. Chumpu, Y. Shengkang, C. Yiou, C. Yufu, X. Ziqian, S. Jin, W. Yin, *J. Cell Plast.* 26 (1990) 39–49.
- [16] J.I. Velasco, M. Antunes, O. Ayyad, C. Saiz-Arroyo, M.A. Rodríguez-Pérez, F. Hidalgo, J.A. de Saja, *J. Appl. Polym. Sci.* 105 (2007) 1658–1667.
- [17] J.I. Velasco, M. Antunes, O. Ayyad, J.M. López-Cuesta, P. Gaudon, C. Saiz, M.A. Rodríguez-Pérez, J.A. de Saja, *Polymer* 48 (2007) 2098–2108.
- [18] E. Solórzano, M. Antunes, C. Saiz-Arroyo, M.A. Rodríguez-Pérez, J.I. Velasco, J.A. de Saja, *Optical chemistry: a technique to analyze the expansion kinetics of expecially blown thermoplastic foams*, *J. Appl. Polym. Sci.* 125 (2012) 1059–1067.
- [19] Q. Guo, J. Wang, C.B. Park, M. Ohshima, *A microcellular foaming simulation system with a high-pressure drop rate*, *Ind. Eng. Chem. Res.* 45 (18) (2006) 6153–6161.
- [20] T.G. Cunningham, S.C. Graham, *Imaging the internal structure of bulk materials by microfocal radiography*, *Materials and Design* 7 (5) (1986) 223–231.
- [21] S. Pardo-Alonso, E. Solórzano, S. Estravís, M.A. Rodríguez-Pérez, J.A. de Saja, *In-situ evidences of nanoparticle nucleating effect in polyurethane-nanoclay foamed systems*, *Soft Matter* 8 (44) (2012) 11262–11270.
- [22] J. Banhart, H. Stanzick, L. Helfen, T. Baumbach, *Appl. Phys. Lett.* 78 (2001) 1152–1154.
- [23] J. Banhart, H. Stanzick, L. Helfen, T. Baumbach, K. Nijhof, *Real-time X-ray investigation of aluminium foam sandwich production*, *Adv. Eng. Mater.* 3 (2001) 407–411.
- [24] F. García-Moreno, M. Fromme, J. Banhart, *Real-time X-ray radiography on metallic foams using a compact micro-focus source*, *Adv. Eng. Mater.* 6 (2004) 416–420.
- [25] F. García-Moreno, N. Babsacan, J. Banhart, *X-ray radiography of liquid metal foams: influence of heating profile, atmosphere and pressure*, *Colloid Surface A* 263 (1–3) (2005) 290–294.

Author's personal copy

E. Solórzano et al. / Polymer Testing 32 (2013) 321–329

329

- [26] N. Babcsán, F. García-Moreno, J. Banhart, Metal foams - high temperature colloids. Part II: In-situ analysis of metal foams, *Colloid Surface A* 309 (1–3) (2007) 254–263.
- [27] F. García-Moreno, C. Jiménez, M. Mukherjee, P. Holm, J. Weise, J. Banhart, Experiments on metallic foams under gravity and microgravity, *Colloid Surface A* 344 (1–3) (2009) 101–106.
- [28] M. Mukherjee, F. García Moreno, J. Banhart, Defect generation during solidification of aluminium foams, *Scripta Mater.* 63 (2) (2010) 235–238.
- [29] O. Brunke, S. Odenbach, In situ observation and numerical calculations of the evolution of metallic foams, *J. Phys. Condens. Matter.* 18 (2006) 6493.
- [30] A. Myagotin, L. Helfen, T. Baumbach, Coalescence measurements for evolving foams monitored by real-time projection imaging, *Meas. Sci. Technol.* 20 (2009) 055703.
- [31] A. Sisniega, J.J. Vaquero, E. Lage, A. de Carlos, J.L. Villena, M. Abella, I. Vidal, G. Tapis, J.C. Antoranz, M. Desco, Comparative study of two flat-panel X-ray detectors applied to small-animal imaging cone-beam Micro-CT, *IEEE Nuclear Science Symposium Conference Record*, 2008.
- [32] J. Banhart, A. Borbély, K. Dzieciol, F. García-Moreno, I. Manke, N. Kardjilov, A.R. Kaysser-Pyzalla, M. Strobl, W. Treimer, X-ray and neutron imaging - complementary techniques for materials science and engineering, *Int. J. Mater. Res.* 101 (9) (2010) 1069–1079.
- [33] http://henke.lbl.gov/optical_constants/filter2.html, January 2012.
- [34] L. Grodzins, Optimum energies for X-ray transmission tomography of small samples, application of synchrotron radiation to computerized tomography I, *Nucl. Instrum. Methods* 206 (1983) 541–545.
- [35] <http://www.nist.gov/pml/data/xraycoef/index.cfm>.
- [36] D. Mery, D. Filbert, Automated flaw detection in aluminum castings based on the tracking of potential defects in a radioscopic image sequence, *IEEE Transactions on Robotic and automation* 18 (6) (2002) 890–901.
- [37] J. Pinto, S. Pardo, E. Solorzano, M.A. Rodriguez-Perez, M. Dumon, J.A. de Saja, Solid skin characterization of PMMA/MAM foams fabricated by gas dissolution foaming over a range of pressures, *Defect Diffus. Forum* 326–328 (2012) 434–439.
- [38] S. Pardo, S. Estravís, E. Solórzano, M.A. Rodríguez-Pérez, J.A. de Saja, Effect of nanoadditives in rigid polyurethane foam nucleation monitored by X-ray radioscopy, *Proceedings of the SPE Eurotec® Conference*, 2011.
- [39] F. Garcia-Moreno, M. Mukherjee, C. Jiménez, A. Rack, J. Banhart, Metal foaming investigated by X-ray radioscopy, *Metals* 2 (1) (2012) 10–21.
- [40] F. García-Moreno, E. Solórzano, J. Banhart, Kinetics of coalescence in liquid aluminium foams, *Soft Matter* 7 (2001) 9216–9223.
- [41] J. Banhart, *Advanced Tomographic Methods in Materials Research and Engineering*, Oxford University Press, 2008.

REFERENCES

[¹] W. C. Röntgen. On a new kind of ray: A preliminary communication. Würzburg's Physical-Medical Society journal, 1895.

[²] Ralf B. Bergmann, Florian T. Bessler and Walter Bauer , Non-Destructive Testing in the Automotive Supply Industry - Requirements, Trends and Examples Using X-ray CT

[³] Jackson, J.D. (1975). Classical electrodynamics,. John Wiley, New York.

[⁴] www.lightsources.org

[⁵] Nugent, K.A.; Gureyev, T.E.; Cookson, D.F.; Paganin, D.; Barnea, Z. Quantitative phase imaging using hard x rays. Phys. Rev. Lett. 1996, 77, 2961–2964.

[⁶] Bronnikov, A.V. Reconstruction formulas in phase-contrast tomography. Opt. Commun. 1999, 171, 239–244.

[⁷] Gureyev, T.E.; Stevenson, A.W.; Paganin, D.; Mayo, S.C.; Pogany, A.; Gao, D.; Wilkins, S.W. Quantitative methods in phase-contrast X-ray imaging. J. Digit. Imaging 2000, 13, 121–126.

[⁸] Paganin, D.; Mayo, S.C.; Gureyev, T.E.; Miller, P.R.; Wilkins, S.W. Simultaneous phase and amplitude extraction from a single defocused image of a homogeneous object. J. Microsc. 2002, 206, 33–40.

[⁹] De Witte, Y.; Boone, M.; Vlassenbroeck, J.; Dierick, M.; Van Hoorebeke, L. Bronnikov-aided correction for X-ray computed tomography. J. Opt. Soc. Am. A-Opt. Image Sci. Vis. 2009, 26, 890–894.

[¹⁰] Olivo, A.; Speller, R. Experimental validation of a simple model capable of predicting the phase contrast imaging capabilities of any X-ray imaging system. Phys. Med. Biol. 2006, 51, 3015–3030.

[¹¹] Weitkamp, T.; Haas, D.; Wegryzynek, D.; Rack, A. ANKAphase: software for single-distance phase retrieval from inline X-ray phase-contrast radiographs. J. Synchrotron. Radiat. 2011, 18, 617–629.

[¹²] Burvall, A.; Lundstrom, U.; Takman, P.A.C.; Larsson, D.H.; Hertz, H.M. Phase retrieval in X-ray phase-contrast imaging suitable for tomography. Opt. Express 2011, 19, 10359–10376.

[¹³] Paganin, D. and Nugent, K.A. (2001) Non interferometric phase determination. In Advances in imaging and electron physics (ed. P. Hawkens, B. Kazan and T. Mulvey) Academic Press Inc. San Diego.

[¹⁴] Momose, A. (2003). Phase sensitive imaging and phase tomography using X-ray interferometers. Optics Express, 11, 2013.

[¹⁵] S.E.Reichenbach, S.K.Park, R.Narayanswamy, "Characterizing digital image acquisition devices", Optical Engineering, 30, pg 170-177, 1991

-
- [1] www.psi.ch/niag
- [2] B.C. Masschaele, V. Cnudde, M. Dierick, P. Jacobs, L. Van Hoorebeke, J. Vlassenbroeck, Nucl. Instrum. Methods Phys. Res., Sect. A 580 (2007) 266.
- [3] M. Stampanoni, A. Groso, A. Isenegger, G. Mikuljan, Q. Chen, A. Bertrand, S. Henein, R. Betemps, U. Frommherz, P. Bohler, D. Meister, M. Lange, and R. Abela, Trends in synchrotron-based tomographic imaging: the SLS experience, _Developments in X-Ray Tomography V, Proceedings of the Society of Photo-Optical Instrumentation Engineers (Spie)_ 6318, U199-U212 (2006).
- [4] R. Mokso, F. Marone, D. Habertur, J. C. Schittny, G. Mikuljan, A. Isenegger, and M. Stampanoni, Following Dynamic Processes by X-ray Tomographic Microscopy with Sub-second Temporal Resolution, 10th International Conference on X-Ray Microscopy, 1365, 38-41 (2011).
- [1] High Performance Image Control System v.8.3, HiPic users manual by Hamamatsu Photonics Deutschland GmbH
- [2] SCHINDELIN, J., ARGANDA-CARRERAS, I., Erwin Frise, Verena Kaynig, Mark Longair, Tobias Pietzsch, Stephan Preibisch, Curtis Rueden, Stephan Saalfeld, Benjamin Schmid, Jean-Yves Tinevez, Daniel James White, Volker Hartenstein, Kevin Eliceiri, Pavel Tomancak and Albert Cardona (2012) Fiji: an open-source platform for biological-image analysis, *Nature Methods* 9(7) 676-682
- [3] AVIZO FIRE reference guide and user's manual. FEI Visualization Sciences Group.
- [4] Brabant, L., Vlassenbroeck, J., De Witte, Y., Cnudde, V., Boone, M., Dewanckele, J., Van Hoorebeke, L., (2011). Three-dimensional analysis of high-resolution X-ray computed tomography data with Morpho+. *Microscopy and Microanalysis* 17(2) 252-63.
- [5] J. Vlassenbroeck, M. Dierick, B. Masschaele, V. Cnudde, L. Van Hoorebeke, P. Jacobs, Nucl. Instrum. Methods Phys. Res., Sect. A 580 (2007) 442.
- [6] Brun, E., Vicente, J., Topin, F., Ocelli, R. (2008). iMorph : A 3D morphological tool to fully analyse all kind of cellular materials. *CellMet*, Dresden.
- [7] Siewerdsen JH, Jaffray DA. A ghost story: spatio-temporal response characteristics of an indirect-detection flatpanel imager. *Med Phys.* 1999;26(8):1624–1641.
- [8] Siewerdsen JH, Jaffray DA. Cone-beam computed tomography with a flat-panel imager: effects of image lag. *Med Phys.* 1999;26(12):2635–2647.
- [9] McDermott LN, Nijsten SM, Sonke JJ, Partridge M, van Herk M, Mijnheer BJ. Comparison of ghosting effects for three commercial a-Si EPIDs. *Med Phys.* 2006;33(7):2448–2451.
- [10] Pang G, Lee DL, Rowlands JA. Investigation of a direct conversion flat panel imager for portal imaging. *Med Phys.* 2001;28(10):2121–2128.

[¹¹] Zhao W, DeCrescenzo G, Kasap SO, Rowlands JA. Ghosting caused by bulk charge trapping in direct conversion flat-panel detectors using amorphous selenium. *Med Phys.* 2005;32(2):488–500.

[¹²] García-Moreno F, Fromme M, Banhart J. *Adv Eng Mater* 2004;6:416-420.

[¹³] P. Cloetens, M. Pateyron-Salome, J. Y. Buffiere, G. Peix, J. Baruchel, F. Peyrin, and M. Schlenker, "Observation of microstructure and damage in materials by phase sensitive radiography and tomography," *J. Appl. Phys.*81, 5878–5886 (1997)

5. STUDIES ON FOAMING MECHANISMS

5.1. SUMMARY

The purpose of this chapter is to present several scientific papers showing the most relevant results about visualization of cellular structure evolution and investigation of physico-chemical foaming mechanisms (nucleation, growth, stabilization and coalescence) by means of time-resolved X-ray radiography and automated image analysis.

There are four researches included and summarized below which describe the work done to accomplish the design, building and adjustment of proper foaming setups aimed at visualizing the cellular structure during the expansion processes. The included works use the CellMat X-ray imaging system described in chapter 4. They basically change either the setup or the polymeric system of interest in each of the four studies. With respect the foaming mechanisms study, we can mention that the four works increase gradually in technical and scientific complexity since more mechanisms and interactions appear in each of them. Namely, we study the effect of three different types of the nanoparticles (nanoclays, nanosilicas and carbon nanotubes) and the amount of particles used in the three works focused on thermosets reactive foaming. We study the particles interaction with the polymer foaming in the second and third works and then coalescence phenomena only appear in the third research. Finally, the polymer rheology and the processing parameters (temperature) are also investigated, but in this case the selected polymeric system is completely different, i.e. thermoplastics.

In all presented works, quantitative methods based on image analysis procedures were developed to allow valuable data extraction from the radiographic images. The collected information about density, cell size and cell density at every stage of the expansion is then correlated with foaming mechanisms for both thermoset and thermoplastic matrices.

The first work attached to this chapter was published in **Soft Matter, 2012,8, 11262-11270** and is titled **“In-situ Evidences of Nanofillers Nucleating Effect in Polyurethane-Nanoclay Foamed Systems”**. The paper presents the characterization of the foaming process of a rigid PU system containing nanoclays by using X-ray radiography. The main focus of the paper was the analysis of the nanoparticles effect on the nucleation process for this specific system. In order to do that it is necessary to measure cell size evolution with time and this requires specific setups design. The essential requirement for this type of experiment is to promote very few cells in depth (2-3 maximum), even ideally just one, to allow later identification of every cell by

image analysis procedures. Otherwise, superposition of several cells would impede trustworthy quantification of bubbles growth rate and cell wall ruptures. High-resolution X-ray imaging, in combination with a specific setup and a self-developed image analysis procedures, reveals as a suitable method to investigate *in-situ* the effect of nanoclays addition on the foaming mechanisms of rigid polyurethane reactive foaming. This paper explains in detail the methodological approach beginning from the X-ray imaging device, the foaming setup design and optimization, the image acquisition and the procedures used to quantify images. Complementarily experimental data obtained are correlated with its physical meaning proving the nucleation enhancement due to nanoclays addition. This research provides clear scientific evidence that enhanced nucleation (due to nanoclays presence) is the responsible mechanism for the final cell size reduction, previously observed by *ex-situ* techniques for the specific PU system under study. Cell size reduction based on a diminution of coalescence was also a plausible possibility discarded by our findings. In the paper we are able to present results on cell density evolution (number of cells per volume unit) for a first time, calculated using the data of foam density and cell size during the foaming process. This work serves as a fundamental basis and validates this technique and image-based methodology, which is applied later in the following works to analyze systems with a different behaviour. It is also proved that the trends showed in the small samples used in this X-ray experiment are equivalent those showed by larger samples (scalable effect).

The second work “**Time-resolved X-ray imaging of nanofiller-polyurethane reactive foam systems**” was presented in an oral communication in the EUFOAM Conference in Lisbon (2012) and then selected for its publication in **Colloids and Surfaces A: Physicochem. Eng. Aspects 438 (2013) 119-125**. It can be seen as an extension on the previous paper. However, in this case the analysis is more focused on different influence of nanoparticles on the chemical reactions taking place during foaming and the different temporal evolution of the processes. In this case, the effects of clays and two different types of silicas are investigated. These nanofillers present different chemical surface modification that result in different interaction with the polymeric reactants. Therefore changes in the reaction kinetics are observed and investigated mainly through changes in density evolution. Thanks to this investigation it has been possible to obtain evidences on the heterogeneous nucleation behaviour of different nanoparticles on these systems. The results indicate that the addition of nanoclays provides enhanced nucleation and thus higher cell size reduction that either hydrophobic or hydrophilic silicas. Finally, the hydro-phobicity/philicity nature of the silica particles seems to have certain influence on the reaction kinetics inducing, in the case of hydrophobic silicas and clays different density evolution throughout the expansion process.

The third research included in this chapter is entitled **“Effect of carbon nanofillers on flexible polyurethane foaming from a chemical and physical perspective”**. This work is done in collaboration with Dr. M.M Bernal and Dr. R. Verdejo from ICTP-CSIC and it is currently under revision for its publication in RSC Advances. It presents a study on the effects of carbon nanoparticles (CNPs) and their surface treatment on the reactive polyurethane foaming. A flexible PU was selected in this case so as to increase a little bit the scientific goals and detect coalescence events. The study addresses the modification of the cellular structure analyzing the materials from a chemical and physical point of view by three complementary techniques: in-situ infrared spectroscopy, rheological characterization and X-ray radioscopy. There were differences observed in the final cellular structure due to addition of different types of particles: MWCNTs, f-MWCNTs and f-GS. These differences were also clearly visualized during foam expansion and thus polymer rheology and chemical evolution can explain its physical evolution. Namely, it has been observed that rheological behaviour and expansion kinetics of the polyol/CNP dispersions are clearly influenced by the CNPs. The paper also discusses the observed cell nucleation enhancement due to MWCNT and f-GS addition at low contents (0.3% wt.). Furthermore, correlation of in-situ FTIR and SAXS results with X-ray radioscopy imaging of cellular structure evolution permitted to confirm discuss how the the surface nature of the CNPs, hydrophilic or hydrophobic, influences the cellular structure evolution, modifying cell size and even promoting cell ruptures.

The fourth work is titled **“X-ray Radioscopy In-situ Studies in Thermoplastic Polymer Foams”** and published in **Colloids and Surfaces A: Physicochem. Eng. Aspects 438 (2013) 167-173**. In this case the polymeric systems selected for foaming are thermoplastics, i.e. polyethylene and polypropylene. The main reason for these materials choice is the purpose of investigating the effect of temperature and polymer rheology on cell nucleation, growth and coalescence. The work presents results on different polyolefin systems foamed with azodicarbonamide (ADC).

It is necessary to note that polyolefin foaming with the use of CBA may present additional inconvenient to achieve a sufficient contrast for successful quantification in the image. They require the use of foaming moulds holding on relatively high pressures generated and/or homogeneous furnaces to provide heating programs. These two particular features add technical difficulties to the low X-ray absorption of polymers and the reduced cell sizes that may hinder cells identification since many of them are present in depth as mentioned for the reactive foaming processes.

Two different setups have been developed aimed at studying separately nucleation and growth at early stages and cellular structure stabilization, respectively. They

provide the necessary temperature homogeneity allowing visualization through X-ray transparent windows made of very low absorbing materials such as polyimide (PI) film in the case of nucleation configuration or carbon (graphite) and aluminium foils for the ruptures detection experiments. Hence it is possible to obtain high-contrast radiographies of the internal cellular structure during foaming.

- Nucleation and growth dynamics study is performed and discussed thanks to a setup aimed at this specific purpose composed by for cartridge heater providing unidirectional heat source, aluminium frame holding the samples and Kapton covers.
- Cellular structure stabilization is studied thanks to a developed setup consisting in a cylindrical mold with a rectangular cavity containing the sample. Two windows of thick aluminum foils close the cavity allowing transmission of enough X-rays flux. A collar heater encloses the cylindrical mold and a thermocouple is placed close to the pellets in order to control the temperature during the foaming.

The research work shows differences in cell nucleation of the different polypropylene (linear PP and HMS PP) and polyethylene formulations. An analysis of the temperature rate effect on cell nucleation ability is also presented. Finally, an analysis of rupture events dynamics in PP during foaming is reported for the first time.

“*IN-SITU* EVIDENCE OF THE NANOPARTICLE NUCLEATING EFFECT IN POLYURETHANE-NANOCLAY FOAMED SYSTEMS”

Soft Matter

View Online / Journal Homepage
Dynamic Article Links ▶

Cite this: DOI: 10.1039/c2sm25983d

www.rsc.org/softmatter

PAPER

In situ evidence of the nanoparticle nucleating effect in polyurethane–nanoclay foamed systems†

S. Pardo-Alonso,* E. Solórzano, S. Estravís, M. A. Rodríguez-Perez and J. A. de Saja

Received 27th April 2012, Accepted 9th August 2012

DOI: 10.1039/c2sm25983d

This paper presents a comparative study on the nanoadditives (nanoclays) effect during the foaming process of rigid polyurethane (PU) foams. A non-standard technique, high-resolution microfocus X-ray radiography, has been applied for the first time on these materials to study the mechanisms (nucleation and coalescence) occurring during the reactive foaming process. Using this technique in combination with image analysis it has been possible to determine the evolution of density and cell size throughout the whole foaming process. Thus, cell density values have been calculated from the beginning of the expansion and, using the cell density data, it has been possible to demonstrate that nucleation at initial foaming stages strongly dominates over the coalescence mechanism – not observed – in the nanocomposite systems under study. These results confirm the theories assuming that nanoparticles act as heterogeneous nucleation sites for this type of materials, which were not undoubtedly confirmed *via ex situ* studies.

1. Introduction

Cellular nanocomposites are the natural evolution of conventional cellular plastics and are very promising materials. However, although cellular plastics present a wide range of applications in industrial sectors such as aeronautical, automotive, cushioning, packaging, medical and renewable energies,^{1,2} the commercial success of cellular nanocomposites is still scarce. One of the key reasons for this limited success is a lack of knowledge on the underlying mechanisms that are responsible for the final structure and properties of the material. This is, in fact, a limiting factor to achieve optimum cellular structures.

The inclusion of nanofillers (clays, fumed silica, carbon nanotubes – CNTs, carbon nanofibers – CNFs, graphenes, *etc.*) as reinforcement in foamed polymer systems is a hot topic involving significant research activity aiming at understanding the physicochemical mechanisms associated with the polymer–nanofillers interaction that yield improved cellular structures and better final properties.^{3–6} The addition of small amounts of well-dispersed nanoadditives to traditional cellular polymers may result in synergistic effects.⁷ The polymeric matrix is reinforced with particles, and in addition the cellular structure might become strongly modified (reducing cell size, improving cell homogeneity, *etc.*). These effects are due to the fact that chemistry and kinetics are considerably altered in the presence of these

nanofillers.⁸ As a result of these two contributions, new and/or superior final properties are obtained.^{9–12}

Namely, PU foams and their interaction with nanofillers have been widely investigated. These materials are produced by the reactive process of two primary components, polyol and isocyanate, in which the nanoparticles are previously dispersed in one of the components.^{13–15} Specifically, reactive PU foaming is an evolving process in which complex physical and chemical mechanisms occur simultaneously,¹⁶ and the presence of nanofillers has, in these reactive systems, a greater influence than on conventional thermoplastics.^{17–19} From the published literature, which is mostly focused on the improvement of the foam properties, only a few works are concentrated on the underlying foaming mechanisms.⁸ Moreover, these papers focus on the problem from a chemical point of view (foaming reaction kinetics). Therefore, there is little or no knowledge on how these particles influence the foaming mechanisms (cell nucleation and growth, pore coalescence, diffusion coarsening and drainage in the plateau borders). Thus, several questions are still open, such as identifying the main mechanisms responsible for cellular structure modification when nanoparticles are included.

Previous studies in our laboratory found a close dependence between the nanoclay content and the final cell size in rigid PU foams.²⁰ Fig. 1 shows two SEM micrographs of the samples under study in this paper. Both foams were produced from the same PU used in this investigation and have the same density (52 kg m⁻³). It can be observed that the cell size becomes sensibly smaller in the presence of a rather low amount of nanoclays (1 wt%). These results are in accordance with previous works of Widya, Macosko, Lee and Kang showing pore size reduction.^{4,11,21}

Cellular Materials Laboratory, Paseo de Belén, 7 Condensed Matter Physics Department, Science Faculty University of Valladolid, 47011 Valladolid, Spain. E-mail: samuel.pardo.alonso@fmc.uva.es

† Electronic supplementary information (ESI) available. See DOI: 10.1039/c2sm25983d

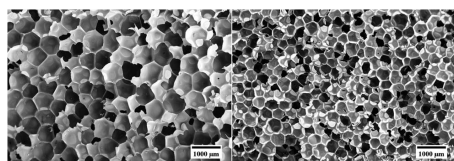


Fig. 1 SEM micrographs of rigid PU foams without nanoclays (density 52 kg m^{-3}) (left) and with 1% of nanoclay (density 52 kg m^{-3}) content (right).

The explanation for this cell size modification is, for most researchers, a result of an enhanced nucleation mechanism produced in the presence of nanoparticles. Thus the improved nucleation efficiency of nanofillers is assigned to the prevalent/active mechanism that justifies the results found for different polymer/nanoparticle systems at very low particle concentrations. Although this nucleating effect is still under investigation,²² it basically consists of the formation of energetically favorable nucleation centers in the particle surroundings, as described by the classical nucleation theory of Colton and Mitsunaga.^{23–25}

On the other hand, it is also known that the presence of nanoparticles may reduce the gas diffusivity, especially if they are platelet-like shaped, and increase the apparent viscosity, providing enhanced stability of the foam system.²⁶ In principle, the modified gas diffusivity through the cell wall films should not affect the cell coarsening mechanism because this is a phenomenon developed only over a long time period^{26,27} whereas typical foaming times for these materials are on the order of seconds/minutes. Nevertheless, a significant influence of nanoparticles on the reduction of coalescence could be expected, as is known from other systems.²⁸

Therefore, it seems that nanoparticles can have an effect on two possible mechanisms: enhanced nucleation or reduced coalescence. In principle, the probability of manifestation of both mechanisms should be the same, at least for those systems not over-stabilized, in which coalescence has been reduced to a minimum. Curiously, researchers have traditionally pointed to the nucleation effect as the most probable acting-mechanism in the presence of nanoparticles, in both kinds of polymeric systems (thermoplastics and thermosets, with no distinction), although actually with no definitive proof.^{4–6,9} In this sense, it must be accepted that it is very difficult to undoubtedly assess such an affirmation only *via ex situ* (after production) examination of the specimens.

It is evident that the *in situ* monitoring of certain processes presents inherent complexities to evaluate a foam state in intermediate stages. In particular, the PU reactive process integrates simultaneously polymerization and foaming that cannot be stopped/frozen. Therefore, *in situ* techniques are the only method to observe the mechanisms occurring during the reactive foaming process of the polyol and the isocyanate, *i.e.* the cellular structure evolution, without any disturbance. In principle, X-ray radiography seems to be the ideal technique providing the desired imaging quality (spatial/time/contrast resolution, field of depth, *etc.*) to study the evolving material²⁹ and apart from cell visualization it offers the possibility of density determination.^{30,31}

Other alternatives to this method are optical microscopy³² or transmitted and/or diffusive light scattering,^{33–35} both satisfactorily used in the field of aqueous foams. Nevertheless optical microscopy does not provide satisfactory imaging for these polymers in either transmitted or direct light mode, essentially due to the varying optical properties that the mixture suffers during the foaming process. Furthermore the depth of field is constrained for the typical high magnification needed. Light scattering provides a quantitative measure of the average cell size, although it is a technique mainly considered for standing foams, and it can be hardly used in the particular case of a very quickly evolving material since the movements in the structure might be perceived as artifact ruptures.

Summing up, the purpose of this work is, on the one hand, to provide real-time monitoring of a rigid PU foaming system by X-ray radiography, which permits a novel insight within the study of foaming mechanisms. On the other hand, the paper is focused on obtaining quantitative experimental data of macroscopic density and pore size evolution during the foaming process, collecting for the first time information of all the stages of the dynamic process of foam polymerization/solidification (rigid PU). Based on the obtained results, this research will try to provide scientific quantitative evidence of whether in the presence of nanofillers the number of nucleation sites increases or the number of cell ruptures (coalescence) is reduced, considering also the possibility that the final structure in the materials under study could be a combination of enhanced nucleation and reduced coalescence.

2. Experimental method

2.1. X-ray radiography setup

X-ray radiography is a technique in which a series of radiographies are acquired over a period of time. This *in situ* technique has been demonstrated to be a suitable choice to investigate the cellular structure evolution during the foaming process both for polymeric and metallic foams.^{30,31,36,37} Fig. 2 shows a sketch of the setup developed and built to perform the X-ray radiography experiments in polymer foams. A microfocus X-ray source and high-resolution detector are the basic elements of the system. The fundamentals of the technique are based on the interaction between radiation and matter, *i.e.* the transmitted radiation is the information captured by a detector as an image (radiography).

In this particular setup an X-ray microfocus tube from Hamamatsu is used to produce the X-rays (spot size: 5–20 μm , voltage: 20–100 kV, current: 0–200 μA) with a maximum output

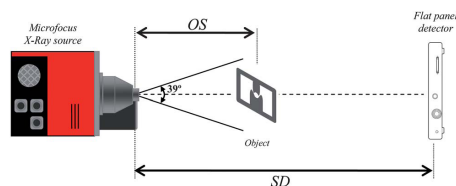


Fig. 2 Schematic view of the X-ray radiography system including the foaming frame for observation placed between the source and the detector.

power of 20 W. In front of the X-ray source, acting as a screen, a high-resolution flat panel detector (12 bits, area 120×120 mm, 2240×2344 pixels, effective pixel size: $100 \mu\text{m}$) is positioned. It is important to remark that both the tube and the detector have been selected aiming to provide an optimum contrast in polymers, even though they are low X-ray absorbing materials.

This customized setup also allows magnification of the radiated object. Conventional magnification, M (see eqn (1)), used for *in situ* studies is in the range 2–10, *i.e.* pixel resolution in the range 25–5 microns. In this presented experiment a source–detector (SD) distance of 580 mm and an object–source (OS) distance of 80 mm were established, yielding a 7.25-fold magnification with a pixel size of approximately 14 microns, by using pixel binning 2×2 .

$$M = \frac{SD}{OS} \quad (1)$$

2.2. Materials

2.2.1. Description. Commercial bi-component rigid PU formulation from BASF was used. The polyol component, Elastopor® H 1501/1 (1.07 g cm^{-3}), is a mixture of polyols, catalysts, stabilizers and a blowing agent (water in this case). The isocyanate, IsoPMDI 92140 (1.23 g cm^{-3}), is a diphenylmethane diisocyanate. The main characteristic for this choice against other existing possibilities was the low viscosity values (650 mPa s for the polyol and 300 mPa s for the isocyanate), which makes the mixing process easier to produce the urethane groups and facilitates nanoparticles dispersion. Component proportions were set at 100/160 for the polyol and isocyanate according to manufacturer's specifications. The density of foamed PU is 52 kg m^{-3} and remains unchanged for the nanoclays/PU-produced samples under investigation.

Cloisite® 30B (Southern Clay Products) was the nanofiller selected to be dispersed in the PU formulation. It is a natural montmorillonite (1.96 g cm^{-3}) organically modified with a quaternary ammonium salt. Different proportions of nanoclay contents were dispersed in the polyol (0.5, 1, 3 and 5 wt%), apart from the neat PU, with 0% nanoclays. Nanoclays are relatively inexpensive, commercially available and exhibit layered morphology with a high aspect ratio and large specific surface areas.^{38,39}

The cream time (the interval between when the two components are mixed in their liquid stage and the prompt rising stage) of the mixed polyol–isocyanate system is approximately 45 seconds. It is important to remark that under our particular experimental conditions the cream time needs to be extended to the maximum (see reasons in the next section). Therefore, the reactants were cooled down to $5 \text{ }^\circ\text{C}$ during 24 hours prior foaming. This procedure reduces the reactivity of the system and delays for a few seconds the beginning of the foaming process, which is crucial for our purpose.

2.2.2. PU/nanoclays preparation. An overhead stirrer EUROSTAR Power control-visc P1 mounting a 50 mm diameter 4-bladed propeller stirrer from IKA was used to disperse/exfoliate the nanoparticles (clays) in the polyol inducing low shear mixing at 200 rpm for 120 seconds. This method offers a proper

dispersion and exfoliation of the nanoclays in the polyol due to the organically modified clays and has been checked with SAXD.²⁰ These blends and the isocyanate component were kept at $5 \text{ }^\circ\text{C}$ in order to extend the cream time as explained in the previous section. Then the mentioned stirrer, mounting a 50 mm diameter lenart-disc from Vollrath™, was used at 1200 rpm for 20 s for the final mixing of the two components (polyol containing clays and isocyanate) promoting the foaming/curing reaction. The moment of initial mixing will be considered in the results section as the zero instant. The span time in between the starting of the mixing and the image (radiography) acquisition was measured with a chronometer. Therefore it is possible to establish image–time correlation with an error of approximately 1 s. This typical span time is around 40 seconds.

2.3. X-ray monitoring

The possibility of obtaining an automatic recognition of nucleated pores throughout the foaming process requires very special foaming conditions. Particularly for this purpose examination of the PU foaming process *via* X-ray imaging was carried out in a very thin mold. Fig. 3 shows the drawing of the 0.6 mm thick mold in which a small droplet of the mixed iso-component and polyol-component was carefully placed with a syringe just after the mixing process. Two thin plastic films (25 microns of PP) were used as covers for the PU to foam inside the 0.6 mm-thick cavity of 10 mm diameter. The acquisition process is focused on the central 10 mm diameter circle where only a few cells in the depth direction are present, allowing proper imaging. Tests with thicker molds were performed but they did not reach satisfactory results since too many pores were present in depth, thus precluding quantification by image analysis. Therefore, for our particular purpose it is indispensable to achieve very few cells in depth (2–3 maximum), even ideally just one, so that a reliable identification of every pore is accessible by image analysis. Otherwise, cell layers would have superposed and clear visualization would be impeded. Two lateral expansion cavities facilitate the foam evacuation out of the main circular cavity, providing in the central cavity an area of visualization large enough for further reliable image analysis without thickness modification.

The foaming process in such a constrained volume may lead to uncertainty in the representativeness of the experiments carried

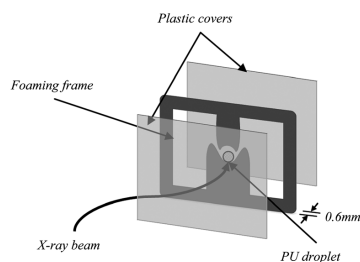


Fig. 3 Sketch of the mold system used for monitoring the foaming process of rigid PU.

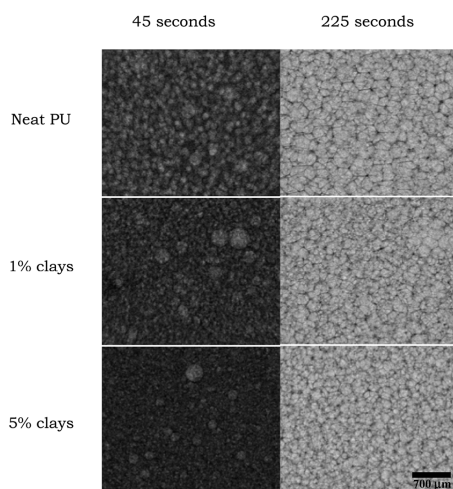


Fig. 4 Comparative sequence of acquired radiographies of neat PU, 1% nanoclay/PU and 5% nanoclay/PU at 45 and 225 seconds reacting time.

out. A detailed discussion on the relationship between the results observed in this setup in comparison with the *ex situ* results for the same foams will be provided in Section 3.4 (scaling-up).

Imaging parameters needed to be carefully selected for our particular setup. A tube voltage below 35 kV and current intensities ranging from 120 to 140 μA were used as optimum measures. Such low energies can only provide a sufficient signal in high sensitivity detectors like the one used for these experiments. The fast foaming behavior at the initial stages of the two reactants mixture after the cream time forced the selection of an exposure time of 700 ms in order to obtain motionless and sharp images. A total of 500 frames were acquired to monitor approximately 6 minutes of the foaming process, which proved to be sufficient for reliable quantification of foaming evolution. Fig. 4 shows selected examples of the radiographies taken during the foaming process.

2.4. Image analysis

Once the radiography sequence has been acquired, it is necessary to compute the images in order to obtain numerical results. Image analysis-based techniques provide powerful methodologies to study the collected radiographies and extract quantitative data from the original gray scale images. Fig. 5 shows the workflow diagram used to obtain the final values. Dedicated software programmed under FIJI (ImageJ), free distribution image analysis software based on Java, was used. This analysis was applied to all the acquired radiosopic images providing values of density and cell size throughout the process.

2.4.1. Density analysis. Density evolution can be calculated according to Beer–Lambert’s attenuation law (see eqn (2)), which relates the transmitted intensity collected in the detector, $I(x,y)$,

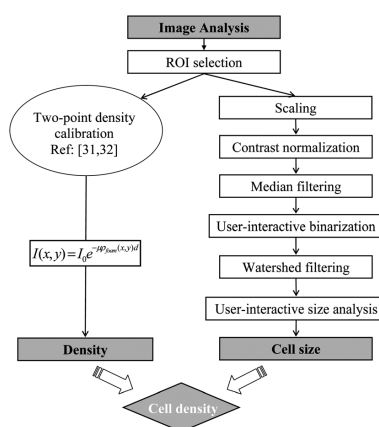


Fig. 5 Workflow of the developed image analysis procedure for density and cell size computed calculation.

with the density of the material, ρ . In this equation μ and d are, respectively, the attenuation coefficient and the thickness while I_0 is the original intensity from the source.

$$I(x,y) = I_0 e^{-\mu \rho_{foam}(x,y)d} \quad (2)$$

Thus density evolution throughout the entire foaming process can be obtained by applying appropriate calibration with known density values (air and final droplet-foam density). Further details on the calibration method are reported elsewhere.³¹ Several foaming tests were carried out leading to an average density evolution representative curve for each nanoclay-content (see Fig. 6).

2.4.2. Cell size analysis. From the region of interest (ROI) selected images were scaled, *i.e.* the distance in pixels converted into real distance values, and contrast was enhanced. A median filter was used to homogenize the grey-level of the images; it is an edge-preserving filter that does not involve image blurring. Subsequently, a grey-level threshold value was selected to binarize the image (convert gray scale to a black and white image) for ten representative images of the whole process. As the foaming process is quicker at the beginning more images in the initial 100 seconds were used. After this manual step, a programmed function uses a logarithmic fit, based on the ten selected thresholds, to apply an automated threshold to the full image sequence. Then a watershed-based algorithm is applied on the binarized images in order to separate every single pore. Size-selective analysis for pore diameter removed pores larger and smaller than a certain criterion. This criterion was defined by the user by means of visual comparison; thus manual minimum and maximum size limits were applied for the ten reference images. The objective of such size discrimination was to remove from the analysis those very small pores having as a source the remaining noise in the image (individual pixels), and the largest pores are a result of incorrect watershed shading or gas entrapments due to

turbulent mixing (visualized as bigger rounded pores, Fig. 4). Similar to what was done previously, two logarithmic fits for the full image sequence were applied separately both for minimum and maximum pore size limits, which enabled selective pore diameter analysis throughout the full foaming process. To sum up, binarization threshold, maximum size and minimum size limits were applied to each individual image by dedicated software based on FIJI (ImageJ) platform after user inputs in the selected ten images.

3. Results and discussion

3.1. Density evolution

Calculation of the density evolution, based on the results of image analysis applied to the X-ray radiography sequences, allowed us to monitor the mesoscopic density evolution of the reactive PU foaming process in our region of analysis. Fig. 6 shows the comparative study of all the investigated blends (neat PU, 0.5%, 1%, 3% and 5% PU/nanoclays). The difference between the pure blend and those with nanoclays is clearly appreciated, as well as the differences among different nanoclay contents. In particular, it seems that nanoclays addition slightly slows down the foaming behavior, in terms of density evolution. The reasons behind this modification could be the interaction between the modified nanoclays surface and the polyol, thus reducing the reactivity with isocyanate.⁴⁰ The small differences in density for PU/nanoclay systems remain at the end of the process, with values slightly higher than the value for neat PU. The values for the final relative density (ratio between foam and solid densities) are approximately 0.15 while these systems would have reached 0.05 under conventional foaming conditions (larger material amount, not a foaming droplet). This aspect will be discussed in detail in Section 3.4.

3.2. Cell size evolution

In situ obtained values for cell size evolution are shown in Fig. 7. The comparison between the different nanoclay content and the neat PU formulation is plotted for the complete foaming process.

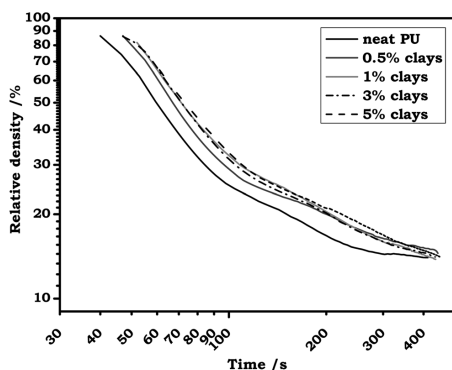


Fig. 6 Relative density evolution curves obtained by two point density calibration image analysis.

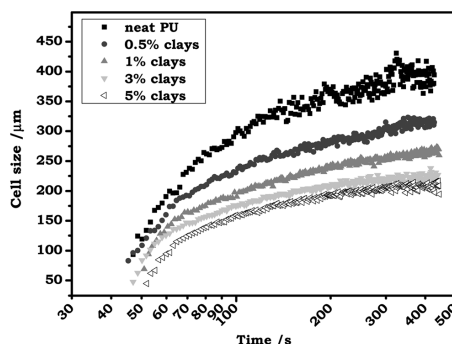


Fig. 7 Mean cell size evolution during PU foaming.

In the analysis, the large round bubbles observed in Fig. 4 (gas entrappings due to turbulent mixing) have been removed, thanks to size thresholding methodology, as already explained. It is evident that pore size remains smaller during the whole process for the nanocomposite PU than for the neat PU evolving foam. Pore size is progressively smaller when a larger amount of nanoclays is present. The frame-by-frame visual observation permitted us to determine the absence of bubble ruptures in both materials throughout the whole process. Therefore this preliminary qualitative observation seems to indicate that nanoclay-addition preferentially influences the nucleation and does not substantially affect the coalescence of bubbles.

Fig. 4 shows the comparative frame sequences of different PU/nanoclay blends zoomed, with and without nanoclays. It can be appreciated how different is the cellular structure in the different materials and, in particular, the average cell size, which could also have been roughly evaluated by manual methods. Clearly, neat PU cellular structures show larger and fewer cells in comparison with nanocomposite PU foam as expected from previous commented results. For instance, the higher the nanoclay content the smaller the cell size at exactly the same reaction time (Fig. 7). These curves present the same trend, nevertheless the pore size during the whole foaming process is different and the differences are especially sensible at the end of the process. As an example a reduction from 400 μm to 210 μm (reduction factor of 1.90) can be found in these *in situ* results for the 5% nanoclay PU in comparison with neat PU.

From the plots in Fig. 7, it is possible to extrapolate the time reaching a zero value for the pore size and therefore to determine the consistency of the experiments with the cream time and its modification due to the presence of nanoclays. Nevertheless the experimental constraints at the beginning make it almost impossible to extrapolate the behavior to earlier times since the very first stages of the process were missed (the mentioned span of 40 s elapses from the beginning of the mixing process to the first acquired radiography). Furthermore, contrast resolution and magnification at the very first images could be insufficient to carry out a reliable analysis on this aspect.

Lastly, it is necessary to comment that this procedure presents certain limits in terms of the accuracy of the measured pore size.

Absolute and relative errors of the obtained values depend on diverse factors associated with the image analysis procedure for cell size determination and the image quality. Part of this uncertainty could be expressed as an error bar linked to the standard deviation of the average pore size measured. Nevertheless the standard deviation does not provide much information about the absolute and/or relative error of the procedure, which is more associated to the intrinsic pore size dispersion, of course in combination with the error of the selected procedure of analysis. In principle the finest achievable results could be associated with a pore monolayer in which cell size determination would be ideal. The liquid fraction and cell size may also account for the error in the method. In our particular case, it is difficult to associate clear absolute and relative errors to the method employed. Nevertheless, based on the results shown in Section 3.4 (a comparison with *ex situ* measurements) and variations on the threshold criterion (peer-user analysis) we have estimated an absolute error of 7% for the pore size determination and a relative error of 4% (*i.e.* for the comparison among measurements). It may seem that errors associated with this type of analysis are high, but, as an example, they are not much higher in comparison with automated image analysis carried out on micrographs obtained by SEM. Moreover, considering the method's difficulty and/or the relevance of these new results it can be said that it is possible to identify differences in pore size for the different materials analyzed.

3.3. Cell density evolution

Cell density, N_v , is defined as the number of cells per unit of volume of the solid material and it is typically expressed in cells per cm^3 . Different equations give approximations for its quantification but the most admitted one calculates the value from the mean cell diameter (ϕ) and the macroscopic density ρ_{foam} .⁴¹

$$N_v = \frac{6}{\pi\phi^3} \left(\frac{\rho_{\text{solid}}}{\rho_{\text{foam}}} - 1 \right) \quad (3)$$

Based on this equation Fig. 8 shows the results for the curves of cell density evolution calculated by using both the experimentally obtained density and cell size evolution data. The

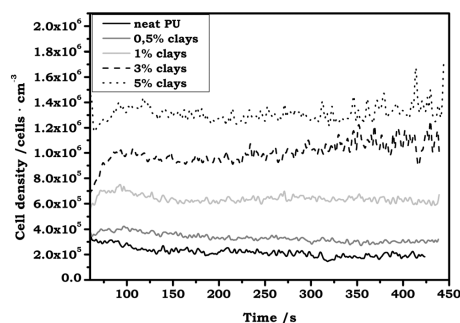


Fig. 8 Cell density evolution during the PU foaming process for neat PU and 0.5%, 1%, 3% and 5% content nanoclays PU.

results show that addition of nanoclays acts to increase the number of nucleation sites although nucleation itself was produced at earlier stages and could not be monitored during these experiments (there is no experimental evidence on significant nuclei increase in the monitored stage). The results indicate that cell density increases with the content of nanoclays, a fact already pointed by different researchers.^{22,23} Moreover, it can also be observed that calculated cell density is constant during the whole process which confirms the fact that pore coalescence is negligible, at least during the post-nucleation stage monitored in this work. Therefore, Fig. 8 experimentally confirms the prevalence of nucleation in the dynamic competition between this mechanism and the coalescence. In principle coalescence should be occurring during the whole foaming process but was not observed and this is the primary reason for determining a nearly constant value of cell density *versus* time, otherwise the cellular degeneration mechanism of coalescence would have produced a progressive reduction of the number of cells, particularly at lower densities when the cell walls are thinner.⁴² At this point, it is important to mention that cell stability in PU systems is generally adjusted by surfactant additions. In the absence of a surfactant, a PU foaming system will normally experience catastrophic coalescence, whereas adequate amounts of surfactant yield stable and cell-size controlled foams. Therefore, it is probable that the particular PU studied system is overstabilized by a surfactant and the presence of clays only yields an enhanced nucleation. Nevertheless, in other systems such as open cell flexible PU, in which the surfactant content is within the limits of stability (low enough to promote cell opening), it is expected that nanoclays will have a certain influence, even more if the neat system presents certain coalescence.⁴³

According to classical nucleation theory shown in eqn (4), the concentration of nanofillers (C_1 , concentration of heterogeneous nucleation sites) directly influences the final concentration of nucleated sites (N_1), assumed to be the final number of generated cells just in the case of no existence of any cell degeneration mechanism. In this equation f_1 is the frequency factor of gas molecules joining the nucleus and ΔG_{crit} the free energy of critical nucleus formation that is similar to the one in homogeneous systems but corrected by a factor depending on the gas-polymer/particle interfacial contact angle. Therefore, heterogeneous nucleation in the presence of nanoclays is expected to have a proportional influence on the concentration of clay nanoparticles (number of induced nucleating centers).

$$N_1 = C_1 f_1 \exp\left(-\frac{\Delta G_{\text{crit}}}{k_B T}\right) \quad (4)$$

Nevertheless, Fig. 9 shows that the total number of pores created is not increased in the same proportion as nanoclay concentration. Moreover, it is possible to calculate the nucleating efficiency, E , (see eqn (5) and (6)) *versus* the nanoparticle content, the results of which are also shown in Fig. 9. This efficiency is calculated in eqn (6) by dividing the experimental cell density by the expected total number of nanoparticles, calculated according to eqn (5), in which w is the weight fraction, ρ_{filler} and ρ_{poly} are the true densities of nanoclays and the polymer blend and V_{filler} is the volume of the individual particle (platelets of $6 \mu\text{m} \times 6 \mu\text{m}$ surface with 1.48 nm thickness).^{44,45} Calculated efficiency (E)

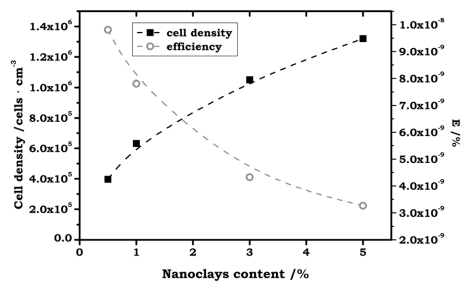


Fig. 9 Efficiency of nanoclay addition on nucleating site creation.

ranges from 3×10^{-9} to 1×10^{-8} %, which is consistent with results from other authors for this particular type of particles on reactive foaming systems.^{9,46} The nucleating efficiency is reported to be conditioned by the shape of the fillers and their compatibility (wettability) with the polymer (contact angle modeled within ΔG_{air}) and is different for different filler types as has already been reported by Cao and Lee.⁹

$$N_{\text{th}} = \frac{w}{\rho_{\text{filler}}} \frac{\rho_{\text{polymer}}}{V_{\text{filler}}} \quad (5)$$

$$E = \frac{N_{\text{v}}}{N_{\text{th}}} \times 100 \quad (6)$$

The results in Fig. 9 indicate that the efficiency tends to decrease when the concentration of particles increases. This fact can be understood considering the presence of un-exfoliated nanoclays stacks, which un-exfoliated fraction tends to increase with the nanoclay content, i.e. the higher wt% of nanoclays the harder is achieving an optimum dispersion and/or exfoliation. The difficulty of dispersing/exfoliating a higher amount of nanoparticles in a polymer matrix is a well-known issue.⁴⁷ Particles are expected to stabilize the polymer foam and therefore reduce coalescence,⁴⁸ even allowing foaming of some polymers which are not possible to foam without fillers addition. Nevertheless, in the material under study neither interfacial (polymer-air) adsorption of clays (observed by high resolution SEM), nor any form of cell degeneration is observed.

3.4. Relationships between radioscopy experiments and macroscopic foams

The results for density in Section 3.1 showed a 3 times higher density for the droplet material foamed in the designed model system in comparison with the typical densities obtained in foamed material with larger dimensions. Nevertheless we will demonstrate in this section that the representativeness of the results is the same even under modified foaming conditions, and this is basically because there is a constant scale factor for the studied variables, density and cell size.

From the results of density, a sensible difference in the pore size observed in this model foaming system is also expected. Fig. 10 shows the comparative pore size measured in the low-volume monitoring system (0.6 mm thick and 10 mm diameter, 0.5 cm³ approximately) and the same material foamed in a

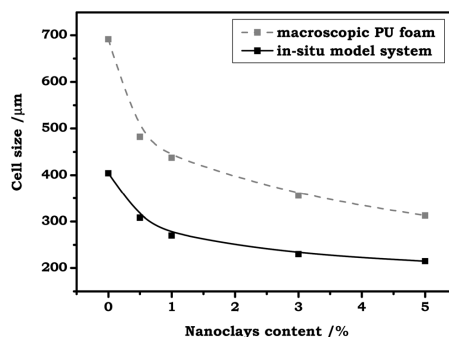


Fig. 10 Comparative cell size for the different nanoclay content PU foams foamed in the model system (0.05 cm³) and larger containers (350 cm³).

350 cm³ container (average cell size obtained by *ex situ* conventional techniques, SEM and 3D tomography analysis). These results confirm the expected cell size difference for both systems but also confirm the existence of a constant scale factor for the pore size, independent of the nanoclay content. The average cell size ratio for both foaming volumes is 1.58 with a standard deviation of 0.08. It is important to mention that the cubic value of this ratio is very near to 3, the density scale factor, which confirms that these findings are correct.

It is important to point out that PU reaction itself is exothermic, and therefore is temperature and mass dependent (heat transfer). The explanation for the lower expansion factor reached in the low-volume model system is a constraining effect of higher surface to volume ratios and a much reduced temperature increase achieved in such a small volume, with almost null thermal mass, thus not reaching typical temperatures produced by reactive foaming in the inner region of big parts (65–160 °C).^{49,50} Subsequently, the lower temperature of the blowing agent may reduce its effective volume and thus the macroscopic expansion factor.

From the obtained scale factor for density and cell size we can conclude that the cell density maintains also a proportionality factor independent of the nanoclay content. The quantitative difference in the absolute number of cells per unit volume (a higher cell density in the model system) is an effect of the higher macroscopic density and smaller pores as a result of not having foamed the same system to 100% of its potential.

4. Conclusions

X-ray radioscopy offers a novel insight into polymer foams especially when studying foaming evolving processes. A valid methodology for *in situ* visualization of PU foaming processes by means of X-ray radioscopy has been established, consisting of the development of a foaming model system of reduced thickness, use of low kV and rather high μA parameters in combination with a high sensitivity detector which enables the possibility of acquiring high spatial/temporal resolution radio-scopic images for low absorbing materials such as polymers.

Furthermore an image-based quantification methodology has been successfully applied enabling the possibility of determining *in situ* cell size and density with sufficient precision, which implies the possibility of calculating cell density throughout the process. It is remarkable that *in situ* information on the cell structure of polymer foams is not accessible by means of conventional *ex situ* techniques such as SEM, X-ray tomography or density determination.

The analyzed comparative foaming behavior of PU systems with properly dispersed nanoclays has revealed that density evolution is not significantly influenced by the presence of nanoclays, although there is an important decrease in the cell size influenced by the presence of nanoclays throughout the whole process. Cell size is almost reduced by half when neat PU is mixed with 5% nanoclays. The higher density of nucleation sites acting as pore formation centers seems to be the main underlying mechanism occurring from the very early stages of the foaming process. There is no visual evidence of cell degeneration, namely pore coalescence, nor coarsening, in any of the studied systems (including the neat PU). Nevertheless extrapolation of the presented results observed in a confined droplet of PU is carefully done taking into consideration the structure (density, cell size and cell density) of simultaneously produced larger foam at the final solidified stage. Furthermore, the results from automated image analysis confirm the absence of cell degeneration since calculation of cell density, derived from cell size and density, remains constant in the analyzed time interval. Therefore novel scientific quantitative information provided in this paper demonstrates that enhanced nucleation is the predominant mechanism over the other plausible reason: coalescence reduction, which caused the observed decrease in the final cell size and higher cell densities.

The effect of nanoclays – or any other nanoparticle – on the cell rupture mechanism in other systems that are prone to coalescence (non-crosslinked thermoplastics, flexible PU, etc.) seems to be also interesting to study. In these systems a double contribution (enhanced nucleation and reduced coalescence) is expected. From this point of view the evidence presented in this paper on the absence of coalescence is applicable only for the particular formulation analyzed.

Acknowledgements

Financial support from the Spanish Ministry of Science and Innovation and FEDER (MAT2009-14001-C02-01), the European Spatial Agency (Project MAP AO-99-075), European Commission (FP7 program, EC project Nancore number 214148), PIRTU contract of S. Pardo-Alonso by Junta of Castile and Leon (EDU/289/2011) and cofinanced by the European Social Fund and Juan de la Cierva contract of E. Solórzano by the Ministry of Economy and Competitiveness (JCI-2011-09775) are gratefully acknowledged. Luis Vela from BASF Company is also acknowledged for supplying the materials used in this research.

References

- 1 L. J. Gibson and M. F. Ashby, in *Cellular Solids: Structure and Properties*, Pergamon Press, Oxford, 2nd edn, 1988.
- 2 V. Kumar, *Prog. Rubber Plast. Technol.*, 1993, 9, 54–70.

- 3 C. C. Ibeh and M. Bubacz, *J. Cell. Plast.*, 2008, 44, 493–514.
- 4 X. Cao, L. J. Lee, T. Widya and C. Macosko, *Polymer*, 2005, 46, 775–783.
- 5 C. Zeng, X. Han, L. J. Lee, K. W. Koelling and D. L. Tomasko, *Adv. Mater.*, 2003, 15, 1743–1747.
- 6 S. C. Tjong, *Mater. Sci. Eng., R*, 2006, 53, 73–197.
- 7 C. Saiz-Arroyo, J. Escudero, M. A. Rodríguez-Pérez and J. A. de Saja, *Cell. Polym.*, 2011, 30, 63–78.
- 8 M. M. Bernal, M. A. López-Manchado and R. Verdejo, *Macromol. Chem. Phys.*, 2011, 212, 971–979.
- 9 L. J. Lee, *et al.*, *Compos. Sci. Technol.*, 2005, 65, 2344–2363.
- 10 I. Javni, *J. Cell. Plast.*, 2002, 38, 229–239.
- 11 T. Widya and C. W. Macosko, *J. Macromol. Sci., Part B: Phys.*, 2005, 44, 897–908.
- 12 M. C. Saha, Md. E. Kabir and S. Jeelani, *Mater. Sci. Eng., A*, 2008, 479, 213–222.
- 13 P. Mondal and D. V. Khakhar, *J. Appl. Polym. Sci.*, 2007, 103, 2802–2809.
- 14 C. P. Park, in *Polymeric Foams and Foam Technology*, ed. D. Klemmner and V. Sendjarevic, Hanser Publishers, Munich, 2nd edn, 2004, ch. 8.
- 15 S. T. Lee and N. S. Ramesh, in *Polymeric Foams: Mechanism and Materials, Polymeric Foams Series*, CRC Press, USA, 2004.
- 16 D. Eaves, in *Handbook of Polymeric Foams*, Rapra Technology, UK, 2004.
- 17 C. H. Dan, M. H. Lee, Y. D. Kim, B. H. Min and J. H. Kim, *Polymer*, 2006, 47, 6718–6730.
- 18 A. Nourbakhsh and A. Ashori, *J. Appl. Polym. Sci.*, 2009, 112, 1386–1390.
- 19 F. Chavarría and D. R. Paul, *Polymer*, 2006, 47, 7760–7773.
- 20 S. Estravís, M. A. Rodríguez-Pérez, *Proceedings of the SPE EUROTEC Conference*, Barcelona, 2011.
- 21 J. W. Kang, *et al.*, *Macromol. Res.*, 2009, 17(11), 856–862.
- 22 G. Hari Krishnan, C. I. Lindsay, M. A. Arunagirinathan and C. W. Macosko, *ACS Appl. Mater. Interfaces*, 2009, 1, 1913–1918.
- 23 J. S. Colton and N. P. Suh, *Polym. Eng. Sci.*, 1987, 27, 485–492.
- 24 J. S. Colton and N. P. Suh, *Polym. Eng. Sci.*, 1987, 27, 493–499.
- 25 M. Mitsuhashi, Y. Ito, S. S. Ray, M. Okamoto and K. Hironaka, *Macromol. Mater. Eng.*, 2003, 288, 543–548.
- 26 D. Weaire and S. Hutzler, in *The Physics of Foams*, OUP, Oxford, UK, 2001.
- 27 A. Saint-Jalmes and D. Langevin, *J. Phys.: Condens. Matter*, 2002, 14, 9397–9412.
- 28 B. P. Binks and T. S. Horozov, *Angew. Chem.*, 2005, 117, 3788–3791.
- 29 A. Myagotin, L. Helfen and T. Baumbach, *Meas. Sci. Technol.*, 2009, 20, 055703.
- 30 F. García-Moreno, M. Mukherjee, C. Jiménez, A. Rack and J. Banhart, *Metals*, 2012, 2, 10–21.
- 31 E. Solórzano, J. Pinto, S. Pardo-Alonso, M. A. Rodríguez-Pérez and F. García-Moreno, *NDT&E International*, submitted.
- 32 F. Rouyer, *et al.*, *Phys. Rev. E: Stat., Nonlinear, Soft Matter Phys.*, 2003, 67, 021405.
- 33 D. J. Durian, D. A. Weitz and D. J. Pine, *Science*, 1991, 252, 686–688.
- 34 M. Vera, A. Saint-Jalmes and D. Durian, *Appl. Opt.*, 2001, 40, 4210–4214.
- 35 A. Stocco, F. García-Moreno, I. Manke, J. Banhart and D. Langevin, *Soft Matter*, 2011, 7, 631–637.
- 36 F. García-Moreno, M. Fromme and J. Banhart, *Adv. Eng. Mater.*, 2004, 6, 416–420.
- 37 O. Brunke and S. Odenbach, *J. Phys.: Condens. Matter*, 2006, 18, 6493–6506.
- 38 A. Dasari, Z. Yu and Y. W. Mai, *Acta Mater.*, 2007, 55, 635–646.
- 39 A. Nourbakhsh and A. Ashori, *J. Appl. Polym. Sci.*, 2009, 112, 1386–1390.
- 40 R. Verdejo, M. Mar Bernal, L. J. Ramsanta, F. J. Tapiador and M. A. López-Manchado, *Cell. Polym.*, 2011, 30, 45–62.
- 41 A. Kwok-Fu Yeung, Ph. D. thesis, University of Toronto, 1998.
- 42 F. García-Moreno, E. Solórzano and J. Banhart, *Soft Matter*, 2011, 7, 9216–9223.
- 43 G. Hari Krishnan, T. Umashankar Patro and D. V. Khakhar, *Ind. Eng. Chem. Res.*, 2006, 45, 7126–7134.
- 44 Southern Clay, Technical data sheet.
- 45 L. A. Utrachi, in *Clay-Containing Polymer Nanocomposite*, Rapra Technology, UK, 2004.

[View Online](#)

-
- 46 G. Harikrishnan, S. N. Singh, E. Kiesel and C. W. Macosko, *Polymer*, 2010, **51**, 3349–3353.
- 47 C. Saiz-Arroyo, Ph. D. thesis, University of Valladolid, 2012.
- 48 P. Thareja, *et al.*, *Macromol. Rapid Commun.*, 2008, **29**, 1329–1334.
- 49 A. J. Rojas, J. H. Marciano and R. J. Williams, *Polym. Eng. Sci.*, 1982, **22**, 840–844.
- 50 K. Ashida, in *Polyurethane and Related Foams*, Taylor & Francis Group, USA, 2007, ch. 4.

Downloaded by University of Perugia on 18 September 2012
Published on 11 September 2012 on <http://pubs.rsc.org> | doi:10.1039/C2SM25983D

"TIME-RESOLVED X-RAY IMAGING OF NANOFILLER-PU REACTIVE FOAM SYSTEMS"

Colloids and Surfaces A: Physicochem. Eng. Aspects 438 (2013) 119–125



Contents lists available at ScienceDirect

Colloids and Surfaces A: Physicochemical and Engineering Aspects

journal homepage: www.elsevier.com/locate/colsurfa



Time-resolved X-ray imaging of nanofiller-polyurethane reactive foam systems



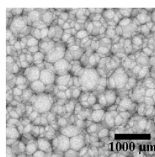
S. Pardo-Alonso^a, E. Solórzano, M.A. Rodríguez-Perez

CellMat Laboratory, Paseo de Belén, 7 – Condensed Matter Physics Department, Science Faculty – University of Valladolid, 47011 – Valladolid, Spain

HIGHLIGHTS

- ▶ Nanofiller-polyurethane foaming process is examined by time-resolved X-ray imaging.
- ▶ Density, cell size and cell density evolution are quantified during PU foam expansion process.
- ▶ The presence of nanofillers produce a significant enhancement in the nucleation mechanism reducing cell size and increasing cell density.
- ▶ Polyurethane foaming kinetics is affected by nanofillers addition.

GRAPHICAL ABSTRACT



ARTICLE INFO

Article history:

Received 14 November 2012
Received in revised form 23 January 2013
Accepted 24 January 2013
Available online 31 January 2013

Keywords:

X-ray imaging
Polymer foams
Polyurethane
Nanoparticles
Foaming kinetics

ABSTRACT

A time-resolved X-ray radiography imaging method has been used to in-situ monitor the foaming process of reactive closed cell rigid polyurethane (PU) foam systems filled with nanofillers (nanoclays and nanosilicas). The method enables the visualization of the cellular structure and, by means of image processing techniques, allows determining the modification of expansion kinetics (density evolution) and cellular structure (cell size evolution). A significant increase of cell nucleation has been found for all the nanoparticles under study. In addition, in several cases, foaming kinetics was also modified in presence of nanoparticles, involving a modification of the blowing and/or polymerization chemical reactions. It has been proved that nanoclays morphology and surface modification of nanosilicas have a determining effect on cell size and density evolution during the foaming processes. The obtained results contribute to obtain a better understanding on the polymer-filler interaction and its influence on the foaming processes of PU systems.

© 2013 Elsevier B.V. All rights reserved.

1. Introduction

Attempts to produce foamed polymer nanocomposites have demonstrated that synergistic effects can appear due to both the influence of nanoparticles during the foaming process that allows obtaining improvements in the cellular structure and a reinforcement of the polymeric matrix [1–6]. These rather new materials are capable to successfully fulfil high-performance lightweight applications as structural sandwich panels, insulating materials,

packaging trays and energy absorbers that cannot be accomplished using conventional polymer foams [2,5–7].

According to the shape, different types of nanofillers can be introduced. Their shape and size determine the specific surface in contact with the polymer matrix, in which the physico-chemical mechanisms governing the foaming process take place. In this sense, the shape of the particles influences the heterogeneous nucleation [1,3,4]. Moreover, nanofillers can also be surface-modified to improve the adhesion between particles and polymer. This surface modification accomplishes a double role promoting both a better dispersion and an improvement of the macroscopic mechanical properties [8–14]. The use of surfactants in inorganic nanoparticles and

^a Corresponding author.

E-mail address: samuelpardo.alonso@fmc.uva.es (S. Pardo-Alonso).

functionalization chemicals in the surface are the most conventional ones [15]. As an example surfactants in the particle surface increase the hydrophobicity and compatibility through ion exchange reactions with polymer matrices [16]. Nevertheless, the surface modification may modify the system chemistry [17] that it is particularly sensible in the case of reactive bi-component thermoset foams (PU, epoxies, etc.). In these materials, the chemical interaction of some reactants with nanoparticles may affect the blowing reaction (gaseous phase generation) and polymerization reaction; this last one is responsible of the liquid viscosity evolution till complete foam solidification.

Therefore the use of nanoparticles with different shapes and sizes in combination with different surface treatments can be expected to modify the foaming mechanisms responsible of the cellular evolution: pore nucleation, coalescence, diffusion coarsening and drainage [18–22] which alter the final cellular structure.

The characteristic evolution of these reactive processes commonly hinders the investigation of the intermediate stages (gelling, rising, packing, solidification) [23] since reaction cannot be stopped and thus only the final solidified foam is available for study. Therefore the majority of studies in these materials are restricted to *ex-situ* analysis of the final foam structure. The *in-situ* analysis of the foaming process (internal evolution of the cellular structure) is not an easy task; there are several technical challenges for proper visualization. From this point of view, time-resolved microfocus X-ray radiography becomes unique and advantageous over other possibilities (e.g. optical microscopy) since it provides real-time information about the internal cellular structure and density of foaming materials such as metals [24] and/or polymers [25,26] with a temporal resolution in the range of seconds. The use of synchrotron radiography has also demonstrated to be useful to examine foaming processes, being possible to resolve these structures with temporal and spatial resolutions in the microscale [27,28]. Finally, recent developments of synchrotron tomographic techniques permit resolving the 3D structure of evolving foams with temporal resolutions of seconds [29,30].

This paper applies microfocus time-resolved radiography to study several foamable nanocomposites based on PU with the main objective of understanding the effect of polymer-filler interaction during the foaming processes. Specifically, this study demonstrates that the specific nanoclays under study show enhanced heterogeneous nucleation and thus smaller cells in comparison with two different types of silica nanoparticles. On the other hand, the influence of surface chemical modification of silica on the temporal evolution of density (liquid fraction) has been studied.

2. Materials and methods

2.1. Nanofillers

Two different kinds of nanofillers (platelet-like and spherical) have been used. Nanoclays are layered nanofillers generally incorporated to improve mechanical properties and also used as gas-barrier fillers. Silica is a spherical nanofiller type commonly used as reinforcing filler for various applications, also providing effective rheology control in complex liquid systems [31].

Cloisite® 30B (Southern Clay Products) was selected to be dispersed in the PU formulation. It is a natural montmorillonite (1.96 g cm^{-3}) organically modified with a quaternary ammonium salt. These particles come commonly grouped into stacks and due to this it is extremely important to exfoliate them in order to achieve the nanometric particles (individual platelets of $6 \mu\text{m} \times 6 \mu\text{m}$ surface with 1.48 nm thickness) that are expected to provide the desired effects [13,32,33].

On the other hand, two types of hydrophilic/hydrophobic fumed silicas (pyrogenic silicon dioxide) provided by Evonik Industries were selected. Their commercial names are Aerosil 200 and R812 respectively. R812 is after-treated with hexamethyldisilazane so only a small fraction of the surface hydroxyl groups are free. These methyl groups protect about 90% of the surface with a low density of 0.29 free OH groups/nm² [35]. Both nanofillers present a specific surface area of $200 \text{ m}^2/\text{g}$ and average primary particle size of 12 nm .

In all cases, two different proportions (1 and 5 wt.% of the total components weight) were dispersed in one of the reactive liquids. Clays were dispersed in the polyol component whereas silicas were dispersed in the isocyanate since hydrophilic Aerosil 200 could absorb some of the water present in the polyol mixture jelling it and hindering a proper mixing.

2.2. Reactive nanocomposite PU foam

A commercial bi-component formulation from BASF was selected for this investigation. The polyol component (Elastopor® H 1501/1) is a mixture of polyols, catalysts, stabilizers and blowing agent (water in this case) and the isocyanate (IsoPMDI 92140) is a diphenylmethane diisocyanate. These materials were selected taking into account the low viscosity values of the bi-component system (650 mPas for the polyol and 300 mPas for the isocyanate). This feature facilitates nanoparticles dispersion and the mechanical stirring to promote the expansion.

A 50 mm diameter 4-bladed impeller mounted on an overhead stirrer (EUROSTAR Power control-visc P1, IKA) was used at 200 rpm to disperse/exfoliate the nanoparticles (clays and silica). Nanoclays were dispersed into the polyol component during 120 s in order to achieve an optimum dispersion/exfoliation thus avoiding particle stacks according to manufacturer recommendations. Silicas (Aerosil 200 and R 812) were also dispersed by mechanical stirring for 120 s ; in this case, into the isocyanate component (IsoPMDI 92140).

Then reactants were cooled down to 5°C for 24 h in order to reduce the reactivity of the system that permits a delay of a few seconds of the beginning of the foaming process. Finally, a stirrer mounting a 50 mm diameter lenart-disc (Vollrath™) was used at 1200 rpm during 20 s to mix the reactants containing the dispersed fillers so promoting the blowing/polymerization reaction. It is important to note the existence of a typical span time of 45 s (time needed to locate the reactive system inside the X-ray cabinet) from the beginning of the mixing to the first acquired radiography so the cream stage was missed. Once the mixing is finished several intermediate stages take place: cream time before a definite expansion appears, rising, cellular structure packing, gelation (when the reaction forms a non-flowing, jelly-like system) and finally solidification of the foam. It is throughout all these stages when bubble nucleation, growth and stabilization/degeneration of the cellular structure occur.

2.3. X-ray radiography setup

In this particular setup (Fig. 1), an X-ray microfocus tube from Hamamatsu, with a maximum output power of 20 W (spot size: $5\text{--}20 \mu\text{m}$, voltage: $20\text{--}100 \text{ kV}$, current: $0\text{--}200 \mu\text{A}$), is used to produce the X-rays. A high-resolution flat panel detector (12 bits, area $120 \text{ mm} \times 120 \text{ mm}$, 2240×2344 pixels, pixel size: $50 \mu\text{m}$) captures the transmitted radiation with spatial resolution, converting the transmitted intensity into a radiographic image. Polymers only absorb a low percentage of emitted X-rays resulting in low contrast images. To solve this inconvenience, a high sensitivity detector and low tube energies are used since the relative absorption of polymers at low energies is higher although detectors response is typically low. Furthermore, the employed tube produces a beam with cone

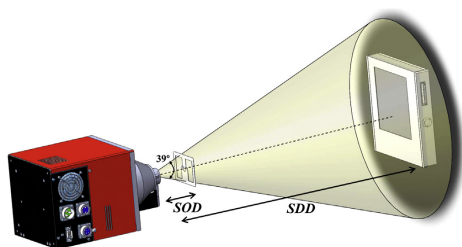


Fig. 1. Cone-beam X-ray radiography setup.

geometry, which allows obtaining up to 20 times magnification of the irradiated sample in the actual working configuration according to Eq. (1). In the presented experiments a 7.25-fold magnification (M) was used with an experimental source-detector distance (SDD) of 580 mm and source-object distance (SOD) of 80 mm. This magnification together with a 2×2 pixel binning yielded a pixel size of $14 \mu\text{m}$. Exposure time was 700 ms and acquisition frame rate 1.43 Hz.

$$M = \frac{SDD}{SOD} \quad (1)$$

2.4. Foam expansion setup

The detection of individual pores using the described X-ray radiography apparatus is difficult if thick foam samples (e.g. 20–30 mm) are examined. Under these conditions pores are overlapped in the transmission image and cannot be clearly identified. Ideal visualization may require from very few pores in depth (ideally one monolayer) to allow visualization and identification of every growing pore during the foaming process. For this reason a special set up was designed to visualize individual pores, see Fig. 2. The designed setup consists in a 0.6 mm-thick stainless steel frame with a central circular cavity (10 mm in diameter) and two lateral evacuating channels. Two thin PP films cover the frame avoiding foam to expand in the direction perpendicular to the frame. A small PU droplet is poured in the centre of the circle for X-ray visualization. Using this system quasi-bidimensional foam grows avoiding flow and movement of the expanding pores in the central region and evacuating the remaining foam.

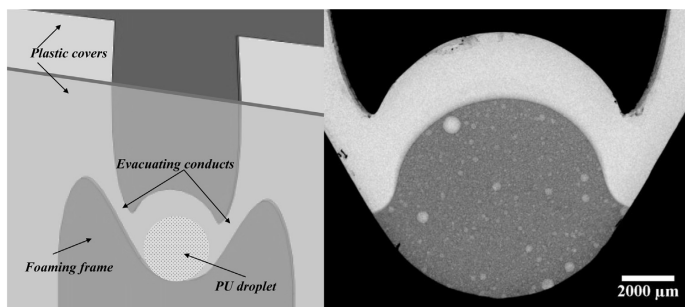


Fig. 2. Setup designed and used for monitoring the foaming process (left) and radiography of the zoomed central cavity with reactive PU droplet (right).

2.5. Image analysis and calculated foam descriptors

2.5.1. Density evolution

Bouguer–Beer–Lambert law (Eq. (2)) permits the determination of material density (ρ) evolution through the transmitted radiation detected (I_1) as already demonstrated by other authors [24]. In this equation, l denotes the material thickness and μ is the attenuation coefficient. The methodology applied for polymer foam density determination has been explained elsewhere [24–26] based on Eq. (3) and using a calibration method with the intensities ($I_{\text{REF-1}}$ and $I_{\text{REF-2}}$) of two already known references (ρ_1 and ρ_2).

$$I_1 = I_0 \cdot e^{-\mu \rho l} \quad (2)$$

$$\rho = \rho_{\text{REF-1}} + \frac{\ln \frac{I_{\text{REF-1}}}{I_1}}{\ln \frac{I_{\text{REF-1}}}{I_{\text{REF-2}}}} (\rho_{\text{REF-2}} - \rho_{\text{REF-1}}) \quad (3)$$

2.5.2. In-situ cell size evolution

Image analysis operations and computing procedures allowed pore size evolution quantification [25]. This methodology basically consists in image optimization and filtering, time-adjustable binarization, application of watershed algorithm and size-selective pore size analysis by using a time-dependent function (adjusted by the operator), optimized to remove too large and too small bubbles under a double time-evolving threshold. This procedure has been demonstrated to provide successful results showing a scaling relationship with 3D tomography pore size data examined in the final foam structure [25].

2.5.3. In-situ cell density calculation

Cell density is defined as the number of bubbles per unit volume of the unfoamed material [1,18,25]. After nucleation cell density reaches a stable value that only decreases by foam degeneration mechanisms such as coalescence or diffusion coarsening. Subsequently cell density is a valid magnitude to evaluate the existence of foam degeneration with independency of cell size evolution and/or density. It is calculated including relative density (liquid fraction, ρ) and pore size values (ϕ) according to Eq. (4).

$$N_V = \frac{6}{\pi \phi^3} \left(\frac{1}{\rho} - 1 \right) \quad (4)$$

3. Results and discussion

3.1. Time-resolved X-ray imaging

Combination of sequenced radiography acquisition and the use of the thin foaming frame allowed monitoring the foaming

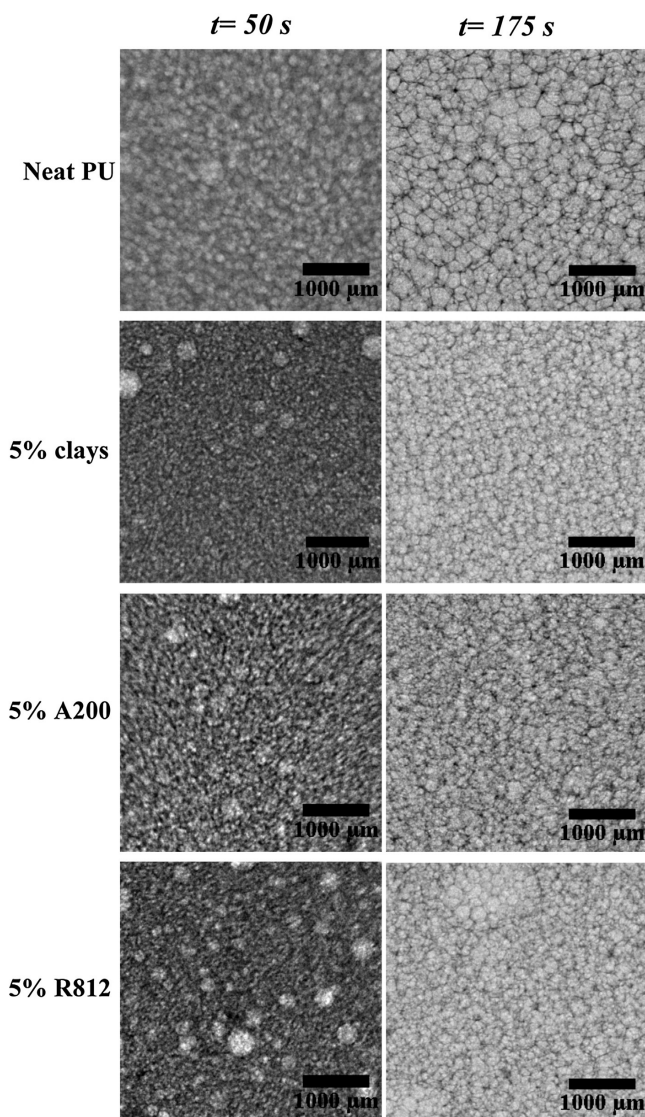


Fig. 3. X-ray radiographies of the nanocomposite PU expanding process at two different foaming times.

processes. In this sense all intermediate stages are available for investigation before cellular structure is completely developed and full polymerization had occurred. Fig. 3 shows a comparative of acquired radiographies at two particular times (50 and 175 s) for the different investigated formulations (neat PU, 5% Cloisite 30B, 5% A200 and 5% R812). It can be appreciated the effect of nanofillers presence on cellular structure both at the early (50 s

after the polyol/isocyanate stirring) and later stages (175 s) in comparison with the neat PU formulation. Furthermore cell size is reduced (finer cellular structure) in the systems containing particles (Cloisite 30B, A200 and R812). It is important to note the presence of some large air entrapments in the radiographies due to the turbulent mixing process carried out to promote the foaming reaction.

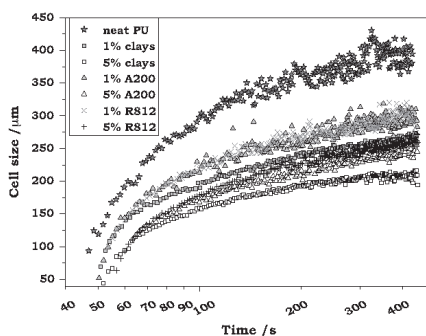


Fig. 4. Cell size evolution: neat PU, 1 and 5 wt.% of Cloisite 30B, Aerosil 200 and Aerosil R812.

3.2. Cell size evolution

Fig. 4 shows average cell size evolution during the expansion process for the neat PU and the nanofilled PU formulations (1 and 5 wt.% contents of Cloisite 30B, Aerosil 200 and Aerosil R812). As it can be observed the cell size increases during the full monitoring time, however cell growth rate is rapid ($8\text{--}10\ \mu\text{m/s}$) during the rising (early stages, 50–100 s) and becomes slower during polymerization ($2\text{--}4\ \mu\text{m/s}$, 100–450 s). From these results, it can be appreciated that the final cell size becomes reduced from $400\ \mu\text{m}$ in the neat PU to $200\ \mu\text{m}$ in the case of 5 wt.% of nanoclays (same but less pronounced effect is observed for 1 wt.% content). This content provides the highest cell size reduction (up to 45% of initial neat PU) whereas the effect of silicas is limited and it yields cell sizes in the range of $230\text{--}260\ \mu\text{m}$. The results clearly indicate that for this particular PU system the platelet-like surface treated clays provide enhanced effect as nucleating agents. Several aspects could be contributing on this better behaviour. On the one hand, the pronounced edges due to the layered shape of Cloisite 30B could reduce the surface tension in these areas making energetically more favourable cells nucleation for this system. On the other hand, the surface treatment applied to these clay particles make possible a good dispersion and exfoliation in the PU matrix under study. This good dispersion is not easy to achieve for materials containing silica [27,36].

It is also interesting to mention that the hydrophilic silica A200 has a slightly higher effect on cell size reduction than the hydrophobic one (A812). Two possible reasons could cause this effect, the first one is that the chemical nature of the surface of the hydrophilic silica should result in a weak interaction with the polymeric matrix, this will produce a polymer–filler interface with a low surface tension and as a consequence a higher nucleating capability. On the other hand the affinity of this hydrophilic silica with water, the blowing agent for the PU system under study, could also increase the efficiency of the particles as nucleating agents.

3.3. Density evolution

Presence of fillers modifies the density evolution due to their interaction with both polymer chemistry and the physical mechanisms controlling the foaming process. Fig. 5 shows curves for relative density evolution for the materials containing 5 wt.% of nanoparticles calculated by using the calibration procedure reported elsewhere [25]. Results for Aerosil 200 – hydrophilic – indicate that density evolution is similar to the one of neat PU whereas a different effect on density evolution (slower expansion)

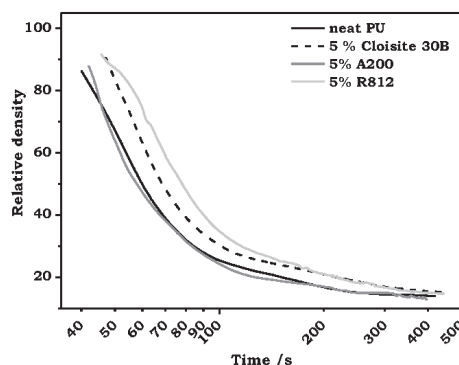


Fig. 5. Relative density evolution in time for neat PU 5 wt.% of Cloisite 30B, Aerosil 200 and Aerosil R812.

is observed for the organomodified nanoclays and the R812 surface-modified silicas both with hydrophobic characteristics.

This type of behaviour has also been observed in other systems containing nanoparticles and the reasons have been attributed to the higher viscosity of the nanofilled systems [17] or the fillers–isocyanate interaction (that decreases the active hydrogen containing compounds reacting with the water present in the polyol to produce the gaseous phase). Both effects could play a role for the systems of this paper containing hydrophobic particles; on the one hand the higher viscosity could reduce the expansion ratio for a given amount of gas generated. On the other hand, the chemical interactions of the particles with the isocyanate compound could reduce the amount of gas created (less isocyanate available for the production of gas) for a fixed time and this would also reduce the expansion ratio at that time.

The similar evolution of the hydrophilic silica in comparison with the pure PU would indicate a very weak chemical interaction of this particle with the other products in the formulations. This weak interaction would keep the chemical reactions the same for this product than for the initial pure material, resulting in a similar density evolution.

3.4. Combined effects

The presented results indicate that both clays and silicas contribute to a significant cell size reduction. The generation of a larger number of nucleation sites led to higher cell density from the very early moments, calculated according to Eq. (4); and this effect remains unchanged throughout all the foaming process, see Fig. 6. This parameter can be conventionally determined only at the final solidified foam [1]. It is also important to point out that neither nanoclays nor silicas induce cell degeneration mechanisms (coalescence), already absent in the neat PU formulation under study. So cell density remains constant during expansion.

Specifically, evolution of cell density values showed that the addition of 5 wt.% Cloisite 30B increases cell density more than four times (from 2.5×10^5 to 1.3×10^6 cells/cm³) with respect to the original formulation. It is possible to appreciate that silica type R812 presents poorer nucleation capacity since a 5 wt.% of these particles provides similar compliance than nanoclays at much lower contents (1 wt.%). Finally, if we compare the hydrophilic and hydrophobic silicas, A200 showed higher efficiency than R812. This was probably due to its poor affinity with the polymer matrix and its water philicity. In any case it seems that nucleation capacity of

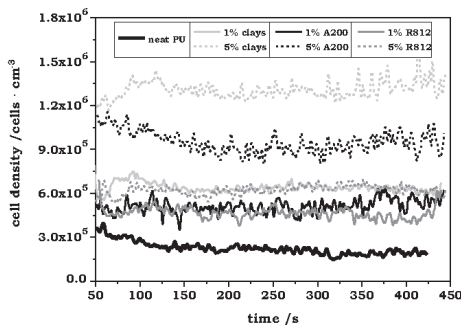


Fig. 6. Cell density evolution during foaming for neat PU, 1 and 5 wt.% of Cloisite 30B, Aerosil 200 and Aerosil R812.

nanoclays is higher probably due to both favourable morphology and/or more efficient dispersion. The fact of adding clays into the polyol instead of the isocyanate might also have influence in the foaming behaviour although previous works have reported similar results when the clays are introduced in the polyol or in the isocyanate [25,36].

The modification of the kinetics of the chemical reactions (blowing and polymerization) due to the chemical interactions of the particles with the reactants has also influence on the cellular structure at intermediate stages, even when the initial or final solid structure is similar. Fig. 7 shows a 3D graph where the time-synchronized cell size versus density evolution is plotted for the two studied contents creating a surface which gives an idea on the evolution at intermediate contents between 1% and 5%. As can be seen, the evolution of the three studied materials is developed mostly in parallel at 1% content, with only a displacement in the cell size due to different nucleation promoted. At 5% content the hydrophobic nanofillers evolve similarly but this is not the case of the hydrophilic silica (A200) that evolves completely different. It is also possible to observe a transition on the behaviour at contents around 3%.

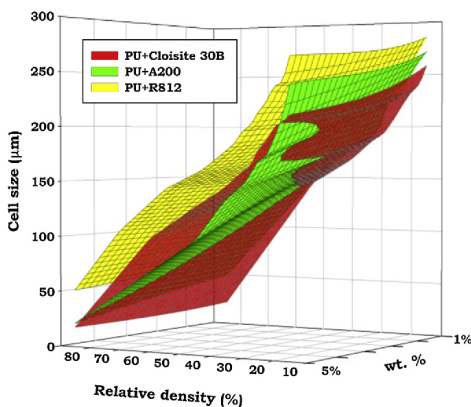


Fig. 7. Evolution of cell size versus relative density at the two studied contents.

4. Conclusions

Time-resolved X-ray radiography allowed monitoring the evolution of the cellular structure from the early stages of the reactive foaming processes. Image analysis procedures provided quantification of cell size and density at any instant, which permits the investigation on the effects of nanofillers during all intermediate stages of the process. This approach is very helpful to obtain a better understanding of the complicated chemical and physical phenomena that take place during the foaming of these multi-component systems.

Nanometric fillers (clays and silicas) have a determinant effect on the cellular structure of reactive closed cell PU. These particles primarily modify the nucleation stage, which results into changes of the cellular morphology evolution throughout the full process. According to the cell density results, nanoclays promote an enhanced cell nucleation yielding smaller cell size than silicas since coalescence resulted to be absent in this particular rigid PU formulation. Particularly, the addition of increasing contents of nanoclays to the rigid closed cell PU system under study resulted into 45% reduction of cell size for 5 wt.% and more than four times increase in the number of cells per unit volume.

On the other hand, density evolution is significantly altered by hydrophobic, surface-treated particles (i.e. R812 silicas and Cloisite 30B clays) that are found to slow down the expansion process. Silicas with no surface modification (A200) did not alter the expansion process. The specific chemical interactions of the particles with the reactants of the PU system under analysis together with the modification of the system viscosity play a key role on the modifications observed.

Acknowledgements

Financial support from the Spanish Ministry of Science and Innovation and FEDER (MAT2009-14001-C02-01 and MAT 2012-34901), the European Spatial Agency (Project MAP AO-99-075), the European Commission (FP7 program, EC project Nancore number 214148), PIRTU contract of S. Pardo-Alonso by Junta de Castile and Leon (EDU/289/2011) and co-financed by the European Social Fund and Juan de la Cierva contract of E. Solórzano by the Ministry of Economy and Competitiveness (JCI-2011-09775) are gratefully acknowledged.

References

- [1] L.J. Lee, C. Zeng, X. Cao, X. Han, J. Shen, G. Xu, Polymer nanocomposite foams, *Compos. Sci. Technol.* 65 (2005) 2344–2636.
- [2] C.C. Ibeh, M. Bubacz, Current trends in nanocomposite foams, *J. Cell. Plastics* 44 (2008) 493–514.
- [3] X. Cao, L.J. Lee, T. Widya, C. Macosko, Polyurethane/clay nanocomposites foams: processing, structure and properties, *Polymer* 46 (2005) 775.
- [4] T. Widya, C.W. Macosko, Nanoclay-modified rigid polyurethane foam, *J. Macromol. Sci.: B* 44 (2005) 897–908.
- [5] S.C. Tjong, Structural and mechanical properties of polymer nanocomposites, *Mater. Sci. Eng. R* 53 (2006) 73–197.
- [6] M.C. Saha, Md.E. Kabir, S. Jeelani, Enhancement in thermal and mechanical properties of polyurethane foam infused with nanoparticles, *Mater. Sci. Eng. A* 479 (2008) 213–222.
- [7] R. Verdejo, R. Stämpfli, M. Alvarez-Lainez, S. Mourad, M.A. Rodriguez-Perez, P.A. Brühlwiler, M. Shaffer, Enhanced acoustic damping in flexible polyurethane foams filled with carbon nanotubes O, *Compos. Sci. Technol.* 69 (2009) 1564.
- [8] M.M. Bernal, M. Martín-Gallego, L.J. Romasanta, A.C. Mortameth, M.A. López-Manchado, A.J. Ryan, R. Verdejo, Effect of hard segment content and carbon-based nanostructures on the kinetics of flexible polyurethane nanocomposite foams, *Polymer* 53 (2012) 4025.
- [9] W.J. Seo, Y.T. Sung, S.B. Kim, Y.B. Lee, K.H. Choe, S.H. Choe, J.Y. Sung, W.N. Kim, Effects of ultrasound on the synthesis and properties of polyurethane foam/clay nanocomposites, *J. Appl. Polym. Sci.* 102 (2006) 3764.
- [10] W.J. Seo, Y.T. Sung, S.J. Han, I.H. Kym, O.H. Ryu, H.S. Lee, W.N. Kim, Synthesis and properties of polyurethane/clay nanocomposite by clay modified with polymeric methane diisocyanate, *Appl. Polym. Sci.* 101 (2006) 2879.

- [11] M. Mar Bernal, I. Molenberg, S. Estravis, M.A. Rodríguez-Pérez, I. Huynen, M.A. Lopez-Manchado, R. Verdejo, Comparing the effect of carbon-based nanofillers on the physical properties of flexible polyurethane foams, *J. Mater. Sci.* 47 (2012) 5673–5679.
- [12] C. Saiz-Arroyo, J. Escudero, M.A. Rodríguez-Pérez, J.A. de Saja, Improving the structure and physical properties of LDPE foams using silica nanoparticles as an additive, *Cell. Polym.* 30 (2011) 63–78.
- [13] A. Lorenzetti, D. Hrelja, S. Besco, M. Roso, Improvement of nanoclays dispersion through microwaves processing in polyurethane rigid nanocomposite foams, *J. Appl. Polym. Sci.* 115 (2010) 3667.
- [14] P. Mondal, D.V. Khakhar, Rigid polyurethane-clay nanocomposite foams: preparation and properties, *J. Appl. Polym. Sci.* 103 (2007) 2802.
- [15] X. Gong, J. Liu, S. Baskaran, R.D. Voise, J.S. Young, *Chem. Mater.* 12 (2000) 1049.
- [16] B.K.G. Theng, in: *The Chemistry of Clay-Organic Reactions*, Wiley, New York, 1974.
- [17] M.M. Bernal, M.A. Lopez-Manchado, R. Verdejo, In situ foaming evolution of flexible polyurethane foam nanocomposites, *Macromol. Chem. Phys.* 212 (2011) 971–979.
- [18] S. Colton, N.P. Suh, Nucleation of microcellular foam: theory and practice, *Polym. Eng. Sci.* 27 (1987) 500–503.
- [19] S.N.S. Leung, Ph.D. Thesis, University of Toronto (2009).
- [20] M. Mitsunaga, Y. Ito, S.S. Ray, M. Okamoto, K. Hironaka, Intercalated polycarbonate/clay nanocomposites: nanostructure control and foam processing, *Macromol. Mater. Eng.* 288 (2003) 543–548.
- [21] B.P. Binks, T.S. Horozov, Aqueous foams stabilized solely by silica nanoparticles, *Angew. Chem. Int. Ed.* 117 (2005) 3788–3791.
- [22] D. Weaire, S. Hutzler, in: *The Physics of Foams*, OUP, Oxford, UK, 2001.
- [23] C. Torres-Sánchez, J. Comey, Identification of formation stages in a polymeric foam customised by sonication via electrical resistivity measurements, *J. Polym. Res.* 16 (2009) 461–470.
- [24] F. García Moreno, M. Fromme, J. Banhart, Real time X-ray radiography on metallic foams using a compact microfocus source, *Adv. Eng. Mater.* 6 (2004) 416–420.
- [25] S. Pardo-Alonso, In-situ evidences of nanoparticles nucleating effect in polyurethane-nanoclays systems, *Soft Matter* 44 (8) (2012) 11262–11270.
- [26] E. Solórzano, J. Pinto, S. Pardo-Alonso, F. García-Moreno, M.A. Rodríguez-Pérez, Application of a microfocus X-ray imaging apparatus to the study of cellular polymers, *Polym. Test.* 32 (2013) 321–329.
- [27] A. Rack, F. García-Moreno, C. Schmitt, O. Betz, A. Cecilia, A. Ershov, T. Rack, J. Banhart, S. Zabler, On the possibilities of hard X-ray imaging with high spatio-temporal resolution using polychromatic synchrotron radiation, *J. X-Ray Sci Technol.* 18 (2010) 429–441.
- [28] A. Rack, F. García Moreno, T. Baumbach, J. Banhart, Synchrotron-based radiography employing spatio-temporal micro-resolution for studying fast phenomena in liquid metal foams, *J. Synchrotron Radiat.* 16 (2009) 432–434.
- [29] R. Mokso, F. Marone, M. Stamparoni, Real time tomography at the Swiss Light Source, in: *AIP Conf. Proc.*, 2012, pp. 87–90.
- [30] J. Lambert, R. Mokso, I. Cantat, P. Cloetens, J.A. Glazier, F. Graner, R. Delamay, Coarsening foams robustly reach a self-similar growth regime, *Phys. Rev. Lett.* 104 (2010), 248304.
- [31] S. Jacob, K.K. Suma, J.M. Mendez, K.E. George, Reinforcing effect of nanosilica on polypropylene-nylon fibre composite, *Mater. Sci. Eng. B* 168 (2010) 245–249.
- [32] T.J. Pinnavia, G.W. Beall, in: *Polymer-Clay Nanocomposites*, John Wiley & Sons, Chichester-England, 2000.
- [33] S. Estravis, M.A. Rodríguez-Pérez, Polyurethane foam composites: relationship between mechanical properties and filler-matrix chemical interaction, in: *SPE Eurotec Conference*, November 14–15, Barcelona, Spain, 2011.
- [35] A.A. Chuiko, Y.I. Gorlov, in: *Chemistry of a Silica Surface*, Naukova Dumka, Kyiv, 1992.
- [36] H. Zou, S. Wu, J. Shen, Polymer/silica nanocomposites: preparation, characterization, properties, and applications, *Chem. Rev.* 108 (2008) 3893–3957.

“EFFECT OF CARBON NANOFILLERS ON FLEXIBLE POLYURETHANE FOAMING FROM A CHEMICAL AND PHYSICAL PERSPECTIVE”

M.Mar Bernal,^{a*} Samuel Pardo-Alonso^{b*}, Eusebio Solórzano^b, Miguel Ángel Lopez-Manchado^a, Raquel Verdejo^a and Miguel Ángel Rodríguez-Perez^b

The effect of carbon nanoparticles (CNPs) on the physical and chemical events taking place during the foaming evolution of flexible polyurethane (FPU) foams is analysed by *in-situ* X-ray time-resolved imaging. The differences observed in the cellular structure and density evolution of nanocomposite foams are explained in terms of the type of nanoparticles and the functional groups on their surface. The presence of certain types of particles enhanced the bubble nucleation at the beginning of the process although some others did not. The chemical interaction seems to produce delays in the blowing reaction process and promotes coalescence events during foam evolution as regards of the cell density results obtained. This study on the kinetics of polymerization and morphology development of reactive PU nanocomposite foams contribute to understand the physical phenomena occurring as a consequence of the CNP-FPU chemical interaction.

1. Introduction

Polymer nanocomposite foams are receiving increasing attention since the synergy between foams and nanoparticles attributes results in multifunctional and lightweight materials that can find interesting applications at industrial level.¹⁻³ The nanofillers have the ability to reinforce the fine cellular structure of polymeric foams enhancing their mechanical strength, electrical conductivity, nanoscale surface features and biocompatibility. Nevertheless, the properties of the nanocomposite foams are also determined by their final cellular structure, which strongly depends on the nanoparticles type and their interaction with polymer matrix during foaming.

In this field, one of the most interesting polymer foams is reactive polyurethane (PU) foam in congruence with its industrial relevance. In this particular case, the nanofillers are expected to have important effects during the simultaneous interplay of chemical and physical processes, i.e. the polymerization and foaming of a block copolymer.⁴⁻⁶ PU foams are essentially produced by two exothermic reactions between the isocyanate with the hydrogen-active groups of polyol and with water. The reaction between the isocyanate and the polyol is called the *gelling reaction* and forms urethane linkages. Likewise, the reaction between the isocyanate and water is called the *blowing reaction* and produces urea hard segments (HS) and carbon dioxide (CO₂) gas.⁷⁻¹¹ Hence, PU foaming is a balance process between the gas formation and expansion and the viscosity increase occurring during the polymerization. The presence of any additional substance, from surfactants to fillers, may intervene in this subtle balance promoting or holding back the reaction. Therefore, real-time monitoring of these systems is an essential study to understand nanoparticle-PU interactions during the reactive foaming process.

Different *in-situ* techniques have been used in the study of foaming evolution both from a chemical and a physical perspective. Infrared spectroscopy and small angle X-ray

scattering (SAXS) studies have shown the effect of the added substances on the kinetics of polymerization and matrix phase-separated block copolymer structure development of PU foams.^{5, 6, 12-15} Meanwhile, both rheology^{5, 14, 16} and radioscopy¹⁷⁻¹⁹ have been used to analyse the foaming process from a physical perspective. In particular, previous studies of PU nanocomposite foams carried out,^{5, 6} demonstrated the influence of carbon-based nanoparticles (CNPs), multi-walled carbon nanotubes (MWCNTs) and functionalized graphene sheets (f-GS), on the reaction kinetics and the development of the phase-separated morphology of flexible PU nanocomposite foams. These studies showed that the kinetics of polymerization strongly depends on the morphology and surface bearing groups of the CNPs, delaying the extent of the reaction and affecting the micro-phase separated structure of PU foams. Studies on the foam structure evolution of PU nanocomposite foams have only recently been accomplished. The use of real-time X-ray monitoring has been developed as a suitable technique for the study of both polymer and metal foaming. Verdejo *et al.*¹⁹ studied the evolution of reactive polydimethylsiloxane (PDMS) foams reinforced with carbon nanotubes and graphene sheets by *in-situ* synchrotron X-ray radioscopy. They reported differences in both the trend and speed of foaming and the dominating coarsening phenomena in the expansion and solidification processes. Pardo-Alonso *et al.*^{17, 18} applied a similar X-ray technique, based on microfocus tube imaging,²⁰ to observe the nucleation and expansion process of rigid PU nanocomposite foams. Thanks to the methodology developed it was possible to reach an excellent visualization of the individual cells and thus a methodology to quantify the cell size and cell density during foaming was developed. Furthermore, the kinetics of density evolution could also be determined analysing the images obtained from the radiography sequences. These studies established suitability of this technique to quantify the effect of the nanofillers during the foaming process. Therefore, in the present work, the effects of carbon-based nanoparticles on the physical events taking place during the foaming evolution of flexible PU foams are studied, for the first time, by *in-situ* microfocus X-ray radioscopy.

Present paper accomplishes a novel insight on the evolution of reactive PU nanocomposite systems by comparing the kinetics of blowing, polymerization and cell structure degeneration mechanisms, which strongly influence the morphology and cellular structure of these systems and hence their final properties.

2. Materials and Methods

2.1. Flexible Polyurethane (FPU) Foams

The polyol component used to prepare FPU foams was a highly reactive polyether-based triol, Voranol 6150 (Dow Plastics) with OH value of 27 mg KOH/g, an average functionality of 3 and M_w of 6000 g/mol and a viscosity of 1150 mPa·s. The isocyanate was a methylene diphenyl diisocyanate (MDI), Voranate M2940 (Dow Plastics) with NCO content of 31.4 % and viscosity 49 mPa·s⁻¹ at 25 °C. The polyether-based triol, Voranol CP1421 (Dow Plastics) with OH values of 31 mg KOH/g was used as a cell-opener in the reaction. The additives employed in this formulation were: FASCAT 4202 (dibutyl tin dilaurate from Arkema Inc.) which was used as a tin catalyst for the gelling reaction; TEDA L-33B (a solution of 33% triethylendiamine

in 1,4-butanediol from Torch Europe B.V.) and NIAX E-A-1 (a solution of 70 % bis(2-dimethylaminoethyl) ether in 30 wt.-% dipropylene glycol from Momentive Performance Materials GmbH) as amine derivative catalysts in the *blowing* and *gelling* reactions, respectively; DEOA (85 % diethanolamine in water) as a cross-linker agent, SH-209 (Momentive Performance Materials GmbH) as silicone surfactant and distilled water as blowing agent.

2.2. Carbon Based Nanofillers

Multi-walled carbon nanotubes (MWCNTs) were grown by the chemical vapor deposition (CVD) injection method based on the injection of a ferrocene (Aldrich 98 %)/toluene solution

(3 wt.-% of ferrocene in toluene) at a constant rate in a tube furnace, under an inert argon atmosphere ($325 \text{ ml}\cdot\text{min}^{-1}$) and at a temperature of $760 \text{ }^\circ\text{C}$ in atmospheric pressure.^{21, 22} These MWCNTs were chemically treated with a 3:1 concentrated sulfuric/nitric acid mixture and refluxed at $120 \text{ }^\circ\text{C}$ for 30 min. Then, the mixture was filtered through a glass filter funnel using a PTFE membrane ($0.2 \text{ }\mu\text{m}$ pore size, Millipore) and washed with distilled water several times until neutral pH. The oxidized MWCNTs (f-MWCNTs) were then dried at $120 \text{ }^\circ\text{C}$ and stored in a sealed container under vacuum prior to use to avoid possible effects of chemisorbed water due to their hydrophilic nature.^{23,24} The functional groups attached on the sidewalls of f-MWCNTs due to the oxidation are mainly hydroxyl and carboxyl groups.²⁵

The synthesis of functionalized graphene sheets (f-GS) was carried out following different steps reported elsewhere.²⁶ First, graphite oxide (GO) was produced using natural graphite (NG) powder (universal grade, 200 mesh, 99.9995 %, Fluka) according to the Brödie method.^{27, 28} In a typical preparation procedure, a reaction flask with 20 ml fuming nitric acid was cooled to $0 \text{ }^\circ\text{C}$ in a cryostat bath for 20 min. Then, the graphite powder (1 g) was carefully added to avoid its agglomeration. After that, KClO_3 (8 g) was gradually added over 1 h, in order to avoid sudden increases in temperature due to the exothermic nature of the reaction. The mixture was stirred for 21 h maintaining the reaction temperature at $0 \text{ }^\circ\text{C}$. Next, it was diluted in distilled water and filtered using a PTFE membrane until the filtrate reached a neutral pH. The GO obtained was dried and stored in a vacuum oven at $50 \text{ }^\circ\text{C}$ until use. Then, the GO was thermally exfoliated at $1000 \text{ }^\circ\text{C}$ and under an inert argon atmosphere for a short time, usually less than 1 min, to produce the f-GS. Finally, f-GS were stored in a sealed container prior to use. As produced f-GS contain epoxy, hydroxyl and carboxyl groups on their surface.²⁵

2.3. Preparation of FPU nanocomposite foams

FPU foams were prepared from 100 phpp (parts per hundred parts of polyol) of Voranol 6150, 4 phpp of Voranol CP1421, 0.8 phpp of DEOA, 0.25 phpp of TEDA-L33B, 0.1 phpp of NIAX E-A-1, 0.05 phpp of FASCAT, 0.4 phpp of silicone SH 209, 2 phpp of water and 43.4 phpp of Voranate M2940. For comparison purposes, a fixed amount of nanofillers (0.5 phpp), 0.3 wt.-% in the final foam, was dispersed in the polyol (Voranol 6150). The mixture was initially sonicated for 10 min with an ultrasonication probe (Sonics VibraCell) in a water/ice bath, and was then stirred under high shear at 2400 rpm for 6 h.

Subsequently, the surfactant, catalysts and distilled water were added to the polyol/nanofiller mixture and stirred at 2400 rpm for 3 min.

The foaming stage was promoted by stirring of the original polyol/nanofiller mixture and the additives with the isocyanate for 20 seconds. In order to delay/slow down the reaction rate the components were cooled to 5 °C prior to the liquid-liquid dispersion.

2.4. Rheological Characterization

The rheological behaviour of the polyol/nanofiller dispersions was measured using a TA Instruments Advanced Rheometer AR1000. The particular geometry used was a stainless-steel corrugated parallel plate with a diameter of 20 mm. The gap was fixed to 0.3 mm and a dynamic frequency sweep from 0.01 to 100 $\text{rad}\cdot\text{s}^{-1}$ at 21 °C was employed.

2.5. Time-resolved radiography

The setup used for radiography acquisition with temporal resolution includes a microfocus X-ray source from Hamamatsu producing polychromatic X-rays and cone-beam geometry with a spot size 5-20 microns which allows up to 20 times magnification of the irradiated sample.²⁰ The X-ray transmitted radiation is detected by a high sensitivity flat panel (2240 x 2344 pixels, 12bits and 50 microns pixel size) which allows high speed imaging up to 9 fps (at 4x4 pixel binning). Finally a frame grabber records the radiography sequences for later image processing. The setup is customized for low absorbing materials such as polymers and typically works at low energies 20-60 kV and high currents 100-200 μA in order to achieve an optimum contrast keeping small exposure times (600ms, typically) and high acquisition rates (1.66 fps). Particularly, for this study the magnification used is 7.25 times with effective pixel size (after applying 2x2 binning) of 14 microns by using a source-detector distance of 580 mm and source-object distance of 80 mm. A 3D drawing of the system is shown in Fig. 1.

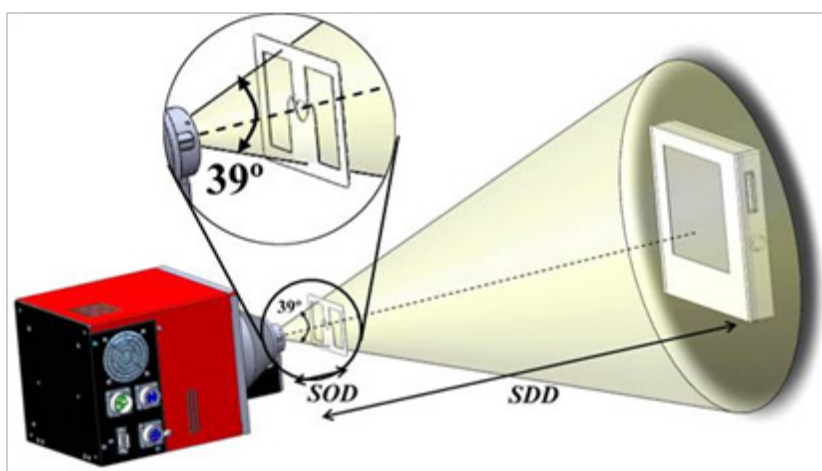


Fig. 1 Microfocus cone-beam radiography setup with including the foaming frame used.

For the radiographic experiments, a 0.6 mm-thick stainless steel foaming frame was designed which allows observing only 2-3 cells in depth so they can be discerned by image analysis procedures. The frame has a circular cavity ($\varnothing=10$ mm) where a reacting droplet of FPU foam is placed just after stirring by a syringe for subsequent X-ray monitoring while foaming process takes place. Two evacuating conducts permitted to minimize movement of the expanding droplet improving the X-ray imaging in the central region of the cavity so cell growth can be visualized and further analysed. This very thin foaming frame was layered by two 250 microns-thick polypropylene (PP) films in order to keep the thickness unaltered during the entire observation.

2.6. Image Processing

An image analysis procedure was needed in order to extract density and cell size information. The density evolution can be calculated from the radiograph intensities applying the Beer-Lambert law of attenuation (Eq 1):

$$I(x, z) = I_0 e^{-\mu \rho(x, z) d} \quad (1)$$

where $\rho(x, z)$ is the density of the system, d is the sample thickness in the beam direction assumed to be constant, μ is the attenuation coefficient and I_0 is the initial beam intensity. Furthermore, cell size was measured by an overlay method.²⁹

2.7. Scanning Electron Microscopy (SEM)

The structure of the FPU nanocomposite foams was qualitatively examined using a Philips XL30 environmental scanning electron microscope (ESEM) at 15 kV. Cross-sections of the samples were cryo-fractured perpendicular to the foaming direction and the fracture surface was sputter-coated with gold/palladium.

3. Results and Discussions

3.1. Rheological Behaviour

The formation of the cellular structure of FPU nanocomposite foams depends on different parameters such as viscosity of the initial polyol/CNP dispersions, surface tension and how the polymerization reaction takes place. Hence, the study of the rheological behaviour of polyol/CNP systems is essential to understand the later foaming process on these foaming systems and it is influenced by the concentration of CNPs as well as their size, shape, presence or lack of functional groups, adsorption affinity of the polymer on the surface of the nanoparticles and the chain bridging between the nanofillers.³⁰⁻³⁵ Fig. 2 shows the dependence of the complex viscosity with the angular frequency for polyol and dispersions of 0.5 phpp of MWCNTs, f-MWCNTs and f-GS. It can

be observed that measured values for neat polyol are very similar to the ones given by the producer, i.e. 1150 mPa·s.

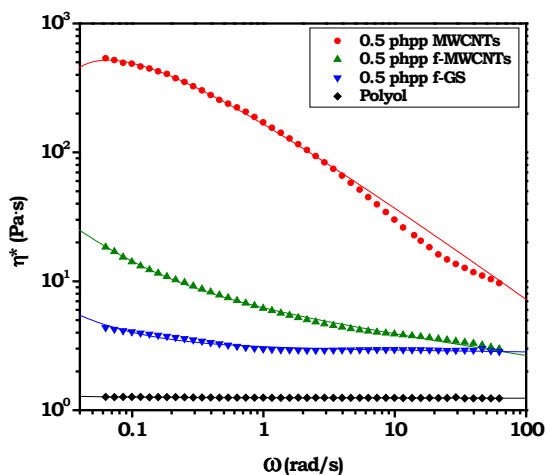


Fig. 2 Complex viscosity (η^*) variation with the angular frequency (ω) of polyol/CNP dispersions.

The Herschel-Bulkley model for polyol/CNP dispersions has previously described the rheological behaviour of these types of dispersions qualitatively.^{5, 36}

$$\eta^* = \frac{\tau_0}{\omega} + k\omega^{n-1} \quad (2)$$

where η^* is the complex viscosity, ω the angular frequency, τ_0 the yield stress, k the consistency index and n is the flow behaviour index which describes the rheological behaviour (for $n < 1$ shear-thinning, for $n > 1$ shear-thickening and for $n = 1$ Newtonian fluid). The parameters obtained from the fitting of the Herschel-Bulkley model are summarized in Table 1.

Table 1 Parameters and the correlation coefficient (r^2) of the Herschel-Bulkley model for the polyol/CNP dispersions.

Sample	τ_0 (Pa)	k (Pa·s ⁿ)	n	r^2
Polyol	≈0	1.25	0.99	0.91
0.5 phpp MWCNTs	18.14	162.23	0.51	0.82
0.5 phpp f-MWCNTs	0.61	5.62	0.85	0.99
0.5 phpp f-GS	0.09	3.01	0.98	0.95

The results show that the polyol exhibits the typical behaviour of a Newtonian fluid, in which the viscosity is independent of the frequency. However, the polyol dispersions at 0.5 phpp MWCNTs and f-MWCNTs show a shear-thinning behaviour, in particular pristine MWCNTs, while the polyol/f-GS dispersions exhibit still a quasi-linear behaviour at this concentration.

The dispersions of carbon nanotubes can be considered as rods in solution and, according to Doi and Edwards theory,^{37, 38} the rheology of rods in solution is strongly dependent on rod concentration and aspect ratio. The oxidation of the f-MWCNTs produces a less marked change of the complex viscosity compared to pristine MWCNTs, which is attributed to a shorter nanotube length as a result of the aggressive acid treatment.³¹

The increase of the viscosity on polymer nanocomposites has been related to the formation of a nanoparticles network, via direct contacts or bridging by polymer chains.^{32, 39} While polyol/MWCNTs dispersions present a shear-thinning behaviour, dispersions with f-GS only show a weak increase of the viscosity compared to the neat polyol. This different behaviour is ascribed to their different morphology. MWCNTs are rod-shape nanoparticles that facilitate interchain and entanglement interactions, and lead to a strong network as described by Knauert *et al.*³² and Pujari *et al.*⁴⁰ Meanwhile, f-GS are considered as platelet-like nanoparticles with high aspect ratio and large interfacial areas, which in addition possess functional groups on their surface. Therefore, a great amount of molecules are adsorbed on the f-GS surface through hydrogen-bonding or electrostatic interactions, reducing the particle-particle interactions within the dispersions.^{32, 41}

3.2. Density Evolution

The density evolution during foaming of FPU nanocomposite foams filled with CNPs has been studied by *in-situ* X-ray radiography as described in the experimental section. Fig. 3 shows the evolution of the relative foam density. These results are plotted having as time reference the beginning of stirring process and therefore all curves show a typical span of 50 seconds in the time scale (20 seconds mixing, droplet positioning, film covering and set up positioning). Therefore, in particular systems, the blowing reaction had already begun in the moment the monitoring started.

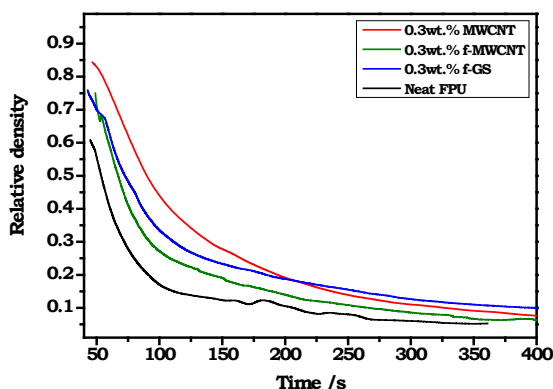


Fig. 3 Relative density evolution curves during foaming of FPU nanocomposite foams.

In Fig. 3 it can be appreciated a typical rapid density decrease at the early stages of the foaming process (50 - 100 s) due to the evolution of CO_2 gas of the blowing reaction. After the nucleation stage, cells start to grow due to the gas diffusion from the higher-pressure regions (liquid phase) to the lower pressure ones (bubbles); meanwhile, the foam consolidates its structure due to the polymerization reaction. Hence, its expansion rate slows down due to a combination of polymerization (viscosity increase) evolution and the reduced amount of gas produced. The density evolution shows that the foams attain their final density after 400 s, which coincides with the Berghmans point of these foams where vitrification freezes the morphology.^{5,6}

The observed differences should mainly be ascribed to changes in the physical characteristics of the initial reactant, in particular the viscosity of the polyol/CNP dispersions and their surface tension. The slope of the relative density (Fig. 3) at the initial stages (60 - 80 s) of the foaming is then related to these characteristics and provides information about the foaming kinetics. The value of the slope (Table 2) decreases for nanocomposite foams containing CNPs, being the smallest for the system with MWCNTs followed by f-GS while the value for f-MWCNTs keeps practically unaltered. This observation seems to be, in part, related with the viscosity of the polyol—already determined in previous section—which agrees with a previous study by Bikard *et al.*⁴² showing that the larger the viscosity of the fluid, the slower the expansion in flexible foams. On the other hand, we can assume that the viscosity of the isocyanate is not having any significant influence considering it is 20 times lower than the one of the polyol. However, the obtained values do not directly correlate with the viscosity increase of the respective polyol/CNP dispersions since the chemical influence of CNPs on the reaction kinetics needs also to be taken into account. According to this, it seems that f-GS delay the reaction further than expected if we only consider the measured viscosity. Hence, the delay in the f-GS system should also respond to the presence of C-O groups on these nanoparticles. Theoretical modelling has shown that these groups can create hydrogen bonds with adsorbed water on their surface.⁴³ Consequently, the number of water molecules available for the reaction with the isocyanate is reduced with respect to the other systems and thus the generation of CO_2 gas, in agreement with previous results by

in-situ FTIR and synchrotron SAXS.⁶ A similar stronger effect needs to be considered in the case of the MWCNT's nanocomposite foam as regards of the results in bubble nucleation shown in next section.

Table 2 Values of the slope of the first points of relative density decrease of FPU nanocomposite foams.

Sample	Slope (-%/s)
Neat	1.36
MWCNTs	0.89
f-MWCNTs	1.31
f-GS	1.08

Besides the delay in the density evolution characterized throughout all the stages of the reaction, the final density of the FPU nanocomposite foams is slightly higher than neat PU foam, such increase is obviously attributed to a reduced volume expansion with no effect of the intrinsic density of the CNPs. This expansion reduction has also been observed in previous studies of CNPs filled PU foams.²⁴ The density increase is attributed to the viscosity increase of the mixtures, the wetting character of the CNPs, which in turn affect the matrix phase-separated morphology, and the mentioned chemical interaction, which reduces the amount of water molecules available.

3.3. Cell Size Evolution

The acquired radiographies of FPU nanocomposite foams at three different times can be observed in Fig. 4 in comparison to neat FPU foams. The simple observation of the images demonstrates that the cell size of the open-cell FPU nanocomposite foams is smaller, at initial foaming stages, than the neat formulation. Nevertheless, this first evaluation is still not completely clarifying since the images, at a same instant, correspond to different expansion grades and thus some corrections need to be considered. On the other hand, in this first approach, CNPs appear to act as nucleating agents in flexible PU foams similar to the results observed for rigid foams with the same CNPs used in this study⁴⁴ and filled with nanoclays or nanosilicas.¹⁷

It can also be observed that final state ($t = 350$ s) of the produced nanocomposite foams does not strictly correspond to the cell size reduction observed in the initial stage, which in principle implies the presence of any degeneration mechanism during foam evolution. Cell diameters at this stage seem to agree with the cell size obtained in SEM micrographs Fig.6.

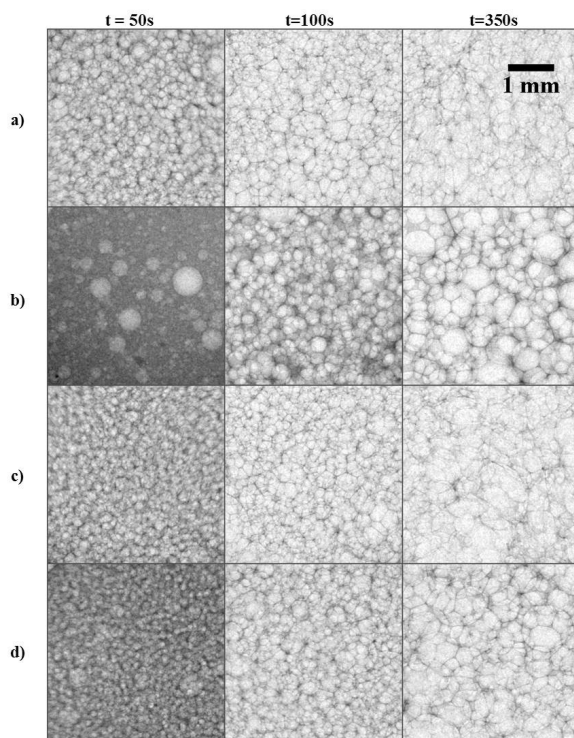


Fig. 4 X-ray radiographs of expanding flexible PU nanocomposite foams for: a) neat, b) MWCNTs, c) f-MWCNTs and d) f-GS.

The results for the quantitative analysis of cell size evolution are given in Fig. 5. This analysis excludes from the average diameter characterization the larger pores shown in the images –actually air entrapments– such as the ones clearly visualized in Fig. 4-b) at $t = 50$ s. The graph in Fig. 5 shows a dissimilar pore-growing slope for the different analysed materials. It is important to keep in mind that cell size evolution of PU depends on both the continuously polymerizing liquid matrix and the amount of dispersed gas phase, having several physico-chemical factors contributing to them.⁴ In our particular case, the slope is much higher in the case of MWCNTs followed by f-GSs and f-MWCNTs with a rather lower value in the case of neat PU. The quicker transition from smaller to larger pores can be interpreted as a sign of cell instability, i.e. presence of coalescence, although the different dynamics in density evolution also needs to be taken into account.

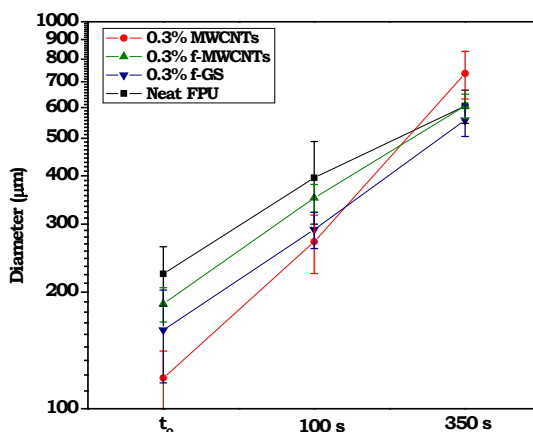


Fig. 5 Diameter of expanding flexible PU nanocomposite foams at 50, 100 s and 350 s.

3.4. Cell Density Evolution

Cell density values were calculated according to Eq 3 and exhibit a varying behaviour depending on the nanocomposite formulation used (Fig. 6). According to the results, it is possible to assess that neat formulation does not show a significant cell density decrease (at least upon the analyzed point), while the nanocomposite formulations seem to promote instability in the evolving foam. Hence, flexible PU foam is largely affected by the presence of both carbon nanotubes and functionalized graphene sheets while the functionalized nanotubes present a smaller interaction. Previous studies on rigid PU nanocomposite closed cell foams reinforced with organoclays showed a constant cell density throughout all the foaming process without film ruptures.^{17, 18} Although in the particular formulations of open cell foams the surfactant content is finely adjusted in order to prevent coalescence upon an optimum viscosity, which subsequently allows cell opening via cell wall thinning but generally prevents coalescence. The results also confirm the apparent nucleation effect observed at the early stages (Fig. 5) both for MWCNT and f-GS nanocomposite foams. In the case of MWCNT the nucleation enhancement reaches 85% whereas in the case of f-GS we can observe a 30% and in the case of f-MWCNT the nucleation is similar.

$$N_c = \frac{6}{\pi\phi^3} \left(\frac{\rho_{solid}}{\rho_{foam}} - 1 \right) \quad (3)$$

The nucleation mechanism mainly depends on the interfacial surface area between the polymer and the nanoparticles and, obviously, on their dispersion and surface character.³ Therefore, the addition of nanofillers induces heterogeneous nucleation in polymer foams, being their efficiency higher as their dispersion and distribution in the polymer matrix are optimal. Nonetheless, one of the main aspects that should be taking into consideration on the effectiveness of the nucleation is the surface nature of the nanoparticles besides their surface morphology. The inclusion of oxygen-bearing groups

during the functionalization of carbon nanotubes and graphene sheets changes the hydrophobic character of these CNPs to hydrophilic. Highly hydrophobic nanofillers, such as MWCNTs, favoured the nucleation mechanism due to their non-wetting surface, inducing destabilizing effects in the thin membranes at longer times via the so-called bridging-dewetting mechanisms.⁴⁵⁻⁴⁷ Meanwhile, hydrophilic nanoparticles, as f-MWCNTs, have the opposite effect and appear to act as foam stabilizers. In this context, it should be expected for f-GS similar behaviour as for f-MWCNTs because of their hydrophilic character thanks to the presence of epoxy, hydroxyl and carboxyl groups. However, systems with f-GS present an intermediate state between MWCNTs and f-MWCNTs. Hence, the flat surface of graphene plays a key role on the initial nucleation mechanism, also observed in nanofillers with the same morphology i.e. nanoclays¹⁷ but their hydrophilic nature avoid the bridging-dewetting mechanisms observed on MWCNTs.

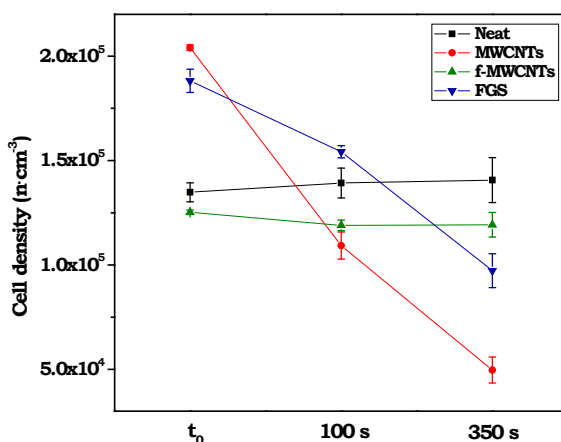


Fig. 6 Cell density values of FPU nanocomposite foams at t_0 , 100 s and 350 s.

With regards the coalescence phenomena we can assess from the numerical results and the visual observation of the process, that MWCNTs induce the largest coalescence throughout the full expansion process. On the other hand, f-MWCNTs show a no appreciable cell density reduction keeping a nearly constant value and, indeed, coalescence is not observed in the process. Finally a similar drastic effect is observed in the case of f-GS with a cell density decaying more than 100% of the initial value. These differences are, in part, attributed to the surface nature of the nanoparticles mentioned above and their effect on the phase-separated matrix morphology.⁶

Micrographs in Fig. 7 show that results obtained via *in-situ* X-ray radioscopy are consistent with the *ex-situ* results of produced and stabilized foams. The results reveal that final cell size in the case of both types of MWCNTs is larger than the one observed in the neat formulation. On the other hand the cell size for f-GS is little smaller although the quality of the micrograph does not allow to clearly evaluate it. It is

important to mention that the foam matrix with f-GS seems to reach uncompleted curing, which causes structure deterioration during sample preparation.

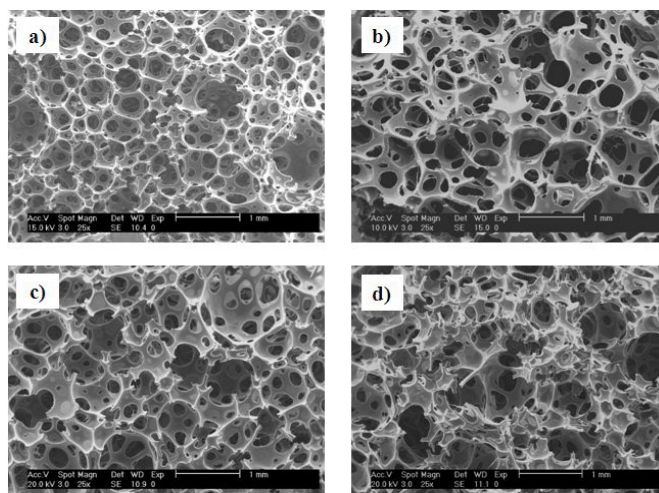


Fig. 7 Representative SEM images of flexible PU nanocomposite foams: a) neat, b) MWCNTs, c) f-MWCNTs and d) f-GS.

4. Conclusions

The foaming evolution of flexible PU nanocomposite foams has been examined by *in-situ* X-ray radioscopy and the effects of carbon-based nanofillers and their surface treatment have been observed. The rheological behaviour of the polyol/CNP dispersions is influenced by the nanoparticles, particularly in the case of MWCNTs. Expansion kinetics is delayed by the CNP, probably due to a combination of enhanced viscosity (physical interaction) and a delay in the blowing kinetics (chemical interaction). The results at early stages also indicate that there is a significant cell nucleation enhancement for MWCNT and the f-GS nanocomposite foams. Only the f-MWCNT's seem to promote a similar number of bubbles that neat FPU. On the other hand, the surface nature of the carbon nanoparticles, hydrophilic or hydrophobic, influences the physical events taking place on the evolved reactive PU nanocomposite foams, which corroborates the chemical processes observed for these systems by *in-situ* FTIR and synchrotron SAXS. Cell size evolution is strongly determined by the chemical interaction of the FPU formulation with the CNP added. Curiously, those particles that actively promoted the nucleation, due to a bridging-dewetting mechanism and surface morphology, seem to chemically interact with the surfactants and/or the curing reaction promoting coalescence that drives to final lower cell densities.

5. Acknowledgements

Financial support from the Spanish Ministry of Science and Innovation and FEDER funds (MAT2009-14001-C02-01, MAT 2010-18749 and MAT 2012-34901), the European Space Agency (Project MAP AO-99-075), the 7th Framework Program of E.U. through HARCANA (NMP3-LA-2008-213277), Juan de la Ciara contract by the Ministry of Economy and

Competitiveness (E. Solórzano, JCI-2011-09775) and PIRTU contract by Junta of Castile and León co-financed by the European Social Fund (S. Pardo-Alonso, EDU/289/2011) are gratefully acknowledged. M.M. Bernal also acknowledges the FPI from MICINN.

Notes and references

^a Institute of Polymer Science and Technology, CSIC, 28006, Madrid, Spain. Email: mar.bernal@imdea.org

^b CellMat Laboratory, Condensed Matter Physics Department, Science Faculty, University of Valladolid, Paseo de Belén, 7, 47011 – Valladolid, Spain. Email: samuelgado.alonso@fmc.uva.es

References

1. L. J. Lee, C. Zeng, X. Cao, X. Han, J. Shen and G. Xu, *Composites Science and Technology*, 2005, **65**, 2344-2363.
2. C. C. Ibeh and M. Bubacz, *Journal of Cellular Plastics*, 2008, **44**, 493-515.
3. L. Chen, D. Rende, L. S. Schadler and R. Ozisik, *Journal of Materials Chemistry A*, 2013, **1**, 3837-3850.
4. G. Harikrishnan, T. U. Patro, A. R. Unni and D. V. Khakhar, *Soft Matter*, 2011, **7**, 6801-6804.
5. M. M. Bernal, M. A. Lopez-Manchado and R. Verdejo, *Macromolecular Chemistry and Physics*, 2011, **212**, 971-979.
6. M. M. Bernal, M. Martin-Gallego, L. J. Romasanta, A.-C. Mortamet, M. A. López-Manchado, A. J. Ryan and R. Verdejo, *Polymer*, 2012, **53**, 4025-4032.
7. G. Woods, *Flexible Polyurethane Foams. Chemistry and Technology*, Applied Science Publishers LTD, London, 1982.
8. D. Klemperer and V. Sendjarevic, *Handbook of polymeric foams and foam technology*, Hanser Publishers, Munich, 2004.
9. S. T. Lee and N. S. Ramesh, *Polymeric foams: mechanisms and materials*, CRC Press LLC, Boca Raton, Florida, USA, 2004.
10. J. Bicerano, R. D. Daussin, M. J. A. Elwell, H. R. v. d. Wal, P. Berthevas, M. Brown, F. Casati, W. Farrissey, J. Fosnaugh, R. d. Genova, R. Herrington, J. Hicks, K. Hinze, K. Hock, D. Hunter, L. Jeng, D. Laycock, W. Lidy, H. Mispereuve, R. Moore, L. Nafziger, M. Norton, D. Parrish, R. Priester, K. Skaggs, L. Stahler, F. Sweet, R. Thomas, R. Turner, G. Wiltz, T. Woods, C. P. Christenson and A. K. Schrock, in *Polymeric Foams. Mechanisms and Materials*, eds. S. T. Lee and N. S. Ramesh, CRC Press, Boca Raton, Florida, USA, 2004.
11. R. A. Neff and C. W. Macosko, *Rheologica Acta*, 1996, **35**, 656-666.
12. G. Harikrishnan, T. U. Patro and D. V. Khakhar, *Industrial & Engineering Chemistry Research*, 2006, **45**, 7126-7134.
13. A. N. Wilkinson, N. H. Fithriyah, J. L. Stanford and D. Suckley, *Macromolecular Symposia*, 2007, **256**, 65-72.
14. W. Li, A. J. Ryan and I. K. Meier, *Macromolecules*, 2002, **35**, 5034-5042.

15. M. J. Elwell, A. J. Ryan, H. J. M. Grünbauer and H. C. Van Lieshout, *Macromolecules*, 1996, **29**, 2960-2968.
16. X. D. Zhang, D. W. Giles, V. H. Barocas, K. Yasunaga and C. W. Macosko, *Journal of Rheology*, 1998, **42**, 871-889.
17. S. Pardo-Alonso, E. Solorzano, S. Estravis, M. A. Rodriguez-Perez and J. A. de Saja, *Soft Matter*, 2012, **8**, 11262-11270.
18. S. Pardo-Alonso, E. Solórzano and M. A. Rodriguez-Perez, *Colloids and Surfaces A: Physicochemical and Engineering Aspects*, 2013, **438**, 119-125.
19. R. Verdejo, F. J. Tapiador, L. Helfen, M. M. Bernal, N. Bitinis and M. A. Lopez-Manchado, *Physical Chemistry Chemical Physics*, 2009, **11**, 10860-10866.
20. E. Solórzano, J. Pinto, S. Pardo, F. Garcia-Moreno and M. A. Rodriguez-Perez, *Polymer Testing*, 2013, **32**, 321-329.
21. C. Singh, M. S. Shaffer and A. H. Windle, *Carbon*, 2003, **41**, 359-368.
22. P. J. F. Harris, *Carbon nanotube science. Synthesis, properties and applications*, Cambridge University Press, 2009.
23. R. Verdejo, S. Lamoriniere, B. Cottam, A. Bismarck and M. Shaffer, *Chemical Communications*, 2007, 513-515.
24. R. Verdejo, R. Stampfli, M. Alvarez-Lainez, S. Mourad, M. A. Rodriguez-Perez, P. A. Bruhwiler and M. Shaffer, *Composites Science and Technology*, 2009, **69**, 1564-1569.
25. M. M. Bernal, PhD Thesis, Universidad Politécnica de Valencia, 2012.
26. R. Verdejo, F. Barroso-Bujans, M. A. Rodriguez-Perez, J. A. de Saja and M. A. Lopez-Manchado, *Journal of Materials Chemistry*, 2008, **18**, 2221-2226.
27. B. C. Brödie, *Philosophical Transactions of the Royal Society of London*, 1859, **149**, 249-259.
28. D. R. Dreyer, S. Park, C. W. Bielawski and R. S. Ruoff, *Chemical Society Reviews*, 2010, **39**, 228-240.
29. E. Solórzano, S. Pardo-Alonso, J. A. d. Saja and M. A. Rodriguez-Perez, *Colloids and Surfaces A: Physicochemical and Engineering Aspects*, 2013, **438**, 167-173.
30. P. Potschke, T. D. Fornes and D. R. Paul, *Polymer*, 2002, **43**, 3247-3255.
31. J. H. Xu, S. Chatterjee, K. W. Koelling, Y. R. Wang and S. E. Bechtel, *Rheologica Acta*, 2005, **44**, 537-562.
32. S. T. Knauert, J. F. Douglas and F. W. Starr, *Journal of Polymer Science Part B-Polymer Physics*, 2007, **45**, 1882-1897.
33. T. Ramanathan, A. A. Abdala, S. Stankovich, D. A. Dikin, M. Herrera-Alonso, R. D. Piner, D. H. Adamson, H. C. Schniepp, X. Chen, R. S. Ruoff, S. T. Nguyen, I. A. Aksay, R. K. Prud'homme and L. C. Brinson, *Nature Nanotechnology*, 2008, **3**, 327-331.
34. H. Kim, A. A. Abdala and C. W. Macosko, *Macromolecules*, 2010, **43**, 6515-6530.

CHAPTER 5

35. D. R. Heine, M. K. Petersen and G. S. Grest, *Journal of Chemical Physics*, 2010, **132**, 184509.
36. H. S. Xia and M. Song, *Soft Matter*, 2005, **1**, 386-394.
37. M. Doi and S. F. Edwards, *The Theory of Polymer Dynamics*, Oxford Press, London, 1986.
38. S. Marceau, P. Dubois, R. Fulchiron and P. Cassagnau, *Macromolecules*, 2009, **42**, 1433-1438.
39. H. Kim and C. W. Macosko, *Polymer*, 2009, **50**, 3797-3809.
40. S. Pujari, S. Rahatekar, J. W. Gilman, K. K. Koziol, A. H. Windle and W. R. Burghardt, *Journal of Rheology*, 2011, **55**, 1033-1058.
41. C. Wan and B. Chen, *Journal of Materials Chemistry*, 2012, **22**, 3637-3646.
42. J. Bikard, J. Bruchon, T. Coupez and B. Vergnes, *Journal of Materials Science*, 2005, **40**, 5875-5881.
43. J. Berashevich and T. Chakraborty, *Physical Review B*, 2010, **81**, 205431.
44. M. M. Bernal, M. Martin-Gallego, I. Molenberg, I. Huynen, M. A. Lopez-Manchado and R. Verdejo, *RSC Advances*, Submitted.
45. R. G. Alargova, D. S. Warhadpande, V. N. Paunov and O. D. Velev, *Langmuir*, 2004, **20**, 10371-10374.
46. B. P. Binks, *Current Opinion in Colloid & Interface Science*, 2002, **7**, 21-41.
47. R. Aveyard, B. P. Binks, P. D. I. Fletcher, T. G. Peck and C. E. Rutherford, *Advances in Colloid and Interface Science*, 1994, **48**, 93-120.

"X-RAY RADIOSCOPY *IN-SITU* STUDIES IN THERMOPLASTIC POLYMER FOAMS"

Colloids and Surfaces A: Physicochem. Eng. Aspects 438 (2013) 167–173



Contents lists available at ScienceDirect

Colloids and Surfaces A: Physicochemical and Engineering Aspects

journal homepage: www.elsevier.com/locate/colsurfa



X-ray radioscapy in-situ studies in thermoplastic polymer foams

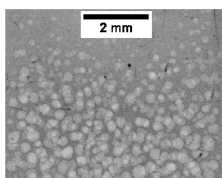
E. Solórzano*, S. Pardo-Alonso, J.A. de Saja, M.A. Rodríguez-Perez

CellMat Laboratory, University of Valladolid, Spain

HIGHLIGHTS

- ▶ Bubble nucleation, growth & coalescence have been studied in viscous PE & PP systems.
- ▶ Results indicate that bubble nucleation and growth velocity are anticorrelated.
- ▶ Coalescence presents long relaxation times over 10 s.
- ▶ Coalescence highly influences on the surrounding structure due to the high viscosity.

GRAPHICAL ABSTRACT



ARTICLE INFO

Article history:
Received 16 November 2012
Received in revised form 21 January 2013
Accepted 23 January 2013
Available online 31 January 2013

Keywords:
Thermoplastic
Polymer
Foam
Nucleation
Coalescence
X-ray imaging

ABSTRACT

The current work addresses results on two types of in-situ studies: bubble nucleation/growth and bubble coalescence for two thermoplastic materials (polypropylene and polyethylene) foamed by a chemical blowing agent (azodicarbonamide) under varying temperature conditions. The foaming process of these high viscosity materials has been in-situ monitored for the first time using a high resolution X-ray radiography set up. The studies were carried out in specially designed X-ray transparent furnaces reaching temperatures over the melting point of the polymer and the decomposition temperature of the blowing agent (which generates the expanding gas). Sequences of radiographies were typically acquired at 0.5 Hz. Image processing allowed evaluating several foam features such as cell nucleation rate and coalescence detection/quantification. Results on pore nucleation and growth indicate a high influence of heating rate for this variable and reveal an apparent competition between pore growth velocity and the number of nucleated pores. Results on cell coalescence highlight special features of this highly viscous systems in comparison to low viscosity ones (aqueous and metallic foams). Ruptures in these materials take much longer times (up to 10 s) and generate a large interaction with the surrounding cells making more difficult the quantification of the process.

© 2013 Elsevier B.V. All rights reserved.

1. Introduction

Thermoplastic foam systems are an attractive set of materials covering a broad spectrum of daily applications such as packaging, thermal/acoustic insulation, cushioning, buoyancy, etc. [1]. Since the early 60s, foam manufacturing technologies have been widely used in the industry to produce different foamed thermoplastic polymers [2] and nowadays they cover nearly 50% of the total foam

market [3]. Although thousands of final products have been successfully commercialized, some fundamentals on foam physics for these systems have not been sufficiently studied and most of the research works are limited to examination of the cellular structure and properties on already produced foams.

Thermoplastic foams produced using chemical blowing agents can be manufactured either in continuous or batch processes such as extrusion, injection molding, compression molding and rotomoulding [3]. From the thermal point of view, the foaming process of these materials is carried out at temperatures high enough to melt the polymer and to activate the chemical blowing agent (CBA) decomposition that generates the expanding gas [4]. All the thermoplastic foaming processes have the same stages in common:

* Corresponding author at: Faculty of Science, Paseo de Belén 7, 47011, Valladolid, Spain. Tel.: +34 983 423572; fax: +34 983 423192.
E-mail address: esolo@fmc.uva.es (E. Solórzano).

melting, nucleation, bubble growth/maturation and solidification [5]. Foaming process parameters and chemical composition need to be carefully adjusted in order to minimize the degeneration mechanisms taking place for any of these systems such as bubble coalescence and/or diffusion coarsening in the molten state. The complex equilibrium between the generation and degeneration mechanisms conditions the final cellular structure (cell size distribution, average cell size, cell density, etc). In most of cases thermoplastics present a rather high viscosity in the molten state which contributes to an enhanced stabilization of these systems in comparison to aqueous systems or molten metals. In this sense, these systems are less sensible to present high drain fluxes in the plateau borders [6]. Thus, they generally do not require additional stabilization and, when it is needed (for the production of very low density foams), the stability is promoted by chemical or physical crosslinking methods which provide viscosity enhancement up to several orders of magnitude [4,7]. Solid particles are frequently added but are not used for stabilization purposes, their main function is improving the properties of polymeric matrix and/or to promote heterogeneous nucleation.

Their characteristic high stability has probably contributed to generate a reduced attention to the foaming fundamentals on these systems, according to the scarce literature found. Another reason for the lack of knowledge on this topic is probably related to the fact that most of the foaming processes of thermoplastic are conducted using high pressures, being the foaming induced by a rapid pressure drop of the polymer containing a dissolved blowing agent. Fundamental studies on these materials are mostly focused on the determination of the rheological and extensional properties of thermoplastics at different temperatures or in presence of additives [8–10] but do not provide a real comprehension on the mechanisms acting, during foam generation and its dependence with formulation and processing variables. The in-situ studies on the phenomena taking place during foaming process, even visualization of bubbles in the plastic, are few and mostly oriented to solve practical aspects related to specific processing methods such as in roto-moulding [11,12] or injection moulding [13]. In this sense, the cross effects of matrix rheological properties, blowing agent type and content, additives used, dispersion of both the blowing agent/additives and foaming variables on the foam generation and stability have not been systematically studied although this is an important topic with the potential of generating a vast field for fundamental and applied research. Finally, the reduced number of scientific studies

on this subject is probably connected to technical and experimental difficulties associated to the in-situ observation of the cellular structure during foaming.

This paper aims at providing a first approach to the possibilities of this type of in-situ studies in thermoplastic foams. The paper is focused on the factors conditioning pore nucleation and growth at the early foaming stages in two different polymeric formulations. Particularly, we have analyzed the effect of the onset temperature of gas generation on the pore nucleation and its subsequent evolution as well as the effect of the rheological properties of two different polyolefins on the pore generation and growth. Additionally, a preliminary study on coalescence phenomena shows, the characteristic rupture pattern for these systems which is different to the ones already studied for low viscosity liquids.

2. Materials and methods

Time resolved X-ray imaging becomes unique and advantageous over other techniques since it is able to visualize, in real time, the internal cellular structure evolution during foaming processes [14] as no any other technique. In this investigation a microfocus high resolution X-ray system has been used. It is basically composed by a microfocus X-ray tube and a high resolution detector. Further details on the method and the possibilities of the technique have been reported elsewhere [15].

Two different kinds of experiments have been performed. Bubble nucleation experiments were performed in a thin rigid stainless steel frame with internal dimensions $12 \times 12 \times 1$ mm. In the centre of the frame, the thermoplastic system under study (thickness 0.6 mm) is located, in contact with a 0.5 mm thermocouple and suspended in the middle of the frame with a kapton adhesive strip used in both sides. In the bottom part, a 200 W resistive heater is situated in contact with the frame. The selected set up configuration (thin material, bottom heated) has two aims: on the one hand, to sharply visualize pore growth avoiding excessive bubble superposition that would have impeded the individual bubble recognition and, on the other hand, to provide a desired unidirectional heat flux promoting bubble nucleation and growth in a single direction. A schematic description of the system used is provided in Fig. 1 (left). By using this specific configuration it is possible to observe (Fig. 1, right side) the different foaming stages (melting, nucleation and growth) in a single image. In the top region the material is in molten state, in the middle one the pores are being

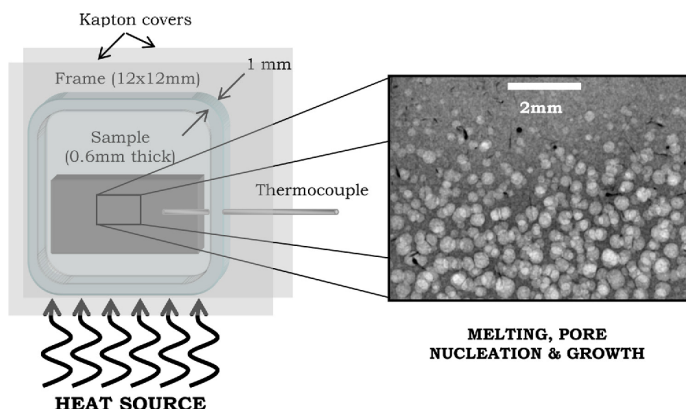


Fig. 1. Set up designed for monitoring the pore nucleation and growth with X-rays (left). X-ray radiography obtained during the foaming process (right).

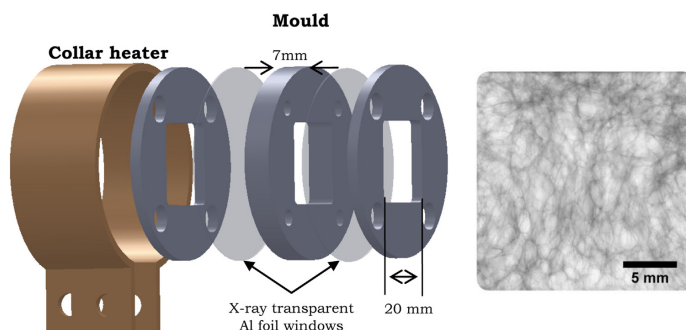


Fig. 2. Sketch of the mould for X-ray visualization of ruptures in molten state (left) and a typical radiography of the polymer foam obtained in this mould (right).

generated while at the bottom area all the pores are already generated and bubbles are growing. Pixel resolution achieved in this experimental configuration is 6.5 microns/pixel. Frame rate acquisition was fixed at 1500 ms although improved temporal resolution could be obtained by reducing the effective pixel size Fig. 2.

The second developed set-up was used to study coalescence phenomena. For this purpose an aluminium mould was specially machined. The cylindrical mould presents a rectangular cavity where the polymer containing the blowing agent is located. Two aluminium foil lids maintain the polymer into the cavity providing maximum contrast and two frames are used to keep the full system closed. A collar heater (power 250 W) is used to heat up the system under controlled conditions. A thermocouple is located in a drilled bore in the aluminium mould in a position close to the polymer. Temperature control was carried out by means of a PID controller. Pixel resolution achieved in this experimental configuration was 15 microns/pixel. Frame rate acquisition was fixed at 0.5 Hz since no improved temporal resolution is needed.

Image processing permitted to quantify diverse aspects on the gray-scale images obtained by radiographic acquisition. Different image analysis procedures were applied aimed at extracting different results. Manual contour tracing methodology (see Fig. 3) on a LCD tablet board was used to precisely monitor the cell size growth of selected pores by drawing the bubble contours. Additionally, the nucleation density was measured at different stages by marking the number of pores in the LDC display. Cell size evolution and cell density were calculated after computing the overlaid images by using ImageJ [16]. Automatic recognition of nucleated pores throughout the foaming process could have been also applied [14] but the low number of pores present in this material suggested the possibility of attempting a different methodology. Bubble coalescence recognition was carried out by the subtraction and comparison

of consecutive X-ray images with the aim of detecting localized pixel changes above a given threshold that correspond to cell wall ruptures. The methodology is similar to the one applied by Garcia-Moreno et al. [17] and further details on the analysis can be found there. A quantitative analysis of coalescence was performed only after foam expansion was completed (when the mould has been filled), otherwise macroscopic movement of features within the foam could produce significant artefacts. The number of rupture events detected automatically represented true ruptures in more than 95% of cases as verified by visual inspection. Detection problems associated to the particular rupture behaviour of this system led to a modification of the current established methodology as will be explained in the results section.

Different thermoplastic formulations have been studied. Low density polyethylene (LDPE, PE003 from Repsol, MFI 2.0 g/10 min – 190 °C, 2.16 kg-) has been mixed with 1 wt.% azodicarbonamide (Porofor ADC/M-C1, Lanxess) in a twin screw extruder. Complementarily, a second modified formulation, based on this one, was prepared by adding 0.15% of ZnO which allows reducing the temperature of gas release for this blowing agent. The amount of ZnO added shifts the onset of azodicarbonamide decomposition from 235 °C to 190 °C (data measured by thermogravimetric analysis in solid precursors using a heating rate of 10 °C/min). Finally, two different classes of polypropylenes (PP) have been comparatively used, both incorporating 2wt.% azodicarbonamide introduced by using a twin screw extruder. The selected materials are a linear polypropylene (PPH 4070 from Total Petrochemicals, MFI 3 g/10 min – 230 °C, 2.16 kg-) and a branched high melt strength (HMS) polypropylene (Daploy WB135 from Borealis MFI 2.4 g/10 min – 230 °C, 2.16 kg-). It is known that the different molecular structure of these polymers changes completely the extensional viscosity and melt strength, the branched material shows strain

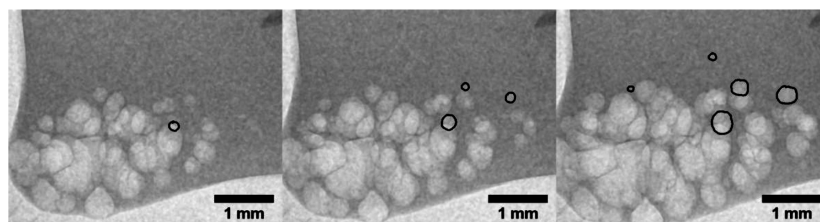


Fig. 3. Radiographic sequences at t , $t + 3$ s and $t + 9$ s. Manual contours are drawn in selected pores.

Table 1
Shear viscosity and Trouton ratio of the polymers under study.

Polymer	Extensional viscosity (Pas)	Trouton ratio
LDPE PE003	1.0×10^4	8.5
PPH4070	5.1×10^3	3
PPWB135 HMS	7.0×10^3	8.1

hardening and a higher melt strength [18] while the linear one does not, which is associated to a poorer foamability. Some key rheological characteristics of the polymers are included in Table 1. These measurements were performed by means of an AR2000EX TA Instruments rheometer with an extensional fixture using a strain rate of 1 s^{-1} . The shear viscosity value for the LDPE was measured at 135°C and Trouton ratio was obtained from the extensional curve at a time of 2.6 s. The shear viscosity values for the polypropylene materials were measured at 200°C and 1 s^{-1} and the Trouton ratio values were determined, similarly, at a time of 2.6 s.

The two polypropylenes under study present similar values of extensional viscosities. The main difference between these two materials is the much higher Trouton ratio of the HMS material. This rheological characteristic is a measurement of the polymer's strain hardening and was measured according to the procedure explained by Spitael et al. [10]. According to scale definition for Trouton ratio, a value of 3 indicates no strain hardening, which is a common result for linear polymers. The value showed by the HMS PP, around 8, is an indication of a significant strain hardening effect taking place due to the branched nature of this specific polymer.

Different heating conditions were applied up to a maximum set point of 240°C for LDPE and 260°C for PP. Table 2 summarizes the different tests performed for the two main classes of experiments. The table collects the experimental aim of each test, the two compared materials and the experimental conditions.

3. Results and discussion

3.1. Nucleation and pore growth

The analysis of the pore growth velocities by the methodology described in the previous section allowed obtaining precise results on the bubble growing velocity from the very early stages. Fig. 3 shows an image sequence of the manually contour-traced recognized pores in polyethylene. The very early nucleated pores in the corner have been skipped in order to avoid temperature inaccuracies expected in that region. The number of pores analyzed per sequence was approx. 10. Different sequences were analyzed in order to provide more robust statistics. The pore growing in the other non-overlaid pores can be clearly identified (left side of the images) which permits the confirmation that pores generated at similar time follow a very similar growth pattern.

One example of the results obtained after image processing is shown in Fig. 4. It can be observed that all the tracked bubbles grow at a similar velocity. The tracking process was stopped when pore diameter reached the sample thickness or when the analyzed pore was surrounded by an excessive number of pores that limit the free bubble growth. A transition in bubble expansion velocity is expected in both situations. The slope of the curves was calculated

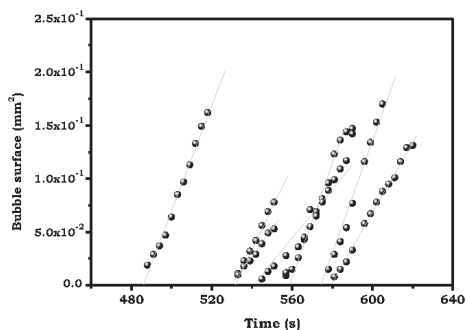


Fig. 4. Bubble growth tracking curves for different selected pores in linear PP.

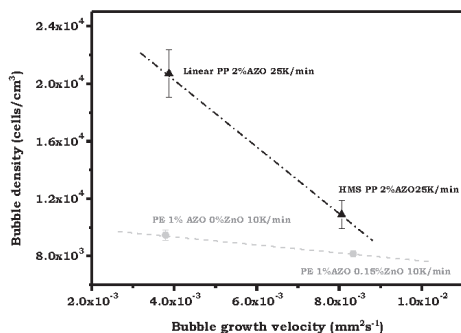


Fig. 5. Relationship between bubble growth velocity and number of bubbles per cubic centimetre for the two couples of materials studied.

from the individual bubble tracking curves and subsequently averaged. Cell density analysis was carried out in a similar region for the tracked pores after all the pores were already nucleated. The analysis was done with special care in selecting regions where coalescence was still not present. The analysis can be done by assuming that identified pores correspond to a known volume (surface and thickness) since all the pores produced in thickness can be visualized by this methodology. Temporal evolution of nucleation was not evaluated, in fact the value obtained can be considered as the maximum nucleation density since, on the one hand, at earlier stages not all the pores might be nucleated and, on the other hand, cell density will be reduced at longer times due to coalescence during foam maturation.

The results for the two couples of materials analyzed are shown in Fig. 5. According to these results it seems that bubble growth and bubble density are anticorrelated. This assumption seems to be, in principle, congruent with the fact that the blowing agent is generating a certain amount of gas that creates a volume expansion. If the expansion is distributed in a reduced number of bubbles

Table 2
Summary of experiments, materials and heating conditions performed.

	Experimental aim	Material-A	Material-B
Nucleation & growth	AZO onset temperature	LDPE + 1 wt.% AZO @10K/min	LDPE + 1 wt.% AZO + 0.15 wt.% ZnO@10 K/min
	Effect of melt strength	Linear PP + 2 wt.% AZO @ 25 K/min	HMS PP + 2 wt.% AZO @ 25 K/min
Coalescence	Effect of melt strength	Linear PP + 2 wt.% AZO 240°C	HMS PP + 2 wt.% AZO 240°C

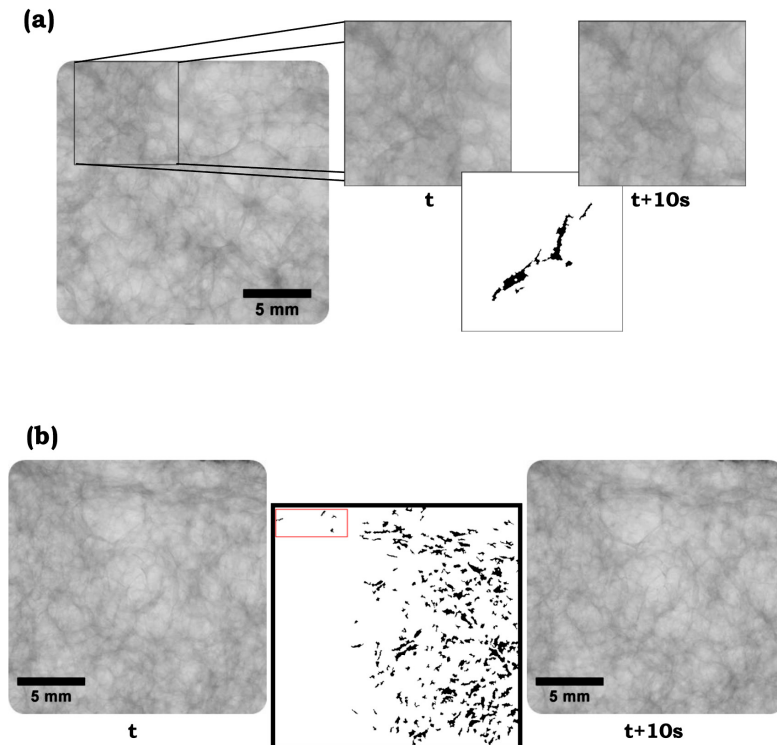


Fig. 6. (a) Local rupture detected; (b) local and massive rupture detected both within a time span of 10s in high melt strength PP.

they are forced to expand faster while the unitary expansion rate of individual bubbles becomes smaller when a higher number of pores are nucleated. Fig. 5 allows comparing the analyzed materials. In the case of polyethylene the effect of azodicarbonamide activation seems to cause a significant increase in the expansion rate (double value) although the number of nucleated pores does not significantly change. The higher bubble expansion rate is mostly associated to a significant increase in the gas generation rate and macroscopic expansion. On the other hand, the two studied polypropylenes generate a significantly different bubble density at early stages. In this sense linear PP generates almost double bubbles which growth approximately at half velocity in comparison to the high melt strength PP. Causes for this fact are unclear although it might be an effect related to a better dispersion of the blowing agent particles into the polymer matrix or an effect of polymer melt resistance to nucleate bubbles, which seems to be favourable in the case of linear PP with a lower extensional viscosity (Table 1). As regards of the results found here, heating rate might have a certain effect and it is expected that higher heating rates contribute to enhanced nucleation. Nevertheless further studies are needed to confirm this fact.

Finally, the azodicarbonamide content seems to have a combined effect on the overall nucleation capacity of the system. This is the reason why polypropylenes containing 2% of blowing agent are over polyethylenes in the graph (higher cell density) which is

already expected since the PP-systems contains, theoretically, double nucleation points by having double content of the chemical blowing agent. According to these results it could be also possible that polyethylene presented improved nucleation capacity at similar azodicarbonamide contents in comparison to HMS PP, fact which might also be related to the polymer viscosity during bubble generation. Nevertheless this fact needs from further experimental evidences.

3.2. Analysis of coalescence

The analysis of coalescence phenomena in polypropylenes has been carried out under the protocol explained in Section 2 which was previously successfully applied in the analysis of ruptures in metallic foams [17]. Nevertheless the analysis in these materials is by far more complicated in comparison to the referred one, especially due to the large viscosity of polymeric systems. In this sense, the observed experiments showed that most of ruptures take more than 10 s to be developed which require a modification of the standard procedure. To this end, a reduced number of radiographic images was analyzed and eliminating some intermediate images to modify 5 times the original frame rate, down to an effective one of 0.1 Hz. Otherwise the slight progressive movement developed during the rupture would have not been detected or, in case of being detected, the same rupture would be counted n-times till its

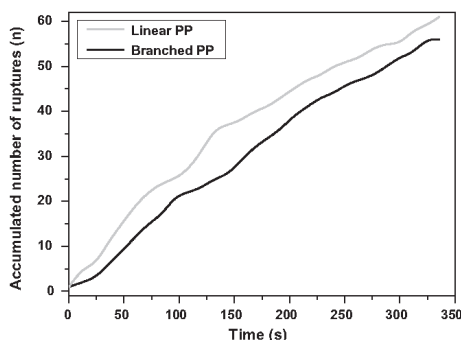


Fig. 7. Number of accumulated ruptures over a time of 330s for the two studied materials.

complete development. Another difficulty is related to the large foam volume involved in a rupture since the large viscosity implies much larger relaxation volumes. This effect significantly increases the effective area of the rupture although the rupture was originated due to a single cell wall tearing. As a direct consequence, no rupture area analysis will be reported in this section due to these artefacting aspects. Lastly, the high viscosity, in combination with the reduced mould thickness and the high polymer–surface adhesion may cause artefacts on the apparent stability and, possibly, coalesce phenomena are slowed down and propagated to a larger volume due to these surface effects. Nevertheless, it has been possible to perform a comparative study for the polypropylene materials.

Two image pairs show the different types of ruptures detected in the studied polymeric systems (Fig. 6). The first one, (a), is a local rupture developed within 10 s while the second image pair (b) shows two ruptures, one involving a large material movement and the other (top corner, marked in a square) a rather local one, involving only a limited foam volume. In most of cases, ruptures detected cause a massive displacement within the foam in the rupture direction. It is difficult to discriminate whether this displacement is causing additional ruptures (cascades, avalanches) and only the triggering rupture can be clearly identified. Local ruptures under the configuration used in this work are rather atypical. Differences in rupture pattern for both types of polypropylene studied are not very large although it seems that the slightly higher viscosity of HMS PP (Table 1) causes that a higher volume is involved in each rupture event.

Fig. 7 shows the accumulated total number of ruptures detected in the two studied polypropylenes over a total time of 330 s. The differences between the polymers are not very clear but point in the direction of a higher stability for the HMS PP (the material with a higher Trouton ratio, Table 1). The reduced thickness (7 mm) of the mould used is probably causing an enhanced apparent stability, thus reducing the expected differences among these two polymers. It is also important to point out that total number of ruptures in these systems are much less in comparison to the ones detected in other low viscosity systems such as molten aluminium [17] or not stabilized aqueous systems [19].

4. Conclusions

Time resolved X-ray imaging has been successfully applied for the first time to in-situ study bubble generation, growth and degeneration mechanisms of thermoplastic foamed materials by using innovative image processing techniques. The different

polypropylene and polyethylene formulations have showed significant differences in bubble nucleation. On the one hand, it seems that polyethylene present a better nucleation capability, probably similar to that of linear PP while HMS PP exhibits a rather low nucleation ability. Results also indicate that bubble growth and number of nucleated pores are anticorrelated when the same heating conditions are applied which is a microscopic manifestation of the macroscopic expansion, distributed in between the individual expansion of the pores. The analysis of ruptures in PP has been challenging due to the long rupture relaxation times and the large amount of material involved in each rupture. The characteristic pattern of coalescence in these systems has been reported for the first time. The results obtained might be influenced by the set up conditions and do not reveal the higher differences expected in between polymers. The set-up should be optimized for future work on this area.

The novel methodology developed during this research work can be potentially applied to almost any thermoplastic system and it will be very helpful to gain knowledge and fundamental understanding on the foam physics involved in the production of thermoplastic foams by using chemical blowing agents. This knowledge is necessary to develop novel and better formulations with improved nucleation efficiency and better stability on the molten state, which would be finally reflected in the physical properties of the foamed material.

Acknowledgements

Financial support from the Spanish Ministry of Science and Innovation and FEDER funds (MAT2009-14001-C02-01 and MAT 2012-34901), the European Commission (FP7 program, EC project Nancore number 214148), the European Spatial Agency (Project MAP AO-99-075), the Junta of Castile and Leon (project VA174A12-2), Juan de la Cierva contract by the Ministry of Economy and Competitiveness (E. Solórzano, JCI-2011-09775) and PIRTU contract by Junta de Castile and León co-financed by the European Social Fund (S. Pardo-Alonso, EDU/289/2011) are gratefully acknowledged.

References

- [1] K.C. Khemani, Polymeric foams: an overview, in: K.C. Khemani (Ed.), Polymeric Foams: Science and Technology, ACS Symposium Series, USA, 1997, Chap. 1.
- [2] D. Eaves, in: Handbook of Polymeric Foams, Rapra Technology, UK, 2004.
- [3] Business Communications Company 2004 Inc RP-120X Polymeric Foams - Updated Edition, USA.
- [4] M.A. Rodríguez-Pérez, Crosslinked Polyolefin Foams: Production, Structure, Properties.
- [5] D. Klempner, V. Sendjarevic, in: Handbook of Polymeric Foams and Foam Technology, 2nd Edition, Hanser Publishers, Munich, 2004.
- [6] S.A. Koehler, S. Hilgenfeldt, E.R. Weeks, H.A. Stone, Drainage of single Plateau borders: Direct observation of rigid and mobile interfaces, 66, Phys. Rev. E 040601 (2002).
- [7] D. Xu, R. Pop-Iliev, C.B. Park, R.C. Fenton, Fundamental study of CBA-blown bubble growth and collapse under atmospheric pressure, J. Cell. Plastics 41 (2005) 519–538.
- [8] M. Sugimoto, T. Tanaka, Y. Masubuchi, J.K. Takimoto Koyama, Effect of chain structure on the melt rheology of modified polypropylene, J. Appl. Polym. Sci. 73 (1999) 1493–1500.
- [9] G.J. Nam, J.H. Yoo, J.W. Lee, Effect of long-chain branches of polypropylene on rheological properties and foam-extrusion performances, J. Appl. Polym. Sci. 96 (2005) 1793–1800.
- [10] P. Spitaler, C.W. Macosko, Strain hardening in polypropylenes and its role in extrusion foaming, Polym. Eng. Sci. 44 (2004) 2090–2100.
- [11] R. Pop-Iliev, D. Xu, C.B. Park, Manufacturability of fine-celled cellular structures in rotational foam molding, J. Cell. Plastics 40 (2004) 13–25.
- [12] R. Pop-Iliev, K.H. Lee, C.B. Park, Manufacture of integral skin PP foam composites in rotational molding, J. Cell. Plastics 42 (2006) 139–152.
- [13] M. Mahmoodi, A.H. Behravesi, S.A.M. Rezavand, A. Pashaei, Visualization of bubble dynamics in foam injection molding, J. Appl. Polym. Sci. 116 (2010) 3346–3355.

- [14] S. Pardo-Alonso, E. Solórzano, S. Estravis, M.A. Rodríguez-Perez, J.A. de Saja, In situ evidence of the nanoparticle nucleating effect in polyurethane – nanoclay foamed systems, *Soft Matter* 8 (2012) 11262–11270.
- [15] E. Solórzano, J. Pinto, S. Pardo-Alonso, F. Garcia-Moreno, M.A. Rodríguez-Perez, Application of a microfocus X-Ray imaging apparatus to the study of cellular polymers, *Polym. Test.* 32 (2013) 321–329.
- [16] C.A. Schneider, W.S. Rasband, K.W. Eliceiri, NIH Image to ImageJ: 25 years of image analysis, *Nat. Methods* 9 (2012) 671–675.
- [17] F. Garcia-Moreno, E. Solórzano, J. Banhart, Kinetics of coalescence in liquid aluminium foams, *Soft Matter* 7 (2011) 9216–9223.
- [18] J. Stabge, H. Münstedt, Effect of long-chain branching on the foaming of polypropylene with azodiamide, *J. Cell Plastics* 42 (2006) 445–467.
- [19] N. Vandewalle, J.F. Lentz, S. Dorbolo, F. Brisbois, Avalanches of popping bubbles in collapsing foams, *Phys. Rev. Lett.* 86 (2001) 179–182.

6. 3D STUDIES ON CELLULAR STRUCTURE

This chapter presents two publications that use computed microtomography to characterize the cellular structure of solid foams. In this case, the study is limited to the *ex-situ* final stage of the foamed material. Therefore, a more advanced image quantification analysis is done since the image is not limited to 2D radiographic sequences.

If we have a look to the general scheme of this thesis presented in the introduction, this chapter corresponds to the *ex-situ* part in which the main objective is the development of new strategies to characterize in detail the structure of foams based on X-ray. The diagram in Figure 6-1 visually summarizes this chapter which presents the works focused on analyzing 3D cellular structure of polymer foams.

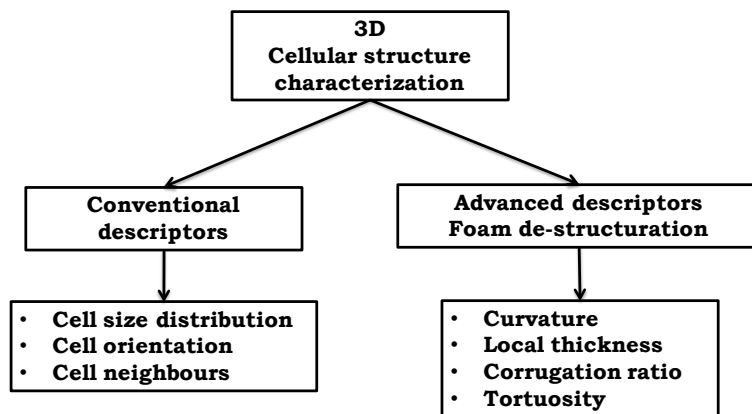


FIGURE 6-1.- OVERVIEW SCHEME OF THE CONTENTS INCLUDED IN THE WORKS CONTRIBUTING TO THIS CHAPTER.

6.1. SUMMARY

The first work "***3D Analysis of Progressive Modification of Cellular Architecture in Nanocomposite Polyurethane Foams***" was published in **European Polymer Journal Volume 49 (2013) 5, 999–1006**. It addresses the effect of nanoclays addition on the cellular descriptors of nanocomposite (nanoclays, Cloisite 30B) rigid polyurethane foams. In this work, conventional and some non-conventional cellular descriptors (not studied before) are calculated. The basis is the X-ray microtomography technique in combination with self-developed image analysis procedures and software. The non-conventional cellular architecture descriptors analyzed have been previously scarcely explored by microtomography although they contain important information to understand the final properties of these materials.

Conventional parameters such as pore size distribution, anisotropy or the existence of preferred orientation are calculated and related to nanoclays content. Nevertheless it is important to highlight results on the coordination number (number of neighbours) and polymer mass distribution in struts and walls. This last parameter has been calculated for the first time by microtomography and using a special image-based method specifically developed. This method enables foam de-structuration on the different foam components (basically walls and edges) permitting the calculation of mass redistribution in these foam components at increasing nanoclays contents.

Since one of the common handicaps of vast tomographic data post-processing is the long time often needed. We present one method that is simple and timesaving based on binary operations. This procedure is based on the dissimilarities of the two elements aimed to separate; struts and walls. Iterative erosion-dilation operations allow eliminating the walls whereas struts remain preserved. This procedure can be applied to PU foams since they show large differences between material fraction located at struts and walls. Finally, it was possible to estimate average cell wall thickness by using indirect geometry foam modelling. Furthermore, this de-structuration methodology that allows virtual separation of struts and walls is essential for the development of the second work presented in this chapter.

The 3D analysis investigates the effects on cellular structure of nanoclays addition to rigid PU foam in terms of average cell size, cell size distribution and cell wall thickness. The work also studies modification affecting other features such as cell anisotropy, cell free orientation, strut volumetric fraction and the distribution of cell coordination number.

The second paper is entitled "***μCT-based analysis of the solid phase in foams: cell wall corrugation and other practical microscopic features***". It has been sent for its consideration as an article in the journal *Microscopy and Microanalysis* after being part

of an oral communication at ICTMS 2013 International Conference in Gent (Belgium). It presents a second order analysis of features characterizing cellular structures such as cell wall thickness, curvature, corrugation ratio and cell wall tortuosity. The study of all these parameters is focused on process-induced corrugation at the cell walls identification and analysis. From the materials point of view, it is important to note that non-flat cell walls are known to be the origin of mechanical failure; therefore the quantification of corrugation of cell walls is an advanced and valuable descriptor to characterize foams. As an example Gibson-Ashby model for collapse-stress assumes that the microstructure of these materials consists of a large number of thin threads, connected at their ends by non-deformable volumes constituting a three-dimensional network. Nevertheless, foams often present corrugated cell walls due to temperature changes during foam solidification and after-process gas diffusion that induces shrinkage of polymer matrix constituting cellular structure.

The presence of these non-flat cell walls is typically observed in LDPE foams by means of thermo-mechanical analysis (TMA). During the first stages of gas expansion in a TMA experiment the thermal expansion is large due to the stretching of these corrugations in the cell walls. Then the expansion becomes significantly reduced as the walls are completely stretched. Alternatively, this work proposes a methodology based on 3D image analysis. It firstly uses the virtual separation of the struts and walls as the fundamental basis of de-structuration technique proposed in the previous work. The choice of samples with presence of corrugation impeded to fit the requirement of large differences between struts and walls. Subsequently, in this specific a methodology based on solid classification algorithm implemented in Imorph software was run in order to overcome this inconvenient and separate the struts from walls satisfactory.

Then a collection of four different analysis is presented and discussed. Some of them, as curvatures and local thickness calculations, are available for comparison either applied to the continuous foam network or the de-structured cell walls. On the other hand, a geometric parameter named corrugation ratio is defined and calculated together with solid phase tortuosity based on fast marching algorithm implemented in Imorph. The obtained results show that the performed analysis is very sensitive to small differences among samples. In fact, they provide very interesting and helpful information in order to develop better models for predicting the properties of foams.

“3D ANALYSIS OF PROGRESSIVE MODIFICATION OF THE CELLULAR ARCHITECTURE IN POLYURETHANE NANOCOMPOSITE FOAMS VIA X-RAY MICROTOMOGRAPHY”

European Polymer Journal 49 (2013) 999–1006



Contents lists available at SciVerse ScienceDirect

European Polymer Journal

journal homepage: www.elsevier.com/locate/europolj



Macromolecular Nanotechnology

3D Analysis of the progressive modification of the cellular architecture in polyurethane nanocomposite foams via X-ray microtomography



S. Pardo-Alonso^{a,*}, E. Solórzano^a, L. Brabant^b, P. Vanderniepen^b, M. Dierick^b, L. Van Hoorebeke^b, M.A. Rodríguez-Pérez^a

^a CellMat Laboratory, University of Valladolid, Valladolid, Spain

^b Department of Physics and Astronomy – UGCT, Ghent University, Ghent, Belgium

ARTICLE INFO

Article history:

Received 7 July 2012

Received in revised form 4 January 2013

Accepted 13 January 2013

Available online 23 January 2013

Keywords:

Nanocomposites

Foam

Microtomography

3D analysis

ABSTRACT

This paper presents a detailed characterization of the cellular architecture of rigid polyurethane (PU) nanocomposite foams with increasing contents of nanoadditives (nanoclays) by X-ray computed micro-tomography. The comparative study also includes the unfilled PU foam. Based on this technique and using 3D image analysis, a complete study on the evolution of the most typically analysed cellular descriptors (cell size distribution, cell size and anisotropy ratio) is provided. Furthermore, non-conventional descriptors such the cell-coordination number, strut volumetric fraction (f_v) and cell wall thickness are studied. Results confirm that nanoclays addition modifies the mean cell size and cell size distribution. In addition, it is also proved that the pore orientation, cell-coordination number and strut volume fraction are clearly influenced by nanoclays presence. The presented methodology allows obtaining a better understanding of the effects of nanoparticles during the foaming process and is important to gain knowledge on the structure–property relationships for these materials.

© 2013 Elsevier Ltd. All rights reserved.

1. Introduction

Cellular nanocomposites combine both the low density of cellular materials and enhanced properties due to nanofillers inclusion in the polymer matrix [1–4]. Nowadays, they are an attractive set of materials since they broaden the range of properties of solid composites and improve the properties of conventional foams. Therefore, they are suitable candidates to fulfil the necessities of a wide range of lightweight applications in industrial sectors such as aeronautical, automotive, cushioning, packaging, medical and renewal energies, although research efforts are still needed to satisfy the necessities of these markets.

Vast investigation has been carried out in both thermoplastics and thermosets nanocomposite foams [1–4] and from this experience it has been found that, apart from

an important role on final properties, nanofillers have significant impact during the foaming stages varying the chemistry, rheology and the key foaming mechanisms (nucleation, growth, coalescence, coarsening, etc.) of the system and as a consequence they modify the final cellular structure. As an example, it is known from the literature [3–11] and also from our laboratory experience that the infusion of nanoclays in a PU matrix [12] results in significant changes in the cellular structure.

Conventional imaging techniques, such as optical microscopy and scanning electron microscopy (SEM) provide 2D information about the cellular structure by examining cross sections [13–16]. Complementarily, several existing models in the literature aim to introduce stereological corrections to calculate 3D values from the experimentally measured 2D data [17–19].

Under these limitations X-ray microtomography seems to be a suitable technique to analyse the real structure of cellular materials since it is a high resolution non-destructive

* Corresponding author. Tel.: +34 983423572; fax: +34 983423192.
E-mail address: samuelpardo.alonso@fmc.uva.es (S. Pardo-Alonso).

technique (NDT) that offers reliable three dimensional (3D) visualization of unaltered samples [20–22], whereas the 2D examination needs from cutting operations or vacuum (in SEM) that may alter the cellular structure [23].

Nevertheless, microtomography is not exempt of difficulties and, as an example, the numerical quantification of 3D images implies the use of software that exceeds the computation capabilities of conventional computers and needs experienced users. Furthermore, in the case of polymer foams, their examination implies some technical difficulties. Particularly, there exist large dimensional disparities between the different foam constituents (example: pores with mean cell sizes of $10^2 \mu\text{m}$ combined with ultrathin cell walls with thickness ranging 1–5 μm) which complicates the choice of a resolution capable to resolve those very thin walls, having at the same time sufficient field of view to scan/analyse a representative number of pores.

Many existing works describing X-ray tomography results in cellular polymers use synchrotron X-ray sources [24–27] and more recently lab-scale devices using cone-beam microtomography [28,29]. However, there are few works in the literature specifically focused on polymer foams and their cellular architecture description using microtomography. The existing ones are limited to the analysis of conventional cellular parameters such as cell size distribution, average cell size, anisotropy and porosity [29,30] but they do not describe cellular structure in terms of indirectly calculated descriptors such as the number of neighbours, volumetric strut fraction and average cell wall thickness.

The purpose of this investigation is to carry out a complete microtomography study on the progressive modification of the cellular structure of rigid PU nanocomposites foams with different nanoclays contents. In combination with 3D image analysis, accurate quantitative values of the main cellular descriptors will be obtained. In particular the parameters under study are cell size distribution, average cell size anisotropy (pore orientation), the topological cell relations (number of neighbours), the volumetric strut distribution (in walls and struts) and the cell wall thickness. The developed methodology, that could be used for other materials, allows obtaining important information for both getting a better understanding of the foaming process and gaining knowledge on the structure–property relationships for this intricate systems.

2. Materials and methods

2.1. Materials

A rigid commercial PU formulation supplied by BASF was used. The polyol blend component, Elastopor® H 1501/1, contains catalysts, stabilizers and blowing agent (water). The isocyanate, IsoPMDI 92140, is a diphenylmethane diisocyanate. The low viscosity values (650 mPa s for the polyol and 300 mPa s for the isocyanate) facilitate both the mixing process to produce optimum nanoparticles dispersion, which, as it is described in the literature [1,8], it is essential to observe the potential effects of nanofillers. According to supplier technical data sheet,

parts proportions were set at 100/160 for the polyol and isocyanate.

Clonite® 30B (Southern Clay Products) a natural montmorillonite organically modified, was the nanofiller selected. Contrary to other nanofillers, nanoclays are relatively inexpensive, commercial available and their layered morphology ($d_{001} = 18.5 \text{ \AA}$, 90% particles less than $13 \mu\text{m}$) with high aspect ratio and large specific surface areas enhances nucleation, and thus reduction of pore size [31,32].

An overhead stirrer (EUROSTAR Power control-visc P1), equipped with a 50 mm diameter 4-bladed propeller stirrer from IKA, was used to promote the dispersion and exfoliation of nanoclays in the polyol component. This process was carried out at low shear stress values (200 rpm during 120 s). Proper dispersion and exfoliation of the nanoclays were achieved and checked by SAXD it was used for revision process. Finally the previously mentioned stirrer but mounting a 50 mm diameter lenart-disc from Vollrath™, was used at 1200 rpm during 20 s for the two components mixing (polyol containing clays and isocyanate) that promotes the blowing and curing reactions. Once the reaction started, the reacting mixture was poured for free foaming into a cubic paper mould ($150 \times 150 \times 150 \text{ mm}^3$).

A series of increasing proportions of nanoclays contents (0.5%, 1%, 3% and 5%), apart from the neat PU –0% nanoclays – were produced for this investigation. Once the bulk foams were produced, they were frozen in liquid nitrogen and small cubes ($5 \times 5 \times 5 \text{ mm}$) were cut using a scalpel for the microtomography scans.

2.2. Methods

2.2.1. X-ray tomography

Microtomography scans were performed using X-ray customized equipment built at the Centre for X-ray Tomography at Ghent University (UGCT) [28]. This particular setup consists in a microfocuss X-ray tube FXE-160.50 source from Feinfocus (minimal spot size: 0.9 μm , Voltage: 20–160 kV, Current: 0–200 μA) with a maximum output power of 20 W, and a detection system PerkinElmer XRD 1620 CN3 CS a-Si flat panel with CSI screen (2048×2048 , 200 μm pixel size). A rotary stage from MICOS (UPR-160F AIR) is placed in between these two basic components. It is mounted over a linear stage which allows for movement in a wide gap (1.4 m approx.) in between the source and the detector varying the magnification factor, M , as described in Eq. (1) (SDD : source-detector distance, SOD : source-object distance). Some extra piezoelectric components facilitate the sample centering.

$$M = \frac{SDD}{SOD} \quad (1)$$

Two scanner settings were used in present work for and $SDD = 1388.28 \text{ mm}$ with a $SOD = 34.70 \text{ mm}$ ($M = 40$) and $SOD = 17.35$ ($M = 80$) used according to foam samples requirements. The higher magnification choice permitted to resolve better the cell walls (double resolution) although the field of view was also reduced by a factor 2.

A tube voltage below 60 kV and tube currents ranging 160–170 μA were used, the detector exposure time was 4000 ms, the rotation step size was 0.2° and the total scan time took 2 h.

Once the projections were acquired, the reconstruction of the tomogram was done using the Octopus, server/client reconstruction package [33].

2.2.2. 3D image quantification

Image quantification first implies certain histogram equalization and noise removal (median 3D filter, 1 pixel, 26-neighborhood conditions). This image enhancement protocol was applied “a posteriori” in selected subvolumes containing 1000^3 voxels of the reconstructed slices. Subsequently, analysis with Morpho+ [34] software allowed quantitative data analysis.

Image quantification under Morpho+ software involves several steps: image binarization (phase separation between air and polymer), removal of isolated pixels, first-stage pores identification, pores separation by watershed-based algorithm (whistling up non-resolved cell walls, see Fig. 1) and final quantitative computation of every pore and its neighbourhood. Border pores (those pores that are incomplete at the image margins) were removed to avoid statistics inaccuracy.

After applying this workflow, several cellular descriptors (cell size distribution, anisotropy, pore orientation, number of neighbours and strut volumetric fraction.) were obtained. The parameter used in this work, as descriptor of the pore diameter is the *equivalent diameter*; i.e. the diameter of an equivalent sphere containing the same number of voxels of the analysed pore. Additionally, the *bounding box* has been used for the calculations of anisotropy. It is related with the 3D pore dimensions (width, depth and height) of the smallest prism that includes all the voxels of the object, thus giving dimensions of the pore referred to the three space directions, X, Y and Z of a Cartesian system. Similarly to anisotropy, *pore orientation* indicates the largest elongation direction of each individual pore. To determine this orientation, an equivalent ellipsoid with the same moments of inertia than the object, is used. To accomplish this, the 3D moment of inertia tensor is

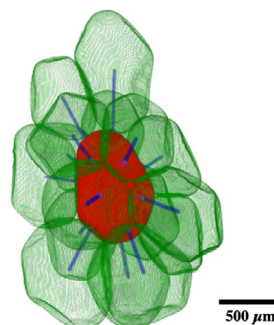


Fig. 2. 3D schematic view of cell coordination number. Lines connect the central pore with its nearest neighbours.

calculated and diagonalized. The corresponding rotation of the eigenvectors defines the orientation of the object, while the eigenvalues indicate the lengths of the principal axes of the equivalent ellipsoid. This descriptor will be used to construct the stereographic projection diagrams. The *cell coordination number* (or number of pore neighbours) is defined as the number of pores surrounding a certain one. Fig. 2 illustrates this concept by means of 3D imaging which lines connecting the central pore with the centres of the other neighbouring pores have been plotted. Finally, special image analysis procedures based on binary operations (erode or dilate) were used to study the *strut volumetric fraction*. (i.e. the volume in the struts with respects the total polymer volume within the foam).

Fig. 3 shows examples of reconstructed cellular structure of the unfilled PU and the PU containing 5% of nanoclays once the original slices were analysed according to the described workflow. The number of pores analysed for all the samples is high enough to have good statistics. A minimum of 220 pores were analysed for neat PU sample with the largest mean pore size and a maximum of 2900 pores were considered for the material containing 5% clays (the material with the lowest mean cell size).

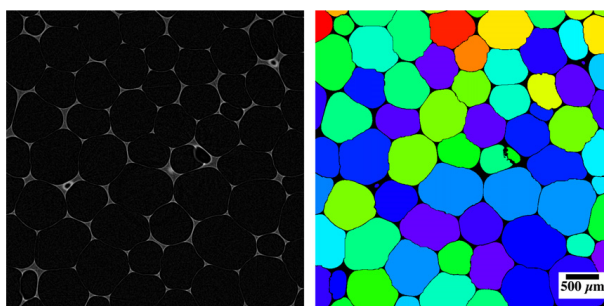


Fig. 1. Original acquired X-ray radiography and final mask of separated pores obtained after watershed segmentation.

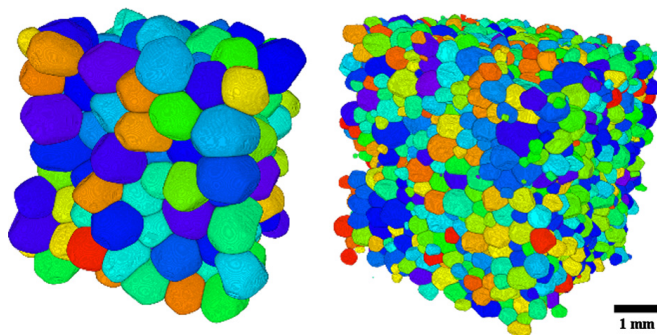


Fig. 3. 3D pores visualization of two reconstructed foams (neat PU –left– and 5% nanoclays-PU –right–).

3. Results and discussion

3.1. Average cell size and volume distribution

Equivalent diameter calculation provides directly the data for cell (pore) size and cell volume distribution. Fig. 4 indicates that average cell size is reduced 2.3 times, from 792 μm (neat PU) to 337 μm (5% nanoclays added), while the porosity and density across the investigated foams remains unchanged (porosity 94.5%, density 52 kg/m^3). Error bars in the graph represent the standard deviation of the calculated average cell size. In the top of Fig. 4, a 3D rendering of a representative cell is observed (a cell in the analysed material with a diameter similar to the calculated average). The results of the pore size analysis clearly shows the expected effect of nanoclays, previously commented in the introduction: they reduce the final cell size, probably due to an enhanced nucleation at initial foam stages creating larger number of small pores which are preserved till the final solid foam state in absence of significant coalescence and coarsening [12].

The cell volume can be derived from the equivalent diameter by geometric calculation as the volume of the equivalent sphere – it contains the same number of voxels as the pore –. Cell volume becomes reduced approximately 12 times when 5% clays are introduced.

Moreover, cell density calculations (number of pores per unit volume) confirm that the increase of nanoclays content results in higher cell densities according to the cubic inverse dependence shown in Eq. (2). Taking into account that foam density remains unchanged, cell density increased up to 290% when just 0.5% nanoclays are present and up to 1200% when nanoclays content is increased to the maximum of this study.

$$N_v = \frac{6}{\pi \phi^3} \left(\frac{\rho_{\text{solid}}}{\rho_{\text{foam}}} - 1 \right) \quad (2)$$

Fig. 5 shows cell size histograms in which the relative fraction of pores of a given volume has been multiplied by the pore volume to obtain the so-called volume fraction. The comparative results indicate that the shape of the

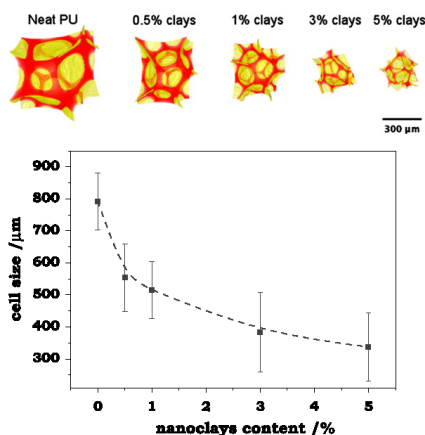


Fig. 4. (Top) Representative average cell 3D rendering (struts and walls) for each material and (bottom) mean cell size as a function of the nanoclays content.

distribution is not significantly altered by the presence of nanoclays and basically the distributions are shifted to smaller sizes. Nevertheless, residual large pores are still present in most nanocomposite foams and the curves present a tail at larger cells, which indicates that a low fraction of these pores is still present. It is interesting to note the connection of pore size descriptors with foam physical properties; for instance finer and homogeneous foamed structures show better mechanical response since stresses distribute better. Nevertheless, the existence of this low fraction of larger pores may suppress the benefits of having smaller pores in which stress is better distributed.

3.2. Anisotropy and pore orientation

Anisotropy and pore orientation are often related to manufacturing conditions and/or the gravity [35]. This

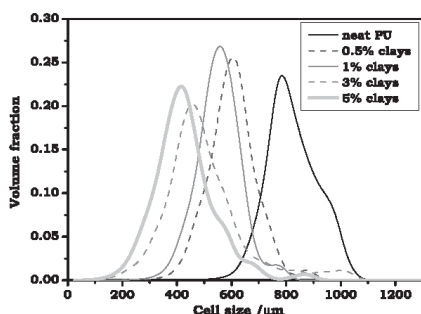


Fig. 5. Cell size distributions of the materials under analysis (0%, 0.5%, 1%, 3% and 5% nanoclays).

characteristic conditions the mechanical behaviour and transport properties (thermal, electrical). Therefore, we aimed to characterize possible modifications that occur in the samples when adding different percentages of nanoclays.

As previously commented, anisotropy is generally referred to Cartesian axes which are subsequently associated to processing direction. In this particular case Z is the foaming direction, coincident with the gravity direction. Thus, bounding box, offers width (X), depth (Y) and height (Z) magnitudes necessary to investigate anisotropy. It is important to mention that during the processing step Z-axis is kept as the free foaming direction, whereas X and Y remain slightly constrained due to recipient boundaries.

In this study, Z-anisotropy, or anisotropy ratio, R_z , was calculated as the average of Z/X and Z/Y ratios of the bounding box dimensions calculated for each analysed pore. Fig. 6 shows the Z-anisotropy comparative histograms for the different samples investigated, where the unit value would represent isotropic “spherical” cells and

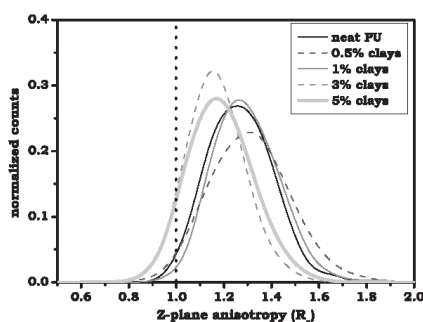


Fig. 6. Z-anisotropy histogram for the different samples examined in this work.

values higher than one represent elongated pores (prolate ellipsoids) in the Z-direction. Average anisotropy values obtained are in the range of 1.17–1.30. This value is congruent with that expected for polymeric foams [36].

It is observed a displacement of the distribution to unitary values when higher nanoclays contents are dispersed. Indeed, for 3% and 5% nanocomposites foams higher fraction of pores are elongated out of the Z-plane, i.e. X or Y-axis (5.4% contrary to 0.5% for the neat PU foam); and the mode value is situated nearer to the isotropic unitary value (see Fig. 6) while the average remains unchanged. One of the most feasible explanations for this behaviour is the influence of nanoclays in the curing reaction in combination with the quasi-unidirectional foam expansion in the Z direction during processing. Under this consideration, polymerization process tends to be slowed down and/or delayed in presence of nanoparticles [37] permitting an easier bubble re-accommodation while they still grow unidirectionally. In normal conditions (or at low nanoclays content) the polymerization occurs faster and foam bubbles are unidirectionally deformed at the very end of the foaming stage.

Stereographic diagrams (Fig. 7) are useful representations to understand the pores free-orientation. These stereograms show the orientation of every pore projected onto Cartesian planes and thus preserving angle values. As it was inferred from Fig. 6 the presence of high amount of nanoclays reduce the existing Z-orientation and cause that more pores are oriented in the X or Y direction. In Fig. 7 it is also possible to observe a non-perfect alignment of the preferred free orientation axis with the Z one. Thus foam orientation presents some angle deviation respect to Z-axis. This angle is probably associated to small deviation from foaming direction during sample preparation. Under this consideration, maximum orientation anisotropy, R_{max} , would be more sensitive to differences among samples.

Both anisotropy and pores orientation are closely related to mechanical and transport properties. As an example, Young's modulus and strength varies with R^2 and strength with R [36]. This behaviour makes anisotropy and orientation suitable parameters to be adapted in order to fit specific requirements (not always orthotropic foams fulfil the necessities).

3.3. Cell coordination number

Cell coordination number is a parameter not frequently reported in the literature although it contains important topological information on the cell shape, homogeneity and regularity. In principle, cell size reduction should not influence this parameter if pore homogeneity and regularity are maintained. Nevertheless, pores larger than mean size have to be surrounded by smaller neighbours leading to a higher coordination number. These larger pores are also sources of mechanical failure and introduce inhomogeneity. On the other hand, smaller pores than the average typically present smaller coordination numbers. The effect in mechanical properties of these smaller pores is not completely understood and might be diverse according to the literature [38].

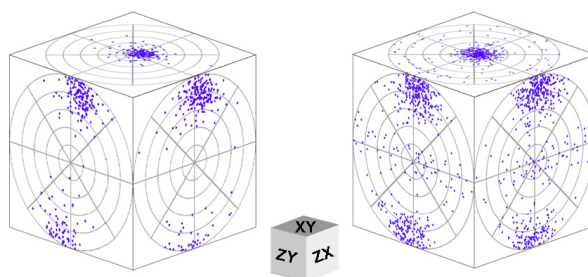


Fig. 7. Stereographic projections for 0% clays (left) and 5% clays samples.

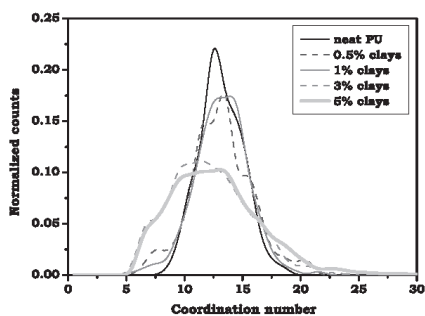


Fig. 8. Coordination number distribution comparative graph (0%, 0.5%, 1%, 3% and 5% nanoclays-content PU foam).

Under these considerations, it is necessary to analyse the effect of cell size on the coordination number. Detailed analysis of the histograms (Fig. 8) confirms that not only nanoclays are promoting cell size reduction but also they are definitely affecting the coordination number. In this case, there is an important curve shape modification with no significant shift in the X -axis. In all the cases both, mode and average values are around 12 neighbours, which is the coordination number for monodisperse foam with pores modelled as dodecahedrons [36,39]. In our case, at high nanoclays content, we find a significant population of pores with very low and high coordination numbers (although pores keep their average dodecahedron coordination). To this extent, the dodecahedron shape may also cohabit with other different polyhedron, for example tetrakaidecahedral shaped pores (14 faces) or even icosahedra (20 faces) yielding to higher number of neighbours and subsequently higher coordination number [36]. Random foams (3D Voronoi tessellations) show in average 15.54 faces per pore [40,41]. Looking in detail at Fig. 8, we observe the existence of cells with high coordination number similar to those already mentioned (Voronoi, tetrakaidecahedral or icosahedra). These larger cells, previously mentioned in Fig. 5 (with cell sizes in the range 700–900 μm), have high coordination numbers and are

surrounded by pores smaller than average size (around 200 μm in diameter, see Fig. 5) having smaller coordination number (less than 10 neighbours, see end-shoulder at 3% and 5% nanoclays in Fig. 8). It is important to mention that the 1% clays content appears to show an optimum coordination number Gaussian distribution. On the other hand, higher nanoclays contents (3% and 5%) shows pores larger and smaller than mean size introducing inhomogeneity.

3.4. Strut volume fraction and cell wall thickness

The developed foam solid network is basically composed of walls, struts (also called plateau borders) and vertices (or triple points). Vertices can be evaluated as an extension of struts since they are actually the junctions of these microstructures. Thus, it is possible to consider the existence of only two foam components (walls and struts). It is well known that presence/absence of walls (closed/open cell) is a determinant factor for the physical behaviour of the materials regarding mechanical, thermal, electrical or acoustic properties [36]. Furthermore, it is possible to consider intermediate situations, over the simplistic presence/absence of walls, by means of the strut volume fraction (f_s) that accounts for the amount of material contained in the struts referenced to the material in the whole foam (struts + walls). This parameter takes a value of 1 in the particular case of open cell foams and reaches particularly low values (0.1 approx.) in the case of low-density closed cell cross-linked polyolefin foams [42].

The conventional methodology to determine this parameter is based in 2D techniques. Literature reports two similar modelling approaches aiming to approximate the cross section of the strut to either an equivalent circle or triangle. Thus, Kuhn determines the equivalent circle in every cross section [15] whereas Glicksman uses a strut cross-section occupying two-thirds area of an equilateral triangle formed at the struts [16].

To our knowledge no 3D image-based methodology has been implemented to evaluate the strut volume fraction. Nevertheless, thanks to binary operations it is possible to de-structure the foam components and separate/distinguish the solid material forming the struts from the very thin cell walls. The success in foam de-structuration by



Fig. 9. 2D slice of a single cell after applying the struts identification methodology to the 1% clays/PU foamed material (identified struts are pure white).

erosion-dilation techniques is particularly possible for this kind of materials, rigid closed cell polyurethane foams, with sufficiently different sizes between walls and struts. Thus, two consecutive erosions (6-pixels neighbourhood condition) followed by three consecutive dilations allowed obtaining the regions where struts are located in order to separate them from the walls. Previously, the original pixel size was scaled with the calculated cell size by using bi-cubic interpolation methodology (this methodology eliminates possible effects of dissimilar resolution adapting the erosion “size” to the pore size). It is important to remark that the use of an extra dilation step (3 dilations versus 2 erosions) helps to compensate the non-dilated material in the strut-wall transition. Final eroded/dilated images are subtracted from the original binary image. The effect of this operation is equivalent to the use of a “smart mask” located at every strut, enabling the proper separation/identification of this material within the foam structure. Over-dilated pixels, which are not in correspondence with white pixels in the original image, are not considered. Fig. 9 shows an example of the result of applying this technique to the system containing 1% nanoclays. This technique does not modify the original shape of the strut, giving as a result a more realistic situation in comparison to either Kuhn or Glicksman strut modelling. Finally, f_s is obtained by dividing the number of white pixels constituting the strut architecture by the total number of white pixels (struts + walls) that comprises the original binarized foam.

Fig. 9 shows 2D strut identification (pure white) over the rest of foam structure (walls, in grey). Similar strut identification is showed in Fig. 4 (top) where it is possible to observe in 3D the discrimination between struts (red) and walls (yellow).

Table 1 shows the variation of strut volume fraction for the different nanoclays/PU foam composites examined in this work. Strut volume factor tends to increase with the increasing nanoclays content although the tendency is rather rough. Using the strut volume factor measured in combination with foam relative density, ρ_r and average cell size, ϕ , it is possible to calculate cell wall thickness,

Table 1

Strut volume fraction calculated by the erosion-dilation method.

Nanoclays content (%)	f_s
0	0.66557
0.5	0.62485
1	0.65720
3	0.78371
5	0.76175

δ , and its correlation with nanoclays content using the following equation

$$\phi(1 - f_s) \cdot \rho_r = C_n \cdot \delta \quad (3)$$

In this equation, C_n is a constant that depends on the pore shape modelled and its number of faces, n ($C_{12} = 3.46$ for pentagonal dodecahedron, $C_{14} = 3.35$ for tetrakaidecahedrons and $C_{20} = 2.99$ for icosahedrons) [36]. In congruence with the values obtained in Section 3.3 with an average value of 12.2 neighbours we have used a value of 3.46.

Fig. 10 provides information about the cell wall thickness variation. It is appreciated a significant reduction of the cell wall thickness when nanoclays are added, i.e. foams with smaller cells present a redistribution of polymer mass from cell walls to struts [43]. This is, on the one hand, caused by the cell size reduction (especially in the range up to 1% clays content) and, on the other hand, due to strut volume fraction increase (higher clays content, at 3% and 5%). Consequently, addition of a significant fraction of clays seems to modify the foaming process increasing the relative amount of material in the struts. As it was previously mentioned the presence of nanoclays could slow down the polymerization process permitting on the one hand an easier bubble re-accommodation (and thus reducing anisotropy (see Section 3.2)) and on the other hand due to the longer time between blowing and gelling giving more time to capillary forces to enhance drainage in the cell walls and then increasing the strut volumetric fraction.

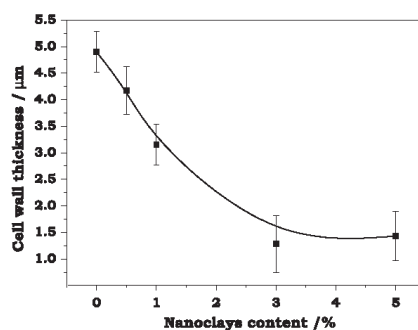


Fig. 10. Cell wall thickness variation as a function of the nanoclays content.

Apart from the fact that cell wall thickness implicitly influences mechanical properties through a higher strut volume fraction, dimensions of cell walls have a clear influence on the radiative and conductive properties of foams [44,45] and, thus, effective thermal conductivity largely depend on wall thickness.

This presented method based on image analysis is highly valuable since it allows indirect calculation of the cell wall thickness even when dimensions of the cell walls are in the limits of spatial/contrast resolution.

4. Conclusions

Cellular structure of foamed PU nanocomposites are non-destructively resolved by high resolution X-ray microtomography, which in combination with 3D image analysis, allowed the calculation of precise 3D quantitative structural information difficult to obtain with the same accuracy by 2D imaging techniques. Furthermore, special 3D image analysis workflow, based on binary operations, allowed determining the strut volumetric fraction of the foam network for the first time using microtomography.

The 3D analysis revealed important effects of nanoclays addition to rigid PU foam, which are particularly evident in terms of average pore size, pore size distribution and cell wall thickness. Intermediate influences of nanoclays were found for pore anisotropy, pore free orientation, strut volumetric fraction and the distribution of cell coordination number; although the average value of this last parameter resulted unaltered. The optimum combination of cellular parameters seems to be found at 1% of added nanoclays, considering that cell size is reduced and its size distribution becomes quasi-Gaussian. In this material the other parameters (anisotropy, coordination number, and polymer mass distribution) remains practically unaltered.

The developed methodology provides precise information of the cellular architecture of a given material. In addition it permits establishing with a better accuracy the effect of nanoparticles during the foaming process and is useful to gain knowledge on the foaming mechanisms taking place. It is also very helpful to establish the structure-property relationships for these systems.

Acknowledgements

UGCT (Ghent University) collaboration is acknowledged for the X-ray CT experiments and Samuel Pardo-Alonso research visit funded by University of Valladolid. Financial support from the Spanish Ministry of Science and Innovation and FEDER (MAT2009-14001-C02-01 and MAT 2012-34901), the European Space Agency (Project MAP AO-99-075), European Commission (FP7 program, EC Project Nan-core Number 214148), the Junta of Castile and Leon (VA174A12-2) PIRTU Contract of Samuel Pardo-Alonso by Junta of Castile and Leon (EDU/289/2011) and co-financed by European Social Fund and Juan de la Cierva contract JCI-2011-09775 (Spanish Ministry of Economy and Competitiveness) of Eusebio Solórzano are also gratefully acknowledged. The Special Research Fund of the Ghent University (BOF) is acknowledged for the doctoral grant

to Loes Brabant. Luis Vela from BASF Company supplying materials is also acknowledged.

References

- [1] Lee IJ, Zeng C, Cao X, Han X, Shen J, Xu G. *Compos Sci Technol* 2005;65:2344.
- [2] Ibeh CC, Bubac M. *J Cell Plast* 2008;44:493.
- [3] Cao X, Lee IJ, Widya T, Macosko C. *Polymer* 2005;46:775.
- [4] Widya T, Macosko CW. *J Macromol Sci, Part B: Phys* 2005;44:897.
- [5] Bernal MM, Martín-Gallego M, Romasanta IJ, Mortamet AC, López-Manchado MA, Ryan AJ, et al. *Polymer* 2012;53:4025.
- [6] Bernal MM, Molenberg I, Estravis S, Rodríguez-Pérez MA, Huynen I, López-Manchado MA, et al. *J Mater Sci* 2012;47:5673.
- [7] Mondal P, Khakhar DV. *J Appl Polym Sci* 2007;103:2802.
- [8] Lorenzetti A, Hrelja D, Besco S, Roso M. *J Appl Polym Sci* 2010;115:3667.
- [9] Verdejo R, Stämpfli R, Alvarez-Laine M, Mourad S, Rodríguez-Pérez MA, Brühwiler PA, et al. *Compos Sci Technol* 2009;69:1564.
- [10] Seo WJ, Sung YT, Kim SB, Lee YB, Choe KH, Choe SH, et al. *Polym Sci* 2006;102:3764.
- [11] Seo WJ, Sung YT, Han SJ, Kym IH, Ryu OH, Lee HS, et al. *Appl Polym Sci* 2006;101:2879.
- [12] Pardo-Alonso S, Solórzano E, Estravis S, Rodríguez-Pérez MA, de Saja JA. *Soft Matter* 2012;8(44):11262.
- [13] Rodríguez-Pérez MA. *Cell Polym* 2002;21:165.
- [14] ASTM D3572, Annual Book of ASTM standards, 8.02, 1994.
- [15] Kuhn J, Ebert HP, Arduini-Schuster MC, Buttner D, Fricke J. *Int J Heat Mass Transfer* 1992;35:1795.
- [16] Glicksman LR. In: low density cellular plastics: physical basis of behaviour. In: Hilyard NC, Cunningham A, editors. London: Chapman & Hall; 1994.
- [17] Sahagian DL, Prousevitch AA. *J Volcanol Geoth Res* 1998;84:173.
- [18] Rhodes MB, Khaykin B. Foam characterization and quantitative stereology. *Langmuir* 1986;2:643.
- [19] Montminy MD, Tannenbaum AR, Macosko CW. *J Cell Plast* 2001;37:501.
- [20] Banhart J. *Advanced tomographic methods in materials research and engineering*. UK: Oxford University Press; 2008.
- [21] Ohser J, Schladitz K. *3D images of materials structures: processing and analysis*. Wiley-VCH Verlag GmbH & Co. KGaA; 2009.
- [22] Lambert J, Cantat I, Delannay R, Renault A, Graner F, Glazier JA, et al. *Colloids Surf A* 2005;263:295.
- [23] Montminy MD, Tannenbaum AR, Macosko CW. *J Colloid Interface Sci* 2004;280:202.
- [24] Banhart J, Borbely A, Dzieciol K, et al. *Int J Mater Res* 2010;101:1069.
- [25] Baruchel J, Buffiere JY, Cloetens P, et al. *Scr Mater* 2006;55:41.
- [26] Müller B, Beckmann F, Huser M, et al. *Biomol Eng* 2002;19:73.
- [27] Elmoutaouakkil A, Fuchs G, Bergounhon P, et al. *J Phys D: Appl Phys* 2003;36:37.
- [28] Masschaele BC, Cnudde V, Dierick M, Jacobs P, Van Hoorebeke L, Vlassenbroeck J. *Nucl Instrum Methods Phys Res, Sect A* 2007;580:266.
- [29] Ma Y, Pyrz R, Rodríguez-Pérez MA, Escudero J, Rauche JCh, Su X. *Cell Polym* 2011;30:95.
- [30] Istrate OM, Chen B. *Soft Matter* 2011;7:1840.
- [31] Dasari A, Yu Z, Mai YW. *Acta Mater* 2005;55:635.
- [32] Nourbakhsh A, Ashori AJ. *Appl Polym Sci* 2009;112:1386.
- [33] Vlassenbroeck J, Dierick M, Masschaele B, Cnudde V, Van Hoorebeke L, Jacobs P. *Nucl Instrum Methods Phys Res, Sect A* 2007;580:442.
- [34] Brabant L, Vlassenbroeck J, De Witte V, Cnudde V, Boone MN, Dewanckele J, et al. *Micros Microanal* 2011;17:252.
- [35] Huber AT, Gibson LJ. *J Mater Sci* 1988;23:3031.
- [36] Gibson LJ, Ashby MF. In: *cellular solids: structure and properties*. 2nd ed. Oxford: Pergamon Press; 1988.
- [37] Bernal MM, López-Manchado MA, Verdejo R. *Macromol Chem Phys* 2011;212:971.
- [38] Kang JW et al. *Macromol Res* 2009;17:856.
- [39] Kraynik AM et al. *Phys Rev Lett* 2004;93:20.
- [40] Meijering JL. *Philips Res Rep* 1953;8:270.
- [41] Rivier N. *J Phys* 1992;43:91.
- [42] Rodríguez-Pérez MA. *Adv Polym Sci* 2005;184:97.
- [43] Placido E, Arduini-Schuster MC, Kuhn J. *Infrared Phys Technol* 2005;46:219.
- [44] Kaemmerlen A, Vo C, Aslanaj F, Jeandel G, Bailis D. *J Quant Spectrosc Radiat Transfer* 2010;110:865.
- [45] Biedermann A, Kudoke C, Merten A, Minogue E, Rotermund U, Ebert H-P, et al. *J Cell Plast* 2001;1:467–83.

“ μ CT-BASED ANALYSIS OF THE SOLID PHASE IN FOAMS: CELL WALL CORRUGATION AND OTHER PRACTICAL MICROSCOPIC FEATURES”

S. Pardo-Alonso¹, E. Solórzano¹, J. Vicente², L. Brabant³, L. M. Dierick³,
I. Manke⁴, A. Hilger⁴, E. Laguna¹, M.A. Rodríguez Pérez¹

¹CellMat Laboratory, Condensed Matter Physics Department, University of Valladolid, Paseo de Belén, 7 47011, Valladolid [email: samuelpardo.alonso@fmc.uva.es]

²Laboratoire IUSTI, CNRS UMR 7343, Aix Marseille Université, France

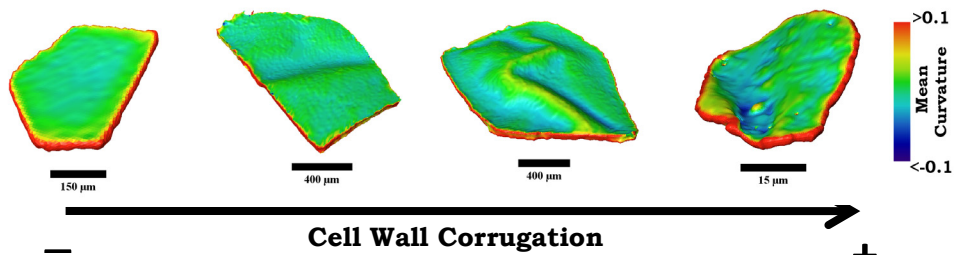
³UGCT-Department of Physics and Astronomy, Faculty of Sciences, Proeftuinstraat 86
9000 Ghent, Belgium

⁴FI-1 Helmholtz Zentrum Berlin, XXX

Keywords: tomography, image processing, 3D analysis, corrugation, tortuosity, cellular structure

ABSTRACT

This work presents a series of 3D computational methodologies with the objective of analyzing and quantifying the cell wall corrugation characteristics and other important microstructural parameters over a collection of low density polyolefin foams. Solid phase tortuosity, curvature and local thickness analysis have been used to study the presence of wrinkles located in the cell walls, which are strongly associated to the macroscopic mechanical behaviour of these materials. Complementary, a novel segmentation technique has been applied in the continuous solid phase offering a separate analysis of the constituting elements (struts and cell walls). The methodology is based on a solid classification algorithm and evaluates the local topological dissimilarities existing in between the constituting elements, which finally permits to separate the mentioned components. The separate analysis of curvature and thickness of the two solid constituents revealed additional differences which were not detected in the prior analysis over the continuous structure. The methodologies developed in this work are applicable to other types of porous materials in fields such as geosciences, biomedicine, etc



1. INTRODUCTION

Cellular materials are two-phase systems constituted by a solid continuous network and a continuous/discontinuous gaseous phase. Among the different types of cellular materials we can distinguish the, so called, *foams* in which the cellular structure is generated by induced gas-nucleation process in the liquid/molten state, thus generating stochastic structures [1]. These materials are largely produced and provide density reduction with respect to their solid precursors and nowadays are used in hundred of lightweight, comfort, insulation and cushioning applications for a wide variety of industrial sectors and markets such as automotive, aeronautical, renewal energies, leisure, etc. Foams can be generated via different processes [2, 3] giving as a result a large variety of structures (closed and open cell ones) and densities. Particularly, closed cell foams are characterized by a discontinuous gaseous phase separated by thin membranes denoted as *cell walls* while the edges and vertexes can be denoted by the term *struts*.

It is well known that physical properties (mechanical, thermal, acoustic, etc) of porous structures are strongly connected to their micro-scale morphology. Analytical models aim at predicting the macroscopic properties of these materials by considering several aspects in the micro-scale. A typical example is the mechanical response of foams subjected to compression. In this case, the stress is modelled to be supported both by walls and struts and gas compression (for low density flexible foams). The finest models consider, among other parameters, how the material is distributed between walls and struts using the mass fraction in the struts as a critical parameter to predict the mechanical behaviour [4]. The effect of cell wall corrugation has complementarily been studied and the results point to a high influence of this feature in the mechanical compliance [5,6,7]. Thermal and mass transport properties also depend largely on the microstructural features of foams as proposed by different authors [8, 9, 10, 11]. Therefore, there is a clear need to study, in detail, foams characteristics such as cell size, anisotropy/orientation, open-cell content, interconnections size, cell wall thickness, mass fraction in the struts or corrugation.

Most of these descriptors have been traditionally determined by 2D imaging techniques (optical or scanning electron microscopy) that limit the examination to the sample surface [6]. These techniques are combined with the implementation of tedious manual methodologies or semiautomatic computer-aid methods [12] that allow determining some of the critical parameters. In the last decade, thanks to the last advances in X-ray microcomputed tomography (μ CT), a more accurate 3D characterization of these materials can be obtained by semi-automatic 3D analysis methods [13, 14]. These methods have rapidly improved and evolved so, nowadays, the complete analysis workflow lasts 1-2 hours per sample.

In general, the 3D analysis of these cellular structures has been mainly focused on the gaseous-phase (pores) [15, 16] whereas the solid phase is less studied or even omitted; although some features related to solid phase are, indeed, relevant for modelling. In fact, the 3D processing techniques currently used are restricted/oriented to equivalent descriptors than the ones measured using 2D techniques. An illustrative example is the rather common use of a watershed algorithm [17, 18] to separate the continuous gaseous phase into isolated entities –pores– to later analyze them individually while, paradoxically, there is no available algorithm to separate the continuous solid phase into the required entities –struts and walls– to properly model both parts of the structure. The complexity of such type of algorithm is an obvious trammel but it still does not exempt this particular need since the application of a non-dedicated algorithm (watershed) fails catastrophically when it is applied for solid phase separation in walls and struts. In this sense, novel advanced 3D methodologies are needed in order to determine structural aspects linked to final properties and to achieve a further understanding on the micro/macro-scale interrelationship in these structures.

Furthermore, one of the expected advantages of using novel adapted methodologies is the possibility of obtaining skew-free 3D parameters up now only calculated by 2D methods using optical microscopy or SEM. Using other words, similarly to the skewed values found for 2D analysis in the pore size versus the 3D values [10], much larger deviations are expected for the determination of complex structural parameters such as in the case of material repartition in struts/walls, typically accomplished by indirect methodologies which combine complex manual measurements with simplified models for the cells shape [5, 6]. Finally, other specific descriptors such as the solid/gaseous phase tortuosity or cell walls corrugation ratio cannot be addressed by 2D methods and can only be reliably determined in 3D.

Aiming to cover the mentioned lack of methodologies, this work proposes a number of evaluation strategies for the solid phase analysis, by orienting our attention to the particular case of closed cell foamed materials. The workflow presented in this study analyzes the tortuosity, curvature and local thickness in the continuous solid phase. Then in a second order analysis carried out after a de-structuration step, evaluates again the mentioned features (curvature, local thickness) in the new discrete phases and, additionally, the presence of directional corrugation.

Despite the apparent specificity of the developed tools they can be extrapolated to analyze other materials and structures characterized, not only by X-ray tomography but by any other 3D methodology such as TEM, FIB, or neutron tomography, confocal microscopy, etc.

2. MATERIALS AND METHODS

2.1. MATERIALS

Four different commercial non-crosslinked and crosslinked low density polyethylene (LDPE) and ethylene-vinyl acetate copolymer (EVA) foams with densities ranging 27-65 kg/m³ were selected for this work. Fig.1 shows tomographic sections for a volume of interest (VOI) of 6003 voxels. The selected volume contains a minimum of 157 pores, although the solid phase is distributed in a much larger number of individual solid components (12-14 walls per pore and 30-38 edges per pore [2]) resulting in a high total number of elements, even when taking into account that faces are shared by two pores and edges by 3 pores [2]. The presented materials have been produced by different techniques, thus they have different cellular structures and properties [19, 20].

From left to right the processing methods are: gas dissolution (Foam-1, crosslinked EVA, 65Kg/m³), extrusion foaming (Foam-2 and Foam-3, non-crosslinked LDPE, 28Kg/m³) and compression moulding (Foam-4, crosslinked LDPE, 32Kg/m³). A detailed description of these processing methods can be found elsewhere [14, 3].

As it can be appreciated (see scales), the materials present significant variations in average pore size (150-1500 µm). It can also be observed that materials are presented according to their apparent crumpled grade (the cropped single cells show increasing presence of corrugation in the cell walls) that depends on the processing technique used. In all the foaming methods used to produce the foams of this paper the material are foamed at high temperatures and then cool down to room temperature, during this cooling the gas pressure is reduced and there is gas diffusion from the internal structure of the foam. These two effects combined with the low dimensions and stiffness of the cell walls and struts cause the deformation/corrugation of the cell walls. As a matter of fact this type of corrugation is typical of closed cell flexible foams and has important effects on the final properties [21]. Foam-2 and Foam-3 are completely equivalent materials (similar density, cell size and open cell content) processed under similar extrusion conditions but with a different mechanical response in compression in the vertical direction Z (see table 1, normalized values are divided by the properties of the corresponding solid material and divided by the square of the relative density). Foam 2 presented higher collapse strength than foam 3. These two materials were selected for this reason. The other two materials were selected for validation purposes since from previous characterizations it was known that foam 1 has almost flat cell walls (and foam 4 highly corrugated ones).

Figure 1: Tomographic projections from left to right of foam-1, foam-2, foam-3 and foam-4.

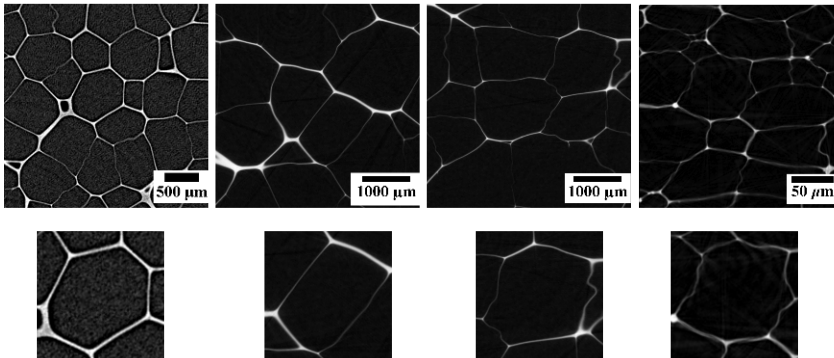


Table 1: Morphological and mechanical characteristics of the foams under study.

Specimen	Density (Kg·m ⁻³)	Cell size (μm)	Surface/Volume ratio (μm ⁻¹)	Collapse strength (kPa)	Norm. collapse strength (m ⁶ ·Kg ⁻²)
<i>Foam-1</i>	65	664	0.0892	60.2	0.119
<i>Foam-2</i>	27	1515	0.0529	9.7	0.067
<i>Foam-3</i>	29	1532	0.0631	7.1	0.042
<i>Foam-4</i>	27	152	0.116	25	0.094*

*This material presents a significant anisotropy and some other microstructural differences.

In the case of strictly comparison among foam-2 and foam-3, no significant differences were observed in the typical morphological parameters (cell size, cells surface, cells sphericity, anisotropy, etc). Nevertheless, the average surface to volume ratio of the individual pores was expected to be a good indicator of the presence of wrinkled cell walls. The values obtained (see table 1) offer a different result (influence of cell size since the smaller is the pore the larger is this value) and do not completely reveal the expected differences among materials. Only in the case of Foam-2 and Foam-3, with similar pore size we can appreciate a significant influence. Sphericity was also scanned as possible indicator but the polyhedral shape led to very similar values for all the studied samples.

2.2. X-RAY μ CT

Cone-beam tomograms (foam-1, foam-2 and foam-3) were performed both at the Centre for X-ray Tomography at Ghent University (UGCT) and FI-1 Helmholtz-Zentrum Berlin (HZB) X-ray scanner. The scanner settings allowed a final voxel size of approximately 7 microns for these materials. On the other hand, due to its smaller cell size and cell wall thickness foam-4 was scanned using synchrotron microtomography at BAMline (BESSY, HZB) obtaining a final voxel size of 0.41 microns. Octopus[®] 8.6 server/client reconstruction package [22, 23] was used for the reconstruction of the tomograms.

2.3. FOAM SEGMENTATION PROCESS

The shape classification process consists in separating the cell walls from the edges and vertexes (struts). This method has been previously developed to characterize the trabecular bone microstructure by computing the volume fraction between walls and struts to obtain a geometrical based osteoporosis diagnose [24].

We calculate for every voxel of the inertia moment of its neighbourhood obtained by a local geodesic dilation of the voxel in the solid foam volume. To be scale independent, the geodesic propagation computed with Fast Marching algorithms is driven by the local thickness at the considered voxel. We arbitrary fix the geodesic distance to 3 times the local thickness, and the elongation ratio between the three inertia moments of the resulting shape are then computed to describe the morphology. iMorph software [25] implements this algorithm that performs an iterative analysis of elongation inertial moment at every voxel within the selected phase. In this way, voxels showing unidirectional continuity are identified as plateau borders (edges, uniaxial oriented), whereas those showing 2D or 3D connectivity constitute either walls or vertexes (biaxial or triaxial oriented). A solid voxel is belonging to a strut if its elongated ratio between the principal and the secondary axis of its local shape is under an arbitrary value fixed to 1.6. Once the struts have been identified (edges + vertexes), the remaining steps are refinements based on simple binary and arithmetical operations, as seen in fig.2. The identified struts are 1-2 pixels 3D-dilated depending on the material type (fig. 2b and 2c) and the mask containing the over-dilated struts is subtracted from the original binary image to calculate the final cell walls (fig. 2d.). The final cell walls are complementary subtracted from the original binary image to get the separated struts (fig. 2e.). A two-channel image is created, containing both independent struts and cell walls (fig. 2f.). The data can be represented as a red-green (struts-cell walls) composite 3D image. This procedure was applied over a reduced volume of 400^3 voxels due to the high computation requirements needed. This volume can be considered as representative of the specimens' due to the high number of walls and struts contained within this volume.

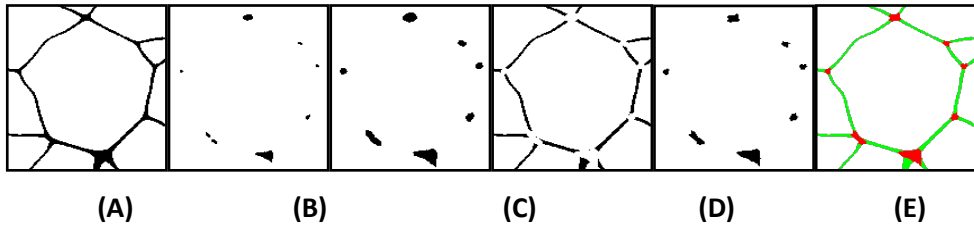


Figure 2: Sequence of erosion-dilation procedure: (A) original binary pore, (B) segmented struts (C) overdilated mask (D) resulting cell walls (E) resulting struts and (F) combined struts and walls.

It is difficult to compare this methodology with any classical or well-established one. To our knowledge, the precedents used to determine the solid fraction in the struts (f_s) for foams materials are based on 2D cross-sections images, requiring the approximation of the strut shape either to be a circle or a triangle [5, 6] and subsequently needs to assume a given cell shape as for instance pentagonal dodecahedra. We can also mention a precedent, developed by the current authors, that allows a 3D struts-walls separation for closed cell rigid polyurethane foams in which the solid fraction in the struts is higher (between 0.6 and 0.9) in comparison with the expected values for these materials under study [26]. The used method permits the calculation of an equivalent parameter to f_s , denoted as struts volumetric fraction (SVF). It was, nevertheless, based on a much simpler methodology (erosion-dilation) that does not provide satisfactory results with lower SVF values (lower than 0.35 -cell wall thickness similar to strut thickness-). Figure 3 shows the 3D rendering for the full volume of Foam 1 and, in detail, for a single pore in this material. It can be clearly appreciated the success of the de-structuration method in these complex materials.

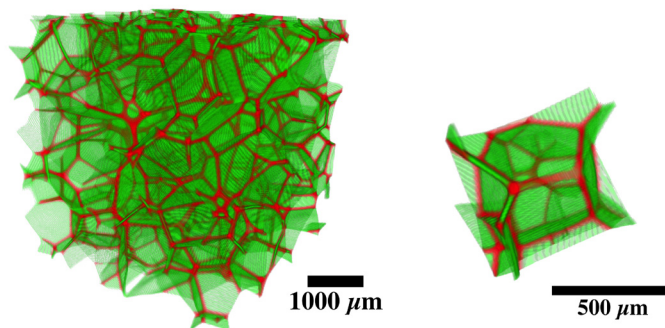


Figure 3: 400^3 voxels VOI and single pore 3D renderings with identified struts (in red) and cell walls (in green).

2.4. IMAGE ANALYSIS PROCEDURES

It is possible to apply different approaches to analyse the key morphological characteristics of cell walls. The most straightforward way would be through the analyzed pore parameters. In this sense, one of the first evaluated parameters was the average surface to volume ratio since it was expected to be a good indicator of existence of corrugated cell walls, although the results (table-1) have shown the opposite.

This section revises the alternative complementary procedures to evaluate corrugation and other microscopic structural aspects. These procedures could be applied, depending on their own characteristics, in the continuous solid structure (walls + struts), in the de-structured one (walls) or either in both types of solid-phase structures (walls and struts). Among the methods exposed in this investigation, the solid phase tortuosity method needs a continuous phase (walls + struts), the curvatures and thickness analysis can be applied in both walls and struts and the last proposed method in this section, cross-sectional corrugation, needs the separated cell walls as unique input.

2.4.1. Solid Phase Tortuosity

Tortuosity is a dimensionless parameter that expresses the ratio of the real pathway distance and the straightest one when travelling along a certain direction through the internal structure contained within selected phase boundaries. It is often calculated and used to model/predict transport properties either in solid phase (thermal, electrical) and/or fluid one (acoustic, mass/heat flow, etc) but it is not an easy task to measure or calculate it. Most common computation strategies are based on the ratio in between the geodesic and Euclidean distances [24,27, 28]. The geodesic distance includes the extra distance that has to be covered by “travelling” through the gaseous/solid phase. Under this definition it easy to understand that tortuosity is a directional parameter; therefore it is possible to define a tortuosity for any direction in the 3D space. In our particular case we will consider as a reference the 3 Cartesian axes (X, Y and Z) so the three principal directional values will be calculated. The results would then give an idea on how corrugated are the walls in the three defined directions, which is useful to establish correlation with the mechanical properties.

A self-developed algorithm, based on the Fast Marching technique included in iMorph package has been used. This numerical algorithm solves the Eikonal equation on an orthogonal grid. The method is based on the fluid propagation technique and follows a different concept that a simple ratio between two distances. It mainly consists in computation of a parallel fluid wave virtually travelling from a certain point and propagating at virtual constant speed without intersecting any other pixel than those contained in the selected phase [24]. This procedure calculates the virtual arrival time

of the fluid at the end points in the final plane and calculates an average. This result is normalized by the arrival time obtained for a single-phase material and the ratio is directly outputted as a tortuosity value. The assumption is correct because during the process the virtual velocity has been kept constant and thus the delay directly corresponds to a higher distance tracked.

2.4.2. Local Thickness

Local thickness analysis was implemented by using the 3D local thickness plugin for ImageJ and FIJI. This plug-in, initially developed for the study of trabecular bone, calculates a 3D thickness calibrated grey-scale map based on a Euclidean distance transformation algorithm and distance ridge computation [29, 30]. A grey-level histogram of the calibrated map allows determining the thickness distribution. This type of analysis does not provide directional information due to its intrinsic characteristics. It is important to remark that this approach does not indicate corrugation presence but the results might be correlated with this parameter. Local thickness analysis also allows establishing a correlation between the structural characteristics and the differences observed in the mechanical behaviour of the investigated materials.

2.4.3. Curvature Analysis

The determination of principal radii of curvatures permits to analyse and quantify a high number of topological features closely related to cell walls corrugation. Several procedures are described in the literature although the general methodology is based on surface discretization by means of surface meshing using polygons and a later approximation of the local curvatures by continuous mathematical functions [31, 32]. From this analysis different parameters can be obtained, although all are based on two primeval parameters: the principal radii of curvatures, r_1 and r_2 . Different derived curvatures aspects such as the Gaussian or mean curvatures can be defined. In our particular case we have selected the mean curvature (H) as indicator of corrugation in our materials. Mean curvature is defined in eq. 1 as a function of the two principal curvatures. It takes a negative value parameter in strictly concave regions and positive in strictly convex regions. It can be zero in regions where positive and negative principal curvatures cancel each other. The advantage of mean curvature versus Gaussian is the wider distribution and the higher sensibility to local variations [33]. It is important to remind that, in contrast to tortuosity computation, mean curvatures analysis does not provide any directional information.

$$H = \frac{1}{2} \left(\frac{1}{r_1} + \frac{1}{r_2} \right) \quad (\text{eq 1})$$

In this work, we carried out a curvature analysis using Avizo Fire [34]. The particular method consists in the generation of a triangular mesh template in the foam surface, obtained by an algorithm based on the marching cubes technique [35]. This mesh is subsequently smoothed by an iterative methodology so the local pixel “roughness” is partially eliminated. Smoothing is accomplished by shifting the vertices of triangles towards an average position considering the neighbours. A maximum of 50% of shifting (a rather low value) but a high number of iterations (10) was considered as good enough to remove local variance without modifying the real surface significantly. The subsequent analysis of mean curvature was based on a surface field with curvature values being defined on the surface’s triangles. In order to reduce scattering due to local values the computation has been extended to a significant number of neighbour triangles. An optimization process gave as a result a number of 20 triangles to be considered in the mean curvature computation. The optimum compliance reached by using such neighbourhood conditions made unnecessary to increase the number of iterations for the calculation, thus obtaining similar values for 1, 2 or more iterations in the initial curvature values. Under these conditions, the typical computation time was between 3 and 5 hours. The final output is represented as mean curvature distribution using a similar representation range and number of bins.

As mentioned, curvature analysis was carried out both in the continuous solid structure and in the de-structured one (walls).

2.4.4. Cross-sectional Corrugation ratio

Based on the analysis of the separated walls this technique calculates, in all the individual cell walls, the corrugation ratio. This value is obtained from the 2D cross-sectional images in the three different planes and it is defined, according to eq. 2, as the ratio in between Feret diameter (Φ_f) and the half of the wall perimeter (P). For this purpose the cell wall cross-sections have been previously skeletonised in order to minimize the perimeter being, then, a more realistic calculation. These calculations were performed using the 2D analyse particles function available at ImageJ/FIJI software [36,37]. Although this parameter is obtained from 2D images, thus based on skewed information, corrugation ratio expresses a 1-D ratio, valuable for analytical modelling purposes. The directional information obtained is, indeed, also valuable in analytical modelling, processing and experimental issues.

$$CR = \frac{P}{2 \cdot \Phi_f} \quad (\text{eq 2})$$

This particular analysis has been done over the 400 slices reconstructed in the three Cartesian planes.

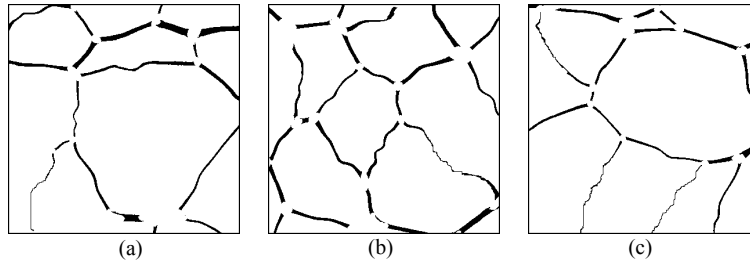


Figure 4: Cross-section projections of cell walls over planes (a) X^\perp (b) Y^\perp (c) Z^\perp . Presented cross-sections are the non-skeletonised ones for a better visualization.

3. RESULTS AND DISCUSSION

3.1. Struts volumetric fraction (SVF)

The most direct output of the de-structuration process is the possibility of determining the SVF, an updated equivalent 3D parameter to the conventional material fraction in the struts (f_s). This is done by simply calculating the total number of voxels in the struts (red in fig. 3) divided by the total amount of voxels in the whole solid network (red+green in fig. 3) expressing the final ratio as a percentage. The results shown in Table 2 for the investigated materials reveal that *Foam-1* presents rather lower strut factor than the other samples. The results can be understood in terms of the thicker walls of this material in comparison to *Foam-2*, *Foam-3* and *Foam-4* (see Fig. 1). Thus the thinner walls the higher material is in the struts and the higher the SVF value. On the other hand, obtained values are in agreement with those reported in the literature for similar materials and measured using the 2D conventional method previously mentioned [38,39,40].

Table 2: Material volume fraction at struts for different investigated materials.

Specimen	SVF (%)
<i>Foam-1</i>	15
<i>Foam-2</i>	28
<i>Foam-3</i>	30
<i>Foam-4</i>	31

Regarding the error estimation for this 3D methodology it is difficult to estimate an exact value. One of the reasons is based on the un-clear frontier separating the strut from the wall since it is a continuous structure and the alternative methodologies are more inexact [5, 6]. On the other hand there is no exact reference method for comparison although the values are in congruence with the literature for these

materials [16, 17, 18]. In any case the absolute error must be below 5% and the relative error (material comparison purposes) should be below 3%. According to this, then differences in between foam 2, 3 and 4 are meaningless.

3.2. Tortuosity

The presented results for directional tortuosity (figure 5) reveal the existence of preferred directions for the existing corrugations with exception of Foam-1 that behaves as an isotropic material from this point of view. On the contrary, Foam 2, 3 and 4 present significant anisotropies. Particularly, Foam-4 is the most anisotropic material with a high tortuosity value in the Y direction which means cells are oriented in the XZ plane, in agreement with the high mechanical properties determined in this direction. Foam 2 and 3 show higher tortuosity values in the Z direction although they also present certain tortuosity increase in the Y direction. This result yields small cell orientation in the XY plane.

Regarding the absolute tortuosity obtained, it is important to note that fast marching technique seems to provide lower values than other methods and does not directly correspond to the geometrical tortuosity of the system [41] although it generates valuable relative differences useful for comparison purposes.

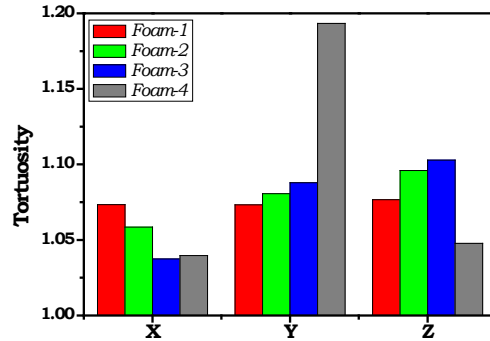


Figure 5: Values of directional tortuosity compared for the 4 materials under study.

3.3. Curvature analysis

The curvature analysis revealed important results both from the methodological and materials point of view. According to the curvatures theory for the H parameter, a narrow distribution centred at zero would represent flat surfaces while a wide distribution represents corrugated cell walls (topology variations). Fig.6 (a and b) shows the mean curvature distribution for the four investigated materials computed both for the complete foam structures and for the de-structured walls. In the case of

the whole structure the results are contrary to the expected ones and foam 1 presents the higher concavity (negative values) and wider distribution. Nevertheless, these results are likely associated to the polyhedron shape of the individual cells, thus cumulating higher concavity values in the strut regions (plateau borders) when approaching from completely flat cell walls. This is why, under this perspective, the higher cell wall corrugation induce more positive values considering that local concavity in the struts is less defined. On the other hand, the results for de-structured walls are ordered according to the expected trend. In this sense, the positive tail is associated to the individual cell walls borders, regions owing a high positive curvature that is more defined in the materials with lower corrugation. Both the average value and width (excluding the mentioned tail) of the distributions correspond to the expected results. A summary of the obtained values is presented in table 3 (see below).

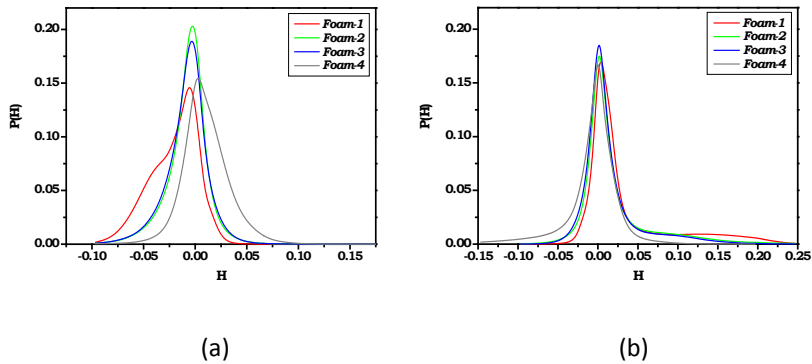


Figure 6: Mean curvature distribution both in (a) continuous foam structure and (b) de-structured cell walls.

3.4. Local Thickness

The results of local thickness distribution (fig. 7(a)) clearly show the advantages and potential capabilities of de-structuration technique. These particular results are comparatively presented for the two materials with a similar structure (foam-2 and foam-3) since these results are not strictly related to corrugation. As seen, almost no difference is observed for these materials, when the local thickness analysis is carried out in the complete structure. Nevertheless, the results reveal higher differences when the thickness distribution of struts and cell walls is analyzed separately, these differences were not appreciable in the complete structure (walls + struts). The average thickness values shown in fig. 7(b) are appreciated to be more different when the two structures, struts and cell walls, are analyzed separately. In this sense the struts are thinner in foam-2 and its cells walls are thicker whereas the opposite results are found in the case of foam-3. This result is in agreement with the lower struts

volume fraction measured for foam 2. This fact further justifies the better mechanical performance of foam 2. An additional result is that, in average, the struts are two times thicker than cell walls for these materials.

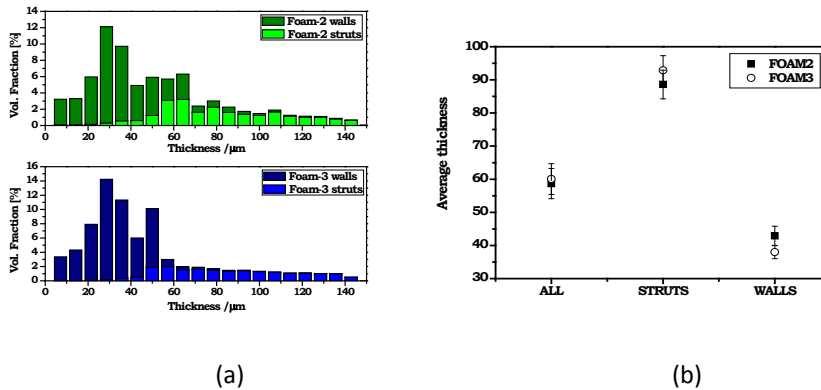


Figure 7: Local thickness distribution and average values for foam-2 and foam-3 before and after de-structuration process.

3.5. Corrugation ratio

The results obtained for this linear parameter are showed in Fig.8. The corrugation ratio distributions are plotted for the 3 different planes and showed in Figs 8a, 8b and 8c. Each plane is denoted by the orthogonal direction, thus the Z^{\perp} plane gives the information about the cell wall corrugation when aligned in the X, Y directions or any other one contained in the XY plane. The results for these graphs clearly indicate that cell wall corrugation is ordered according the materials' labelling, thus Foam-4 presents the higher corrugation and Foam-1 the lower values. Average values are presented in table 3 having selected the percentile 90 (P90) as a more robust indicator although the P50 also pointed differences among the studied materials. P90 yields values of 1.06 for the Foam-1 and 1.61 for Foam 4, in the X^{\perp} plane, the one with higher corrugation. P90 also shows an increase from 1.34 to 1.46 in the specimens 2 and 3, which helps to justify the mechanical differences found. This difference quantifies the nearly undetectable dissimilarity existing between Foam-2 and Foam-3. Fig 8d exemplifies that corrugation is particularly located in the X^{\perp} plane which contains the expansion (Z) and the transverse (Y) directions for Foam 3. Thus, it is complicated to indicate a clearly unidirectional value, as done by the tortuosity calculations, however, at least, it is possible estimate and quantify the linear corrugation factor in a plane containing multiple directions.

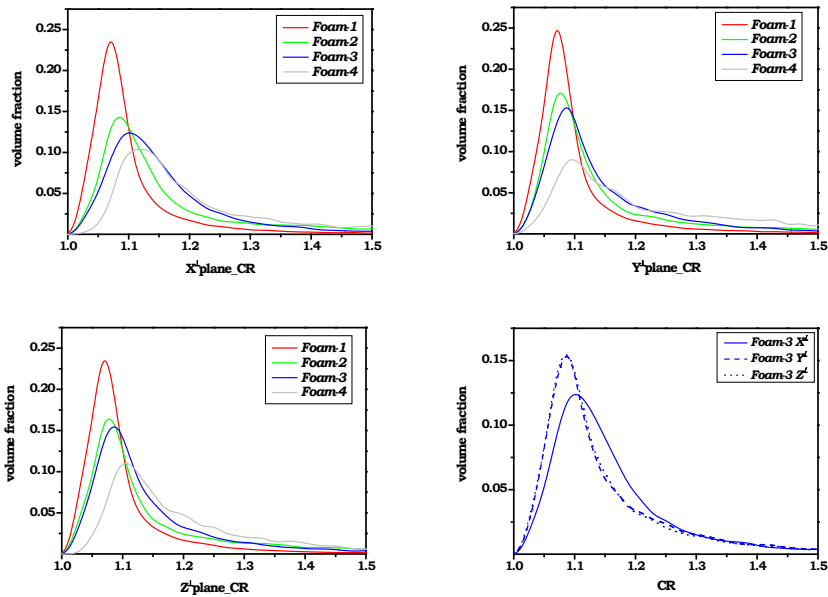


Figure 8: Corrugation ratio (CR) distribution in the three planes (a) X^\perp (b) Y^\perp (c) Z^\perp for the analysed materials. (d) Corrugation ratio distribution for Foam-3 in the three planes.

4. CONCLUSIONS

All numerical results for corrugation ratio, tortuosity, curvatures and local thickness are summarized in table 3. The four methods presented and discussed provide valuable information that correlates well with observed the structure and the expected response of the foams under study. It is expected that these microstructural parameters will be helpful in obtaining a better understanding of the physical properties of these materials. It is clear from the values presented in Table 3 that the values correlate with each other and that they are mutual supported.

Table 3: Summary of calculated values by using the different approaches.

	Tortuosity			Local thickness			H		CR (P90)		
	X	Y	Z	All	Struts	Walls	All	Walls	X	Y	Z
Foam-1	1.07	1.07	1.07	53.05	79.02	42.66	-0.0203	0.0327	1.06	1.07	1.06
Foam-2	1.06	1.08	1.08	58.69	88.60	42.91	-0.0074	0.0188	1.33	1.32	1.34
Foam-3	1.04	1.09	1.11	60.04	92.89	37.98	-0.0080	0.0142	1.43	1.42	1.46
Foam-4	1.04	1.19	1.05	4.81	4.93	4.22	0.0102	-0.0052	1.60	1.74	1.61

The novel 3D computational methodologies presented allow measuring several important microstructural characteristics of foams that are difficult to obtain by applying conventional methods. Some of these methods are supported in the frame of a novel concept, the solid de-structuration. A solid classification algorithm permits to de-structure the solid skeleton of the foams into two main parts, the cell walls and the struts (edges + vertexes).

The developed methodologies have been applied to four low-density closed cell polyolefin based foams and the analysis has been focused on characterizing the presence of wrinkled cell walls in these materials. Nevertheless, solid classification can be applied to any type of cellular material, (even to those with a small strut volume fraction) and allows obtaining accurate SVF data, which are known to have an important effect of the physical properties. Similar structures in biology, geology, etc are susceptible to be analyzed by using this strategy and subsequently applying the reported methodologies (local thickness, tortuosity, curvatures and corrugation ratio).

Some of these geometrical descriptors such as tortuosity and local thickness work in a continuous network and get information over the complete cellular structure whereas corrugation ratio can be only computed after the application of the de-structuration procedure. In addition, local thickness and curvatures analysis seems to report different values before and after de-structuration. In our particular purpose the values after de-structuration were, by far, more reliable. As additional appreciation, tortuosity and corrugation ratio calculation provide directional information that can be used for correlation with mechanical and/or transport properties. The main remarkable capabilities of the analysis performed are summarized in table 4.

Table 4: Main characteristics of the methodologies used in this investigation.

Method	Continuous	Discontinuous	Direction-sensitive	3D
<i>Tortuosity</i>	✓	✗	✓	✓
<i>Curvatures</i>	✓	✓	✗	✓
<i>Local thickness</i>	✓	✓	✗	✓
<i>Corrugation ratio</i>	✗	✓	✓	✗

The results indicate that there is no a single method based on 3D imaging to investigate the presence of wrinkled cell walls (or similar features in other types of porous materials). The procedures described in this paper open new possibilities for further applied studies correlating solid phase features with the materials properties and thus developing advanced analytical modelling.

5. ACKNOWLEDGEMENTS

Financial support from the Spanish Ministry of Economy and FEDER (MAT2009-14001-C02-01 and MAT2012-34901), the Junta of Castile and Leon (projects VA174A12-2 and VA035U13) the ESA (Project MAP AO-99-075), PIRTU contract of S. Pardo-Alonso by Junta of Castile and Leon (EDU/289/2011) co-funded by the European Social Fund and Juan de la Cierva contract of E. Solórzano by the Ministry of Economy (JCI-2011-09775) are acknowledged. The Special Research Fund of the Ghent University (BOF) is also acknowledged for the doctoral grant to L. Brabant.

6. REFERENCES

-
- [1] WEAIRE, D., HUTZLER, S. (1999). *The Physics of Foams*, UK: Oxford University Press.
- [2] GIBSON, L.J. & ASHBY, M. F. (1997). *Cellular Solids – Structure and Properties*, UK: Cambridge University Press.
- [3] EAVES, D. (2004). *Handbook of Polymer Foams*. UK: Rapra Technology.
- [4] SIMONE, A.E. & GIBSON, L.J. (1998). Effects of solid distribution on the stiffness and strength of metallic foams. *Acta Materialia* 46 (6), 2139–2150
- [5] SIMONE, A.E. & GIBSON, L.J. (1998). The effects of cell face curvature and corrugations on the stiffness and strength of metallic foams, *Acta Materialia* 46 (11), 3929-3935
- [6] GRENESTEDT, J.L. (1998) Influence of wavy imperfections in cell walls on elastic stiffness of cellular solids, *Journal of the Mechanics and Physics of Solids*, 46 (1), 29-50
- [7] ANDREWS, E., SANDERS, W., GIBSON, L.J. (1999). Compressive and tensile behaviour of aluminum foams, *Materials Science and Engineering: A* **270**, 2, 30, 113-124
- [8] KUHN, J., J., EBERT, H. P., ARDUINI-SCHUSTER, M. C., BUTTNER, D. & FRICKE, J. (1992). Thermal transport in polystyrene and polyurethane foam insulations. *Int. J. of Heat and Mass trans.* **35**(7), 1795-1801.
- [9] GLICKSMAN, L.R. (1994). *In Low Density Cellular Plastics: Physical Basis of Behaviour*, UK: Chapman & Hall.
- [10] ALMANZA, O., RODRIGUEZ-PEREZ, M.A., DE SAJA, J.A., Prediction of the Radiation Term in the Thermal Conductivity of Crosslined Closed Cell Polyolefin Foams, *Journal of Polymer Science: Part B. Polymer Physics* **38**, 993-1004 (2000)
- [11] ALVAREZ-LAINEZ, M.A., RODRIGUEZ-PEREZ, M.A., DE SAJA, J.A., Thermal Conductivity of Open Cell Polyolefin Foams, *Journal of Polymer Science, Part B: Polymer Physics* **46** (2), 212-221.
- [12] PINTO, J., SOLÓRZANO, E., RODÍGUEZ-PÉREZ, M.A., & DE SAJA, J.A. (2013). Characterization of the cellular structure based on user-interactive image analysis

procedures, *Journal of Cellular Plastics* **49** (6), 554 – 574.

[13] MADER, K., MOKSO, R., RAUFASTE, C., DOLLET, B., SANTUCCI, S., LAMBERT, J., STAMPANONI, M., (2012). Quantitative 3D characterization of cellular materials: Segmentation and morphology of foam, *Colloids and Surfaces A Physicochemical and Engineering Aspects* **12** 415:230-238.

[14] BRABANT, L., VLASSENBROECK, J., DE WITTE, Y., CNUUDE, V., BOONE, M., DEWANCKELE, J., VAN HOOREBEKE, L., (2011). Three-dimensional analysis of high-resolution X-ray computed tomography data with Morpho+. *Microscopy and Microanalysis* **17** (2) 252-63.

[15] MA, Y., PYRZ, R., RODRIGUEZ-PEREZ, M.A., ESCUDERO, J., RAUHE, J.C., SU, X. (2011), X-Ray Microtomographic Study of Nanoclay-Polypropylene Foams, *Cellular Polymers* **30** (3) 95-110.

[16] MEAGHER, A.J., MUKHERJEE, M., WEAIRE, D., HUTZLER, S., BANHART, J., GARCIA MORENO, F. (2011), Analysis of the internal structure of monodisperse liquid foams by X-ray tomography, *Soft Matter* **7** 9881-9885.

[17] RUSS, J.C. (2007). *Image Processing Handbook*, US: CRC Editors

[18] VINCENT, L. SOILLE, P., Watersheds in Digital Spaces - an Efficient Algorithm Based on Immersion Simulation,. *IEEE Transactions on Pattern Analysis and Machine Intelligence*, Vol. 13 Issue 6, pp. 583-598, 1991

[19] RODÍGUEZ-PÉREZ, M.A. (2005). Crosslinked Polyolefin Foams: Production, Structure, properties and Applications, *Adv. Polym. Sci.* **184**, 97-126.

[20] RODÍGUEZ-PÉREZ, M.A., ALMANZA, O., RUIZ-HERRERO, J.L., DE SAJA, J.A. (2008). The effect of processing on the structure and properties of crosslinked closed cell polyethylene foams, *Cell. Polym.* **27**, 179-200.

[21] ALMANZA, O., MASSO-MOREU, Y., MILLS, N.J., RODRÍGUEZ-PÉREZ, M.A. (2004). Thermal Expansion Coefficient And Bulk Modulus Of Polyethylene Closed-Cell Foams, *J. Polymer Sc. (B)* **42**, 3741.

[22] VLASSENBROECK, J, DIERICK, M, MASSCHAELE, B, CNUUDE V, VAN HOOREBEKE, L, JACOBS, P. (2007) Software tools for quantification of X-ray microtomography. *Nuclear Instruments & Methods in Physics Research, Section A: Accelerators, Spectrometers, Detectors, and Associated Equipment* **580** (1) 442.

[23] <http://www.insidematters.eu>

[24] BRUN, E., VICENTE,J., TOPIN, F., OCCELLI, R. (2007), Characterization of the full thermal conductivity tensor of anisotropic metal foams – Influence of the fluid phase *In proceeding of: Metfoam 2007*

[25]<http://imorph.fr>

[26] PARDO-ALONSO, S., SOLÓRZANO, E., BRABANT, L., VANDERNIEPEN, P., DIERICK, M., VAN HOOREBEKE, L., RODRÍGUEZ-PÉREZ, M.A. (2013). 3D Analysis of the progressive modification of the cellular architecture in polyurethane nanocomposite

foams via X-ray microtomography, *Eur. Polym. J.* **49**, 999–1006

[27] BULLITT, E., GERIG, G., PIZE, S., LIN, W., AYLWARD, S.R. (2003) Measuring Tortuosity of the Intracerebral Vasculature From MRA Images. *IEEE Transactions on Medical Imaging*, **22**(9), 1163-1171.

[28] GOMMES, C.J., BONS, A.J., BLACHER, S., DUNSMUIR, J.H., TSOU, A.H. (2009). Practical Methods for Measuring the Tortuosity of Porous Materials from Binary or Gray-Tone Tomographic Reconstructions. *AIChE Journal* **55**(8), 2000-2012.

[29] HILDEBRAND, T., RÜESEGGER, P. (1997). A new method for the model-independent assessment of thickness in three-dimensional images, *J. Microsc.* **185**, 1, 67–75.

[30] TOYOFUMI, S., JUN-ICHIRO, T. (1994). New algorithms for euclidean distance transformation of an n -dimensional digitized picture with applications to pattern Recognition **27** (11), 1551–1565.

[31] KAMMER, D., VORHEES, P.W., (2006) The morphological evolution of dendritic microstructures during coarsening, *Acta Mat.* **54**, 1549–1558.

[32] JINNAI, H., KOGA, T., NISHIKAWA, Y., HASHIMOTO, T. & HYDE, S.T. (1997), Curvature Determination of Spinodal Interface in a Condensed Matter System, *Phys. Rev. Lett.* **78**, 2248–2251

[33] ALKEMPER, J. & VORHEES, P.W. (2001). Three-Dimensional Characterization of Dendritic Microstructures, *Acta Mater.* **49**, 897–902

[34] <http://www.vsg3d.com/avizo/fire>

[35] LORENSEN, W.E. & CLINE, H.E. (1987). Marching Cubes: A high resolution 3-D surface construction algorithm, *ACM Siggraph Computer Graphics* **21**, 163–169

[36] RASBAND, W.S. (1997-2012). ImageJ, U. S. National Institutes of Health, Bethesda, Maryland, USA, <http://imagej.nih.gov/ij/>

[37] SCHINDELIN, J., ARGANDA-CARRERAS, I., Erwin Frise, Verena Kaynig, Mark Longair, Tobias Pietzsch, Stephan Preibisch, Curtis Rueden, Stephan Saalfeld, Benjamin Schmid, Jean-Yves Tinevez, Daniel James White, Volker Hartenstein, Kevin Eliceiri, Pavel Tomancak and Albert Cardona (2012) Fiji: an open-source platform for biological-image analysis, *Nature Methods* **9**(7) 676-682

[38] MARTINEZ-DIEZ, J.A., RODRIGUEZ-PEREZ, M.A., DE SAJA, J.A., ARCOS Y RABAGO, L.O., ALMANZA, O. (2001). The Thermal conductivity of a Polyethylene Foam Block produced by a Compression Molding Process, *J. Cell. Plast.* **37**, 21-42.

[39] ALMANZA, O. RODRIGUEZ-PEREZ, M.A., DE SAJA, J.A. (2001). The microstructure of polyethylene foams produced by a nitrogen solution process, *Polym.* **42**, 7117-7126

[40] ALMANZA, O. RODRIGUEZ-PEREZ, M.A., DE SAJA, J.A. (1999). The Thermal Conductivity of Polyethylene Foams Manufactured by a Nitrogen Solution Process, *Cell. Polym.* **18** (6) 385-401

[41] SOLORZANO, E., PARDO-ALONSO, S., BRABANT, L., VICENTE, J., VAN HOOREBEKE, L., & RODRIGUEZ-PEREZ, M.A. (2013). Computational approaches for tortuosity determination in 3D structures. In V. Cnudde (Ed.), *Tomography of materials and structures: book of abstracts: talks* (pp. 71–74). Presented at the 1st International conference on Tomography of Materials and Structures (ICTMS 2013), Ghent, Belgium

7. ULTRAFAST TOMOGRAPHY AT TOMCAT BEAMLINE

7.1. SUMMARY OF THE SYNCHROTRON CAMPAIGN

This chapter presents the description of the main results obtained during the experimental campaign carried out at TOMCAT beamline at Swiss Light Source (SLS) in Paul Scherrer Institute (PSI).

The results previously presented in *Soft Matter*, 2012, 8, 11262 reported results on nanoclays effect on cell nucleation enhancement in reactive polyurethane foams by means of X-ray radioscopy and image analysis application. Nevertheless, X-ray radioscopy requires imaging very thin foams in depth to discern cells successfully. This fact actually modifies the normal foaming behaviour of these systems inside a quasi-2D mould. The system used in that experiment also presented the handicap of a typical time span of 40s existing between the end of mixing and the first image acquisition. Subsequently, cells were already nucleated and cell growth had already begun. Nevertheless, discussion about the scaling relationship existing between the small droplet foaming model and a foamed material with larger dimensions was carefully done in the mentioned work. In this sense, the representativeness of that investigation was demonstrated as valid even under the commented constrictions imposed by the setup. A constant scaling factor for density, cell size and cell density was found by comparison with *ex-situ* results of foaming systems with larger volume. Nevertheless, limitations of this method, which is based in the analysis of 2D radiographies of quasi-2D (0.6 mm thick) and small (10mm diameter) foam, are sensible. Also temperature of the exothermic foaming reaction for such a small volume, with almost null thermal mass, limits the possibilities of this methodology. In any case, this type of analysis permitted to obtain information to conclude the effect of nanoclays presence leading to cell nucleation enhancement.

These promising results were followed by investigations based on the same X-ray analysis methodology. They basically present similar investigations but aimed at investigating the effect of other nanofillers such as nanosilicas and CNPs. *Colloids and Surfaces A: Physicochem. Eng. Aspects* 2013, 438, 119 together with the work about CNPs effect explained in chapter 5 present these investigations.

We have cited several results by time-resolved X-ray radiography of foaming polyurethane. This acquired know-how served as initial basis and starting point for beamtime proposal at TOMCAT. Moreover, latest advances at this beamline instrument at SLS permits to do ultrafast X-ray synchrotron tomography with sub-second temporal resolution. This technique is able to combine temporal resolution of X-ray radioscopy and 3D spatial resolution of X-ray μ CT. Therefore, this technique offers kind of 4D high resolution images. The high photons flux is one of the main requirements to perform ultrafast scans since the information need to be as much as possible in the shortest possible interval time of tomogram acquisition. It allows even

temporal resolution below 1s and pixel size of a few microns ($<5\mu\text{m}$). Of course, the real spatial resolution still depends on sample and MTF of the imaging system.

We want to note some other experimental details that were necessarily done previous to the synchrotron campaign. A selection of polymer foaming system was done regarding the experience acquired during the mentioned precedent works. Bi-component BASF rigid PU system was a suitable choice for this type of experiment. Long cream time and relatively slow expansion are desired since samples displacement is one of the main constrictions to perform avoid motion artifacts such as blurring in tomograms, i.e. all the projections around 360° for a tomogram reconstruction need to be acquired faster than sample displacement during expansion. Concretely, this means that velocity of structural changes (v) needs to be smaller than the ratio between spatial resolution (δR) and the acquisition time (t)

$$v < \frac{\delta R}{t} \quad \text{EQ. 7-1}$$

Furthermore, a special care was taken during setup design to allow *in-situ* mixing during a few seconds to promote the reaction between isocyanate and polyol. It is important to remark that the presence of a span time (circa. 40 seconds) was one of the main limitations in the works by X-ray radiography. In those investigations, the possibility of performing an *in-situ* stirring to promote foaming reaction was not available. Therefore, the very early stages were not monitored and valuable information missed. This way, it is hard to obtain scientific information at earlier stages since reactive process cannot be stopped. In fact, tiny cells nucleation is typically initiated at this stage. Subsequently, an automatism for stirring the bi-component PU formulation and promote of liquids was designed since we are mainly interested in the very first foaming stages when cells are starting to nucleate. Figure 7-1 shows the mixing automatism mounted on a mechanical arm allowing remote control for positioning over the rotary stage. Thanks to a small motor with an overhead stirrer with a miniaturized propeller (4.5mm diameter) and remote control, mixing of the reactants is now possible and thus the early stages of the foaming process are not missed anymore.

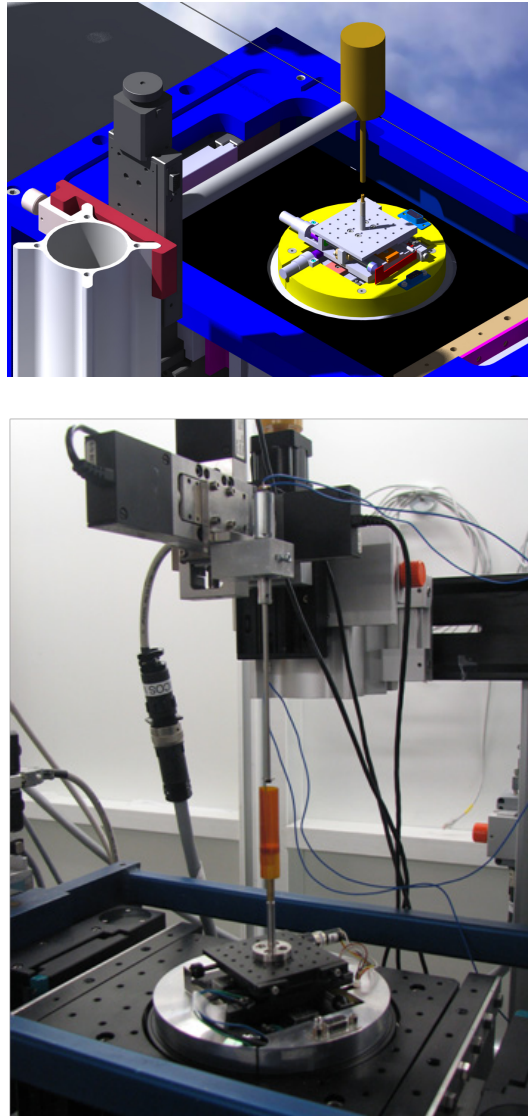


FIGURE 7-1.- STIRRING AUTOMATISM DESIGN FOR IN-SITU PU REACTION ACTIVATION.

The foaming mould designed and build to perform the scans during foam rising is a low X-ray absorbing (Kapton) 5mm diameter cylinder. This cylinder was carefully placed and stuck with adhesive Kapton over a Teflon cylinder directly mounted on the axis of the rotary stage. It is shown in Figure 7-2. Contrary to previous commented works, these experiments permitted to investigate 3D PU foam with reasonable dimension: 0.4 cm^3 instead of 0.047 cm^3 . Moreover, for such ultrafast tomographic applications, the rotation stage (see in Figure 7-1 and Figure 7-2). In this case the rotation speed available thanks to the model Aerotech ABRT-200 is typically up to 600 rpm (20 Hz tomograms acquisition).

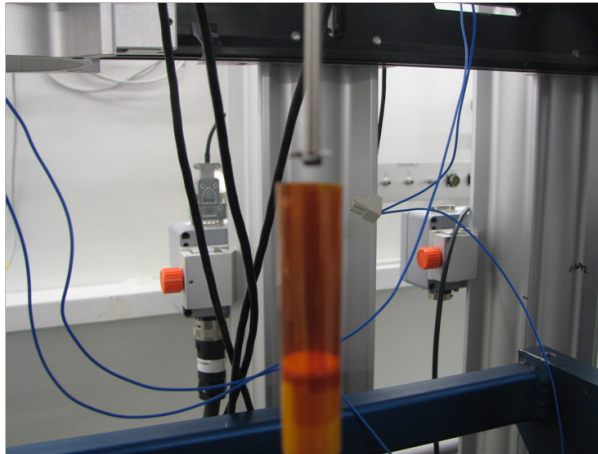
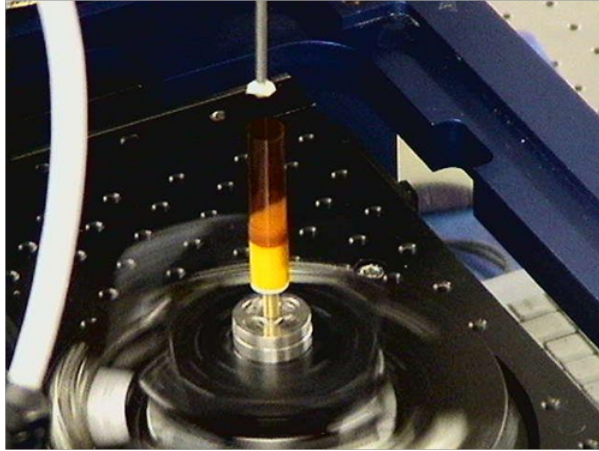


FIGURE 7-2.- STIRRING HEAD OVER THE KAPTON MOULD WITH THE ISOCYANATE AND POLYOL.

The campaign was basically focused on studying samples of the same rigid BASF PU formulation with different nanofillers at different contents. Increasing contents of Cloisite 30B, Aerosil R812 and Aerosil A200 were selected for this purpose. The reactants were carefully placed inside the mould by a syringe (0.23g of polyol and 0.36g of isocyanate).

Structural changes of foaming system were also taken into account to select the optimum interval time between tomograms acquisition. Every foaming experiment was divided in four stages. The velocities of structural displacements were calculated based on previous experiments by optical expandometry. An example of these expansion curves is shown in Figure 7-3. This allowed estimating the increment values in height (Δz) for every stage and thus defining a concrete number of tomograms to be acquired and fixed the interval time between each of them.

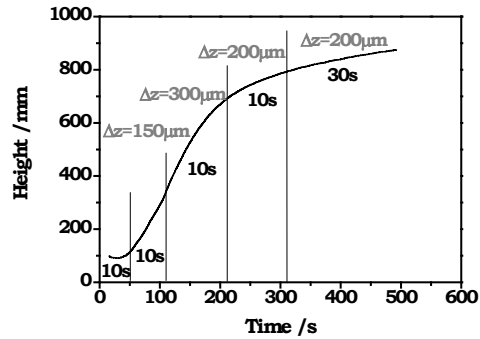


FIGURE 7-3.- OPTICAL EXPANDOMETRY EXPANSION CURVE WITH INTERVAL TIME AND HEIGHT DISPLACEMENT FOR EVERY FOAMING STAGE.

The scanning parameters were pixel size of 3.333 mm, 0.5ms exposure time for every radiogram and total of 300 projections around the 360°. This gives a total scan time for every single tomogram of 156.8ms. 50 flatfields and 20 darkfield images were acquired for image correction purposes. Field of view was an area of 11.28 mm². Simultaneous displacement in z-axis was run to follow by the tomographic acquisition nearly the same region while expanding. This yielded a total Δz of 9mm. Table 7-1 summarizes the selected intervals and the acquisition parameters used in each foaming stage. For instance, during the second stage (60-100 seconds), the application of Eq. 7-1 indicates a velocity of structural displacement of 15 μ m/s. This is considerably below the ratio between 3.333 μ m of pixel size and 156.8ms of acquisition time for a tomogram (22.22 μ m/s).

TABLE 7-1

Time (s)	Interval (s)	Scans (no.)	Δz (μ m)
10-50	10	5	0
60-100	10	5	150
110-200	10	10	300
210-300	10	10	200
310-600	30	10	200

Figure 7-4 shows a selection of acquired tomograms reconstruction. All the reconstructions were done with the Fourier-based tomographic reconstruction method in Fourier space [1]. This pipeline implemented at TOMCAT handles the data flow resulting from high-resolution scans acquired in a few minutes. The

reconstruction is down in a two step process. First dark and flatfield corrections and sinograms are produced from the original raw projections using in-house developed software [2]. Then, gridrec, an alternative approach to filtered back-projection (FBP) is used [3]. This highly optimized Fourier transform method routine combines accuracy with computational performance, without the need for GPU technology.

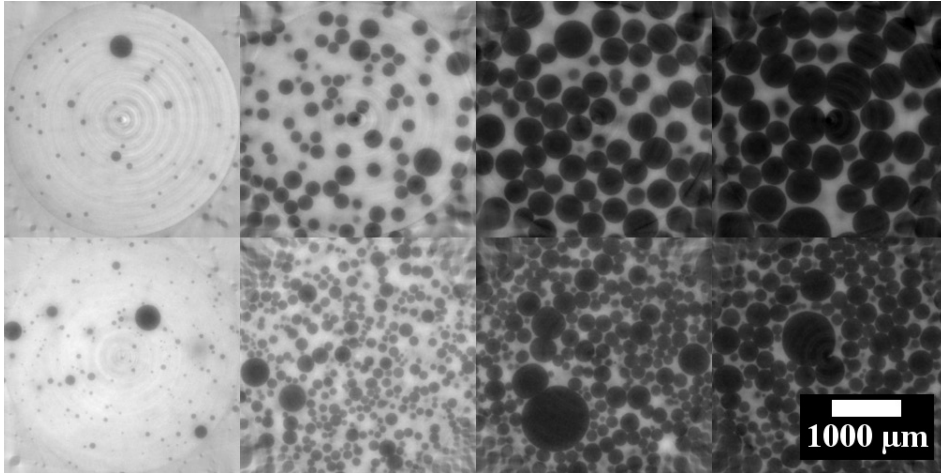


FIGURE 7-4.- RECONSTRUCTED PROJECTIONS OF TWO EXPERIMENTS AT 30S, 60S, 90S AND 120S AFTER COMPONENTS MIXING.

Finally, ultrafast scans with short interval time were also performed to visualize plastically the very early stages with the highest temporal resolution. These sequences of tomograms were initiated 9.8s after the components mixing. They consisted in 60 scans lasting 156ms/scan and only 1.4s of interval time. It is important to mention that in previous experiments the interval time was slightly increase as the expansion slows down so as to monitor as long as possible the complete foaming process. The buffer of RAM memory in TOMCAT pipeline is limited to about 60 scan under the selected conditions without any data downloading.

The results based on these challenging scans are presented below for two concrete selected formulations of the neat PU and Aerosil R812 3% wt. These examples were selected to characterize the enhanced nucleation provided by nanofillers addition for the first time.

“BUBBLE NUCLEATION AND GROWTH BY REAL-TIME SYNCHROTRON TOMOGRAPHY: A COMPARISON WITH CLASSICAL MODELS”

E. Solórzano¹, S. Pardo-Alonso¹, R. Mokso², M.A. Rodríguez-Pérez¹

¹CellMat Laboratory, Condensed Matter Physics Department, University of Valladolid, Paseo de Belén, 7 47011, Valladolid

²Swiss Light Source, Paul Scherrer Institute, Villigen, Switzerland

[email: esolo@fmc.uva.es]

Abstract

Bubble generation and growth has been observed by means of time-resolved synchrotron tomography for the first time in liquid materials showing spontaneous chemically-driven bubble generation in presence/absence of nucleating nanoparticles. The 3D computing allowed the determination of absolute nucleation rate versus time as well as the individual and average bubble growth dynamics. Complementarily, inhomogeneous spatial distribution of the bubbles at early stages could be addressed. Comparison with classical nucleation and growth models have been founded and reported in this work.

Introduction

Bubble generation and growing is an interesting issue both from the applicative (engineering analysis of industrial processes, i.e., polymeric foam production in injection moulding [4], elaboration of microcellular plastics [5], carbonated drinks [6,7], chemical industry [8], etc) and the theoretical (phase separation [9], solubility [10], nucleation [11], statistical mechanics [12]) points of view. The simultaneous generation and later growth of these individual entities is the result of thermodynamic instability in a specific gas-liquid system. Gas is dissolved in the liquid until it reaches its solubility limit and precipitated as metastable sub-microscopic bubble nucleus that may collapse or grow upon a critical –generally non reversible- diameter. This process requires overcoming a certain energy barrier from the thermodynamical point of view assumed in the classical homogeneous nucleation theory [13,14,15]. The subsequent bubble growth is a separate process involving, as well, diverse physical interactions. The classical equations governing these interactions are also well described in the literature and, among other facts, depend on the kinematic characteristics of the fluid [16,17,18,19].

The developed theoretical models may also consider further physical interactions altering the homogeneous bubble nucleation typical of purified media. This is the case

of presence of particles and/or solid impurities in the liquids or melts. Under this situation, perturbations at solid-liquid interface facilitate the formation of bubble nuclei nearby the solid surface that may increase the total number nucleated bubbles. This is the so-called heterogeneous nucleation process [11, 20] typically yielding superior bubble densities [21]. It is known that the shape and size of the particle influence the nucleation potential which tends to increase with particle-shape irregularity and downsizing [22]. Thus nanoparticles are ideal nucleating agents for bubbles [23]. Further physical and chemical interactions not considered within the models may occur after nucleation. As an example, bubble precipitation generally takes place during evolving conditions for the surrounding fluid thus varying viscosity, surface tension and other rheological properties [24,25]. Also the particles can be collected at bubble surface during bubble movement [26, 27] thus altering the predicted growth. Finally, it is also known that nanoparticles and specially those surface-treated ones may have a strong interaction with the chemistry of the fluid system [28], promoting particular reactions and definitely altering the rheological properties influencing the bubble evolution [29]. As a consequence, one of the most valid alternatives for studying non-ideal systems consists in carrying out empirical studies on those complex and rapidly evolving bubbles-liquid mixtures.

From the experimental point of view, there exist inherent difficulties for direct observation of nucleation since this phenomenon is strictly occurring at the nanoscale. In addition, the fast evolving dynamics require a high temporal resolution to visualize the created nuclei. Therefore the experimental approaches on nucleation are generally based on already nucleated bubbles when have grown up to the micrometer range. If we assume no reversibility of nucleation and/or absence of any degeneration mechanism -likely improbable at this early stage- the study of micrometric size “pubescent” bubbles is equivalent. A rather low number of works focused on these experimental studies can be found in the literature. Most of them use 2D optical methods which require transparent or translucent fluids allowing bubbles visualization in the container surface, in light-transmission mode, and generally using high spatio-temporal resolution. Among others examples of complexity we can cite the work by Guo *et. al* studying nucleation at ultra-high depressurization rates and using high pressures [2] and the work by Katagari *et. al* focused on the bubble nucleation of 3He at low temperatures [30]. In all these studies the low representativeness of the bubbles at surface might skew the results obtained. The use of penetrating radiation (X-rays) yields important improvements since it is possible to visualize all the bubbles present in depth. The time-resolved X-ray imaging –radioscopy- presents enormous potential for 2D examination of such systems, including molten metal/gas ones [31,32] but also brings collateral problems since a reduced thickness is needed to avoid excessive pore overlapping and the study is, then, still constrained to the bidimensional projection of evolving bubbles. This technique has been recently used to study the bubble nucleation and evolution in polyurethane/nanoparticles systems

yielding interesting results [33, 34]. The use of X-rays also brings the possibility of performing 3D studies –tomography- but they generally needed quasi-static conditions due to the high number of projections and the relatively long exposure time of X-ray detectors. Thanks to the last developments at synchrotron beamlines it is possible to carry out time-resolved X-ray tomography reaching unthinkable time resolutions few years ago. Special mention for the works of Mokso et al. [35] reaching up to 10Hz microtomography and the recent studies of gas bubbles formation in basaltic rocs [36].

This study makes use of time-resolved X-ray tomography to study the bubble generation and evolution of reactive polyurethane by reaching temporal resolutions of 156ms per tomographic scan which is, up to our knowledge, the second fastest tomographic scans published until now. The analysis of the results offered us a unique 3D insight to compare the real obtained data with the models predicting nucleation and growth of bubbles. We have constrained the analysis to the wet foam regimen in which still the bubbles are significantly separated one from the other and thus allowing free movements and growth.

Instrumentation

Materials:

A commercial bi-component polyurethane (PU) formulation from BASF was selected for this investigation. The turbulent mixing to two liquids (polyol and isocyanate) promotes a simultaneous blowing and gelling reaction that results into solid foam after a few minutes. The polyol and isocyanate components were Elastopor[®] H 1501/1 and IsoPMDI 92140 respectively, both owing low viscosity values [30, 31] which facilitates particle dispersion and makes easier the mechanical stirring. Hydrophobic fumed silica (pyrogenic silicon dioxide, aerosil R812, Evonik Industries, Germany) was the nucleating nanoparticle selected for the comparative study. Characteristics on the organo-compatibilization of this material can be founded at [37]. The nanocomposite formulation incorporated 3 %wt silica and was previously dispersed for 120 s in the isocyanate. *In-situ* turbulent mixing was promoted in order to follow the bubble generation from the very early instants. Polyol and isocyanate components were placed in a dedicated miniature cylindrical foaming mould (h=40mm, \varnothing =12mm, 75 μ m Kapton walls), coupled with the tomography rotating table. A motorized miniature stirrer in the top was automatically inversed in the liquids and stirred the mixture for 15 seconds at 1500 rpm promoting the blowing/polymerization reaction. The tomography scans started 10 seconds after the end of the mixing process.

***In situ* X-ray tomographic microscopy:**

X-ray tomographic microscopy was performed at the TOMCAT beamline of the Swiss Light Source at the Paul Scherrer Institute (Villigen, Switzerland). The ultrafast endstation incorporates a PCO.Dimax camera, which acquires and transfers data orders of magnitude faster than CCD cameras. The optics were coupled to LuAG:Ce 100 μm thick scintillator screen. Optical microscope lenses, with an adjustable magnification, were tuned to fourfold for this experiment. This corresponds to a pixel size of $3.2 \times 3.2 \mu\text{m}^2$ and a field of view of $6.44 \times 6.44 \text{ mm}^2$. Monochromatic X-rays (20KeV, no filter) were used; generating 500 projections captured over 180° of rotation with a total scan time of 150ms. Span time of 5 s was used in between scans. Reconstructions were performed by using the GRIDREC algorithm [38, 39] coupled with parzen filtering of the sinograms.

Image analysis and quantification:

Data collected at TOMCAT were quantitatively analysed with imageJ/FIJI and the *Pore3D* software library [40]. An edge preserving smoothing filter was applied, followed by a region growing segmentation algorithm to separate pore space (bubbles) from liquid. Basic 3D descriptors based on bubble number, bubble diameter and pore interspacing were analyzed at every scan (first 40 scans) and used to determine the statistics presented in the results sections.

Results:

Reconstruction of the time series of the tomographic scans allows to visualize, in 3D the process for bubbles nucleation and growth from the very beginning of the foaming process. Fig.1 shows the corresponding 3D renderings for four selected instants during the foaming process. It is clearly possible to appreciate the much higher bubble density in the nanocomposite foam containing hydrophobic silica (bottom).

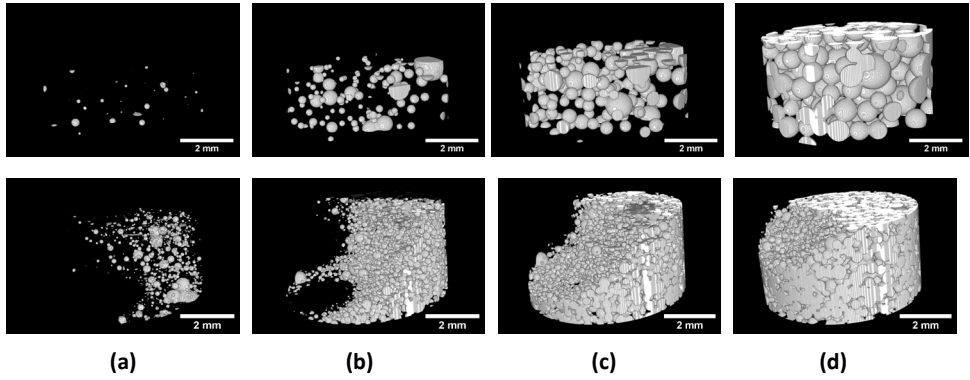


Fig 1. 3D rendering at different instants for the two examined materials –top, pure PU; bottom PU with 3 wt. nanosilica) at (a) 9.8s, (b) 21.7s, (c) 26.3s and (d) 32.6s.

Thanks to the tomograms acquisition and analysis major interesting results can be quantified. Fig.2 shows bubbles density evolution during expansion. The nucleation rate expresses the number of bubbles formed per unit time and appears to stabilize as foam expands as an Arrhenius law [41,42]. The values of nucleation density, $\langle N \rangle$, seems to follow sigmoid tendency, typically reported for theoretical models and simulations, at the very early stages of foaming processes [22,43]. These models combine thermodynamics and kinetics to determine the bubble nucleation rate during foaming processes. Blander and Katz [44] work permitted to derive final expressions, $\langle N \rangle$, also extensively reported in the literature, for the maximum nucleation rate at every instant in a heterogeneous nucleation process according to classical nucleation theory. However the actual nucleation rate may be significantly lower due to mass, heat or momentum transport limitations in the polymer. The terms involved in this process are the surface tension (σ), pressure difference (Δp), n that indicates the number of gas molecules per unit surface area of the nucleating centres, m which is the mass of a gas molecule and Q that is the ratio of the surface area of the liquid-gas interface to that of a spherical bubble with the same radius. It is also important to note that temperature, pressure increment and surface tension are evolving with time in this equation. Since the reactive foaming of PU generates the gaseous phase from an exothermic chemical reaction, it is feasible to attribute temperature the responsibility of nucleation rate evolution.

$$\langle N \rangle = n^{2/3} Q \sqrt{\frac{2\sigma}{\pi m f}} \exp\left(-\frac{16\pi\sigma^3 f}{3K_B T \Delta p^2}\right) \quad (\text{eq. 1})$$

It is also important to comment that the nucleation rate is higher for the material containing 3% wt. of nanosilicas since these fillers facilitate bubbles formation at solid/liquid interfaces due to free energy barrier reduction [45].

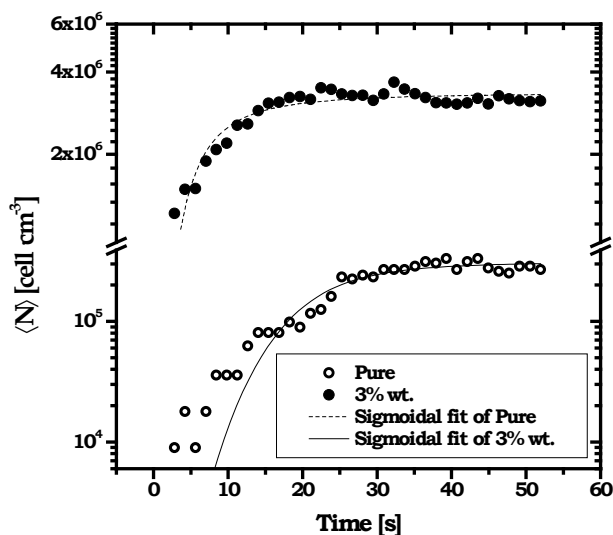


Figure 2. *In-situ* 3D cell density evolution compared with exponential growth tendency.

Experimental results on *in-situ* bubble equivalent diameter evolution are shown in fig.3. These values seem to fit well with infinite exponential growth model as the one reported by Patel [46] solving differential equations 2 and 3. In these equations the simultaneous bubble growth and pressure evolution are coupled together with the considered pressures inside (P_g) and outside (P_a) the expanding bubble, the viscosity (η_0), surface tension (σ) and bubble diameter (ϕ). In addition, the parameter a accounts for the gas diffusion coefficient and concentration, the molecular weight and density that are also involved into the process.

$$\frac{dP_g}{dt} = a \left(\frac{(P_{g0} - P_g)^2}{P_g \langle \phi \rangle^3 - P_{g0} \langle \phi \rangle^3} \right) - \frac{6P_g}{\phi} \frac{d\langle \phi \rangle}{dt} \quad (\text{eq. 2})$$

$$\frac{d\langle \phi \rangle}{dt} = \phi \left(\frac{P_g - P_a - \frac{\sigma}{\phi}}{4\eta_0} \right) \quad (\text{eq. 3})$$

Nevertheless, Amon and Denson model improves the single cell model initially used by Patel [47]. They introduced the necessary conditions and did not simplify the diffusion equation and considered limited amount of gas available to predict a finite bubble growth. However, this bubble growth stabilization is not observed in this study since the results presented here only focus on the first 60s of the expansion.

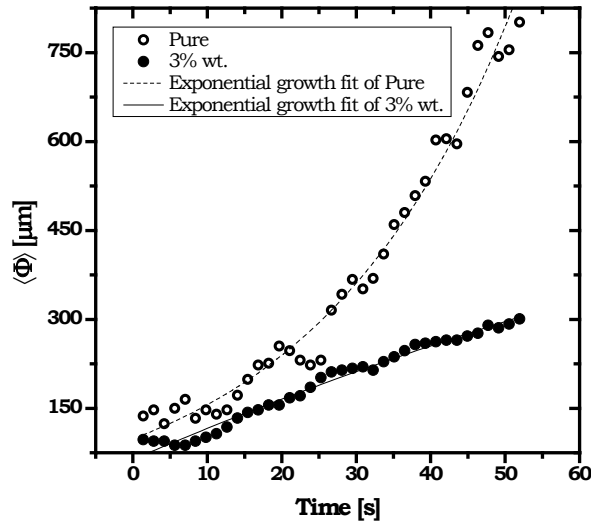


Figure 3. *In-situ* cell equivalent diameter compared with the theoretical models in the literature.

Furthermore we calculated the evolution of average pore interspacing during bubbles growth. This accounts for liquid distribution within the studied volume. Fig.4 shows a decrease of this magnitude both during the bubble nucleation (first order partitioning) and bubble expansion stages (second order partitioning). In the particular case of pure formulation we can visualize two clear trends for the first and second order volume partitioning which accounts for a clearer temporal separation among nucleation and growth. On the other hand in the modified formulation the volume is largely fragmented by the bubbles at initial stage. This aspect is not related to an enhanced nucleation but more probably to the air entrapments (first particle dispersion stage) combined with the lower gas diffusivity of the nanocomposite liquid. The standard deviation provides an idea about the bubble non-uniform distribution since some of them appear concentrated in certain regions where thermodynamic conditions are favourable due to the existing bubble interfaces. A clearer visualization of the fact mentioned is provided by the visualization of the pore interspacing analysis in two slices for the analyzed materials.

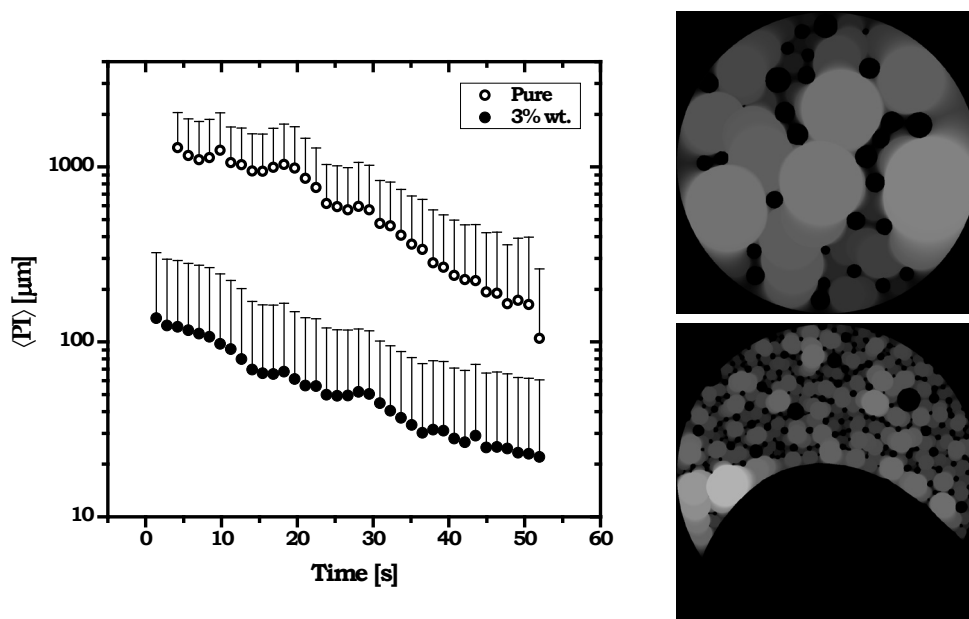


Figure 4. Average pore interspacing graph evolution with time and standard deviation. In the right it is possible to visualize two slice of the pure (top) and modified (bottom) formulations where the spatial in-homogeneity of nucleation is showed.

Conclusions

Bubble nucleation and growth phenomenon have been monitored for a first time in 3D with optimum time resolutions by using ultrafast synchrotron microtomography. The comparative foaming process of original and modified including nanoparticles- PU formulations has been studied with particular interest in the early stages. The nucleation process has been successfully monitored as regards of the evolving cell density results obtained. The results are compared with diverse theoretical models in the literature surprisingly finding a reasonably good fitting both in the case of nucleation rate and bubble growth which take place partially simultaneously with a refractory time for the bubble growth in comparison with nucleation. Nucleation inhomogeneity has been complementarily observed, since grouped bubble clusters seem to be formed while remaining volume remain unaltered. Differences in nucleation, growth and pore interspacing between the materials studied are justified within the proposed literature models.

REFERENCES

-
- [1] F. Marone, C. Hintermueller, R. Geus, and M. Stampanoni, IEEE Nuclear Science Symp. Conf. Proc., 2009, p. 5469.
- [2] Hintermueller C, Marone F, Isenegger A and Stampanoni M, 2010 Image processing pipeline for synchrotron-radiation-based tomographic microscopy, J. Synchrotron Radiat. 17 550–9
- [3] Marone F and Stampanoni M 2012 Regridding reconstruction algorithm for real-time tomographic imaging, J. Synchrotron Radiat. 19 1029–37
- [4] Mehdi Mahmoodi, Amir H. Behraves, S. A. Mohammad Rezavand, Amir Pashaei Visualization of Bubble Dynamics in Foam Injection Molding Journal of Applied Polymer Science, Vol. 116, 3346–3355 (2010)
- [5] Qingping Guo, Jin Wang, and Chul B. Park, Masahiro Ohshima A Microcellular Foaming Simulation System with a High Pressure-Drop Rate Ind. Eng. Chem. Res. 2006, 45, 6153-6161
- [6] Liger-Belair, G., Vignes-Adler, M., Voisin, C., Robillard, B., Jeandet, P., 2002. Kinetics of gas discharging in a glass of champagne: the role of nucleation sites. Langmuir 18, 1294–1301.
- [7] Barker, G.S., Jefferson, B., Judd, S.J., 2002. The control of bubble size in carbonated beverages. Chemical Engineering Science 57, 565–573.
- [8] M. Blander, D. Hengstenberg, J. L. Katz Bubble nucleation in n-pentane, n-hexane and n-pentane + hexadecane mixtures and water J. Phys. Chem., 1971, 75 (23), pp 3613–3619
- [9] I. N. Mishustin Nonequilibrium Phase Transition in Rapidly Expanding Matter Phys. Rev. Lett. 82, 4779–4782 (1999)
- [10] Gor GY, Kuchma AE. Dynamics of gas bubble growth in a supersaturated solution with Sievert's solubility law J Chem Phys. 2009 131(3):034507
- [11] Vincent K. Shen and Pablo G. Debenedetti A kinetic theory of homogeneous bubble nucleation JOURNAL OF CHEMICAL PHYSICS 118, 2, 768-783 (2003)
- [12] X.F Penga, Y Tien, D.J Lee Bubble nucleation in microchannels: statistical mechanics approach International Journal of Heat and Mass Transfer 44, 15, 2001, 2957–2964

-
- [13] Abraham, F.F., 1974. Homogeneous Nucleation Theory. Academic Press, New York.
- [14] Blander, M., 1975. Bubble nucleation in liquids. A.I.Ch.E. Journal 21,833–848.
- [15] Jones, S.F., Evans, G.M., Galvin, K.P., 1999. Bubble nucleation from gas cavities—a review. Advances in Colloid and Interface Science 80, 27–51.
- [16] Patel, R.D., 1980. Bubble growth in a viscous Newtonian liquid. Chemical Engineering Science 35, 2352–2356.
- [17] Street, J.R., Fricke, A.L., Reiss, L.P., 1971. Dynamics of phase growth in viscous non-Newtonian liquids. Industrial Engineering Chemical Fundamentals 10, 54–64.
- [18] Shafi, M.A., Flumerfelt, R.W., 1997. Initial bubble growth in polymer foam processes. Chemical Engineering Science 52, 627–633.
- [19] Moshe Favelukis , Ramon J. Albalak Bubble growth in viscous newtonian and non-newtonian liquids The Chemical Engineering Journal 63 (1996) 149-155
- [20] James J. Feng Prediction of bubble growth and size distribution in polymer foaming based on a new heterogeneous nucleation model
- [21] W.L. Ryan, E.A. Hemmingsen, Bubble formation in water at smooth hydrophobic surfaces. J.Colloid Interf. Sci. 157 1993 312-317
- [22] Colton, J.S. and Suh, N.P., “The Nucleation of Microcellular Thermoplastic Foam with Additives: Part I: Theoretical Considerations,” 27, 7, 485–492, 1987
- [23] L. James Lee, Changchun Zeng, Xia Cao, Xiangming Han, Jiong Shen, Guojun Xu Polymer nanocomposite foams, Composites Science and Technology 65, 15–16, 2005, 2344–2363
- [24] Lu Feng, M.S. Experimental Study of Nucleation in Polystyrene/CO₂ System Ph. D Thesis The Ohio State University 2012
- [25] Siu Ning Sunny Mechanisms of cell nucleation, growth, and coarsening in plastic foaming: theory, simulation, and experiment, Ph.D. Thesis Leung University of Toronto 2009
- [26] David Reay, G. A. Ratcliff, Removal of fine particles from water by dispersed air flotation: Effects of bubble size and particle size on collection efficiency The Canadian Journal of Chemical Engineering 51, 2, 178–185, 1973

-
- [27] Zongfu Dai, Stanislav Dukhin, Daniel Fornasiero, John Ralston, The Inertial Hydrodynamic Interaction of Particles and Rising Bubbles with Mobile Surfaces *Journal of Colloid and Interface Science* 197, 2, 1998, 275–292
- [28] M. Mar Bernal, Miguel Angel Lopez-Manchado, Raquel Verdejo In situ Foaming Evolution of Flexible Polyurethane Foam Nanocomposites *Macromolecular Chemistry and Physics* 212, 9, 971–979, 2011
- [29] Raquel Verdejo, Francisco J. Tapiador, Lukas Helfen, M. Mar Bernal, Natacha Bitinis, Miguel A. Lopez-Manchado Fluid dynamics of evolving foams, *Phys. Chem. Chem. Phys.*, 2009, 11, 10860-10866
- [30] Masanori Katagiri, Shigeyuki Izumi, Jun'ya Hori, Yoshiko Fujii, Keisaku Hatanaka Visualization of Bubble Nucleation in Boiling 3He *Journal of Low Temperature Physics* 2007, 148, 3-4, 127-132
- [31] F García Moreno, M Fromme, J Banhart Real-time X-ray Radioscopy on Metallic Foams Using a Compact Micro-Focus Source *Advanced Engineering Materials* 6 (6), 416-420
- [32] Alexander Rack, Francisco García-Moreno, Lukas Helfen, Manas Mukherjee, Catalina Jiménez, Tatjana Rack, Peter Cloetens, and John Banhart Hierarchical radioscopy using polychromatic and partially coherent hard synchrotron radiation *Applied Optics*, Vol. 52, Issue 33, pp. 8122-8127 (2013)
- [33] S. Pardo-Alonso, E. Solórzano, S. Estravís, M. A. Rodríguez-Perez and J. A. de Saja In situ evidence of the nanoparticle nucleating effect in polyurethane–nanoclay foamed systems *Soft Matter*, 2012, 8, 11262-11270
- [34] S. Pardo-Alonso, E. Solórzano, M.A. Rodríguez-Perez Time-resolved X-ray imaging of nanofiller-polyurethane reactive foam systems *Colloids and Surfaces A: Physicochemical and Engineering Aspects*, 438, 2013, 119-125
- [35] R. Mokso, F. Marone, D. Haberthur, J. C. Schittny, G. Mikuljan, A. Isenegger, and M. Stampanoni, Following Dynamic Processes by X-ray Tomographic Microscopy with Sub-second Temporal Resolution, 10th International Conference on X-Ray Microscopy, 1365, 38-41 (2011).
- [36] Baker, D.R. et al. A four-dimensional X-ray tomographic microscopy study of bubble growth in basaltic foam. *Nat. Commun.* 3:1135
- [37] A.A. Chuiko, Y.I. Gorlov Chemistry of a silica surface, *Naukova Dumka*, Kyiv (1992)

[38] Dowd, B. et al. Developments in synchrotron X-ray computed tomography at the National Synchrotron Light Source. *Developments in X-ray tomography II*. Proc. SPIE 3772, 224–236 (1999).

[39] Rivers, M. L. & Wang, Y. Recent developments in microtomography at GeoSoilEnviroCARS. *Developments in X-ray tomography V*. Proc. SPIE 6318, J3180 (2006).

[40] Brun, F. et al. Pore3D: a software library for quantitative analysis of porous media. *Nucl. Instr. Methods Phys. Res. A* 615, 326–332 (2010).

[41] Colton, J.S., “The Nucleation of Microcellular Foams in Semicrystalline Thermoplastics,” *Materials and Manufacturing Processes*, Vol. 4, No. 2, pp. 253-262, 1989

[42] Colton, J.S. and Suh, N.P., “The Nucleation of Microcellular Thermoplastic Foam with Additives: Part II: Experimental Results and Discussion,” *Polymer Engineering and Science*, Vol. 27, No. 7, pp. 493-499, 1987

[43] Shimoda, M., Tsujimura, I., Tanigaki, M. and Ohshima, M., “Polymeric Foaming Simulation for Extrusion Processes,” *Journal of Cellular Plastics*, Vol. 37, No. 6, pp. 517-536, 2001.

[44] Blander, M. and Katz, J.L., “Bubble Nucleation in Liquids,” *AIChE Journal*, Vol. 21, No. 5, pp. 833-848, 1975.

[45] Ramesh, N.S., Rasmussen, D.H. and Campbell, G.A., “The Heterogeneous Nucleation of Microcellular Foams assisted by the Survival of Microvoids in Polymers Containing Low Glass Transition Particles. Part I: Mathematical Modeling and Numerical Simulation,” *Polymer Engineering and Science*, Vol. 34, No. 22, pp. 1685-1697, 1994.

[46] Patel, R.D. (1980), “Bubble growth in a viscous Newtonian liquid”, *Chemical Engineering Science*, Vol. 35, pp. 2352-6.

[47] Amon, M. and Denson, C.D. (1984), “A study of the dynamics of foam growth: analysis of the growth of closely spaced spherical bubbles”, *Polymer Engineering Science*, Vol. 24, pp. 1026-34.

8. CONCLUSIONS AND PERSPECTIVES

This section summarizes the main conclusions and remarkable achievements accomplished in this investigation.

The main objective of this investigation was to reveal X-ray imaging as a powerful characterization technique when it is applied to low X-ray absorbing materials, i.e. polymer foams. The main conclusion achieved is that X-ray imaging permits to investigate cellular structure both *in-situ* during foaming and *ex-situ* in its final state. This conclusion is drawn from the results provided by the developments on X-ray imaging devices (1), the design of experimental setups aimed at cellular structure investigation during foaming (2), the methodologies based on image analysis to quantify characteristic parameters (3) and the studies on foaming mechanisms (4) and cellular structure (5) of selected foams.

(1) X-RAY IMAGING DEVICES TO INVESTIGATE CELLULAR STRUCTURE EVOLUTION AND FOAMING MECHANISMS:

We have design, built and optimized high-resolution X-ray imaging system with high sensitivity for polymer foams visualization and characterization of the cellular structure evolution during expansion.

(2) EXPERIMENTAL SETUPS TO VISUALIZE CELLULAR STRUCTURE EVOLUTION DURING FOAMING:

We have designed and built different foaming setups to obtain information from radiographic sequences:

- A thin foaming frame permitted visualization of a few cells in depth allowing quantification of density and cell size evolution by image analysis in reactive foaming processes at room temperature. This allowed to investigate cell nucleation, growth and coalescence in some particular formulations.
- Cell nucleation was studied in thermoplastic foaming processes requiring heating conditions inside a thin frame with a resistive heater providing unidirectional heat flux and a thermocouple to control temperature evolution.
- Cell degeneration mechanisms, i.e. coalescence/ruptures, in thermoplastics to evaluate and discuss the effect of temperature and polymer rheology.

Moreover, an *in-situ* stirrer to promote reactive polyurethane foaming was developed together with a setup aimed at ultrafast tomography experiments for cell nucleation characterization in 3D with temporal resolution.

(3) THE DEVELOPMENT OF IMAGE ANALYSIS BASED METHODOLOGIES:

The developments of methodologies permitted to obtain quantitative data on density profiles and cell size evolution during the foaming processes. Information about all the stages of a dynamic process has been collected for the first time. It has been possible to obtain *in-situ* quantitative cell density evolution from density and cell size values to understand phenomena related to foam physics in polymeric systems (nucleation, growth and stabilization).

On the other hand, tomograms analysis and advanced 3D computation algorithms allowed a new approach into the analysis of cellular materials thanks to the chances of de-structure the continuous solid network in its constituents: struts and cell walls. The separation of this components permits to calculate the material distribution at the walls, edges and vertexes across the solid skeleton that can be translated into valuable information for modelling and understanding cellular structures.

Design and development of image analysis procedures and methodologies allowed extracting advanced cellular architecture descriptors from tomograms. Part of these advanced methods is supported in the frame of the de-structuration concept developed. The developed process permits to de-structure the solid skeleton of the foams into two main parts, the cell walls and the struts (edges + vertexes). This is done with reasonable simplicity based on the morphological dissimilarities of struts and walls by either an iterative method based on binary operations or a solid classification algorithm. The methodology provides an essential tool to evaluate advanced characteristics that are not accessible by analysing the cellular structure of foams as continuous entities.

(4) FOAMING MECHANISMS AND CELLULAR STRUCTURE EVOLUTION OF POLYMER FOAMS:

The X-ray visualization offers a novel insight with temporal resolution in the modification of foaming mechanisms when formulations and/or processing variables are modified. A collection of thermoset (rigid and flexible PU foams) and thermoplastic (low density polyethylene, linear and high melt strength polypropylenes) systems has been selected to investigate cellular structure evolution and obtain new knowledge about foaming mechanisms. We sum up some of the main results concerning the specific materials selected for each purpose:

- Nanoclays (Cloisite 30B) addition to a BASF rigid PU formulation does not significantly affect density evolution. On the other hand, cell size is influenced by presence of nanoclays throughout the foaming process. 5% wt. content of this filler reduces up to 45% the cell size. A higher density of nucleation sites acts as pore formation centres from the very early stages of the foaming process. There is no visual evidence of cell degeneration, namely pore

coalescence, nor coarsening, in any of the studied systems. The cell density calculations confirm the absence of cell degeneration: this is a constant value during expansion. Therefore, the main effect of nanoclays in this system is as nucleating agent.

- Density evolution is altered by hydrophobic surface-treated particles (i.e. Aerosil R812 silicas) that are found to slow down the expansion process. Contrary, nanosilicas with no surface modification (Aerosil A200) did not alter the expansion process. The specific chemical interactions of the particles with the reactants of the PU system under analysis together with the modification of the system viscosity play a key role on the expansion kinetics modifications observed.
- According to the cell density evolution results, nanoclays promoted an enhanced cell nucleation yielding smaller cell size than nanosilicas.
- The rheological behaviour of the selected formulations of flexible polyol/CNP dispersions is influenced by the nanoparticles, particularly in the case of MWCNTs. Expansion kinetics is delayed by the CNPs, probably due to a combination of enhanced viscosity (physical interaction) and a delay in the blowing kinetics (chemical interaction). Addition of MWCNT and f-GS provides a significant enhancement of cell nucleation.
- The hydrophilic or hydrophobic behaviour of carbon nanoparticles surface influences the cellular structure evolution of reactive PU nanocomposite foams. This is also corroborated by the chemical processes observed for these systems by *in-situ* FTIR and synchrotron SAXS. Cell size evolution is determined by the chemical interaction of the PU formulation with the CNPs added. Particles promoting higher nucleation rate due to a bridging-dewetting mechanism and surface morphology, also promoted coalescence driving to lower cell densities.
- ALCUDIA PE-003 polyethylene presents a similar nucleation capability for cells generation of linear polypropylene from Total (PPH 4070). Contrary, PP DAPLOY WB135HMS exhibits rather low nucleation ability.
- Calculations on cell size evolution indicate that cell growth and number of nucleated pores are anticorrelated when the same heating conditions are applied in the polyolefin foams under study.

- The analysis of ruptures in PP has been challenging due to the long rupture relaxation times and the large amount of material involved in each rupture. The characteristic pattern of coalescence in these systems has been reported for the first time. The results obtained might be influenced by the set up conditions and do not reveal the higher differences expected in between polymers.
- Ultrafast synchrotron microtomography permitted to monitor cells nucleation and growth for the first time in 3D with optimum time resolutions. This permitted to study foaming process at the early stages of original and modified -including nanoparticles- PU formulations. The results are compared with diverse theoretical models in the literature surprisingly found a good fitting both in the case of nucleation rate and bubble growth which take place partially simultaneously with a refractory time for the bubble growth in comparison with nucleation. Additionally, nucleation was observed to occur inhomogeneously, since bubble nucleate in grouped clusters.

(5) 3D ADVANCED CHARACTERIZATION OF POLYMER FOAMS' CELLULAR STRUCTURE:

3D micromography based study permitted to characterize the final cellular structure of PU foams in terms of morphological and topological cellular architecture descriptors. Some concrete results are listed below:

- Average cell size decreases and cell size distribution displaces towards smaller values due to nanoclays (Cloisite 30B) addition to rigid PU from BASF. Nanoclays presence also altered cell anisotropy and pore free orientation.
- It is found that 1% wt. content of these clays provides optimum cellular structure since cell size becomes significantly reduced and distribution is quasi-Gaussian while anisotropy, coordination number and material distribution across the foam skeleton remain unaltered. The incorporation of amounts above 3% wt. in this system increased the strut volume fraction.
- Strut volumetric fraction is calculated for the first time using mCT in rigid closed cell PU foams with high dissimilarities in between struts and walls thickness. Strut solid fraction above 0.7 was determined.
- In particular, four methods are presented and discussed to study four low-density closed cell polyolefin based foams, i.e. local thickness, tortuosity, curvatures and corrugation ratio. The identified presence of corrugated cell

walls correlates well with mechanical behaviour at compression load. This 3D computational methodology allowed to measure several important microstructural features of foams that are difficult to obtain applying conventional methods.

FUTURE PERSPECTIVES

This is the first investigation in CellMat about imaging techniques applied to polymer foams research. For this reason, it does not only intend to be a dissertation to present and discuss the main results but also to be a manual collecting some of the important concepts and methods to understand the works and carry out further works in this area. This fact closely connects with one of the main objectives stated: *“Establish a solid scientific basis to allow further development of X-ray imaging as a powerful technique in cellular polymers research”*.

We have presented X-ray imaging as a powerful research tool applied to polymer foams characterization. In fact, there is a vast research area for the scientific imaging community which is nowadays focused on 4D imaging thanks to synchrotron sources and latest advances in X-ray tubes. On the other hand, there is also a no less important application; the non-destructive inspection frequently carried out in the industry. Nevertheless, there is still nowadays a gap between scientific imaging community, using large scale facilities and focused on highly developed specific applications, and industrial common necessities. It is at this point in which researchers on materials science and other disciplines such as biology or geology can provide the necessary bridge to connect imaging developments and industrial applications. This dissertation is a tiny part contributing to this purpose since it was originally conceived to *“provide scientific basis and a better understanding of the foaming mechanisms governing the process-structure-properties relationship by and X-ray imaging based methodology”*

To conclude we propose some research topics which are expected to be addressed during the near future work. Challenges are focused on investigating more complex foaming systems (foaming systems involving pressure, etc.), improving time and spatial resolution and the use of other radiation sources such as neutrons. We list below some of these topics:

- CellMat X-ray imaging developed in this investigation can be converted into μ CT scanner optimized for tomograms acquisition of polymer foams.
- To develop more advanced algorithms aimed at detecting ruptures based on image analysis can be developed. The long relaxation time of coalescence mechanism in polymers is a challenging peculiarity to overcome. In fact, this can be of applicability to detect ruptures in 3D by analyzing ultrafast tomograms.

- The advanced 3D procedures presented could be applied to other type of foams, i.e. aqueous foams, metallic foams, etc. Especially de-structuration methodology is of potential applicability to get information about material distribution across any type of foamed structure. In addition, it is now possible to study microporosity at struts, typically found for some foams. This information about material distribution across the cellular structure into struts and walls can be also used for physical properties modelling
- New setups can be designed, especially for time-resolved ultrafast tomography experiments. Thermoplastics foaming is of special interest and at the same time challenging since it involves the use of temperature.
- 4D imaging can be developed at lab-scale imaging devices thanks to latest developments in X-rays tubes technology and detection systems.
- Similar works can be done by using other radiation sources such as neutrons. As it has been shown, neutrons are highly absorbed by polymers which, in principle, facilitates absorption imaging. However, some difficulties related to low flux available still need further efforts.

RESUMEN EN ESPAÑOL

Las espumas poliméricas son materiales celulares que poseen una fase continua y otra gaseosa bien discontinua (celda cerrada) o continua (celda abierta). En particular, las espumas se producen desde el estado fundido. Habitualmente estas estructuras se describen mediante parámetros macroscópicos como la densidad relativa y otros microscópicos como el tamaño de celda o la densidad de celdas. Además, estos materiales poseen características peculiares como anisotropía, orientación de los poros y tortuosidad que les proporcionan propiedades físicas singulares.

Convencionalmente el estudio de las espumas poliméricas se realiza mediante el análisis de la estructura celular final obtenida. Ello se debe principalmente a que no es posible detener el proceso de expansión una vez se ha iniciado. Debido a esto los estadios intermedios durante los procesos de espumado no son accesibles, es decir, no se obtiene información acerca de los mecanismos que generan la estructura final. Estos mecanismos físico-químicos fundamentales que gobiernan la generación y evolución de la estructura celular durante el espumado son la nucleación y el crecimiento. Por el contrario, existen otros mecanismos que son responsables de la degeneración de la estructura celular son el drenaje, la coalescencia y el *coarsening*.

Los inconvenientes que existen para abordar el estudio de estos mecanismos durante el proceso de espumado, junto con las peculiaridades de estos sistemas hacen que las técnicas de imagen mediante rayos X sean una herramienta extraordinaria para el estudio *in-situ* de la evolución de la estructura celular y los mecanismos de espumado. Además, de manera complementaria, la imagen mediante rayos X permite la obtención de tomogramas para el estudio de la estructura celular en el estado final. Incluso es posible llegar más lejos gracias a los últimos desarrollos en tomografía rápida. Esta técnica es capaz de estudiar en 3D la evolución de la estructura celular en el tiempo.

Uno de los requisitos esenciales para el estudio de las espumas poliméricas mediante la imagen con rayos X y que condiciona su aplicabilidad es correcta selección de los componentes y el diseño del equipo de imagen. Esto se debe principalmente a características intrínsecas a las espumas poliméricas: baja absorción de los rayos X, espesores reducidos, estructura de celdas en el rango micrométrico, rápida evolución durante su fabricación y otras peculiaridades morfológicas de su estructura.

Esta investigación se centra en presentar la imagen mediante rayos X como una técnica novedosa capaz de proporcionar datos científicos relevantes sobre el comportamiento de las espumas poliméricas. Para ellos se hace uso del diseño y construcción de un equipo de radioscopia, el desarrollo de experimentos destinados a la realización de ensayos de espumado en el equipo de radioscopia, el desarrollo de procedimientos de cuantificación basados en técnicas de análisis de imagen, el estudio de mecanismos de espumado en sistemas poliméricos seleccionados y el estudio de la estructura celular en 3D.

DISEÑO Y CONSTRUCCIÓN DE UN SISTEMA DE RADIOSCOPIA PARA EL ESTUDIO DE MARTIRIALES CELULARES POLIMÉRICOS:

La investigación presenta la descripción de un equipo de rayos X optimizado para el estudio de los procesos de espumado. El microfoco, la emisión a bajas energías (bajo kilovoltaje y microamperaje) y la conicidad del haz que emite la fuente seleccionada, junto con la alta sensibilidad del panel detector seleccionado, permiten la adquisición de imágenes de alta resolución válidas para la cuantificación de perfiles de densidad y otros parámetros morfológicos como el tamaño de celda.

DESARROLLO EXPERIMENTAL PARA LA REALIZACIÓN DE ENSAYOS DE ESPUMADO Y SU ESTUDIO MEDIANTE RAYOS-X:

Gracias a la combinación del equipo de radioscopia con el diseño de experimentos orientados a la visualización de la estructura celular es posible obtener información *in-situ* durante los procesos de espumado acerca de los mecanismos de generación celular nucleación y crecimiento. Uno de los requisitos fundamentales, para la correcta visualización y su posterior cuantificación, es la presencia de pocas celdas en profundidad; idealmente una.

PROCEDIMIENTOS DE CUANTIFICACIÓN BASADOS EN EL ANÁLISIS DE IMAGEN:

El desarrollo y la aplicación de metodologías basadas en el análisis de imagen permiten obtener datos cuantitativos de las secuencias de radiografías adquiridas. La estrategia seguida consiste fundamentalmente en el filtrado de imágenes para su posterior binarización y aplicación de algoritmos de segmentación. Los resultados que se obtienen del estudio *in-situ* de procesos dinámicos como son los de espumado corresponden básicamente a la evolución de perfiles de densidad macroscópica y del tamaño medio de celda.

De manera complementaria, se estudian en los parámetros morfológicos 3D que se pueden extraer del análisis completo de tomogramas. Los resultados que se obtienen abarcan la distribución de tamaño medio de celda, orientación, anisotropía y número de vecinos. Mediante el desarrollo de algoritmos basados en el análisis de imagen, se evalúan parámetros avanzados. Éstos son capaces de ofrecer información no accesible mediante otras técnicas de imagen de uso convencional, como microscopía óptica o electrónica. En particular, el método de desestructuración que se presenta permite estudiar la distribución del material polimérico a lo largo de la estructura celular. La técnica que se desarrolla separa virtualmente las entidades individuales que constituyen la estructura celular: paredes y aristas. Gracias a esta separación es posible calcular estudiar la fracción de material en aristas y paredes.

Además, un análisis más fino de segundo orden sobre las paredes separadas virtualmente permite evaluar la presencia de arrugas en las paredes, gracias al cálculo de magnitudes como la curvatura, el espesor local, el ratio de arrugas y la tortuosidad de la fase sólida.

APLICACIÓN DEL EQUIPO DE RAYOS X DISEÑADO AL ESTUDIO DE LA EVOLUCIÓN DE LA ESTRUCTURA CELULAR Y LOS MECANISMOS DE ESPUMADO:

De acuerdo con las distintas posibilidades que ofrece la imagen mediante rayos X se presenta una serie de trabajos centrados en el estudio de los mecanismos de espumado mediante radioscopia (radiografía con resolución temporal), microtomografía y tomografía ultrarrápida con resolución temporal.

Gracias a los experimentos diseñados y la aplicación de los procedimientos de análisis de imagen es posible evaluar la influencia de parámetros de proceso, como la temperatura, y otros relacionados con la naturaleza del material, como el comportamiento reológico. Las investigaciones, recogidas en las publicaciones científicas que se presentan, utilizan los moldes y *setups* diseñados en varios sistemas poliméricos: espumado reactivo de poliuretano rígido y flexible y espumas de poliolefinas (polietileno y polipropileno). Estos sistemas se seleccionan fundamentalmente según el objetivo de cada investigación basándose en el conocimiento previo y pretenden observar en cada uno de ellos los efectos de un fenómeno concreto con la menor interferencia de otros posibles mecanismos. Estos resultados se recogen en cuatro trabajos cuyo nivel de dificultad se incrementa progresivamente al abordar cada vez más mecanismos con los siguientes objetivos:

- Estudiar *in-situ* de los efectos de la adición de nanoarcillas en el mecanismo de nucleación de celdas en el espumado reactivo de poliuretano rígido. Se analiza la evolución de la densidad, el tamaño promedio de poro y la densidad de poros.
- Estudiar de los efectos de nanoarcillas y nanosílicas con y sin tratamiento superficial sobre la cinética de expansión y la evolución de la estructura celular del espumado de poliuretano rígido.
- Investigar desde el punto de vista químico y físico el efecto de las nanopartículas de carbono con diferente naturaleza en el espumado de poliuretano flexible.
- Evaluar el efecto de la temperatura y las propiedades reológicas de las poliolefinas en los mecanismos de nucleación y crecimiento de celdas durante el espumado.

De manera complementaria, gracias a la tomografía ultrarrápida, es posible dar un paso más y visualizar y cuantificar en 3D la nucleación y el crecimiento de las celdas. Esta información mediante radioscopia sólo era accesible en 2D. Esto permite

presentar resultados de evolución de la densidad de celdas, la tasa de nucleación con el tiempo, volumen y distancia entre poros con el tiempo. En la literatura existen diversos modelos y simulaciones sobre el comportamiento, pero ninguna otra técnica permite una medida experimental tan directa como en este caso.

ANÁLISIS 3D DE LA ESTRUCTURA CELULAR MICROTOMOGRAFÍAS DE RAYOS X Y CÁLCULO DE DESCRIPTORES MORFOLÓGICOS AVANZADOS:

Mediante el análisis de tomogramas y la aplicación de las metodologías desarrolladas en la investigación se presentan resultados sobre los siguientes objetivos:

- Estudiar la influencia de las nanoarcillas sobre la estructura celular de las espumas rígidas de poliuretano. Para ello, fundamentalmente se centra el estudio en la distribución del tamaño de poro, la anisotropía, la orientación de los poros y el número de vecinos. También se aborda la influencia sobre la distribución del material a lo largo de la estructura celular entre paredes y aristas.
- Investigar la presencia de arrugas en las paredes celulares de espumas poliolefínicas de celda cerrada y relacionarlas posteriormente con propiedades físicas como el esfuerzo de colapso de las espumas seleccionadas. Con este fin se aplican los métodos de análisis de imagen desarrollados para la cuantificación de espesor local, tortuosidad, curvatura y ratio de corrugación. Una de las técnicas de especial importancia a la hora de evaluar estos descriptores avanzados es la segmentación de las estructuras celulares en paredes y aristas para su análisis.

Las conclusiones de la investigación se centran en el desarrollo que se ha hecho de la imagen mediante rayos X como técnica válida y de gran utilidad para el estudio de las espumas poliméricas a través de los resultados presentados y desarrollados sobre:

- La influencia de las nanopartículas, la temperatura y la reología del polímero en los mecanismos de espumado: nucleación, crecimiento y coalescencia.
- La información 3D sobre la estructura celular generada mediante el análisis convencional y avanzado de tomogramas.

